Differential cross section measurements for the production of top quark pairs and of additional jets using dilepton events from pp collisions at $\sqrt{s} = 13\,\text{TeV}$

The CMS Collaboration*

arXiv:2402.08486v2 [hep-ex] 24 Feb 2025

Abstract

Differential cross sections for top quark pair ($t\bar{t}$) production are measured in proton-proton collisions at a center-of-mass energy of 13 TeV using a sample of events containing two oppositely charged leptons. The data were recorded with the CMS detector at the CERN Large Hadron Collider and correspond to an integrated luminosity of 138 fb^{-1}. The differential cross sections are measured as functions of kinematic observables of the $t\bar{t}$ system, the top quark and antiquark and their decay products, as well as of the number of additional jets in the event. The results are presented as functions of up to three variables and are corrected to the parton and particle levels. When compared to standard model predictions based on quantum chromodynamics at different levels of accuracy, it is found that the calculations do not always describe the observed data. The deviations are found to be largest for the multi-differential cross sections.

*See Appendix D for the list of collaboration members

1 Introduction

Measurements of top quark pair ($t\bar{t}$) production play a crucial role in testing the validity of the standard model (SM) and in searching for new phenomena [1]. The large data set of proton-proton (pp) collisions delivered during Run 2 at the CERN Large Hadron Collider (LHC) in the years 2016 through 2018 enables precision studies of $t\bar{t}$ differential production cross sections as functions of kinematic variables of various objects produced in the events. The differential measurements provide sensitivity to many new physics scenarios [2–10] for which the $t\bar{t}$ event topologies and kinematical distributions are different from those in the SM. The present analysis focuses on events in the $t\bar{t}$ dilepton decay channel, shown in Fig. 1, where both W bosons decay into a charged lepton and a neutrino. Kinematic observables of the following objects are studied in the analysis: the $t\bar{t}$ system, the top quark (t) and antiquark ($\bar{t}$), the charged leptons (ℓ and $\bar{\ell}$) and bottom quarks (b and $\bar{b}$) produced in the decay chain, and the additional jets in the event. Electrons and muons produced directly in the W boson decays are considered as signal, while τ leptons are not. The bottom quarks are experimentally accessible through the associated b jets.

In the SM context, the measured cross sections can be used to check predictions of perturbative quantum chromodynamics (pQCD) and electroweak theory. During the last decade, a variety of next-to-next-to-leading order (NNLO) predictions [11–16] have become available for kinematic observables of the $t\bar{t}$ system, top quark and antiquark, and recently also of the final-state leptons and b jets [17]. The situation is different for $t\bar{t}$ events with additional energetic jets in the final state, which, at LHC energies, contribute a large fraction to the total $t\bar{t}$ cross section. The NNLO corrections are not yet established for these high multiplicity radiative processes; nevertheless, a comparison of the available pQCD models to data provides an important benchmark test.
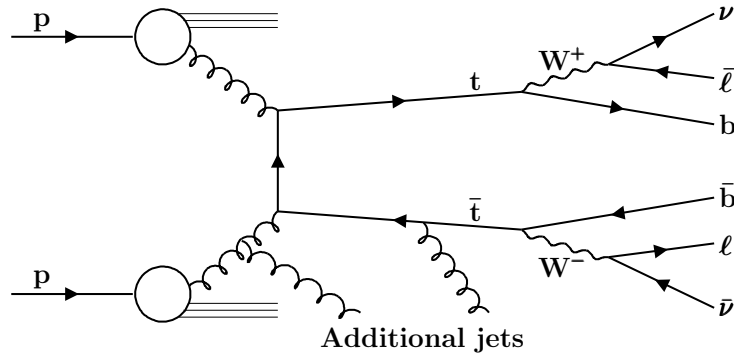

Figure 1: Illustration of a pp collision with $t\bar{t}$ plus additional jet production and subsequent dilepton decay of the $t\bar{t}$ system.

Differential cross sections for $t\bar{t}$ production have been measured previously in pp collisions at the LHC at $\sqrt{s} = 7\,\text{TeV}$ [18–22], $8\,\text{TeV}$ [22–29], and $13\,\text{TeV}$ [30–47], in the channels with either both, one, or neither of the W bosons emitted in the decays of t and $\bar{t}$ decaying leptonically. The nominal predictions of modern pQCD calculations generally fail to describe several kinematic distributions. For instance, most theoretical models predict a spectrum for the transverse momentum p_T of the top quark, that is harder than observed [37, 38].

We present measurements of differential $t\bar{t}$ cross sections in pp collisions at $\sqrt{s} = 13\,\text{TeV}$ using data taken with the CMS detector during the Run-2 operation of the LHC. The analysis is based on an integrated luminosity of $138\,\text{fb}^{-1}$, where $36.3\,\text{fb}^{-1}$ were recorded in 2016, $41.5\,\text{fb}^{-1}$ in 2017, and $59.7\,\text{fb}^{-1}$ in 2018. The dilepton decay channel has a relatively small branching fraction and significantly lower background compared to other $t\bar{t}$ decay channels. As a consequence

of the excellent lepton energy resolution, the precise measurement of kinematic observables based on lepton pairs is unique to the dilepton channel. However, because of the presence of two neutrinos in the final state, the measurement of top quark kinematic observables in the dilepton channel requires specialized kinematic reconstruction techniques.

The analysis follows the procedures and strategies of Refs. [38, 39] for which only the 2016 data were used. All measurements are compared to predictions from Monte Carlo (MC) generators with next-to-leading order (NLO) accuracy in QCD at the matrix element level interfaced to parton shower simulations. Selected cross section measurements are also compared to a variety of predictions with precision beyond NLO.

The distributions studied in this paper are of basic kinematic observables including the p_T, and pseudorapidities η or rapidities y of single objects, e.g. $p_T(t)$ and $y(t)$, or of compound systems, e.g. $p_T(t\bar{t})$ and $y(t\bar{t})$. Distributions of invariant masses of compound objects are also investigated, e.g. $m(t\bar{t})$, as well as the azimuthal or rapidity differences between two objects, e.g. $|\Delta\phi(t,\bar{t})|$, $|y(t)| - |y(\bar{t})|$, and $|\Delta\eta(t,\bar{t})|$, where ϕ is the azimuthal angle in radians. Cross sections are measured at the particle level in a fiducial phase space that is close to that of the detector acceptance. In addition, we extract cross sections for kinematic observables of the top quark and antiquark and the $t\bar{t}$ system defined at the parton level in the full phase space, which allows a comparison to a larger set of higher-order pQCD calculations. Both absolute and normalized differential cross sections are presented. The latter are obtained by dividing the former by the sum of the cross sections measured in the differential bins, leading to a reduction of systematic uncertainties. Cross sections are measured as functions of one kinematic variable (single-differential), or multi-differentially as functions of two or three variables (double- or triple-differential). The improvements of this analysis compared to Refs. [38, 39] fall into two categories:

1. Measurements are expanded by considering new kinematic observables, using refined binnings and extending the phase space range. An example of a new kinematic observable is the ratio $p_T(t)/m(t\bar{t})$, revealing interesting details of the $t\bar{t}$ production dynamics. A finer binning and extended phase space range is used, in particular for the kinematic distributions of leptons and b jets. For measurements with additional jets in the events, a systematic survey of the correlations of the top quark and $t\bar{t}$ kinematic variables with the number of additional jets in the events is performed in the dilepton channel for the first time.

2. The statistical and systematic uncertainties of the measurements are generally reduced by a factor of about two, the latter profiting from the following improvements: using refined procedures and algorithms, such as for identifying b jets and measuring their p_T; applying precise calibrations determined separately for each year of data taking, such as for the jet energy scale; having better estimates for some important background process contributions using in situ constraints from data; exploiting MC simulated samples with reduced statistical uncertainties to correct the data for detector effects and for assessing systematic uncertainties.

The paper is structured as follows: Section 2 provides a brief description of the CMS detector. Details of the event simulation are given in Section 3. The event selection is detailed in Section 4, followed by a description of the kinematic reconstruction in Section 5 where comparisons between data and simulations are shown. The signal extraction and unfolding procedure are explained in Section 6, together with the definitions of the parton and particle level phase

spaces. The method to extract the differential cross sections is discussed in Section 7, and the assessment of the systematic uncertainties is presented in Section 8. Results and comparisons to theoretical predictions are shown in Section 9. Finally, Section 10 provides a summary. Tabulated results can be found in HEPData [48].

2   The CMS detector

The central feature of the CMS apparatus is a superconducting solenoid of 6 m internal diameter, providing a magnetic field of 3.8 T. Within the solenoid volume are a silicon pixel and strip tracker, a lead tungstate crystal electromagnetic calorimeter (ECAL), and a brass and scintillator hadron calorimeter (HCAL), each composed of a barrel and two endcap sections. Forward calorimeters extend the η coverage provided by the barrel and endcap detectors. Muons are measured in gas-ionization detectors embedded in the steel flux-return yoke outside the solenoid. Events of interest are selected using a two-tiered trigger system [49]. The first level (L1), composed of custom hardware processors, uses information from the calorimeters and muon detectors to select events at a rate of around 100 kHz within a time interval of less than 4 μs. The second level, known as the high-level trigger (HLT), consists of a farm of processors running a version of the full event reconstruction software optimized for fast processing, and reduces the event rate to around 1 kHz before data storage. A more detailed description of the CMS detector, together with a definition of the coordinate system used and the relevant kinematic variables, can be found in Ref. [50].

3   Event simulation

Simulations of physics processes are performed with MC event generators for three main purposes. First, to obtain representative predictions of $t\bar{t}$ production cross sections to be compared to the measurements. Second, to determine corrections for the effects of hadronization, reconstruction, and selection efficiencies, as well as resolutions. These corrections are obtained by passing generated $t\bar{t}$ signal events through a detector simulation, and are applied for the unfolding of the data. Last, to obtain predictions for the backgrounds by passing generated background events through the detector simulation. All MC programs used in this analysis perform the event generation in several stages: matrix element (ME) level, parton showering matched to ME, hadronization, and the underlying event (UE), including multi-parton interactions (MPIs). For all simulations, the proton structure is described by the NNPDF3.1 NNLO set [51, 52] of parton distribution functions (PDFs), unless stated otherwise. For all simulations with top quark production, the value of the top quark mass parameter is fixed to $m_{t}^{MC} = 172.5$ GeV. The $t\bar{t}$ signal process is simulated with ME calculations at NLO in QCD. For the nominal signal simulation, the POWHEG (version 2) [53–56] generator is taken. The h_{damp} parameter of POWHEG, which regulates the damping of real emissions in the NLO calculation when matching to the parton shower, is set to $h_{damp} = 1.379\, m_{t}^{MC}$ [57]. The PYTHIA 8 program (version 8.230) [58] with the CP5 tune [57] is used to model parton showering, hadronization, and the UE. This setup, referred to as POWHEG+PYTHIA 8 , is used for the detector corrections of the $t\bar{t}$ signal process in the data, with appropriate variations for assessing the theoretical model uncertainties, described in Section 8.2. The generator-level cross sections of POWHEG+PYTHIA 8 are also used as theoretical predictions that are compared in Section 9 to the measured $t\bar{t}$ cross sections, as well as the predictions from two other models. The first alternative model is based on the MADGRAPH5_aMC@NLO (version 2.4.2) [59] generator, interfaced with PYTHIA 8 using the CP5 tune. At the ME level, up to two extra partons are included at NLO. The events are matched

to PYTHIA 8 using the FxFx prescription [60, 61], and MADSPIN [62] is used to model the decays of the top quarks, while preserving their spin correlation. The whole setup is referred to as MG5_aMC@NLO[FxFx]+PYTHIA 8 . The second alternative model is POWHEG interfaced to HERWIG 7 [63] using the CH3 tune [64] and is referred to as POWHEG+HERWIG 7 .

The main background contributions originate from single top quarks produced in association with a W boson (tW), Z/γ^* bosons produced with additional jets (Z+jets), W boson production with additional jets (W+jets), and diboson (WW, WZ, and ZZ) events. Other backgrounds are negligible.

For all background samples, parton showering, hadronization, and the UE are simulated with PYTHIA 8. For single top quark production, the t-channel and tW processes are simulated at NLO with POWHEG [65–67], and the s-channel process at LO with MADGRAPH5_aMC@NLO. In all three cases the PYTHIA 8 CP5 tune is used. For all other background samples discussed in the following, the CP5 tune is applied for the 2017 and 2018 samples, and the CUETP8M1 tune [61, 68, 69] for the 2016 samples. For the latter, the PDF set NNPDF3.0 [70] is used with the order (e.g. NLO) of the respective simulation. The Z+jets process is simulated at NLO using MG5_aMC@NLO[FxFx] with up to two additional partons at the ME level. The W+jets process is simulated at leading order (LO) using MADGRAPH5_aMC@NLO with up to four additional partons at the ME level and matched to PYTHIA 8 using the MLM prescription [71, 72]. Diboson events are simulated at LO with PYTHIA 8.

Predictions are normalized based on their inclusive theoretical cross sections and the integrated luminosity of the data sample. For s- and t-channel single top quark production, the cross sections are calculated at NLO with HATHOR (version 2.1) [73]. For single top quark production in the tW channel, the approximate NNLO calculations from Ref. [74] are used. For Z+jets and W+jets processes, NNLO predictions obtained with FEWZ [75] are taken, and for diboson production the NLO calculations from Ref. [76] are applied. The $t\bar{t}$ simulation is normalized to a cross section of $831 \pm^{20}_{30}$ (scale) ± 35 (PDF $+ \alpha_s$) pb calculated with the TOP++ (version 2.0) program [77] at NNLO, including resummation of next-to-next-to-leading logarithm (NNLL) soft-gluon terms [78–83], and assuming a top quark pole mass of 172.5 GeV.

The CMS detector response is simulated using GEANT4 [84]. The effect of additional pp interactions within the same or nearby bunch crossings (pileup) is taken into account by adding simulated minimum-bias interactions to the simulated data. Events in the simulation are then weighted to reproduce the pileup distribution in the data, which is estimated from the measured bunch-to-bunch instantaneous luminosity and assuming a total inelastic pp cross section of 69.2 mb [85]. Separate simulations are employed for the data taken in the three years 2016–2018, in order to match the varying detector performance and data-taking conditions. At every step of the analysis, the simulated samples from different years are added together and used as one single sample, both at the detector and the generator levels.

Correction factors described in Sections 6 and 8, subsequently referred to as scale factors, are used to reconcile the number of expected events from simulation with what is observed in data. They are applied, for example, to correct a detector efficiency in the simulation to match the one observed in data, or to scale a background prediction.

4 Event selection

The event selection closely follows that of Ref. [38]. Events are selected corresponding to the decay chain where both top quarks decay into a W boson and a bottom quark, and each of the

W bosons decays directly into an electron or a muon and a neutrino. This specification defines the signal process, while all other $t\bar{t}$ events, including those with at least one electron or muon originating from the decay of a τ lepton, are treated as background which is taken into account, as detailed in Section 6. The signal includes three distinct channels: two same-flavor channels corresponding to two electrons (e^+e^-) or two muons ($\mu^+\mu^-$), and the different-flavor channel corresponding to one electron and one muon ($e^{\pm}\mu^{\mp}$). Results are obtained by combining the three channels and adding, at every step of the analysis, the samples from the years 2016–2018.

At the HLT level, events are selected either by single-lepton or dilepton triggers. The former require the presence of at least one electron or muon, and the latter the presence of either two electrons, two muons, or an electron and a muon. For all employed triggers, the leptons are required to fulfill isolation criteria that are looser than those applied later in the offline analysis. For the single-electron triggers, a p_T threshold of 27 (32) GeV is applied in 2016 (2017–2018), while for single-muon triggers the p_T threshold is 24 (27) GeV in 2016/2018 (2017). The dilepton triggers select events based on the leptons with the highest (leading) and second-highest (trailing) p_T in the event. The same-flavor dilepton triggers require either an electron pair with $p_T > 23$ (12) GeV for the leading (trailing) electron or a muon pair with $p_T > 17$ (8) GeV for the leading (trailing) muon. The different-flavor dilepton triggers require either an electron with $p_T > 23$ GeV and a muon with $p_T > 8$ GeV, or a muon with $p_T > 23$ GeV and an electron with $p_T > 12$ GeV. The analysis mainly relies on the dilepton triggers, while the single-lepton triggers help to improve the overall trigger efficiency by about 10%.

The particle-flow (PF) algorithm [86] aims to reconstruct and identify each individual particle with an optimized combination of information from the various elements of the CMS detector. The energy of muons is obtained from the curvature of the corresponding track. The energy of electrons is inferred from a combination of the electron momentum at the primary interaction vertex as determined by the tracker, the energy of the corresponding ECAL cluster, and the energy sum of all bremsstrahlung photons spatially compatible with originating from the electron track. The energy of photons is directly obtained from the ECAL measurement. The energy of charged hadrons is determined from a combination of their momentum measured in the tracker and the matching ECAL and HCAL energy deposits, corrected for the response function of the calorimeters to hadronic showers. Finally, the energy of neutral hadrons is obtained from the corresponding corrected ECAL and HCAL energies.

The measurements presented in this paper depend on the reconstruction and identification of electrons, muons, jets, and missing transverse momentum $\vec{p}_T^{\,\mathrm{miss}}$ associated with neutrinos. Electrons and muons are selected if they are compatible with originating from the primary pp interaction vertex. The primary vertex (PV) is taken to be the vertex corresponding to the hardest scattering in the event, evaluated using tracking information alone, as described in Section 9.4.1 of Ref. [87].

For both electrons and muons, the "tight" identification criteria as described in Refs. [88, 89] are applied. Reconstructed electrons [88] are required to have $p_T > 25$ (20) GeV for the leading (trailing) candidate and $|\eta| < 2.4$. Electron candidates with ECAL clusters in the transition region between the ECAL barrel and endcap, $1.44 < |\eta_{\mathrm{cluster}}| < 1.57$, are excluded since the reconstruction of an electron object in this region is not optimal. A relative isolation I_{rel} is defined as the p_T sum of all neutral and charged hadrons, and photon candidates within a distance of 0.3 from the electron in η-ϕ space, divided by the p_T of the electron candidate. A maximum value of I_{rel} is allowed, in the range 0.05–0.10, depending on the p_T and η of the electron candidate. Further electron identification requirements are applied to reject misidentified electron candidates and candidates originating from photon conversions. Reconstructed muons [89]

are required to have $p_T > 25\,(20)\,\text{GeV}$ for the leading (trailing) candidate and $|\eta| < 2.4$. An isolation requirement of $I_{\text{rel}} < 0.15$ is applied, including particles within a distance of 0.4 in η-ϕ space from the muon candidate. Furthermore, muon identification requirements are applied to reject misidentified muon candidates and muons originating from in-flight decays. For both electron and muon candidates, I_{rel} is corrected for residual pileup effects. Finally, for the targeted prompt leptons in the $t\bar{t}$ dilepton decay channel, the total selection efficiencies are about 90% for muons and 70% for electrons.

Jets are reconstructed by clustering the PF candidates using the anti-k_T jet algorithm [90, 91] with a distance parameter of 0.4. The jet energies are corrected following the procedures described in Ref. [92]. After correcting for all residual energy deposits from charged and neutral particles from pileup, p_T- and η-dependent jet energy adjustments are applied to correct for the detector response. Jets are required to have $p_T > 30\,\text{GeV}$ and $|\eta| < 2.4$ and a distance in η-ϕ space of at least 0.4 to the closest selected lepton.

The b jets are identified with the deep neural network algorithm DEEPCSV [93], based on tracking and secondary vertex information. The chosen working point of the network discriminator has a b-jet tagging efficiency of ≈ 80–90% and a mistagging efficiency of $\approx 1\%$ for jets originating from gluons, as well as u, d, or s quarks, and ≈ 30–40% for jets originating from c quarks. The energy measurement of the b-tagged jets is improved using a deep neural network estimator [94] that performs a regression after all other jet energy corrections have been applied.

The $\vec{p}_T^{\text{miss}}$ is computed as the negative vector sum of the transverse momenta of all the PF candidates in an event, and its magnitude is denoted as p_T^{miss} [95]. The $\vec{p}_T^{\text{miss}}$ is updated when accounting for corrections to the energy scale of reconstructed jets in the event. The pileup per particle identification algorithm [96] is applied to reduce the pileup dependence of the $\vec{p}_T^{\text{miss}}$ observable. The $\vec{p}_T^{\text{miss}}$ is computed from the PF candidates weighted by their probability to originate from the primary interaction vertex [95].

Events are selected offline if they contain exactly two isolated, oppositely charged electrons or muons, (e^+e^-, $\mu^+\mu^-$, $e^\pm\mu^\mp$) and at least two jets, with at least one of these jets being b tagged. Events with an invariant mass of the lepton pair $m(\ell\bar{\ell})$ below $20\,\text{GeV}$ are removed in order to suppress contributions from resonance decays and low-mass Drell–Yan processes. Backgrounds from Z+jets processes in the e^+e^- and $\mu^+\mu^-$ channels are further reduced by requiring $m(\ell\bar{\ell}) < 76\,\text{GeV}$ or $m(\ell\bar{\ell}) > 106\,\text{GeV}$, and $p_T^{\text{miss}} > 40\,\text{GeV}$.

In this analysis, the $t\bar{t}$ production cross section is also measured as a function of the extra jet multiplicity N_{jet}. Extra jets (also referred to as additional jets) are jets arising primarily from hard QCD radiation and not from the top quark decays. At the reconstruction level, the extra jets in dilepton $t\bar{t}$ candidate events are defined as jets with $p_T > 40\,\text{GeV}$ and $|\eta| < 2.4$ that are isolated from the leptons and from the b jets originating from the top quark decays. These two b jets are identified by the $t\bar{t}$ kinematic reconstruction algorithms discussed in Section 5. The extra jet is considered isolated when having a distance to the leptons in η-ϕ space of at least 0.4 and a distance to the b jets from top quark decays of at least 0.8. The requirements on p_T and isolation of extra jets largely eliminate the expected contributions from gluons radiated off b quarks produced in the top quark decays.

5 Kinematic reconstruction of the t$\bar{\text{t}}$ system

The four-momenta of the top quark and antiquark are determined from the four-momenta of their decay products using a kinematic reconstruction method referred to as the "full kinematic reconstruction" [23]. In this reconstruction, the two pairs consisting of a lepton and a b jet from the decay are identified, and the top quark (antiquark) is associated with the pair containing the lepton with positive (negative) charge. The three-momenta of the neutrino (ν) and antineutrino ($\bar{\nu}$) are reconstructed using algebraic equations deduced from the following six kinematic constraints: the conservation of the total p_T in the event, and the masses of the W bosons and of the top quark and antiquark. The mass values used in the constraints are 172.5 GeV for the top quark and antiquark, and 80.4 GeV for the W bosons. The $\vec{p}_\text{T}^\text{miss}$ in the event is assumed to originate solely from the two neutrinos. An ambiguity can arise due to multiple algebraic solutions of the constraint equations for the neutrino momenta, which is resolved by taking the solution with the smallest invariant mass of the t$\bar{\text{t}}$ system [97]. The reconstruction is performed 100 times. Each time, the measured energies and directions of the reconstructed leptons and jets are randomly smeared in accordance with their resolutions. This procedure recovers events that initially yield no solution because of measurement fluctuations. The three-momenta of the two neutrinos are determined as a weighted average over all smeared solutions. For each solution, the weight is calculated based on the expected true spectrum of the invariant mass of the lepton and the b jet originating from the decay of a top quark $m(\ell\text{b})$ and taking the product of the two weights for the top quark and antiquark decay chains. All possible lepton-jet combinations in the event that satisfy the requirement $m(\ell\text{b}) < 180$ GeV are considered. Combinations are ranked based on the presence of b-tagged jets in the assignments, i.e. a combination with both leptons assigned to b-tagged jets is preferred over those with one or no b-tagged jet. Among assignments with an equal number of b-tagged jets, the one with the highest sum of weights is taken. Events with no solution after smearing are rejected. The efficiency of the full kinematic reconstruction is defined as the number of events for which a solution is found divided by the total number of selected t$\bar{\text{t}}$ events after the full event selection described in Section 4. Consistent results are observed in data and simulation. The efficiency for signal events is about 90%. Performing the reconstruction more than 100 times does not significantly alter the efficiency and kinematic resolutions. After applying the complete event selection and the full kinematic reconstruction, about 1.2 million events are observed, with shares of 56, 14, and 30% for the e$^\pm\mu^\mp$, e$^+$e$^-$, and $\mu^+\mu^-$ channels, respectively. Combining all decay channels, the estimated signal fraction in data is about 80%.

Distributions of the reconstructed top quark and t$\bar{\text{t}}$ kinematic variables, obtained with the full kinematic reconstruction, are shown in Fig. 2 and the upper plots in Fig. 3. Furthermore, the multiplicity of jets in the events is presented in Fig. 2. The $p_\text{T}(\text{t})$ and $y(\text{t})$ spectra include contributions from both the top quark and antiquark. The expected signal and background contributions are estimated as described in Section 6, using the MC simulations for the various processes introduced in Section 3. The events labeled as "t$\bar{\text{t}}$ other" show the expected contributions from t$\bar{\text{t}}$ final states other than the signal, dominated by events with one or both of the W bosons decaying into τ leptons with subsequent decay into electrons or muons. The expected events labeled as "Minor bg" constitute minor background contributions from diboson and W+jets processes. In general, the data are reasonably well described by the simulation that overestimates, however, the total number of events by about 5%. Some trends are visible, in particular for $p_\text{T}(\text{t})$, where the simulation predicts a somewhat harder spectrum than that observed in data, as seen in previous differential t$\bar{\text{t}}$ cross section measurements [23, 26, 28, 30, 34, 37, 38]. The mismodeling of the data by the simulation is accounted for by the relevant systematic uncertainties described in Section 8. The checks discussed in Section 7 confirm that the residual

mismodeling of the $p_T(t)$ distribution does not introduce a significant bias in the measurement.

The $m(t\bar{t})$ value obtained using the full kinematic reconstruction described above is sensitive to the value of the top quark mass used as a kinematic constraint. An alternative algorithm is employed that reconstructs the $t\bar{t}$ kinematic variables without using the top quark mass constraint. This algorithm is referred to as the "loose kinematic reconstruction". It is used in this analysis for measuring differential $t\bar{t}$ cross sections as a function of $m(t\bar{t})$, in order to preserve the sensitivity of the data for a future top quark mass extraction, as performed in Ref. [39]. In contrast to the full kinematic reconstruction, this algorithm tackles the reconstruction of the $\nu\bar{\nu}$ system as a whole. The ℓb pairs are selected and ranked as described for the full kinematic reconstruction. Among combinations with equal number of b-tagged jets, the ones with the leading and trailing p_T jets are chosen. The kinematic variables of the $\nu\bar{\nu}$ system are obtained as follows: its $\vec{p}_T$ is set equal to $\vec{p}_T^{\text{miss}}$ and its unknown longitudinal momentum and energy are set equal to the values of the lepton pair. Additional constraints are applied on the invariant mass of the neutrino pair, $m(\nu\bar{\nu}) \geq 0$, and on the invariant mass of the W bosons, $m(W^+W^-) \geq 2m_W$. These constraints have only minor impact on the performance of the reconstruction. This method achieves an average reconstruction efficiency of approximately 96% for signal events and provides $t\bar{t}$ kinematic resolutions comparable to those obtained with the full kinematic reconstruction. As in the case of the full kinematic reconstruction, events with no valid solution for the loose kinematic reconstruction are excluded from further analysis. The presence of a solution for the full kinematic reconstruction in an event is also required for the cross section measurements as functions of lepton and b jet kinematic variables discussed in Section 9.2. Figure 3 (lower row) displays the distributions of the reconstructed $t\bar{t}$ invariant mass and rapidity using the loose kinematic reconstruction. These distributions are similar to the ones obtained with the full kinematic reconstruction, shown in the upper row, except for $m(t\bar{t})$ in the threshold region that is smeared out due the omission of the top quark mass constraint.

The loose kinematic reconstruction is used for a subset of measurements presented in Section 9, namely, for single-differential cross sections as functions of $m(t\bar{t})$, and for all multi-differential cross sections composed of combinations of $m(t\bar{t})$ with $p_T(t\bar{t})$, $y(t\bar{t})$, or N_{jet}. For all other cross sections as functions of kinematic observables of the $t\bar{t}$ system or of the top quark and antiquark, the full kinematic reconstruction is used.

6 Signal extraction and unfolding

The number of signal events is obtained for each histogram bin by subtracting the expected number of background events from the observed number of events.

The expected background contribution from single top quark, W+jets, and diboson processes are taken directly from the MC simulations. The Z+jets contribution is also estimated from the MC simulation, but corrected by global normalization scale factors, which are determined from a binned template fit to the data, using the method described in Ref. [98], as implemented in the TFRACTIONFITTER class in ROOT [99]. In this procedure, the event fraction of Z+jets process and of the sum of all other contributions are fitted to the $m(\ell\bar{\ell})$ distributions in the data, within the Z boson peak signal region $76 < m(\ell\bar{\ell}) < 106\,\text{GeV}$. The template distributions are obtained from the MC-simulated samples. Separate normalization scale factors are fitted for the simulations of the Z+jets process in the e^+e^- and $\mu^+\mu^-$ channels and the scale factor for the $e^\pm\mu^\mp$ channel is calculated as the geometric mean of these factors. The nominal scale factors are determined for a data selection with relaxed requirements, omitting those on p_T^{miss},
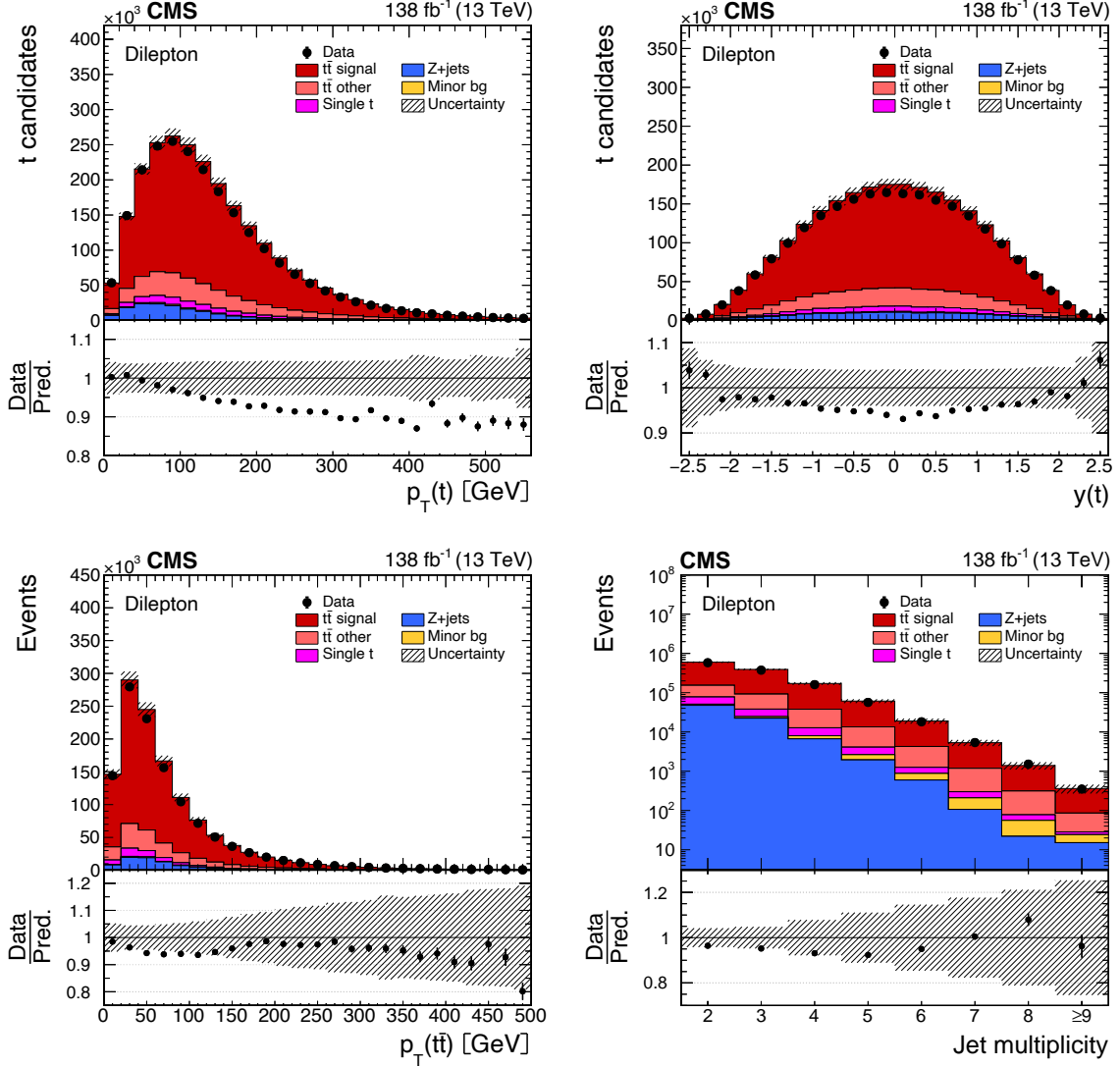
Figure 2: Distributions of $p_T(t)$ (upper left), $y(t)$ (upper right), $p_T(t\bar{t})$ (lower left), and jet multiplicity (lower right) obtained in selected events with the full kinematic reconstruction. For the first two distributions, "t" refers to both top quark and antiquark. The three dilepton channels (e^+e^-, $\mu^+\mu^-$, and $e^\pm\mu^\mp$) are added together. The data with vertical bars corresponding to their statistical uncertainties are plotted together with distributions of simulated signal and background processes. The hatched regions depict the systematic shape uncertainties in the signal and backgrounds (as detailed in Section 8). The lower panel in each plot shows the ratio of the observed data event yields to those expected in the simulation.
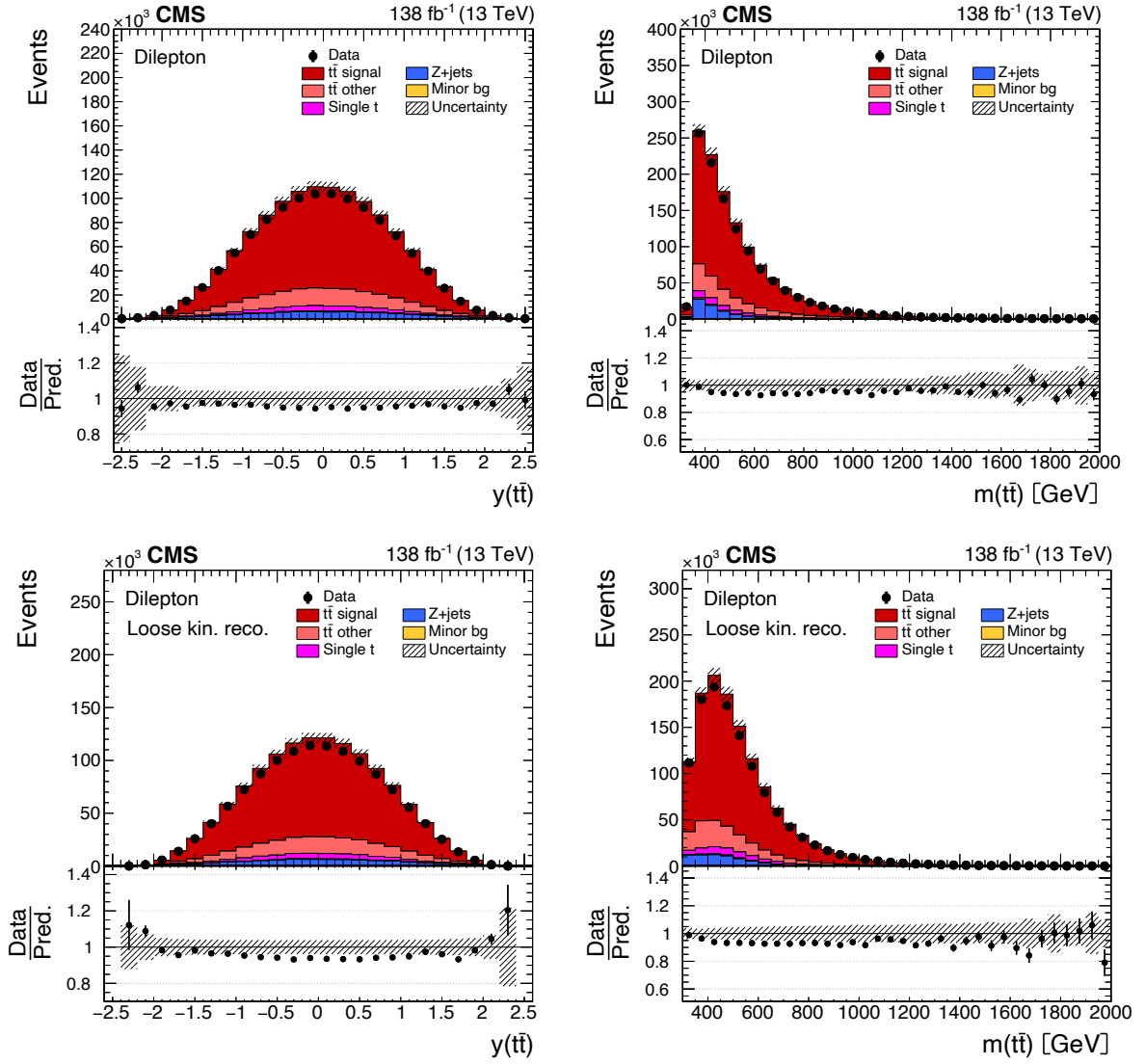
Figure 3: Distributions of $y(t\bar{t})$ (left) and $m(t\bar{t})$ (right) obtained in selected events with the full (upper) and the loose kinematic reconstruction (lower). Further details can be found in the caption of Fig. 2.

the number of b-tagged jets, and the presence of a solution for the kinematic reconstruction, in order to have a clean sample of Z+jets events. The scale factors are compatible, within a few percent, with unity. The $m(\ell\bar{\ell})$ window chosen for the fits ensures that there is no overlap with the sample used for the analysis and is still large enough to provide a good separation of Z+jets from the other processes. As a cross-check, the template fits are performed over a wider $m(\ell\bar{\ell})$ range, starting at 20 GeV and extending to values much above the Z boson peak signal region, and only small scale factor variations are observed of the order of one percent.

After the subtraction of non-$t\bar{t}$ backgrounds, the resulting event yields are corrected for "$t\bar{t}$ other" contributions, introduced in Section 5. These events arise from the same $t\bar{t}$ production process as the signal and thus the normalization of this background is fixed to that of the signal. For each bin, the number of events obtained after the subtraction of all other background sources is multiplied by the ratio of the number of selected $t\bar{t}$ signal events to the total number of selected $t\bar{t}$ events (i.e. the signal and all other $t\bar{t}$ events) in simulation.

The numbers of signal events are obtained by adding together the event yields in the e^+e^-, $\mu^+\mu^-$, and $e^\pm\mu^\mp$ channels, subtracting the background, and correcting for detector effects using the TUNFOLD package [100]. The addition of the three channels before applying detector corrections is justified by the fact that background levels are small in all channels and kinematic resolutions are comparable. The measurements in the separate channels yield consistent results.

In the unfolding procedure the response matrix plays an important role. An element of this matrix specifies the probability for an event originating from one bin of the true distribution to be observed in a specific bin of the reconstructed observables. The response matrix models the effects of acceptance, detector efficiencies, and resolutions in a given phase space. It is calculated for each measured distribution using the $t\bar{t}$ signal simulation, and is defined either at the particle level in a fiducial phase space or at the parton level in the full phase space, using the corresponding generator-level definitions discussed in Section 6.1. At the detector level, the number of bins used per kinematic variable is typically two times larger than the number of bins used at the generator level. Figure 4 shows example response matrices obtained for the $p_T(t)$ and $y(t\bar{t})$ distributions at the parton level. For illustrative reasons, they are displayed with the same binnings at both the parton and detector levels.

In TUNFOLD, the distribution of unfolded event numbers is extracted from the measured signal distribution at the detector level by performing a χ^2 fit. The fit model consists of the sum of template distributions, with one distribution per cross section bin, constructed from the product of the unfolded event number in that bin and the respective column of the response matrix. An additional χ^2 term is included representing Tikhonov regularization [101], based on second-order derivatives and using the nominal $t\bar{t}$ simulation as the bias vector. The regularization reduces unphysically large high-frequency components of the unfolded spectrum. The regularization strength that minimizes the global correlation coefficient [102] is chosen. The statistical uncertainties of the simulated $t\bar{t}$ signal samples used to derive the response matrices introduce small additional uncertainties in the unfolded event yields. These are accounted for in the TUNFOLD procedure through error propagation.

6.1 Generator-level definitions

The definitions of the generator level that are used in the construction of the response matrices follow, to a large extent, those applied in Refs. [38, 39, 103].

For the parton-level results, the momenta of the parton-level top quarks are defined after QCD
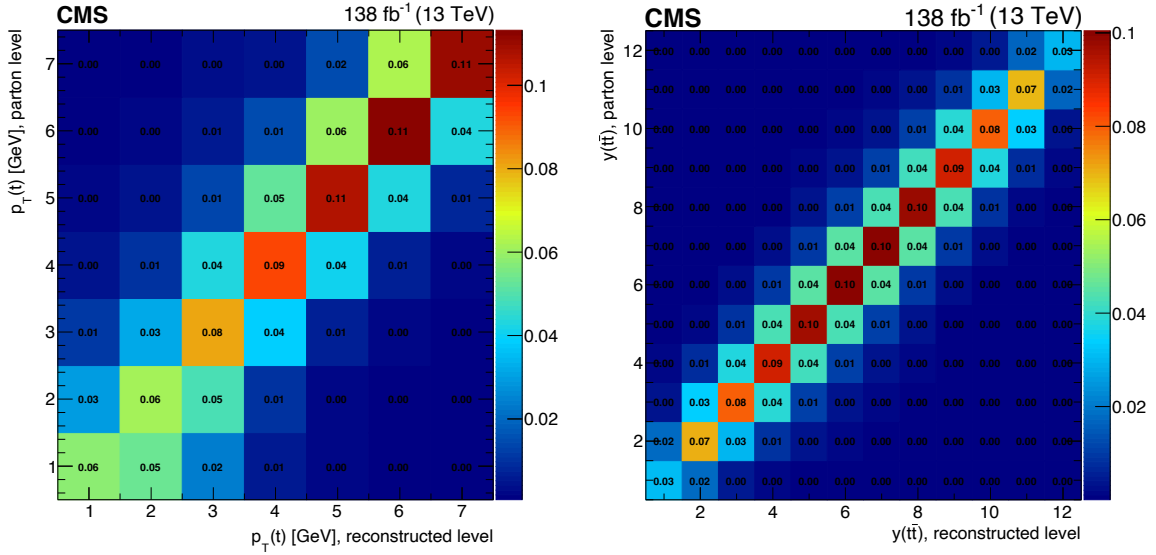
Figure 4: Response matrices for the unfolding of the $p_{\mathrm{T}}(\mathrm{t})$ (left) and $y(\mathrm{t\bar{t}})$ (right) distributions at the parton level, as extracted from the nominal POWHEG+PYTHIA 8 $\mathrm{t\bar{t}}$ signal simulation. The ranges of the observables for a given bin number can be read off from the corresponding cross section distributions in Figs. 8 and 10.

radiation, but before the top quark decays. The unfolded signal event numbers are corrected for the branching fractions $\mathrm{W} \to \ell\nu$. The parton-level results are extrapolated to the full phase space using the default $\mathrm{t\bar{t}}$ simulation. The extrapolation is implicitly performed by counting each simulated event in the response matrix that enters a specific parton-level bin of a differential cross section.

For the particle-level results, the generator-level objects are defined by the stable particles (i.e. those with lifetime $\tau > 0.3 \times 10^{-10}$ s) in the simulation. The selection of these objects is intended to match as closely as possible the detector-level requirements used to select $\mathrm{t\bar{t}}$ events. It is described together with the generator-level top quark kinematic reconstruction procedure in Refs. [38, 103], and is summarized below.

- All simulated electrons and muons, including those from τ lepton decays, but not originating from the decay of a hadron, are corrected ("dressed") for bremsstrahlung effects by adding the momentum of each photon to that of the closest lepton if their separation in η-ϕ space is < 0.1. Leptons are required to have $p_{\mathrm{T}} > 20\,\mathrm{GeV}$ and $|\eta| < 2.4$.

- Only neutrinos originating from nonhadronic decays (i.e. prompt neutrinos) are used.

- Jets are clustered using the anti-k_{T} jet algorithm [90, 91] with a distance parameter of 0.4. All stable particles, with the exception of the dressed leptons and prompt neutrinos, are clustered. Jets with $p_{\mathrm{T}} > 30\,\mathrm{GeV}$ and $|\eta| < 2.4$ are selected if there is no electron or muon, as defined above, within a distance of 0.4 in η-ϕ space.

- b jets are defined as those jets that contain a b hadron using the ghost-matching technique [104]: as a result of the short lifetime of b hadrons, only their decay products are considered for the jet clustering. However, to allow their association with a jet, the b hadrons are also included with their momenta scaled down to a negligible value. This preserves the information of their directions, but removes their impact on the jet clustering.

- The following additional event-level requirements are applied to define the fiducial phase space region in which the particle-level cross sections are measured: we require that the W bosons produced from decays of the top quark and antiquark in a $t\bar{t}$ event themselves decay to an electron or a muon; we reject events where these W bosons decay to τ leptons; we require exactly two selected lepton candidates with opposite charges, $m(\ell\bar{\ell}) > 20\,\text{GeV}$, and at least two b jets.

- The top quark reconstruction at the particle level proceeds as follows. Prompt neutrinos are combined with the dressed leptons to form W boson candidates. We take the permutation of neutrinos and leptons that minimizes the sum of the absolute values of the differences between the mass of each neutrino-lepton pair and the nominal W boson mass of 80.4 GeV. Subsequently, the W boson candidates are combined with b jets to form particle-level top quark candidates by minimizing the sum of the absolute values of the differences between the mass of each pair and the nominal top quark mass of 172.5 GeV.

Due to the finite detector resolution, events that are outside the fiducial phase space region at the generator level can be measured inside the accepted region at the detector level. These events are subtracted, before the unfolding, by a fractional correction of the observed number of events after subtracting all other backgrounds. The correction, performed separately for each detector-level bin, is defined as the number of events in the $t\bar{t}$ signal simulation that pass both the detector- and particle-level selection criteria, divided by the number of all events fulfilling the detector-level requirements.

When measuring the differential cross sections as functions of N_{jet} (see Section 9.3), the top quark and antiquark are measured either at the parton level in the full phase space or at the particle level in a fiducial phase space, as described above, while the additional jets are measured at the particle level only. The definition of these extra jets differs from the one given above only in one aspect: they have to be isolated from the charged leptons (e or μ) and b quarks originating from the top quark decays, as represented by the corresponding particle level leptons and b jets, with a minimal distance to these leptons (b quarks) of 0.4 (0.8) in η-ϕ space. The larger distance to the b quarks is required to avoid selecting jets coming from gluon radiation from the b quarks as additional jets. In addition, the additional jets are required to have $p_{\text{T}} > 40\,\text{GeV}$ and $|\eta| < 2.4$. Specifically for the measurements of the top quark and antiquark at the parton level, two more differences in the definition of the extra jets are introduced [39]. The neutrinos from decays of hadrons are excluded in the clustering of these jets, and the charged leptons and b quarks used in the jet isolation are taken directly after the W boson and top quark decays, respectively.

7 Cross section measurement

For a given variable X, the absolute differential $t\bar{t}$ cross section $\mathrm{d}\sigma_i/\mathrm{d}X$ is extracted via the relation

$$\frac{\mathrm{d}\sigma_i}{\mathrm{d}X} = \frac{1}{\mathcal{L}} \frac{x_i}{\Delta_i^X},$$
(1)

where $\mathcal{L}$ is the integrated luminosity, x_i is the number of unfolded signal events observed in bin i, and Δ_i^X is the bin width. The numbers x_i are calculated with respect to the $t\bar{t}$ parton or particle generator levels defined in Section 6.1. The normalized differential cross section is obtained by dividing the absolute differential cross section by the measured total cross section σ in the same phase space, which is evaluated by summing the binned cross section measurements over all bins of the observable X. For differential cross sections measured simultaneously as

functions of two or three variables, the following criteria are adopted for optimizing their display. The measured cross sections are divided by the bin width of the variable that is chosen as the last one. They present single-differential cross sections as functions of the last variable in different ranges of the first, or first and second variables, and are referred to as double- or triple-differential cross sections, respectively.

The bin widths at generator level are chosen based on the resolutions of the kinematic variables, such that the purity and the stability of each bin are generally above 30% for single-differential cross sections and above 20% for double- or triple-differential cross sections. For assessing the purity and stability, the binning at detector level is adjusted to be equal to the binning at generator level. For a given bin, the purity is defined as the fraction of events in the $t\bar{t}$ signal simulation that are generated and reconstructed in the same bin with respect to the total number of events reconstructed in that bin. To evaluate the stability, the number of events in the $t\bar{t}$ signal simulation that are generated and reconstructed in a given bin are divided by the total number of reconstructed events generated in the bin.

The cross section measurement based on the signal extraction and unfolding procedure described in Section 6 is validated with closure tests. Large numbers (~ 1000) of pseudo-data sets are generated from the $t\bar{t}$ signal MC simulations and analyzed as if they were real data. The unfolded differential cross sections are found to be unbiased and to provide proper 68% confidence intervals within ± 1 estimated standard deviation uncertainties. A second test is performed by unfolding pseudo-data sets, generated using reweighted $t\bar{t}$ signal simulations, with the response matrix and bias vector taken from the nominal simulation. The reweighting is performed as a function of the differential cross section kinematic observables at the generator level and is used to introduce controlled shape variations, e.g., making the $p_{\mathrm{T}}(t)$ spectrum harder or softer. This test probes the robustness of the unfolding procedure with respect to the underlying physics model in the simulation, which impacts both the response matrix and the regularization bias vector. Figure 5 shows two examples of these tests, performed for cross sections as functions of $p_{\mathrm{T}}(t)$ and $m(\ell\bar{\ell})$. The applied reweightings follow approximately parabolic functions and lead to shape distortions of about $\pm 20\%$ at thresholds and end points of the kinematic spectra, comprising the differences observed between data and the nominal simulation (as shown by figures in Section 9). The unfolding is performed with the standard regularization procedure and alternatively with switching it off; the obtained cross sections are found to deviate at most by a few permille, showing that biases induced by the regularization are small. The unfolded cross sections vary visibly from the true values only in the kinematic threshold regions, with maximum differences of the order of 1%. Effects of similar size are also seen for other single- and multi-differential cross sections and demonstrate an overall good robustness of the unfolding procedure. The simple reweighting approach discussed here is not suitable for quantifying the measurement uncertainty from the underlying physics model; this is done, instead, by the dedicated set of variations applied to the $t\bar{t}$ signal simulation detailed in Section 8.2.

8 Systematic uncertainties

The systematic uncertainties in the measured differential cross sections are grouped into three categories: experimental uncertainties from the imperfect modeling of the detector response, theoretical uncertainties from the modeling of the signal, and the uncertainties in the numbers of events from background processes. The systematic uncertainty is assessed source by source largely following the prescriptions used in Refs. [38, 39]. For each change made, the cross section is recalculated, which for most sources involves a repetition of the full analysis. The
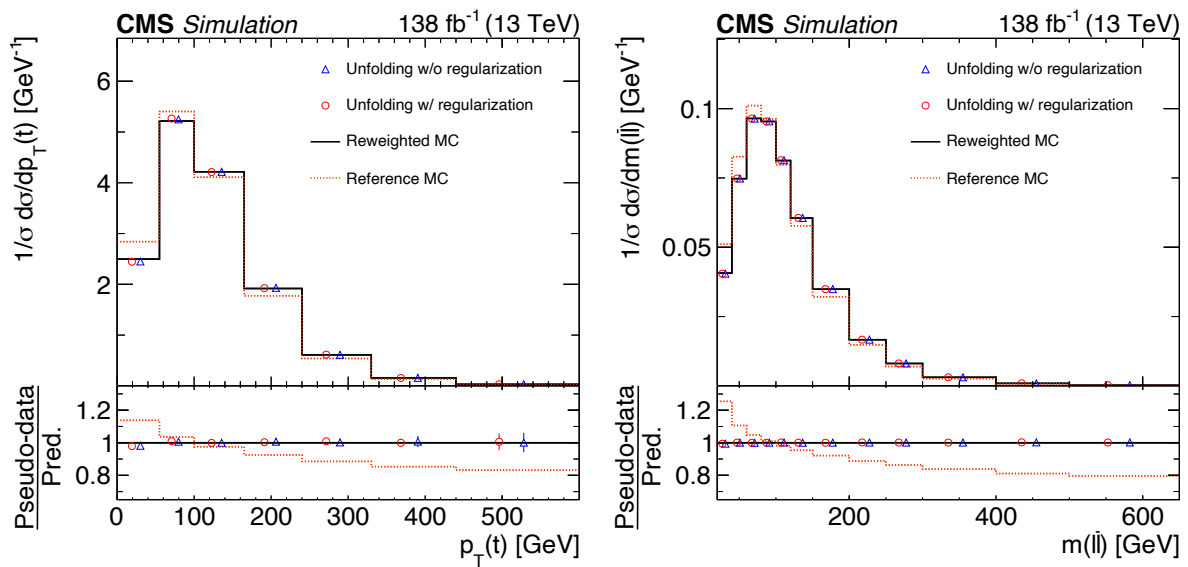
Figure 5: Reweighting test for the extraction of the normalized differential cross sections as functions of $p_T(t)$ (left) and $m(\ell\bar{\ell})$ (right). The former cross section is measured at the parton level in the full phase space and the latter at the particle level in a fiducial phase space. The nominal $t\bar{t}$ signal MC spectra are shown as dotted red histograms and the assumed true spectra, obtained from reweighting, as solid black histograms. The unfolded spectra, using pseudo-data based on the true spectra but using the nominal spectra for the detector corrections and bias vector in the regularization, are presented as open red circles. The unfolded spectra with the regularization switched off are also shown (open blue triangles). The statistical uncertainties in the unfolded cross sections are represented by a vertical bar on the corresponding points. The lower panel in each plot shows the ratios of the pseudo-data to the predicted spectra.

difference with respect to the nominal result in each bin is taken as the systematic uncertainty.

Separate simulations are employed for the data taken in the three years 2016, 2017, and 2018, in order to match the varying detector performance and data-taking conditions. The correlations of systematic uncertainties among the measurements in the different periods must be specified. For theoretical uncertainties we assume a 100% correlation, as the same theoretical models and variations are used for all periods. For experimental uncertainties we use either uncorrelated, partial, or full correlations. For the case of partial correlations we make use of the varied and nominal simulations for each year. The correlated part of the uncertainty is assessed by using the varied simulations for all three years, but rescaling the resulting systematic uncertainty by a factor $\sqrt{\rho}$, where ρ specifies the level of correlation, e.g. 50%. For the uncorrelated part, we separately vary the simulation for each year, keeping the nominal simulation for the other two years, and add the resulting uncertainties in quadrature, after rescaling them by a factor $\sqrt{1-\rho}$.

8.1 Experimental uncertainties

Most experimental uncertainties are assessed by variations that are simultaneously applied to the signal and background simulations. The following sources are considered:

- The uncertainties in the integrated luminosities of the 2016, 2017, and 2018 data samples are 1.2, 2.3, and 2.5%, respectively, and are 30% correlated between the years [105–107]. The resulting total normalization uncertainty on the absolute cross sections is 1.6%.

- The uncertainty in the amount of pileup is assessed by varying the value of the total pp inelastic cross section, which is used to estimate the mean number of additional pp interactions, by its measurement uncertainty of $\pm 4.6\%$ [85], leading to a 100% correlated uncertainty among the three years.

- The efficiencies for the dilepton and single-lepton triggers are measured with independent triggers based on a $p_{\mathrm{T}}^{\mathrm{miss}}$ requirement. Scale factors are calculated in bins of lepton p_{T}, independently for the years 2016, 2017, and 2018. They agree with unity typically within 1%. The scale factors are varied within their uncertainties. The uncertainties are assumed to be uncorrelated among the years.

- Lepton identification and isolation efficiencies are determined using the "tag-and-probe" method with Z+jets event samples [108, 109]. The efficiencies are assessed in two-dimensional bins of lepton η and p_{T}. The corresponding scale factors typically agree with unity within 10% for electrons and 3% for muons. The scale factors are varied within their calibration uncertainties and a 100% correlation among the years is assumed. An implicit assumption made in the analysis is that the scale factors derived from the Z+jets sample are applicable to the $t\bar{t}$ samples, where the efficiency for lepton isolation is reduced due to the typically larger number of jets present in the events. This assumption is validated through studies of $t\bar{t}$-enriched samples using an event selection similar to the current analysis [110]. In these studies, the lepton isolation criteria are relaxed for one lepton, and the efficiency of passing the criteria is measured in both data and simulation. The observed efficiencies for electrons (muons) differ by at most 1% (0.5%) from the nominal values. These maximum variations are taken as additional uncertainties.

- The uncertainty arising from the jet energy scale (JES) is assessed by varying the energy scale correction for all jets in the signal and background simulations by one standard deviation, in bins of p_{T} and η. This uncertainty is divided into seven in-

dependent sources, including those from extrapolating between samples with different jet-flavor compositions and the impact of pileup collisions on the corrections derivation [92]. Most sources are treated as uncorrelated across data-taking periods. However, sources related to theoretical predictions in the MC simulation, such as those used to extrapolate between different jet-flavor compositions, are treated as correlated across data-taking periods. The JES variations are also propagated to the uncertainties in $\vec{p}_T^{\text{miss}}$.

- The uncertainty from the jet energy resolution (JER) is evaluated by the variation of the simulated JER by ± 1 standard deviation in different η regions [92]. An additional uncertainty in the calculation of $\vec{p}_T^{\text{miss}}$ is estimated by varying the energies of reconstructed particles not clustered into jets. Since both sources of uncertainty are primarily affected by varying detector conditions that are not time-correlated, they are treated as uncorrelated across the different years.

- During the 2016–2017 data-taking periods, a gradual shift in the timing of the inputs of the ECAL L1 trigger in the forward endcap region ($|\eta| > 2.4$) led to a particular trigger inefficiency. A correction for this effect was determined using an unbiased data sample and is found to be relevant in events containing high-p_T jets pointing to the most forward ECAL region ($2.4 < |\eta| < 3.0$). While no reconstructed objects at this pseudorapidity enter the measurements, the systematic variation of 20% in this correction for affected events nevertheless leads to a small measurement uncertainty.

- Scale factors for the b tagging efficiency of individual b jets and the mistagging efficiencies of c quark, and light-flavor and gluon jets are measured using dedicated calibration samples [93]. The factors are parameterized as functions of jet p_T and η. For the systematic uncertainty evaluation the scale factors are varied within their estimated uncertainties [93]. The variations for b and c jets are treated as fully correlated, while independent variations are applied to the light jets. The statistical uncertainties of the scale factors, arising from the limited size of the calibration samples, are uncorrelated among the years. These uncertainties play a significant role for the light jets, and hence, the light jet uncertainties are treated as uncorrelated across the years. All other b tagging uncertainties are treated as fully correlated across the years.

8.2   Theoretical uncertainties

The uncertainties in the modeling of the $t\bar{t}$ events, comprising signal and other final states, are assessed with appropriate variations of the nominal simulation based on POWHEG+PYTHIA 8 and the CP5 tune, introduced in Section 3:

- The uncertainty arising from missing higher-order terms in the simulation of the signal process at the ME level is estimated by varying the renormalization and factorization scales (denoted as μ_r and μ_f, respectively) in the POWHEG simulation up and down by factors of two with respect to the nominal values. The nominal scales are defined in the POWHEG sample as $\mu_r = \mu_f = \sqrt{(m_t^{\text{MC}})^2 + p_{T,t}^2}$. Here, $p_{T,t}$ denotes the p_T of the top quark in the $t\bar{t}$ rest frame. In total, six variations are applied: two with μ_r fixed, two with μ_f fixed, and two with both scales varied in the same direction (up or down). For each measurement bin, the envelope of the resulting measurement variations is taken as the final uncertainty.

- For the parton shower simulation, uncertainties are separately assessed for initial- and final-state radiation, by varying the respective shower scales up and down by

factors of two.

- The uncertainty in the damping of real emissions in the NLO calculalation when matching to the parton shower is derived by varying the h_{damp} parameter in POWHEG from its nominal value of $1.379 \, m_{\text{t}}^{\text{MC}}$ to $0.8738 \, m_{\text{t}}^{\text{MC}}$ and $2.305 \, m_{\text{t}}^{\text{MC}}$, according to the tuning results of Ref. [57].

- The uncertainty from the choice of PDFs is assessed by reweighting the $t\bar{t}$ signal simulation according to the ± 1 standard deviation along the directions of the 100 eigenvectors of the NNPDF3.1 error PDF sets [52] and adding the resulting measurement variations in quadrature. In addition, the value of the strong coupling α_{S} is independently varied within its uncertainty in the PDF set.

- The dependence of the measurement on the assumed top quark mass is estimated by varying m_{t}^{MC} in the $t\bar{t}$ simulation by $\pm 1 \, \text{GeV}$ around the nominal value of $172.5 \, \text{GeV}$.

- The uncertainty related to modeling of the UE is estimated by varying the CP5 tune parameters within their uncertainties determined in the tuning process [57].

- The nominal PYTHIA 8 setup includes a model of color reconnection (CR) based on MPIs with early resonance decays switched off. The analysis is repeated with three other CR models within PYTHIA 8: the MPI-based scheme with early resonance decays switched on, a gluon-move scheme [111], and a QCD-inspired scheme [112]. The total CR related uncertainty is taken to be the maximum deviation from the nominal result.

- The b jet energy response is different for semileptonic decays of b hadrons and thus their branching fractions are varied within world average uncertainties [1]. The parton level cross sections are corrected for the branching fractions for $W \rightarrow \ell \nu$ which are taken from Ref. [1] and varied according to their uncertainty of 1.5%.

The uncertainties associated with the values of h_{damp}, m_{t}^{MC}, and the CR treatment are evaluated using separate $t\bar{t}$ simulations incorporating the varied values, while all other theoretical uncertainties are assessed by applying appropriate event weights in the nominal simulations.

8.3 Background uncertainties

The contributions from non-$t\bar{t}$ background processes are overall at the level of a few percent, and the uncertainties are treated as global normalization uncertainties in the MC simulated processes. The uncertainty in the Z+jets background normalization is assessed by repeating the template fits to $m(\ell\bar{\ell})$ distributions, described in Section 6, with varied event selections. The nominal fits are performed with a selection dropping all requirements on $p_{\text{T}}^{\text{miss}}$, the number of b-tagged jets, and the $t\bar{t}$ kinematic reconstruction. In the first varied scenario, the $p_{\text{T}}^{\text{miss}} > 40 \, \text{GeV}$ requirement is switched on again for the e^+e^- and $\mu^+\mu^-$ channels, in the next one it is additionally required to have at least one b-tagged jet in the event, and in the last one the criterion of finding a solution to the full kinematic reconstruction is imposed. The variations are studied separately for each channel (e^+e^- and $\mu^+\mu^-$) and each year. The maximum scale factor variation observed among all channels, years, and event selections is used to derive a $\pm 20\%$ systematic uncertainty in the Z+jets normalization.

For the single top quark, W+jets, and diboson backgrounds, a normalization uncertainty of $\pm 30\%$ is taken, following the prescription from our previous analyses [38, 39]. This value is confirmed for the tW background (the dominant contribution among these processes) by analyzing the ratio of the numbers of events with one and two b-tagged jets in the $e^\pm\mu^\mp$ sample. This ratio is higher for the tW process than for $t\bar{t}$ events. The observed ratio in data agrees well

with the nominal simulations but deteriorates significantly when the assumed tW cross section is varied by more than 30%.

8.4   Summary of uncertainties

The total systematic uncertainty in each measurement bin is assessed by adding all contributions described above in quadrature, separately for positive and negative cross section variations. If a systematic uncertainty leads to two cross section variations of the same sign, the largest one is taken and the opposite variation is set to zero. These procedures are applied only to the cross section plots while the full information on all measurement variations is preserved in HEPdata [48] and also contributes to all theory-to-data χ^2 comparisons presented in this paper, following the χ^2 definition in Appendix A. The total uncertainties for the measured cross sections range 2–20%, depending on the observable and the bin. They are dominated by the systematic uncertainties.

The uncertainties are illustrated in Figs. 6–7, showing the relative contributions from the various sources for selected differential cross sections. Individual sources affecting a particular uncertainty (e.g. JES) are added in quadrature and shown as a single component. Additional experimental systematic uncertainties and all contributions from theoretical uncertainties are also added in quadrature, respectively, and shown as single components. For most bins in a majority of the distributions, the JES is the dominant systematic uncertainty. The evaluation of this uncertainty is also affected by the limited number of simulated $t\bar{t}$ signal events, particularly at high transverse momenta or invariant masses. Important contributions arise from other experimental sources, as well as from theoretical and background uncertainties. Among the significant experimental sources of uncertainties are the lepton and b tagging efficiencies, and for measurements of absolute cross sections, the integrated luminosity. For the theoretical uncertainties, the following sources contribute significantly, with relative magnitudes depending on the observables and phase space region: ME level and final-state radiation scales, h_{damp} parameter, top quark mass, underlying event, and CR.
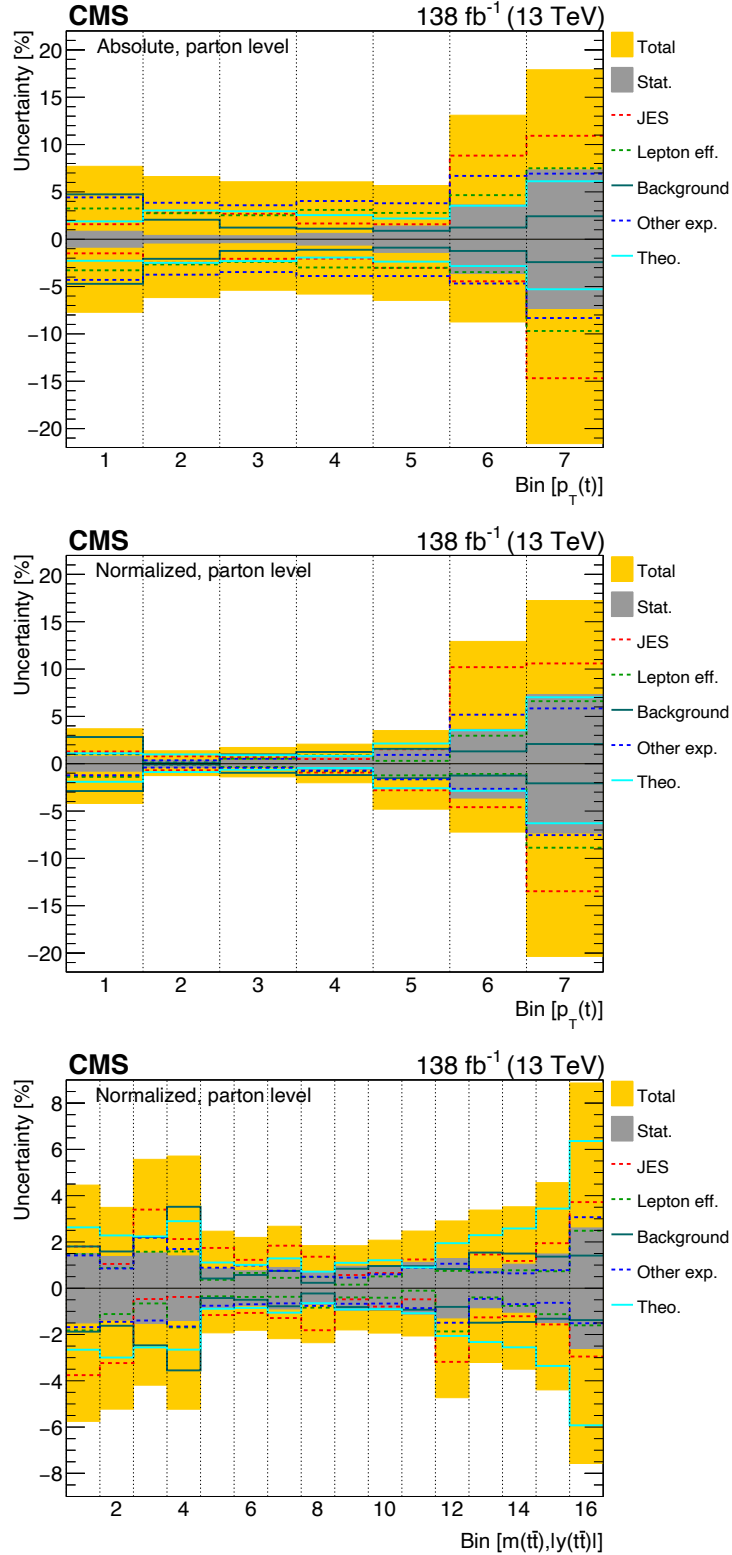
Figure 6: The various sources of systematic uncertainty and their relative contributions to the overall uncertainty are shown for several parton-level measurements: absolute $p_T(t)$ (upper), normalized $p_T(t)$ (middle), and normalized $[m(t\bar{t}), |y(t\bar{t})|]$ (lower). The statistical uncertainties and the total uncertainties (statistical and systematic uncertainties added in quadrature) are shown as grey and yellow bands, respectively. The ranges of the observables for a given bin number can be read off from the corresponding cross section distributions in Figs. 8 and 17.
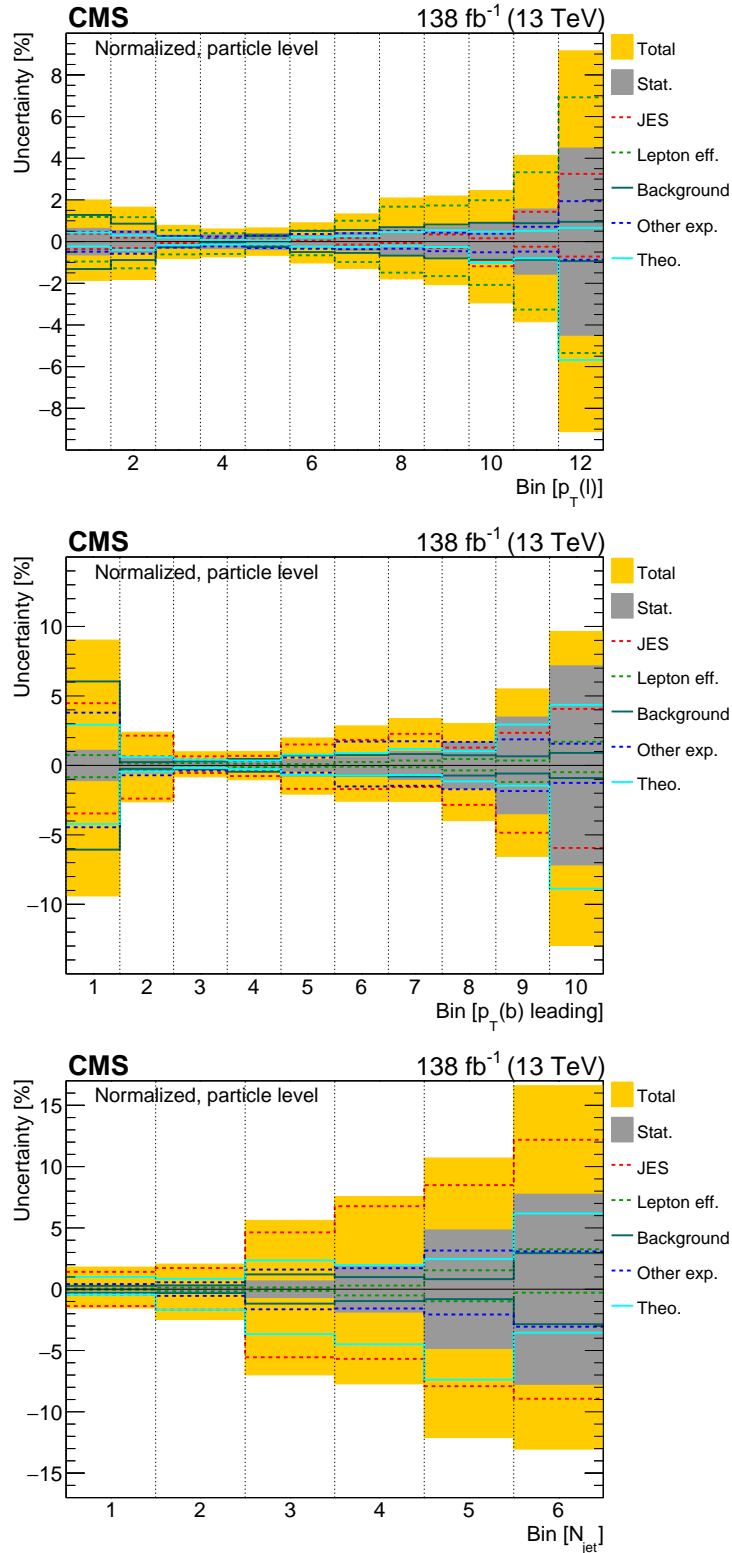
Figure 7: The various sources of systematic uncertainty and their relative contributions to the overall uncertainty are shown for several normalized particle-level measurements: p_T of the lepton (upper), p_T of the leading b jet (middle), and N_{jet} (lower). The statistical uncertainties and the total uncertainties (statistical and systematic uncertainties added in quadrature) are shown as grey and yellow bands, respectively. The ranges of the observables for a given bin number can be read off from the corresponding cross section distributions in Figs. 24, 25, and 31.

9 Results

Cross sections for $t\bar{t}$ and top quark kinematic variables are discussed in Section 9.1, for lepton and b jet variables in Section 9.2, and for events with additional jets in Section 9.3. The three predictions based on MC simulations introduced in Section 3: POWHEG+PYTHIA 8 ('POW+PYT'), POWHEG+HERWIG 7 ('POW+HER'), and MG5_aMC@NLO[FxFx]+PYTHIA 8 ('FxFx+PYT'), are used for comparisons to data. The POW+PYT and POW+HER theoretical predictions differ by the parton-shower method, hadronization and event tune (p_T-ordered parton showering, string hadronization model, and CP5 tune in POW+PYT, or angular ordered parton showering, cluster hadronization model, and CH3 tune in POW+HER), while the POW+PYT and FxFx+PYT predictions adopt different matrix elements (inclusive $t\bar{t}$ production at NLO in POW+PYT, or $t\bar{t}$ with up to two extra partons at NLO in FxFx+PYT) and different methods for matching with parton shower (correcting the first parton shower emission to the NLO result in POW+PYT, or subtracting from the exact NLO result its parton shower approximation in FxFx+PYT). In Section 9.4, several theoretical calculations with beyond-NLO precision are introduced and their predictions compared to the data for a subset of the measured cross sections. Finally, a study of the sensitivity of the normalized cross sections to the PDFs is presented in Section 9.5. For each data-to-theory comparison, a χ^2 statistic and the number of degrees of freedom (dof) are reported. One statistic, denoted in the following as "standard χ^2", probes directly the quality of the nominal predictions. It takes all measurement uncertainties into account, including bin-to-bin correlations, but neglects the uncertainties in the theoretical predictions. For POW+PYT, additional χ^2 values that include prediction uncertainties are also provided, applying the full set of uncertainties discussed in Section 8.2 to the generator-level predictions. The exact definition of the χ^2 values is given in Appendix A. Normalized cross sections and tables providing the χ^2 values are presented in this section, while absolute cross sections and corresponding χ^2 tables are summarized in Appendix B. The p-values denoting the probability for finding a χ^2 of equal or larger size than observed are tabulated, for all results, in Appendix C.

9.1 Results for top quark and $t\bar{t}$ kinematic observables at the parton and particle levels

The studies presented in this subsection aim to provide a comprehensive survey of the kinematic spectra of the top quark and antiquark, the $t\bar{t}$ system, and their correlations.

9.1.1 Single-differential cross sections

The single-differential cross sections are shown in Figs. 8–13. The χ^2 values of the model-to-data comparisons are listed in Tables 1–2, and the corresponding p-values in Tables 25–26. First, we present measurements where the top quark and antiquark kinematics are studied. Figure 8 illustrates the distributions of $p_T(t)$ and $p_T(\bar{t})$. Both the POW+PYT and, in particular, the FxFx+PYT models predict harder spectra than observed, while POW+HER provides a reasonable description of the data, as supported by the p-value of the χ^2 test. The discrepancy between POW+PYT and the data is smaller than what was observed in our previous analysis [38]. This reduction can be attributed to the use of the more-recent tune CP5 [57] for the PYTHIA 8 part of the calculation, whereas in the previous analysis the CUETP8M2T4 tune [61, 68, 69] was applied. The FxFx+PYT model provides the poorest description of the data, as indicated by the particularly large χ^2 values. Figure 9 depicts the $y(t)$ and $y(\bar{t})$ distributions. All models predict a slightly more central distribution than observed in data. One general observation can be made at this point: the comparisons of predictions and data for the cross sections at the parton and particle levels show similar patterns. This is also the case for most other cross sections presented in this paper; consequently, a separate discussion of the parton- and particle-level

cross sections will be only given in case of significant differences.

Figure 10 shows the distributions of the complete set of $t\bar{t}$ kinematic observables: $p_T(t\bar{t})$, $m(t\bar{t})$, and $y(t\bar{t})$. For $p_T(t\bar{t})$, the phase space covered in our previous analysis [38] is extended up to 1 TeV. The description of the $p_T(t\bar{t})$ distribution is particularly difficult, since nonzero values indicate the presence of extra QCD radiation in the event recoiling against the $t\bar{t}$ system, which directly probes higher-order processes in the calculation. This effect is also characterized by large theory uncertainties as shown for the POW+PYT prediction. The three MC models differ in the predicted shape of the $p_T(t\bar{t})$ distribution and none of them is able to describe the data accurately. The best description is provided by POW+PYT, which tends to overshoot the data only in the higher-$p_T(t\bar{t})$ range. The FxFx+PYT model predicts too many events in the intermediate $p_T(t\bar{t})$ ranges, while POW+HER predicts too few. The description by POW+HER is somewhat improved compared to what was observed in our previous analysis [38], which can also be attributed to using a newer version of the HERWIG MC generator, HERWIG 7 [63], instead of HERWIG++ [113]. It is interesting to note that also in two recent measurements [37, 40] by the ATLAS and CMS Collaborations, the $p_T(t\bar{t})$ distribution was found to be rather poorly described by several models. In the present analysis, the $m(t\bar{t})$ spectrum is overall reasonably well described by the models, with the exception of the first bin near the threshold where the predictions lie somewhat below the data. This region is known to be particularly sensitive to the value of the top quark mass assumed in the calculations. To investigate this discrepancy in more detail, the POW+PYT prediction is also shown for two other values of the top quark mass parameter, $m_t^{\text{MC}} = 169.5\,\text{GeV}$ and $m_t^{\text{MC}} = 175.5\,\text{GeV}$, compared to the value of $172.5\,\text{GeV}$ taken in the nominal simulation. For the lower value, the cross section prediction moves up in the lowest $m(t\bar{t})$ bin by about 20% and the whole mass spectrum is a bit softer than in the data, however still providing a χ^2 with a good p-value. Using the higher value, the resulting predicted $m(t\bar{t})$ spectrum is clearly harder than what is observed in data. This discrepancy is also reflected by an increase of the χ^2 value of about 13 units compared to using the central mass value, proving the high sensitivity of the $m(t\bar{t})$ distribution to the top quark mass value, as explored in the CMS analysis [114]. The $y(t\bar{t})$ distribution of the data is described reasonably well by all models.

Moving on to studies of kinematic correlations between top quark and antiquark, we show in Fig. 11 the distribution of the absolute value of the azimuthal angle difference between the top quark and antiquark $|\Delta\phi(t,\bar{t})|$, and the difference of the absolute values of the top quark and antiquark rapidities $|y(t)| - |y(\bar{t})|$, related to the charge asymmetry [115]. For $|\Delta\phi(t,\bar{t})|$, angles smaller than π are directly sensitive to additional QCD radiation in the event. The models provide a good description of the data. The $|y(t)| - |y(\bar{t})|$ spectrum of the data is not perfectly described by the MC models, as they predict more events at small rapidity separations and fewer at larger values $||y(t)| - |y(\bar{t})|| \approx 2$.

Figure 12 presents the distributions of two ratios: $p_T(t)/m(t\bar{t})$ and $p_T(t\bar{t})/m(t\bar{t})$. The study of the first quantity is inspired by the observation in Ref. [39] that at large $m(t\bar{t})$ the effect of the models predicting harder $p_T(t)$ spectra is enhanced. Indeed, all three tested models predict a significantly harder spectrum for the ratio of the two variables and the χ^2 values indicate a poor data description. The distribution of the second ratio, $p_T(t\bar{t})/m(t\bar{t})$, is expected to be sensitive to p_T resummation effects. The description by the three models follows largely the trends observed for $p_T(t\bar{t})$.

Finally, we study two observables ξ_1 and ξ_2, defined as $\xi_1 = [E(t\bar{t}) - p_z(t\bar{t})]/2E_p$ and $\xi_2 = [E(t\bar{t}) + p_z(t\bar{t})]/2E_p$, with E_p denoting the proton beam energy, and $p_z(t\bar{t})$ the magnitude of the $t\bar{t}$ momentum along the beam axis. In the leading order pQCD picture of the $pp \rightarrow t\bar{t}$

process, these variables represent the proton momentum fractions of the two partons entering the hard interaction. Figure 13 depicts the $\log(\xi_1)$ and $\log(\xi_2)$ distributions. Overall, these PDF-sensitive distributions are reasonably well described by all the models. Of special interest is the last bin covering proton momentum fractions above $\approx$0.2, where the uncertainties in the PDFs, in particular for the gluon distribution, start to grow.

The description of the kinematic distributions of top quark, antiquark, and $t\bar{t}$ system by the three MC models can be summarized as follows. The models tend to predict, for the individual quarks, harder p_T spectra and slightly more-central rapidity distributions than those observed in data. A reasonable description is provided for the $t\bar{t}$ rapidity and invariant mass spectra. The latter is described less well by the POW+PYT simulation that uses a larger value of m_t^{MC}, as it predicts a harder spectrum than that observed in data. The $|\Delta\phi(t,\bar{t})|$ distribution is modeled well, and smaller rapidity separations are predicted than observed in data on average. The FxFx+PYT model provides overall the least accurate description of the data, in particular by predicting harder p_T spectra for the top quark, antiquark, and the $t\bar{t}$ system. Among all the models, POW+HER predicts the softest p_T spectra for the top quark, antiquark, and the $t\bar{t}$ system, which matches the data well for the former two, but are too soft for the latter. The POW+PYT model provides the best description of the p_T distribution of the $t\bar{t}$ system. The standard χ^2 values indicate a rather poor description of several distributions by some of the models. For POW+PYT, the χ^2 values that include the prediction uncertainties (see Tables 1–2) are significantly smaller than the standard χ^2 values. However, for a few distributions, such as $p_T(t)/m(t\bar{t})$, the p-values of these additional χ^2 tests remain too low for a reasonable description of the data. This is typically the case for the distributions with the largest visible discrepancies.
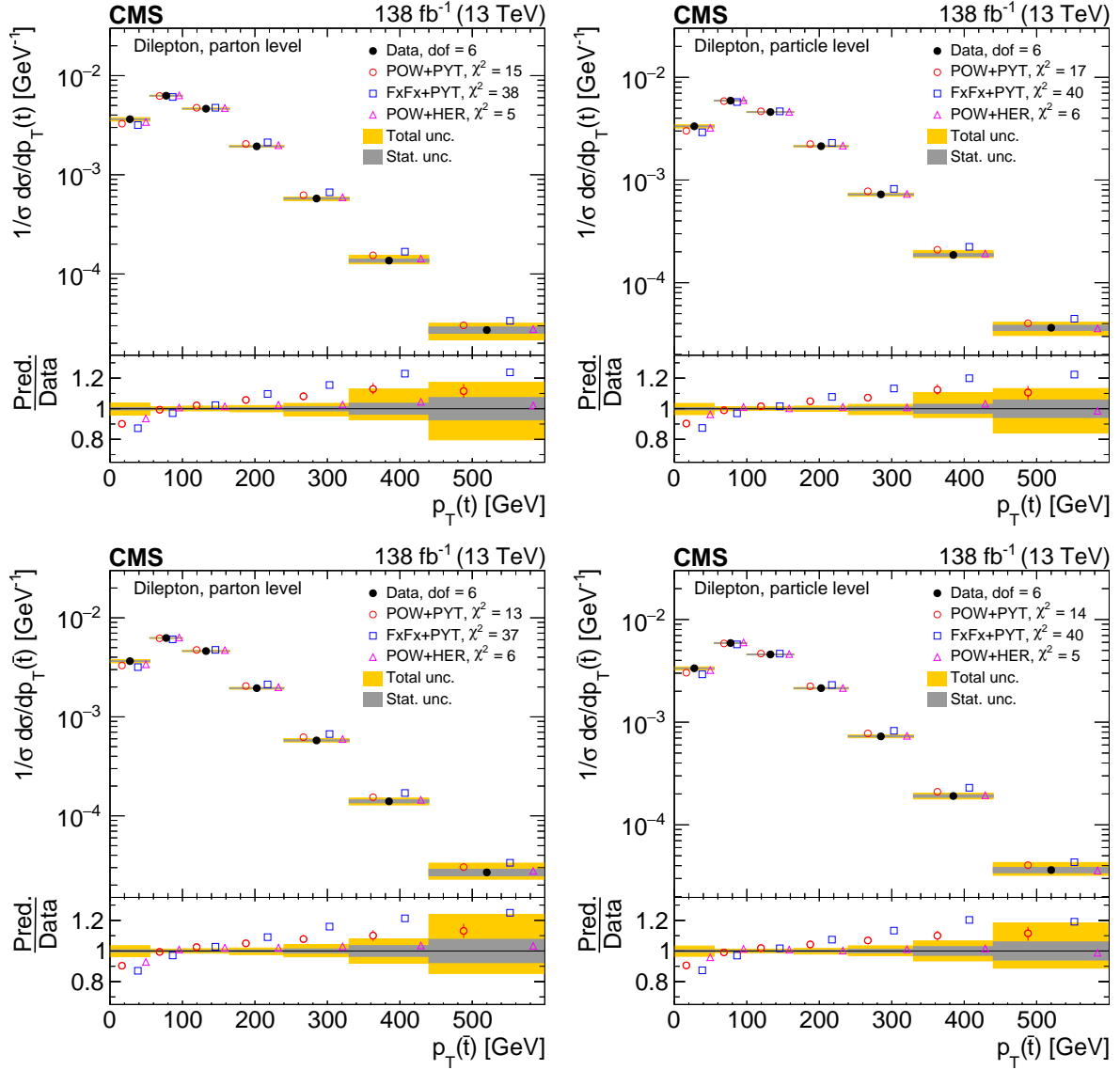
Figure 8: Normalized differential t$\bar{\text{t}}$ production cross sections as functions of $p_{\text{T}}(\text{t})$ (upper) and $p_{\text{T}}(\bar{\text{t}})$ (lower), measured at the parton level in the full phase space (left) and at the particle level in a fiducial phase space (right). The data are shown as filled circles with grey and yellow bands indicating the statistical and total uncertainties (statistical and systematic uncertainties added in quadrature), respectively. For each distribution, the number of degrees of freedom (dof) is also provided. The cross sections are compared to various MC predictions (other points). The estimated uncertainties in the POWHEG+PYTHIA 8 ('POW-PYT') simulation are represented by vertical bars on the corresponding points. For each MC model, a value of χ^2 is reported that takes into account the measurement uncertainties. The lower panel in each plot shows the ratios of the predictions to the data.

Figure 9: Normalized differential $t\bar{t}$ production cross sections as functions of $y(t)$ (upper) and $y(\bar{t})$ (lower) are shown for data (filled circles) and various MC predictions (other points). Further details can be found in the caption of Fig. 8.
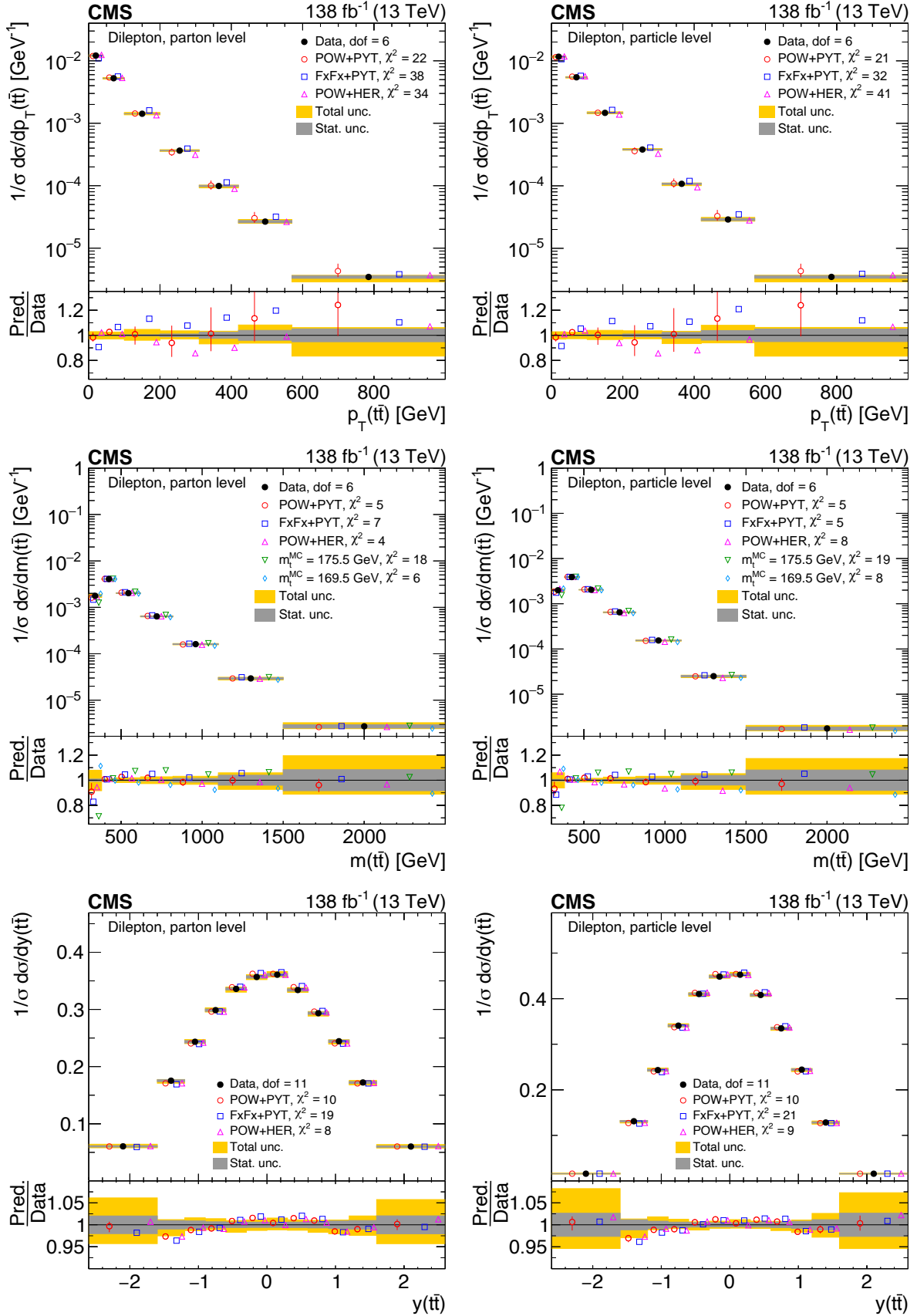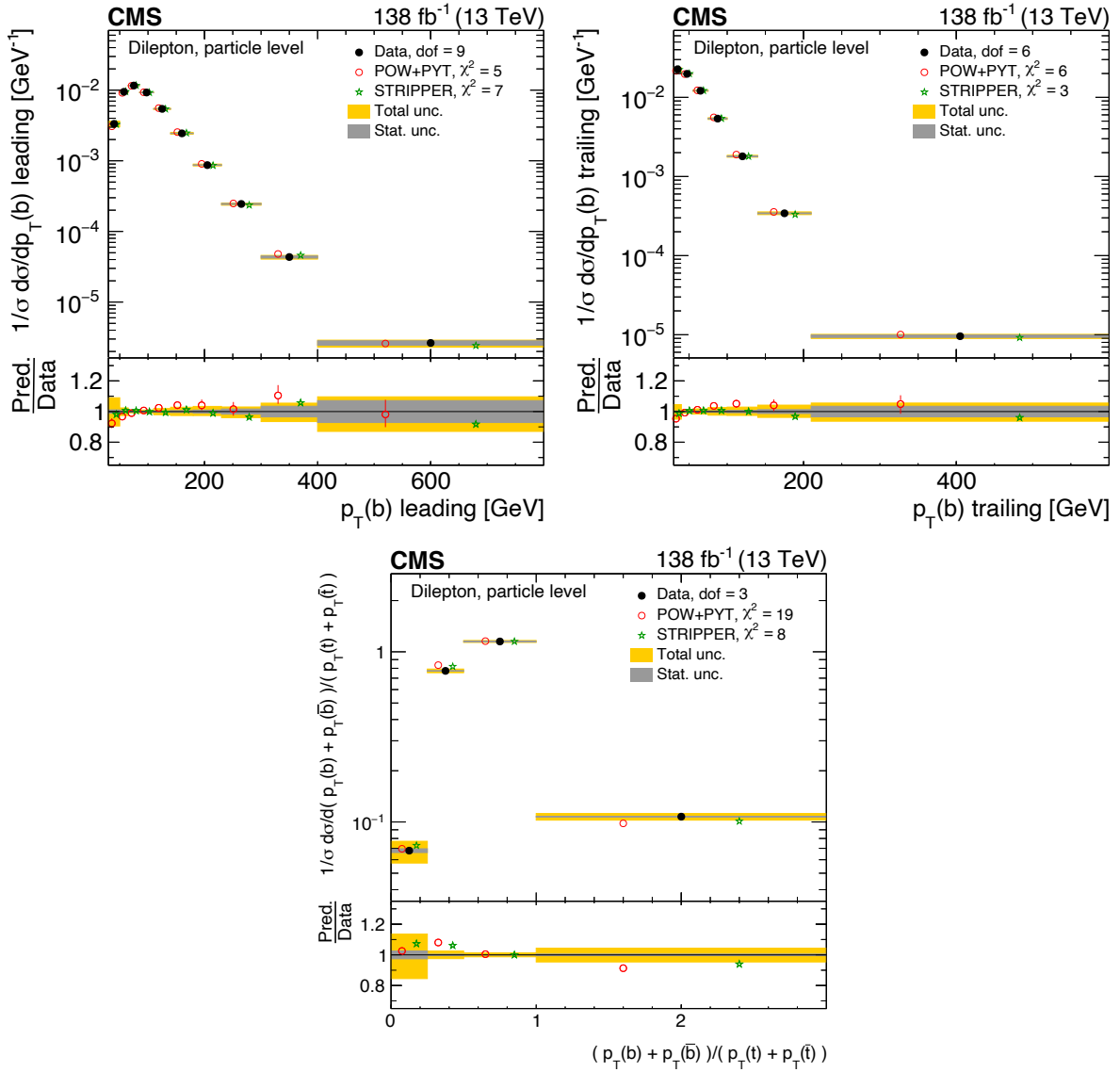
Figure 10: Normalized differential tt̄ production cross sections as functions of $p_T(t\bar{t})$ (upper), $m(t\bar{t})$ (middle) and $y(t\bar{t})$ (lower) are shown for data (filled circles) and various MC predictions (other points). The $m(t\bar{t})$ distributions are also compared to POWHEG+PYTHIA 8 ('POW-PYT') simulations with different values of m_t^{MC}. Further details can be found in the caption of Fig. 8.
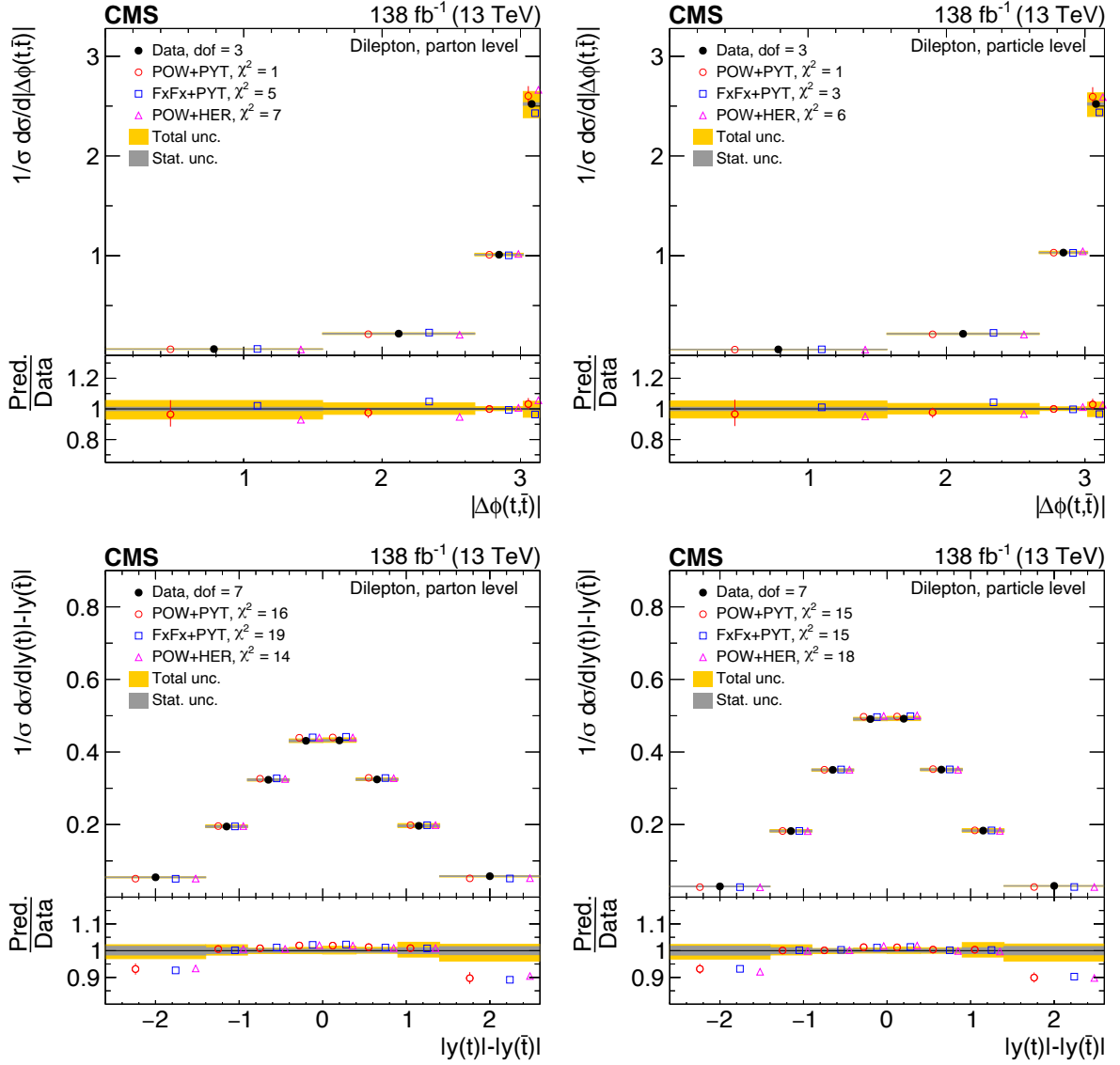
Figure 11: Normalized differential $t\bar{t}$ production cross sections as functions of $|\Delta\phi(t,\bar{t})|$ (upper) and $|y(t)| - |y(\bar{t})|$ (lower) are shown for data (filled circles) and various MC predictions (other points). Further details can be found in the caption of Fig. 8.
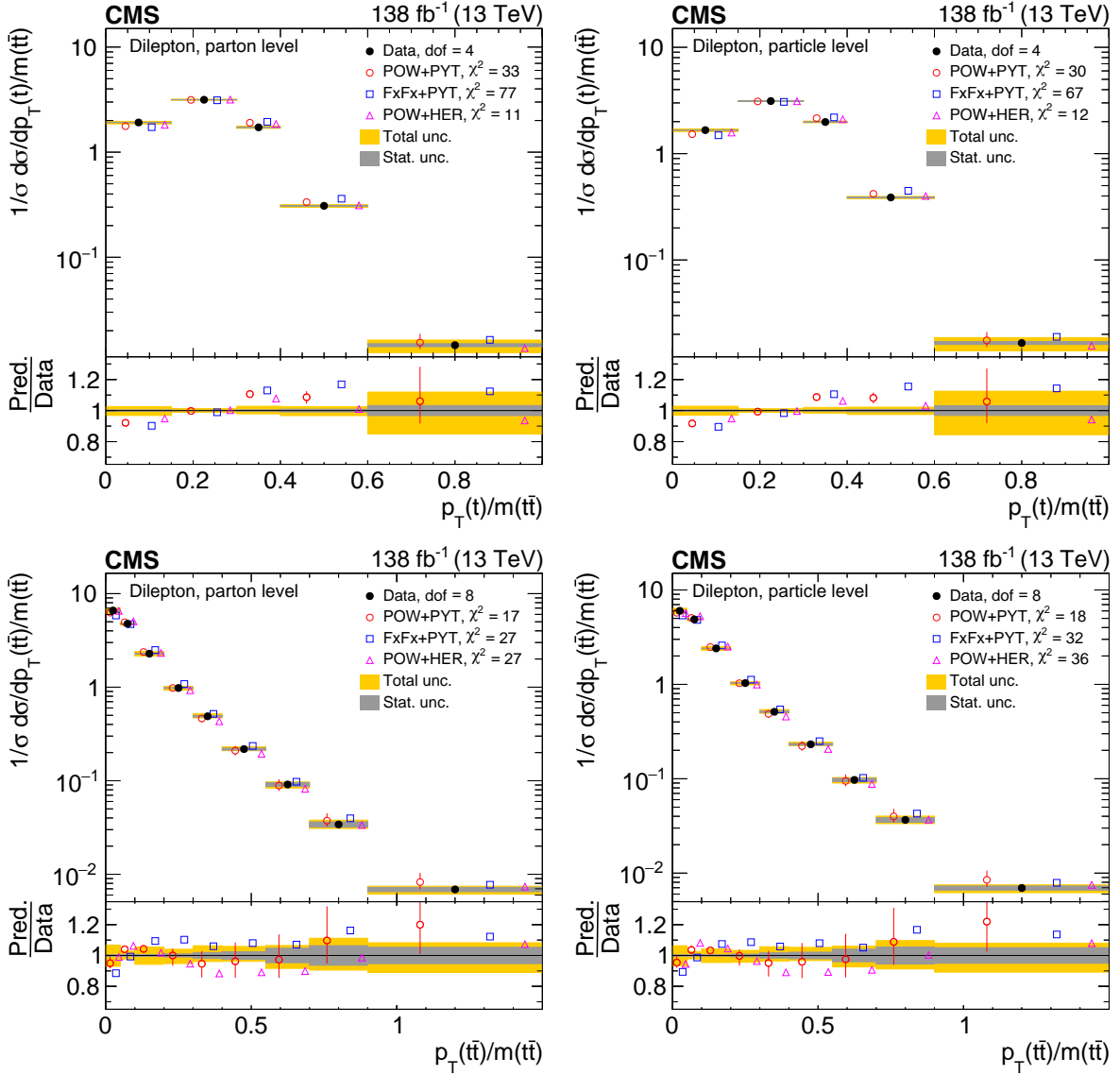
Figure 12: Normalized differential t$\bar{\text{t}}$ production cross sections as functions of $p_\text{T}(\text{t})/m(\text{t}\bar{\text{t}})$ (upper) and $p_\text{T}(\text{t}\bar{\text{t}})/m(\text{t}\bar{\text{t}})$ (lower) are shown for data (filled circles) and various MC predictions (other points). Further details can be found in the caption of Fig. 8.
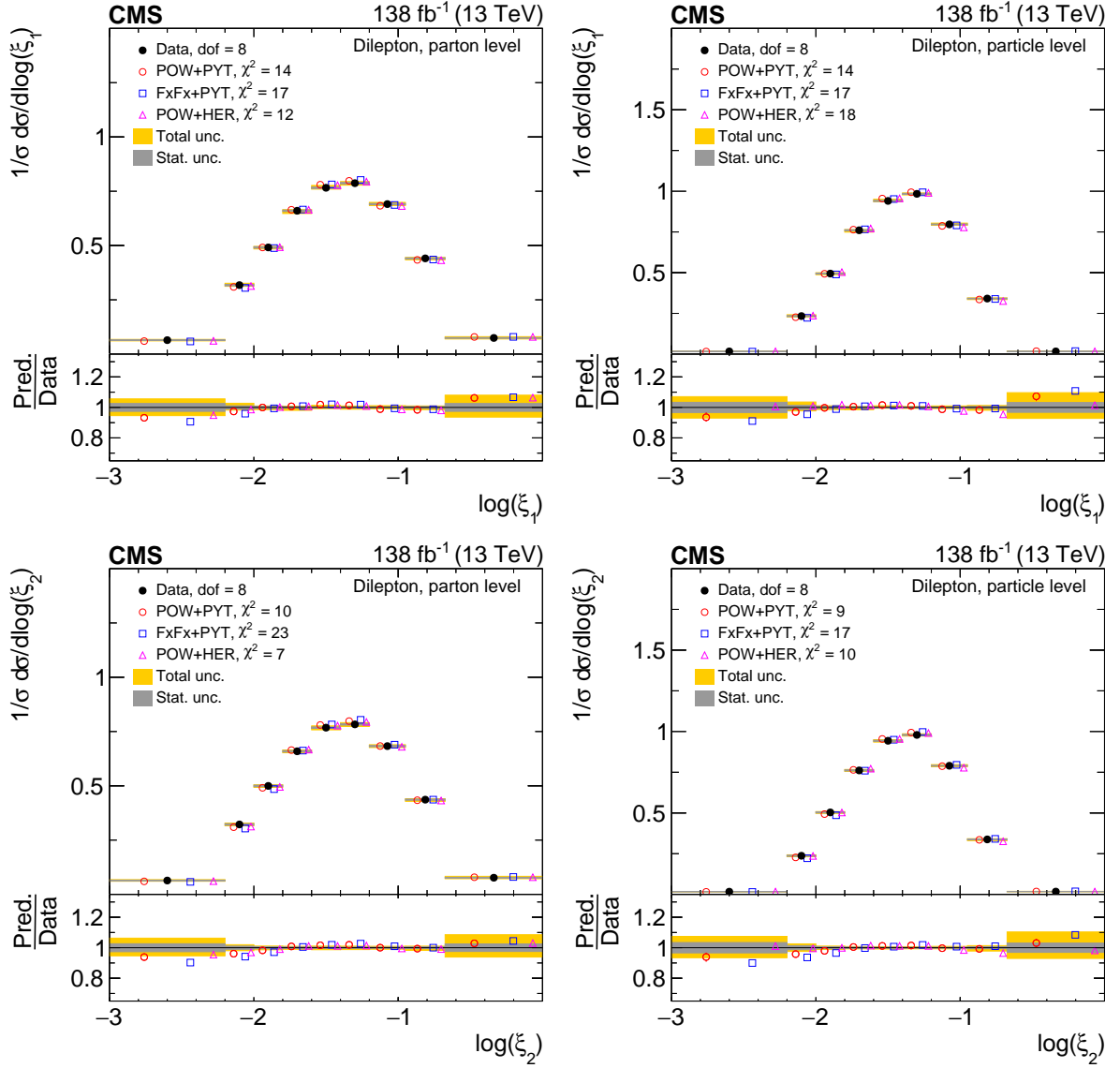
Figure 13: Normalized differential $t\bar{t}$ production cross sections as functions of $\log(\xi_1)$ (upper) and $\log(\xi_2)$ (lower) are shown for data (filled circles) and various MC predictions (other points). Further details can be found in the caption of Fig. 8.

Table 1: The χ^2 values and dof of the measured normalized single-differential cross sections for t$\bar{\text{t}}$ and top quark kinematic observables at the parton level are shown with respect to the predictions of various MC generators. The χ^2 values are calculated taking only measurement uncertainties into account and excluding theory uncertainties. For POW+PYT, the χ^2 values including theory uncertainties are indicated with the brackets (w. unc.).

Cross section variables	dof	χ^2		
		POW+PYT (w. unc.)	FxFx+PYT	POW+HER
$p_{\text{T}}(\text{t})$	6	15 (11)	38	5
$p_{\text{T}}(\bar{\text{t}})$	6	13 (9)	37	6
$y(\text{t})$	9	23 (20)	34	21
$y(\bar{\text{t}})$	9	28 (25)	39	24
$p_{\text{T}}(\text{t}\bar{\text{t}})$	6	22 (7)	38	34
$y(\text{t}\bar{\text{t}})$	11	10 (8)	19	8
$m(\text{t}\bar{\text{t}})$	6	5 (3)	7	4
$\lvert\Delta\phi(\text{t},\bar{\text{t}})\rvert$	3	1 (0)	5	7
$\lvert y(\text{t})\rvert - \lvert y(\bar{\text{t}})\rvert$	7	16 (9)	19	14
$p_{\text{T}}(\text{t})/m(\text{t}\bar{\text{t}})$	4	33 (20)	77	11
$p_{\text{T}}(\text{t}\bar{\text{t}})/m(\text{t}\bar{\text{t}})$	8	17 (6)	27	27
$\log(\xi_1)$	8	14 (10)	17	12
$\log(\xi_2)$	8	10 (7)	23	7

Table 2: The χ^2 values and dof of the measured normalized single-differential cross sections for t$\bar{\text{t}}$ and top quark kinematic observables at the particle level are shown with respect to the predictions of various MC generators. The χ^2 values are calculated taking only measurement uncertainties into account and excluding theory uncertainties. For POW+PYT, the χ^2 values including theory uncertainties are indicated with the brackets (w. unc.).

Cross section variables	dof	χ^2		
		POW+PYT (w. unc.)	FxFx+PYT	POW+HER
$p_{\text{T}}(\text{t})$	6	17 (12)	40	6
$p_{\text{T}}(\bar{\text{t}})$	6	14 (9)	40	5
$y(\text{t})$	9	19 (16)	30	20
$y(\bar{\text{t}})$	9	24 (20)	30	27
$p_{\text{T}}(\text{t}\bar{\text{t}})$	6	21 (7)	32	41
$y(\text{t}\bar{\text{t}})$	11	10 (7)	21	9
$m(\text{t}\bar{\text{t}})$	6	5 (3)	5	8
$|\Delta\phi(\text{t},\bar{\text{t}})|$	3	1 (0)	3	6
$|y(\text{t})| - |y(\bar{\text{t}})|$	7	15 (10)	15	18
$p_{\text{T}}(\text{t})/m(\text{t}\bar{\text{t}})$	4	30 (20)	67	12
$p_{\text{T}}(\text{t}\bar{\text{t}})/m(\text{t}\bar{\text{t}})$	8	18 (7)	32	36
$\log(\xi_1)$	8	14 (9)	17	18
$\log(\xi_2)$	8	9 (6)	17	10

9.1.2 Multi-differential cross section measurements

Studies of differential $t\bar{t}$ cross sections performed as functions of several kinematic observables shed light on the details of the $t\bar{t}$ production dynamics and can help to better understand the origin of model-to-data discrepancies seen in single-differential cross sections. The double-differential measurements performed in this analysis, e.g. as functions of $|y(t)|$ and $p_T(t)$, are denoted in the following as $[|y(t)|,\ p_T(t)]$, etc., and an analogous notation is adopted for triple-differential cross sections. The cross section results are shown in Figs. 14–23. The upper and lower plots show the cross sections at the parton and particle levels, respectively. The χ^2 values of model-to-data comparisons are listed in Tables 3–4, and the corresponding p-values in Tables 27–28.

In the first set of studies, we investigate how the $p_T(t)$ distribution is correlated with other event kinematic observables. In Fig. 14, the $p_T(t)$ distribution is compared in different ranges of $|y(t)|$ to predictions from the same three MC models discussed above. The data distribution is softer than that of the predictions over the entire $y(t)$ range. The POW+HER prediction that gave a reasonable description of the single-differential $p_T(t)$ cross section (Fig. 8), still provides the best description, but exhibits a stronger positive $p_T(t)$ slope with respect to the data in the lowest and highest $|y(t)|$ ranges. Figure 15 shows the $p_T(t)$ distributions in different $m(t\bar{t})$ ranges. Similar to the result of the previous analysis [39], this is among the double-differential cross sections poorly described by the models. While the POW+HER model describes the $p_T(t)$ distribution in the lowest $m(t\bar{t})$ range near threshold reasonably well, it joins POW+PYT and FxFx+PYT in a trend that grows with increasing $m(t\bar{t})$ to predict a $p_T(t)$ spectrum that is harder than observed in the data. Figure 16 illustrates the $p_T(t\bar{t})$ spectrum in different $p_T(t)$ ranges. Larger $p_T(t)$ values can be kinematically correlated with higher $p_T(t\bar{t})$ values when the $t\bar{t}$ system is recoiling against additional QCD radiation in the event. The FxFx+PYT model predicts a harder $p_T(t\bar{t})$ spectrum than observed in the data for all $p_T(t)$ ranges. The POW+PYT and POW+HER predictions tend to overshoot the data in the higher $p_T(t)$ ranges at the lower $p_T(t\bar{t})$ values.

Next we investigate the $t\bar{t}$ kinematic observables. Figure 17 illustrates the $[m(t\bar{t}),\ |y(t\bar{t})|]$ distributions. Both variables are kinematically correlated with the observables ξ_1 and ξ_2 introduced above, and their combination is known to provide optimal information for constraining the PDFs [28]. For low- and medium-$m(t\bar{t})$ regions, the predictions are slightly more central than the data, though in the highest $m(t\bar{t})$ range the opposite effect is observed. In Fig. 18, the spectrum of $p_T(t\bar{t})$ is shown in bins of $|y(t\bar{t})|$. These two observables are rather uncorrelated, and thus it is not surprising that the description of the $p_T(t\bar{t})$ distribution by the models is similar in all $|y(t\bar{t})|$ ranges. Figure 19 presents the $[m(t\bar{t}),\ p_T(t\bar{t})]$ distributions. This is an interesting observable combination since the phase space for QCD radiation that is driving the $p_T(t\bar{t})$ observable is increasing with higher $m(t\bar{t})$. The trends observed in the single-differential $p_T(t\bar{t})$ distribution (see Fig. 10), namely, that FxFx+PYT (POW+HER) predicts a too hard (soft) spectrum, are somewhat enhanced in the higher $m(t\bar{t})$ ranges. Figure 20 shows the first simultaneous study of all three $t\bar{t}$ kinematic observables: p_T, mass, and rapidity. Overall, POW+PYT provides a fairly reasonable description, though FxFx+PYT and POW+HER show deficiencies in specific $m(t\bar{t})$ and $p_T(t\bar{t})$ phase space regions, with mostly small or moderate dependencies on $y(t\bar{t})$.

Finally, we perform several studies of $m(t\bar{t})$, investigating its correlation to several other kinematic observables. Figure 21 illustrates the distributions of $|y(t)|$. The trend that the predictions exhibit a more-central rapidity distribution than the data increases slightly with higher $m(t\bar{t})$. In Fig. 22, the $|\Delta\eta(t,\bar{t})|$ distributions are shown, which are sensitive to the hard scat-

tering dynamics. The data favor larger rapidity separations than predicted by the models, and the significance of this effect increases at larger $m(t\bar{t})$. The disagreement is the strongest for FxFx+PYT. For a given $m(t\bar{t})$ value, larger $|\Delta\eta(t,\bar{t})|$ are correlated with lower $p_T(t)$ values on average. This gives a hint that the effects of the models predicting harder $p_T(t)$ spectra and smaller $|\Delta\eta(t,\bar{t})|$ distributions, which are enhanced in the higher $m(t\bar{t})$ ranges (Figs. 15 and 22), are related. Figure 23 depicts the $[m(t\bar{t}), |\Delta\phi(t,\bar{t})|]$ distributions. At low $m(t\bar{t})$, the data prefer a slightly more back-to-back distribution of the top quark and antiquark compared to the models, but in the highest $m(t\bar{t})$ range, the trend reverses. Of all models considered, the FxFx+PYT simulation provides the best description and POW+HER the worst.

The observations made with the multi-differential cross sections can be summarized as follows. The p_T of the top quark and $t\bar{t}$, and the $t\bar{t}$ invariant mass are, in general, mildly correlated with rapidity of the same objects, and also the quality of their description by the MC models is nearly independent of the rapidity. As expected, larger kinematical correlations are observed between p_T and the mass observables. The trends of harder top quark p_T spectra and smaller rapidity separations between top quark and antiquark, when comparing the models to the data, is clearly enhanced at higher $m(t\bar{t})$. The tendency for FxFx+PYT (POW+HER) to predict p_T spectra for the $t\bar{t}$ system that are too hard (soft) is also stronger at higher $m(t\bar{t})$. In general, the p-values associated with the standard χ^2 values of the model-to-data comparisons are often much lower for the multi-differential $t\bar{t}$ cross sections than for the single-differential results presented in the previous subsection. This result is in line with the observations in recent comparable $t\bar{t}$ differential cross section papers from the ATLAS and CMS Collaborations [37, 40]. Another interesting observation is that the χ^2 values for both the single- and multi-differential $t\bar{t}$ cross sections are, on average, significantly higher than those observed in the corresponding previous measurements [38, 39] based on the 2016 data set only, which can be attributed to a substantially improved measurement precision. The χ^2 values that include the prediction uncertainties for the POW+PYT model (see Tables 3–4) are, in general, significantly lower than the standard ones. However, for several distributions such as $[m(t\bar{t}), |\Delta\phi(t,\bar{t})|]$, the values remain too high to indicate a good description of the data.
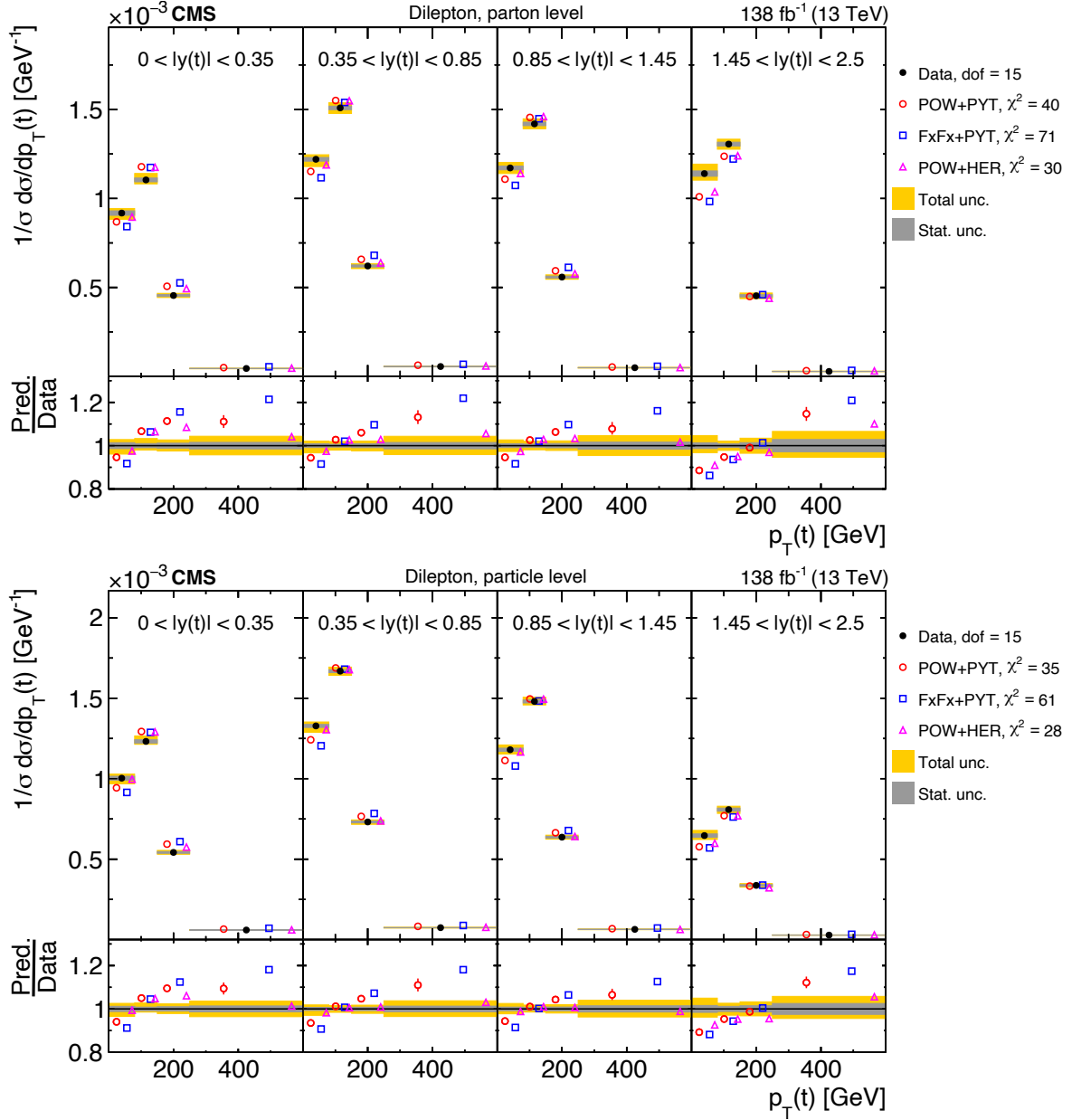
Figure 14: Normalized $[|y(t)|, p_{\mathrm{T}}(t)]$ cross sections measured at the parton level in the full phase space (upper) and at the particle level in a fiducial phase space (lower). The data are shown as filled circles with grey and yellow bands indicating the statistical and total uncertainties (statistical and systematic uncertainties added in quadrature), respectively. For each distribution, the number of degrees of freedom (dof) is also provided. The cross sections are compared to various MC predictions (other points). The estimated uncertainties in the POWHEG+PYTHIA 8 ('POW-PYT') simulation are represented by vertical bars on the corresponding points. For each MC model, a value of χ^2 is reported that takes into account the measurement uncertainties. The lower panel in each plot shows the ratios of the predictions to the data.

Figure 15: Normalized $[m(t\bar{t}), p_T(t)]$ cross sections are shown for data (filled circles) and various MC predictions (other points). Further details can be found in the caption of Fig. 14.
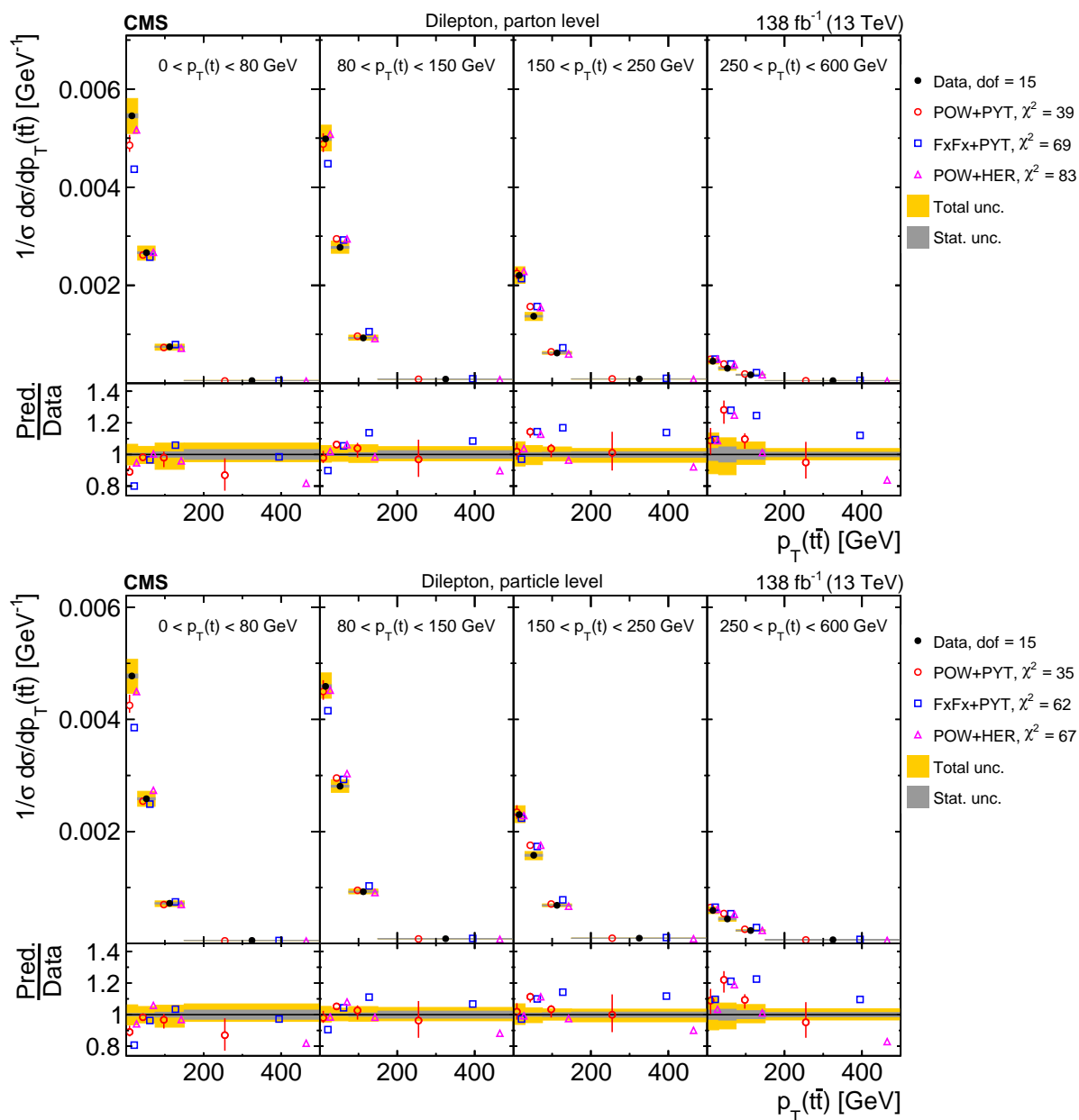
Figure 16: Normalized $[p_T(t),\ p_T(t\bar{t})]$ cross sections are shown for data (filled circles) and various MC predictions (other points). Further details can be found in the caption of Fig. 14.
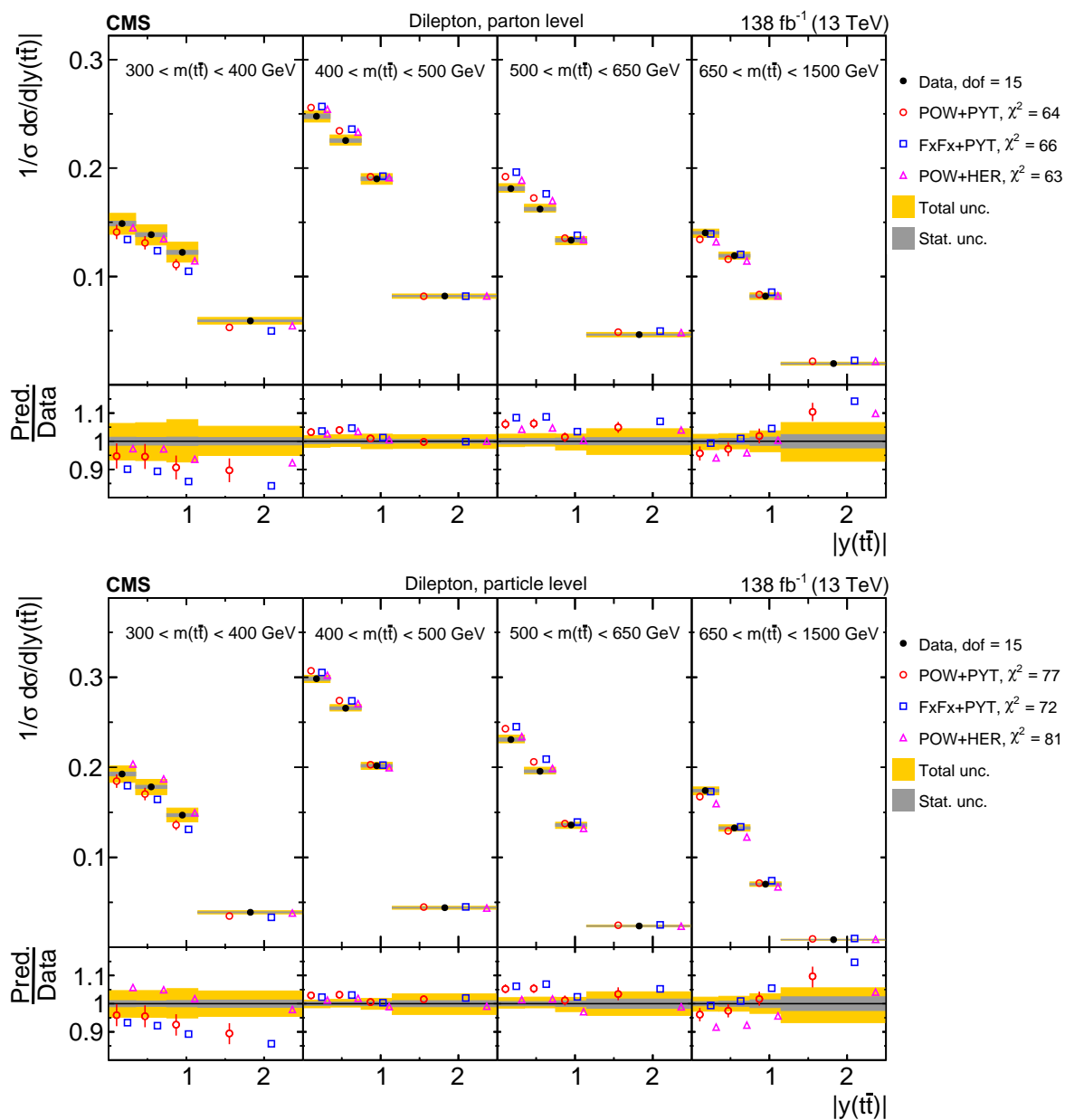
Figure 17: Normalized $[m(t\bar{t}), |y(t\bar{t})|]$ cross sections are shown for data (filled circles) and various MC predictions (other points). Further details can be found in the caption of Fig. 14.
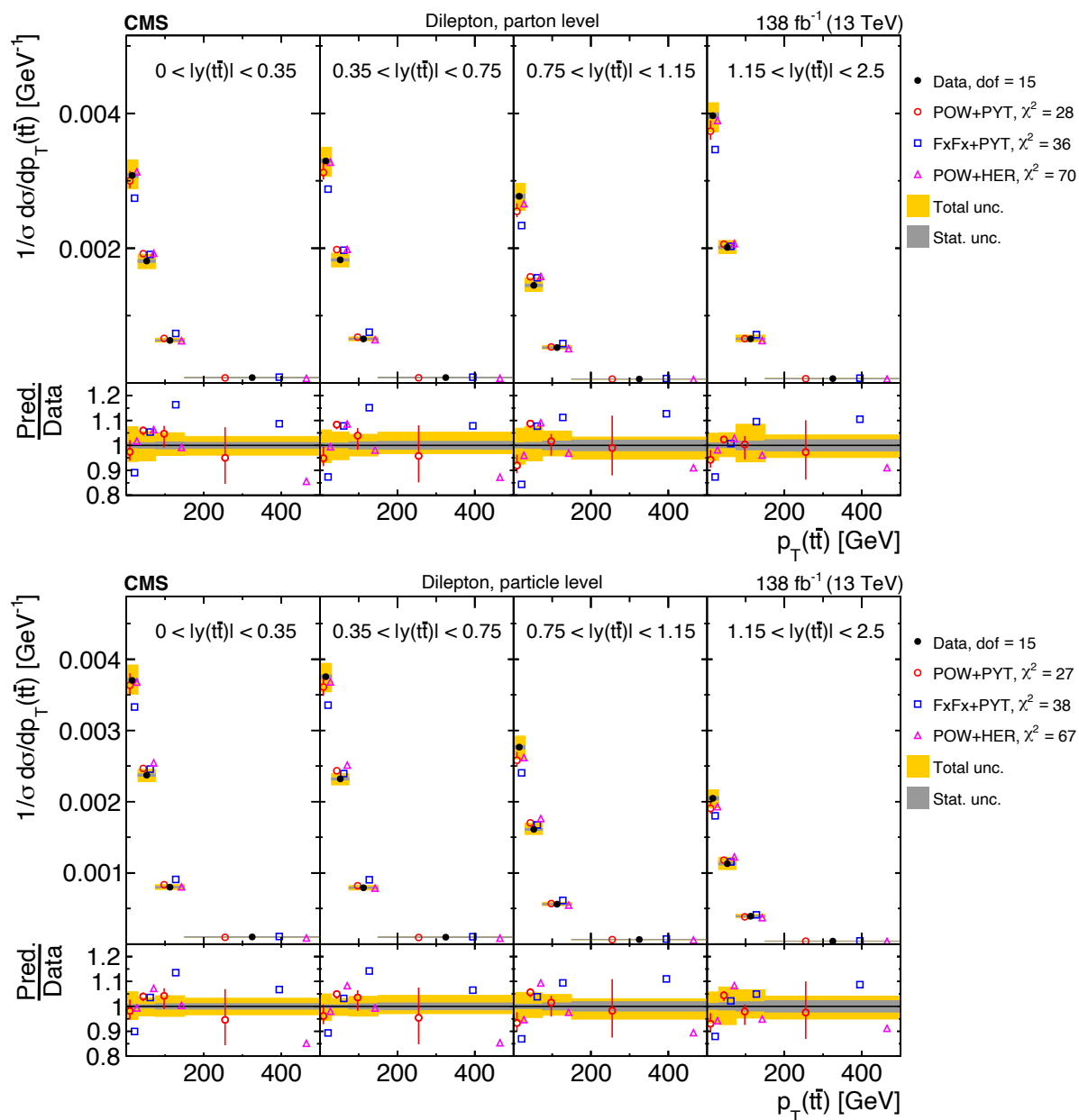
Figure 18: Normalized $[|y(t\bar{t})|, p_T(t\bar{t})]$ cross sections are shown for data (filled circles) and various MC predictions (other points). Further details can be found in the caption of Fig. 14.
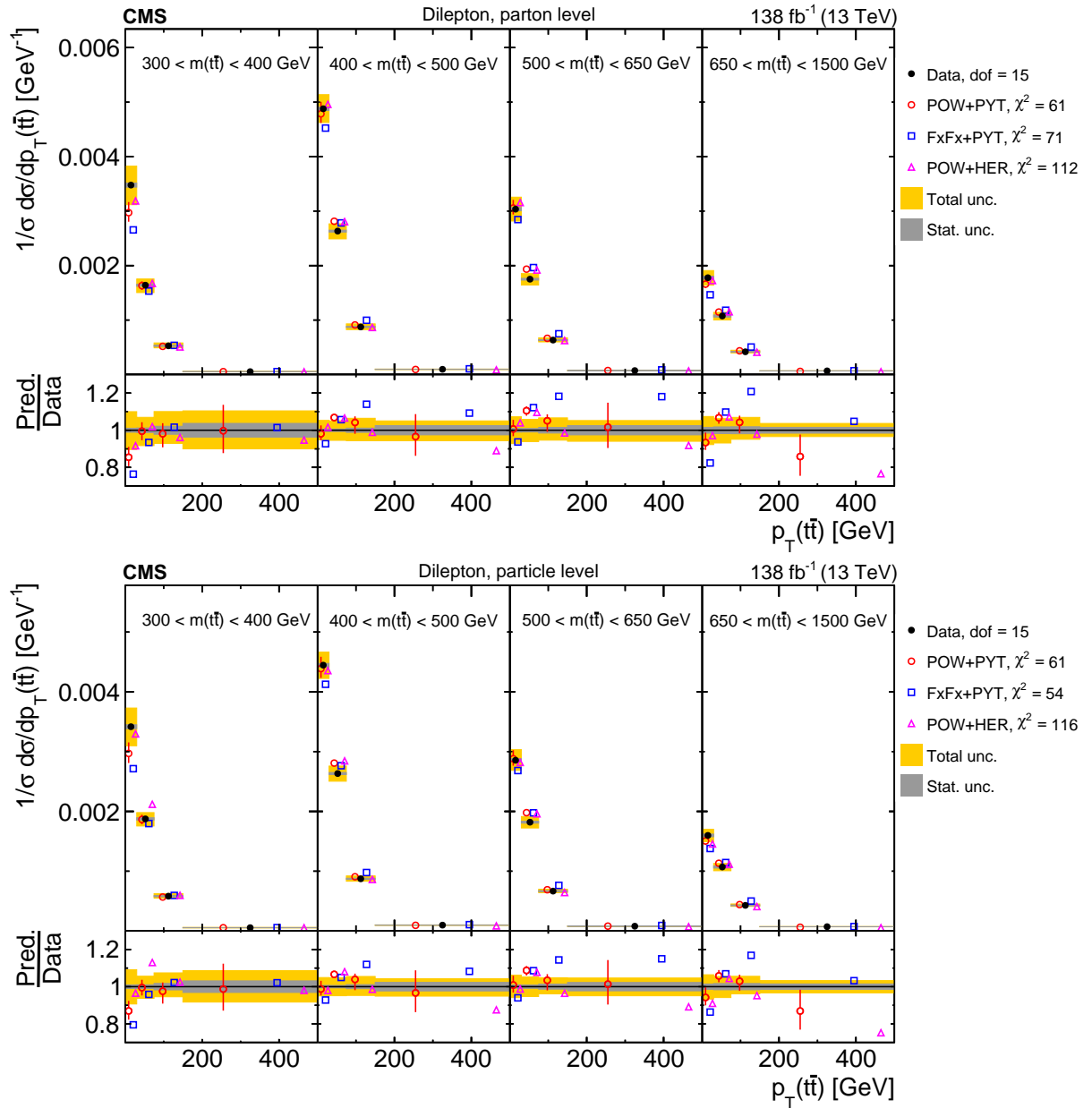
Figure 19: Normalized $[m(t\bar{t}), p_{T}(t\bar{t})]$ cross sections are shown for data (filled circles) and various MC predictions (other points). Further details can be found in the caption of Fig. 14.
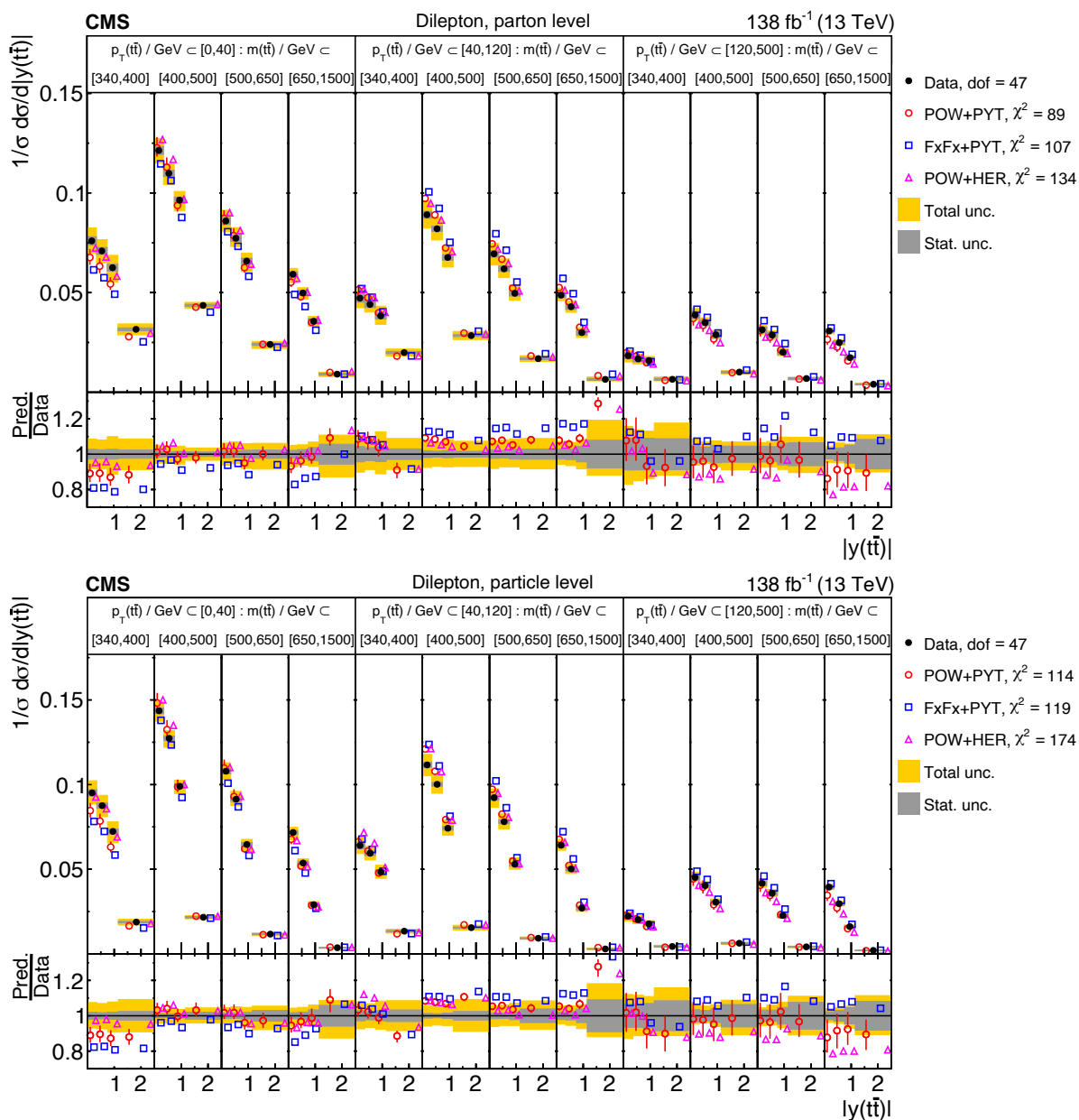
Figure 20: Normalized $[p_{\mathrm{T}}(\mathrm{t\bar{t}}), m(\mathrm{t\bar{t}}), |y(\mathrm{t\bar{t}})|]$ cross sections are shown for data (filled circles) and various MC predictions (other points). Further details can be found in the caption of Fig. 14.
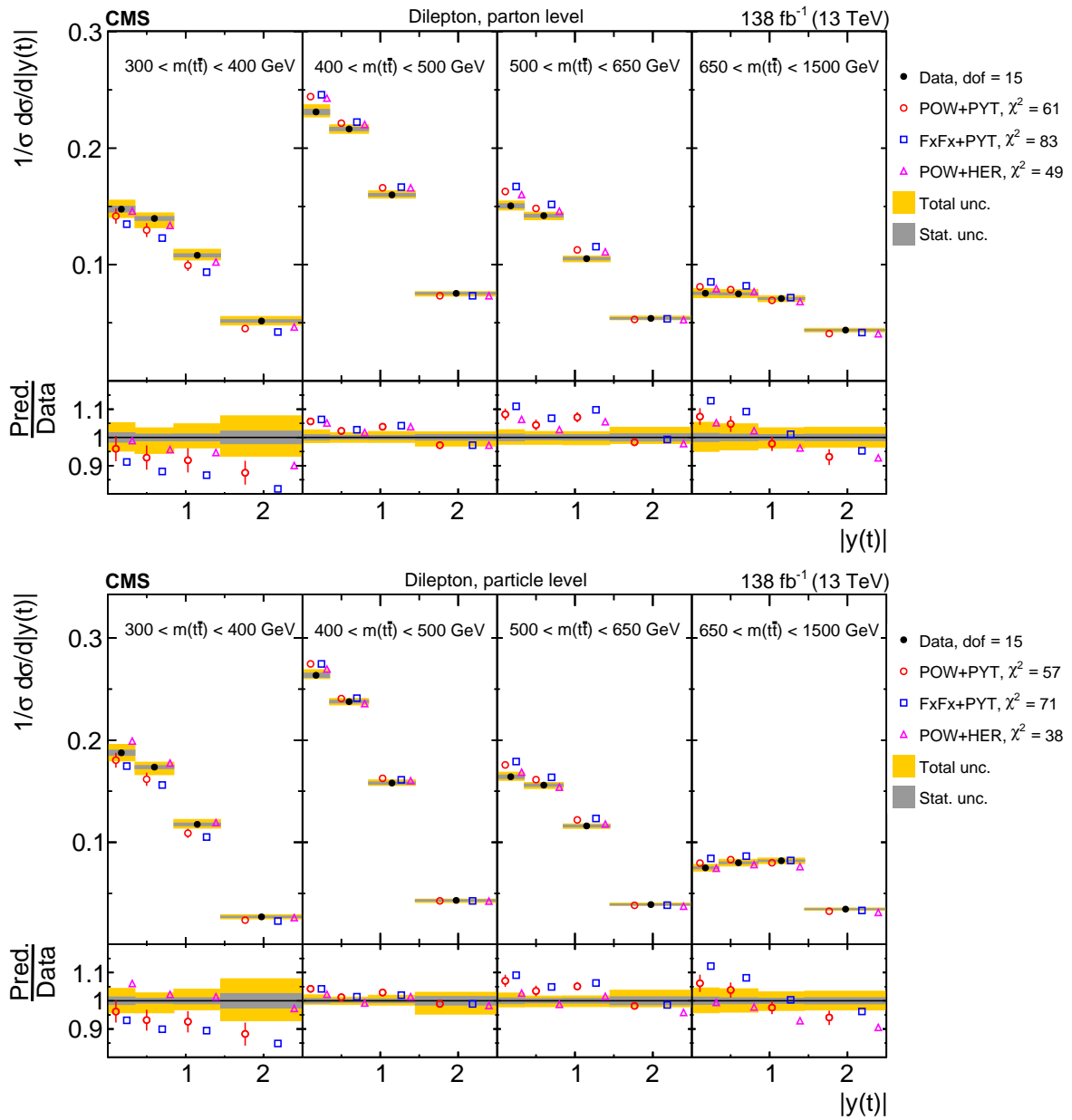
Figure 21: Normalized $[m(t\bar{t}), |y(t)|]$ cross sections are shown for data (filled circles) and various MC predictions (other points). Further details can be found in the caption of Fig. 14.
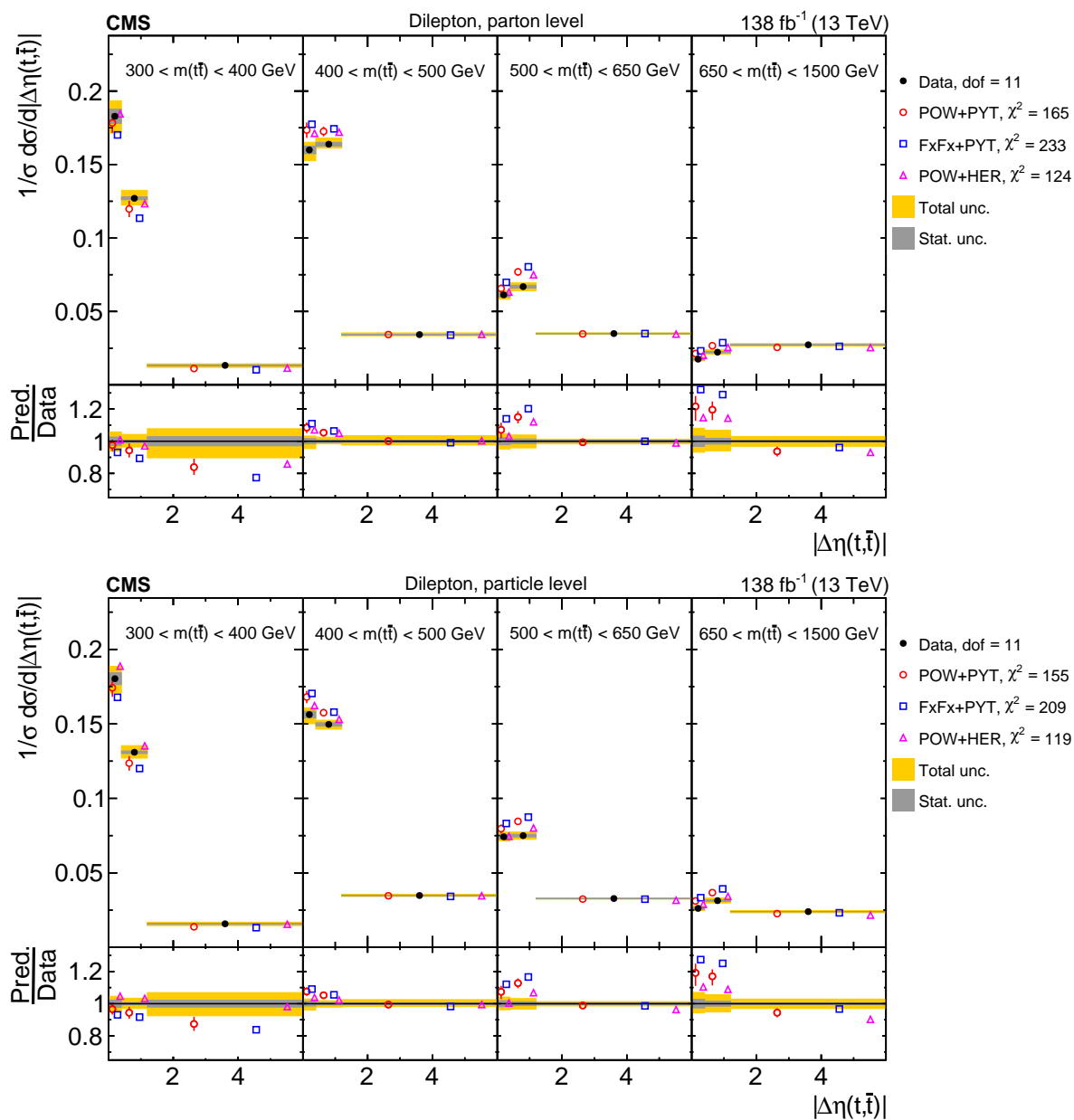
Figure 22: Normalized $[m(\text{t}\bar{\text{t}}), |\Delta\eta(\text{t},\bar{\text{t}})|]$ cross sections are shown for data (filled circles) and various MC predictions (other points). Further details can be found in the caption of Fig. 14.
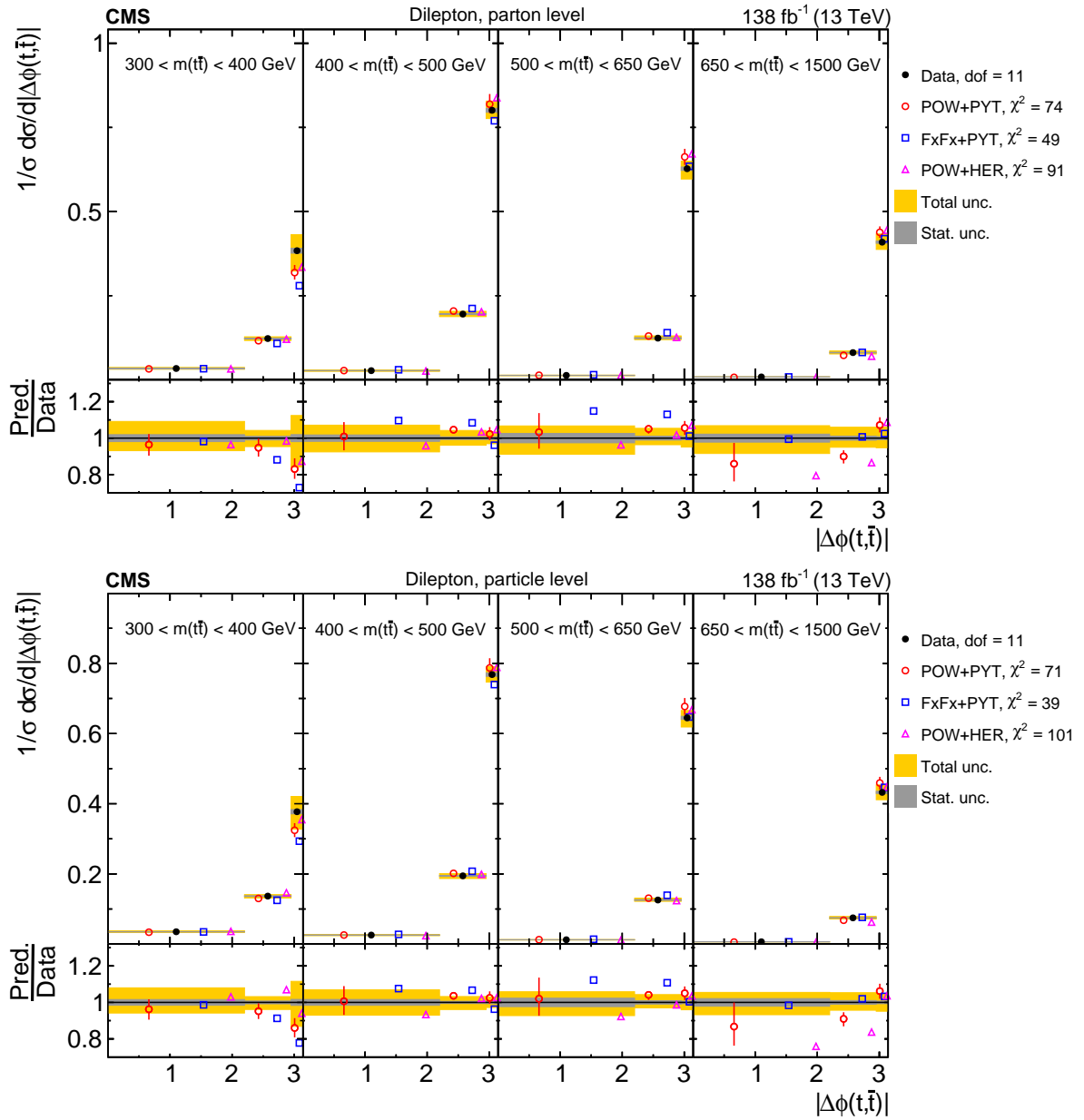
Figure 23: Normalized $[m(t\bar{t}), |\Delta\phi(t,\bar{t})|]$ cross sections are shown for data (filled circles) and various MC predictions (other points). Further details can be found in the caption of Fig. 14.

Table 3: The χ^2 values and dof of the measured normalized multi-differential cross sections for t$\bar{\text{t}}$ and top quark kinematic observables at the parton level are shown with respect to the predictions of various MC generators. The χ^2 values are calculated taking only measurement uncertainties into account and excluding theory uncertainties. For POW+PYT, the χ^2 values including theory uncertainties are indicated with the brackets (w. unc.).

Cross section variables	dof	χ^2		
		POW+PYT (w. unc.)	FxFx+PYT	POW+HER
$[|y(\text{t})|,\, p_{\text{T}}(\text{t})]$	15	40 (31)	71	30
$[m(\text{t}\bar{\text{t}}),\, p_{\text{T}}(\text{t})]$	8	83 (35)	152	41
$[p_{\text{T}}(\text{t}),\, p_{\text{T}}(\text{t}\bar{\text{t}})]$	15	39 (21)	69	83
$[m(\text{t}\bar{\text{t}}),\, |y(\text{t}\bar{\text{t}})|]$	15	64 (42)	66	63
$[|y(\text{t}\bar{\text{t}})|,\, p_{\text{T}}(\text{t}\bar{\text{t}})]$	15	28 (15)	36	70
$[m(\text{t}\bar{\text{t}}),\, p_{\text{T}}(\text{t}\bar{\text{t}})]$	15	61 (43)	71	112
$[p_{\text{T}}(\text{t}\bar{\text{t}}),\, m(\text{t}\bar{\text{t}}),\, |y(\text{t}\bar{\text{t}})|]$	47	89 (64)	107	134
$[m(\text{t}\bar{\text{t}}),\, |y(\text{t})|]$	15	61 (37)	83	49
$[m(\text{t}\bar{\text{t}}),\, |\Delta\eta(\text{t},\bar{\text{t}})|]$	11	165 (31)	233	124
$[m(\text{t}\bar{\text{t}}),\, |\Delta\phi(\text{t},\bar{\text{t}})|]$	11	74 (47)	49	91

Table 4: The χ^2 values and dof of the measured normalized multi-differential cross sections for t$\bar{\text{t}}$ and top quark kinematic observables at the particle level are shown with respect to the predictions of various MC generators. The χ^2 values are calculated taking only measurement uncertainties into account and excluding theory uncertainties. For POW+PYT, the χ^2 values including theory uncertainties are indicated with the brackets (w. unc.).

Cross section variables	dof	χ^2		
		POW+PYT (w. unc.)	FxFx+PYT	POW+HER
$[|y(\text{t})|,\, p_{\text{T}}(\text{t})]$	15	35 (25)	61	28
$[m(\text{t}\bar{\text{t}}),\, p_{\text{T}}(\text{t})]$	8	86 (36)	142	47
$[p_{\text{T}}(\text{t}),\, p_{\text{T}}(\text{t}\bar{\text{t}})]$	15	35 (19)	62	67
$[m(\text{t}\bar{\text{t}}),\, |y(\text{t}\bar{\text{t}})|]$	15	77 (40)	72	81
$[|y(\text{t}\bar{\text{t}})|,\, p_{\text{T}}(\text{t}\bar{\text{t}})]$	15	27 (18)	38	67
$[m(\text{t}\bar{\text{t}}),\, p_{\text{T}}(\text{t}\bar{\text{t}})]$	15	61 (36)	54	116
$[p_{\text{T}}(\text{t}\bar{\text{t}}),\, m(\text{t}\bar{\text{t}}),\, |y(\text{t}\bar{\text{t}})|]$	47	114 (68)	119	174
$[m(\text{t}\bar{\text{t}}),\, |y(\text{t})|]$	15	57 (26)	71	38
$[m(\text{t}\bar{\text{t}}),\, |\Delta\eta(\text{t},\bar{\text{t}})|]$	11	155 (30)	209	119
$[m(\text{t}\bar{\text{t}}),\, |\Delta\phi(\text{t},\bar{\text{t}})|]$	11	71 (42)	39	101

9.2 Results for lepton and b jet kinematic variables at the particle level

In this subsection we present selected kinematic distributions of the leptons and b jets produced in the decays of the top quark and antiquark, at the particle level in a fiducial phase space. These distributions are sensitive to both the dynamics of the $t\bar{t}$ production and its decay. The kinematic observables of these objects are measured very precisely with the CMS detector. The single-differential cross sections studied at the particle level are shown in Figs. 24–26. The model-to-data χ^2 and corresponding p-values are listed in Tables 5 and 29, respectively.

First we investigate the lepton kinematic observables. Figure 24 shows the distributions of the p_T of the lepton (with negative charge), the ratio of the trailing and leading lepton p_T, and the ratio of the lepton and top antiquark p_T. As for the top antiquark (Fig. 8), the MC models predict a harder p_T spectrum for the leptons than observed, with FxFx+PYT exhibiting a stronger discrepancy. For the ratio of the trailing and leading lepton p_T, the models predict distributions that are slightly too soft, with FxFx+PYT again showing a more significant deviation than POW+PYT and POW+HER. The distribution of the ratio of the lepton and top quark p_T shows an interesting excess of data over the predictions for ratios above 0.8, which is an indication of a failure of the models to describe the dynamics of the top quark decay.

Next, we study three b jet observables, as shown in Fig. 25. The leading (trailing) b jet is defined as the b jet from the decay of the $t\bar{t}$ system with the higher (lower) p_T. The distributions of the leading and trailing b jet p_T are reasonably well described by the POW+PYT and POW+HER models, while FxFx+PYT predicts a spectrum that is too hard. The third studied variable is the ratio between the sum of the p_T of the b and $\bar{b}$ jets over the sum of the p_T of the top quark and antiquark $(p_T(b) + p_T(\bar{b}))/(p_T(t) + p_T(\bar{t}))$. All models predict a distribution that is somewhat too soft.

In the next set of studies, shown in Fig. 26, we analyze the invariant mass spectra of the lepton pair $m(\ell\bar{\ell})$, of the b jet pair $m(b\bar{b})$, and of the combined system $m(\ell\bar{\ell}b\bar{b})$. We investigate whether the model descriptions for the mass spectra of these partial decay systems follow the good description observed for the full $t\bar{t}$ system, $m(t\bar{t})$ (Fig. 10, middle plot). The $m(\ell\bar{\ell})$ distributions show a clear trend towards a somewhat harder spectrum in the model predictions compared to the data. The $m(b\bar{b})$ spectra are reasonably well described overall by all three predictions, with a small trend of the data overshooting the predictions near threshold and at large mass values. The $m(\ell\bar{\ell}b\bar{b})$ distributions show a similar trend. Furthermore, we investigate the sensitivity of the different mass spectra to the value of the top quark mass assumed in the POW+PYT calculation, by showing the predictions for $m_t^{MC} = 169.5$ and 175.5 GeV, compared to the nominal prediction using a value of 172.5 GeV. It is clear that the predicted $m(\ell\bar{\ell})$ and $m(b\bar{b})$ spectra become harder with increasing m_t^{MC}, although the effects are diluted in the regions of small invariant masses compared to the $m(t\bar{t})$ distribution shown in Fig. 10. The $m(\ell\bar{\ell}b\bar{b})$ distribution clearly exhibits a better sensitivity to the m_t^{MC} value in the small invariant mass region, comparable to the one observed for the $m(t\bar{t})$ spectrum.

Finally, we study additional dilepton distributions, whose kinematic obervables are among those in the present analysis that are reconstructed with highest precision. Figure 27 shows the $p_T(\ell\bar{\ell})$ and $|\eta(\ell\bar{\ell})|$ distributions. Overall, they are reasonably well described by the three MC models, with FxFx+PYT predicting a $p_T(\ell\bar{\ell})$ spectrum that is slightly too hard and an $|\eta(\ell\bar{\ell})|$ distribution that is a bit too central. Figures 28-30 show double-differential cross sections, illustrating the correlations between the dilepton kinematic observables. The $[|\eta(\ell\bar{\ell})|, m(\ell\bar{\ell})]$ distributions show that the tendency of the MC predictions to provide a $m(\ell\bar{\ell})$ spectrum that is harder than in data is a bit enhanced towards high values of $|\eta(\ell\bar{\ell})|$. The $[|\eta(\ell\bar{\ell})|, p_T(\ell\bar{\ell})]$

spectra are well described by the POW+PYT and POW+HER models, while FxFx+PYT predicts $p_T(\ell\bar{\ell})$ distributions that are somewhat too hard at small $|\eta(\ell\bar{\ell})|$ values. For the $[p_T(\ell\bar{\ell}), m(\ell\bar{\ell})]$ distributions the $m(\ell\bar{\ell})$ spectra clearly become harder towards larger values of $p_T(\ell\bar{\ell})$ and this effect is a bit more pronounced in the MC models than in the data.

The observations made with the differential $t\bar{t}$ cross sections as functions of charged lepton and b jet kinematic observables can be summarized as follows. These measurements are the most accurate of all results presented in this document. Overall, the predictions from the MC models agree rather well with each other. The models predict harder distributions for the lepton p_T and the invariant mass of the lepton pair. The distributions of p_T of leading and trailing b jets, and of $m(b\bar{b})$ are reasonably well described, except for FxFx+PYT, which predicts harder p_T spectra. Among the invariant mass spectra, the $m(\ell\bar{\ell}b\bar{b})$ distribution clearly shows the strongest sensitivity to the value of the top quark mass used in the POW+PYT calculation. The single-differential p_T and η distributions of the dilepton system are reasonably well described by the models overall, although for double-differential distributions, including also $m(\ell\bar{\ell})$ as a possible second variable, some tensions are visible, in particular for FxFx+PYT. The standard χ^2 values indicate, in general, a poor quality in the description of the data by the nominal predictions. The inclusion of the prediction uncertainties for the POW+PYT model (see Table 5) results in χ^2 tests with reasonable p-values in most cases.
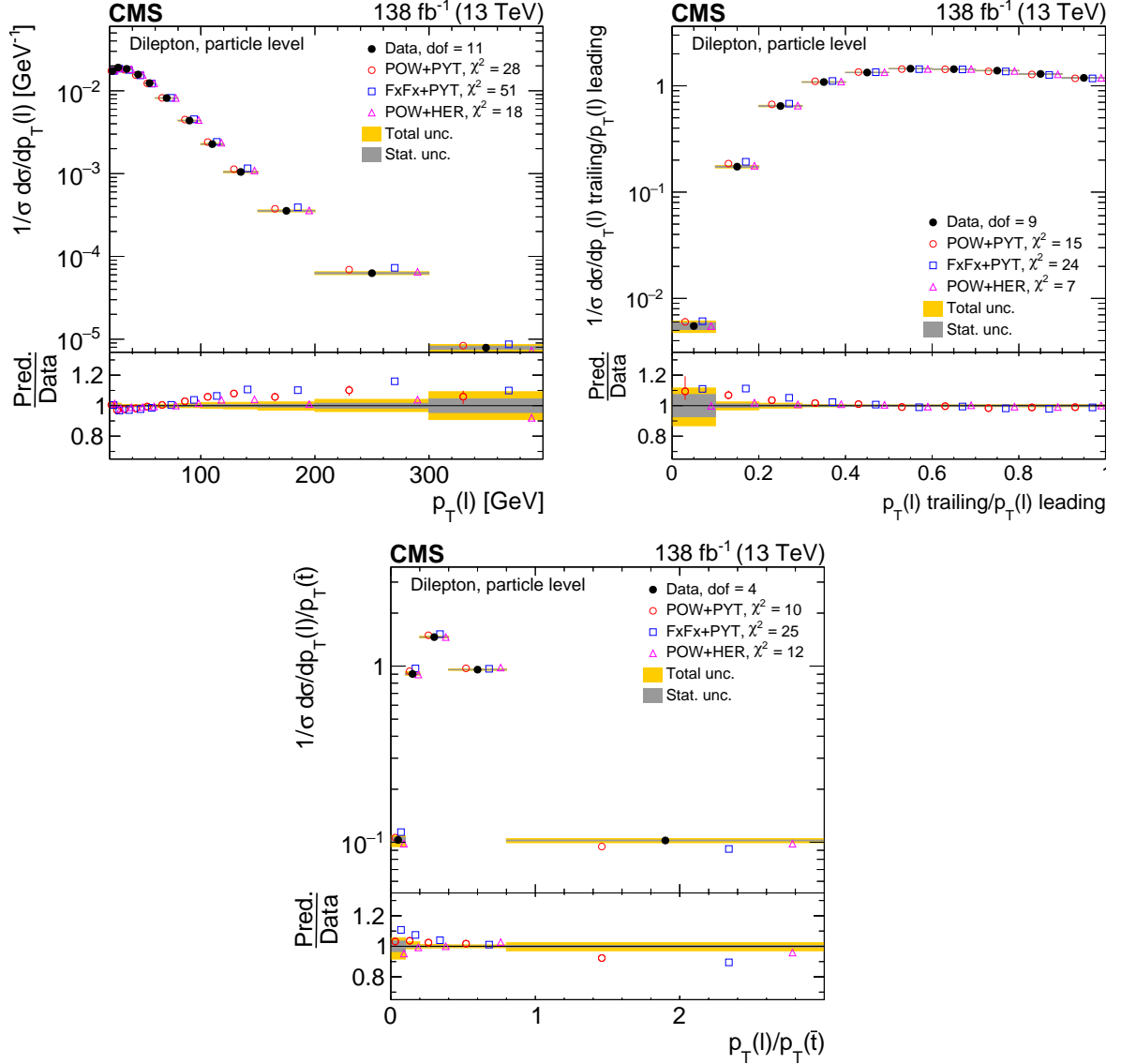
Figure 24: Normalized differential $t\bar{t}$ production cross sections as functions of p_T of the lepton (upper left), of the ratio of the trailing and leading lepton p_T (upper right), and of the ratio of lepton and top antiquark p_T (lower), measured at the particle level in a fiducial phase space. The data are shown as filled circles with grey and yellow bands indicating the statistical and total uncertainties (statistical and systematic uncertainties added in quadrature), respectively. For each distribution, the number of degrees of freedom (dof) is also provided. The cross sections are compared to various MC predictions (other points). The estimated uncertainties in the POWHEG+PYTHIA 8 ('POW-PYT') simulation are represented by vertical bars on the corresponding points. For each MC model, a value of χ^2 is reported that takes into account the measurement uncertainties. The lower panel in each plot shows the ratios of the predictions to the data.

Figure 25: Normalized differential $t\bar{t}$ production cross sections as functions of the p_T of the leading (upper left) and trailing (upper right) b jet, and $(p_T(b) + p_T(\bar{b}))/(p_T(t) + p_T(\bar{t}))$ (lower). Further details can be found in the caption of Fig. 24.
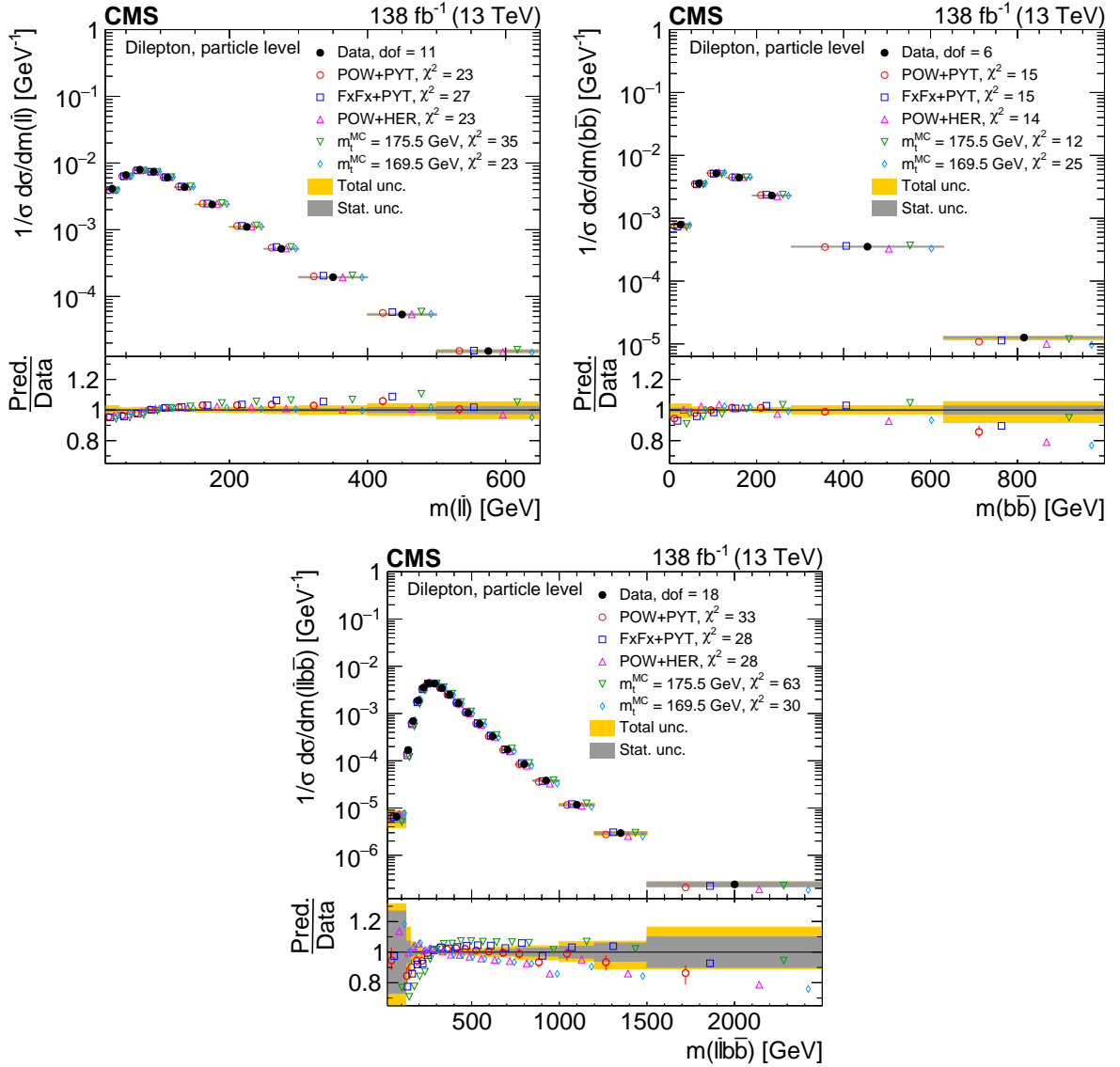
Figure 26: Normalized differential $t\bar{t}$ production cross sections as functions of $m(\ell\bar{\ell})$ (upper left), $m(b\bar{b})$ (upper right), and $m(\ell\bar{\ell}b\bar{b})$ (lower) are shown for data (filled circles) and various MC predictions (other points). The distributions are also compared to POWHEG+PYTHIA 8 ('POW-PYT') simulations with different values of m_t^{MC}. Further details can be found in the caption of Fig. 24.
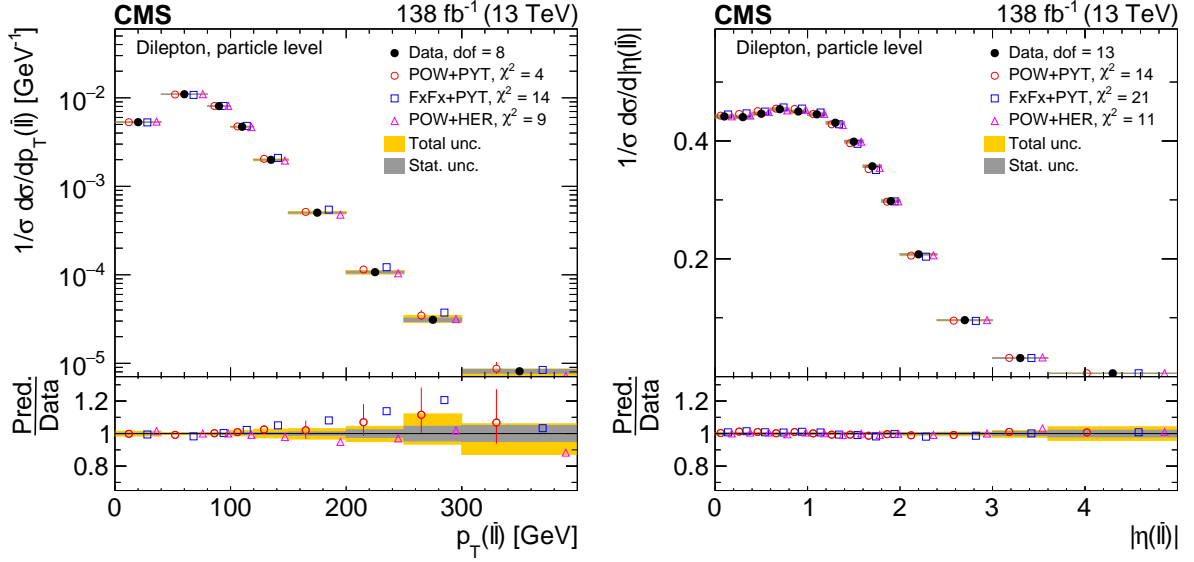
Figure 27: Normalized differential $t\bar{t}$ production cross sections as functions of $p_T(\ell\bar{\ell})$ (left) and $|\eta(\ell\bar{\ell})|$ (right) are shown for data (filled circles) and various MC predictions (other points). Further details can be found in the caption of Fig. 24.
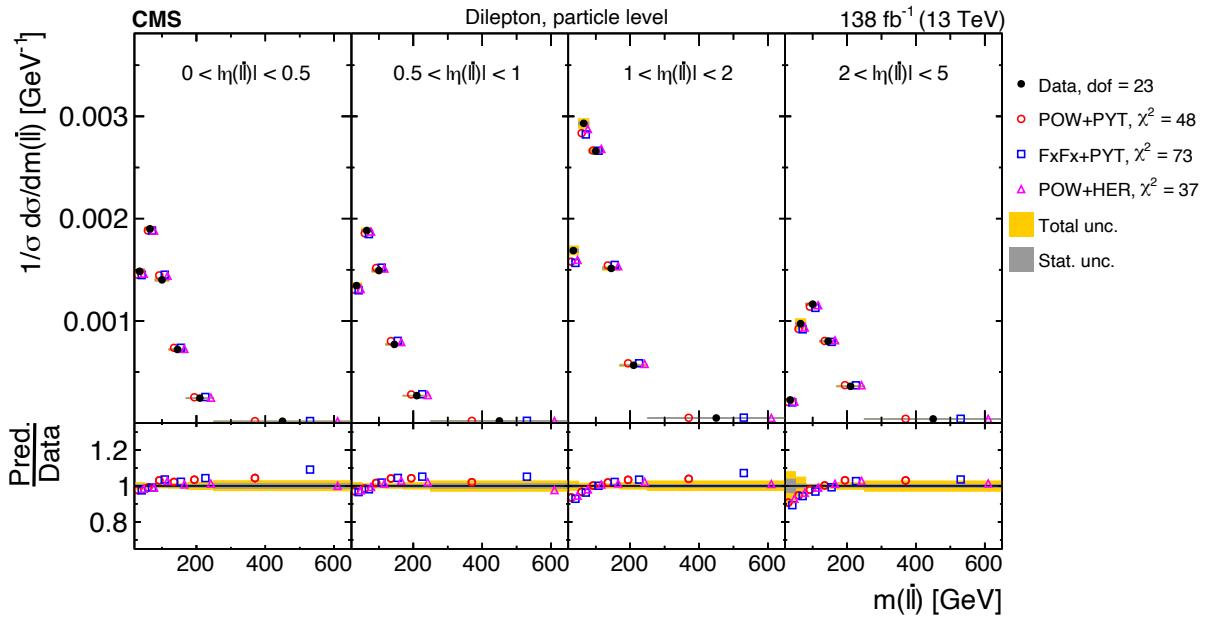
Figure 28: Normalized $[|\eta(\ell\bar{\ell})|, m(\ell\bar{\ell})]$ cross sections are shown for data (filled circles) and various MC predictions (other points). Further details can be found in the caption of Fig. 24.
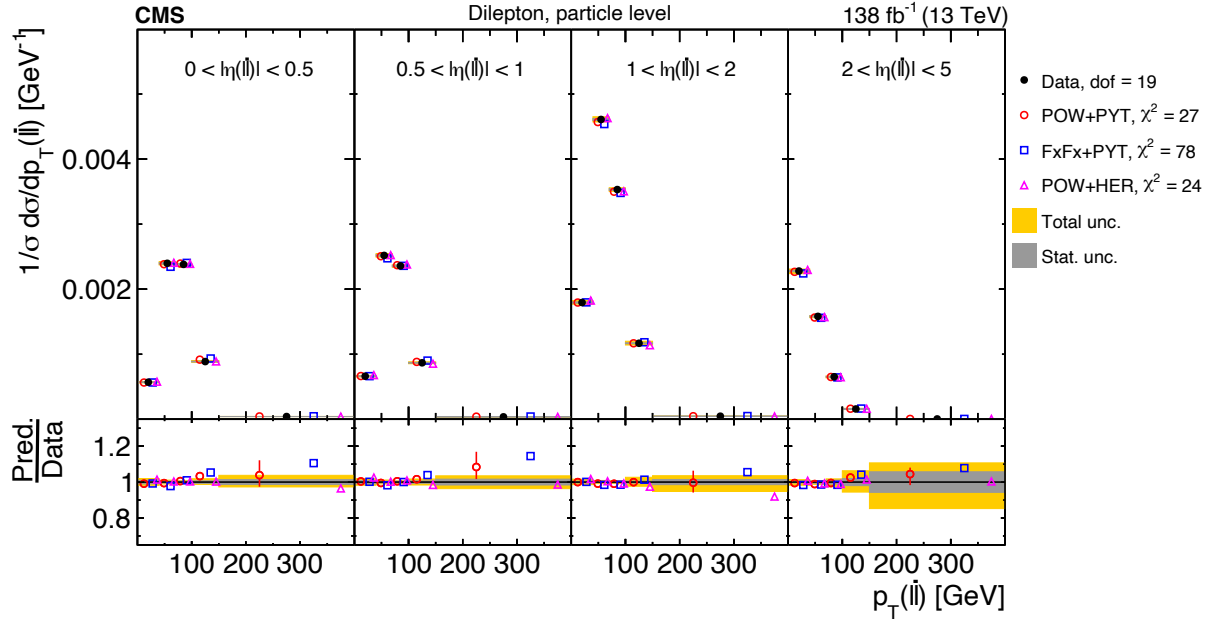
Figure 29: Normalized $[|\eta(\ell\bar{\ell})|, p_{\mathrm{T}}(\ell\bar{\ell})]$ cross sections are shown for data (filled circles) and various MC predictions (other points). Further details can be found in the caption of Fig. 24.
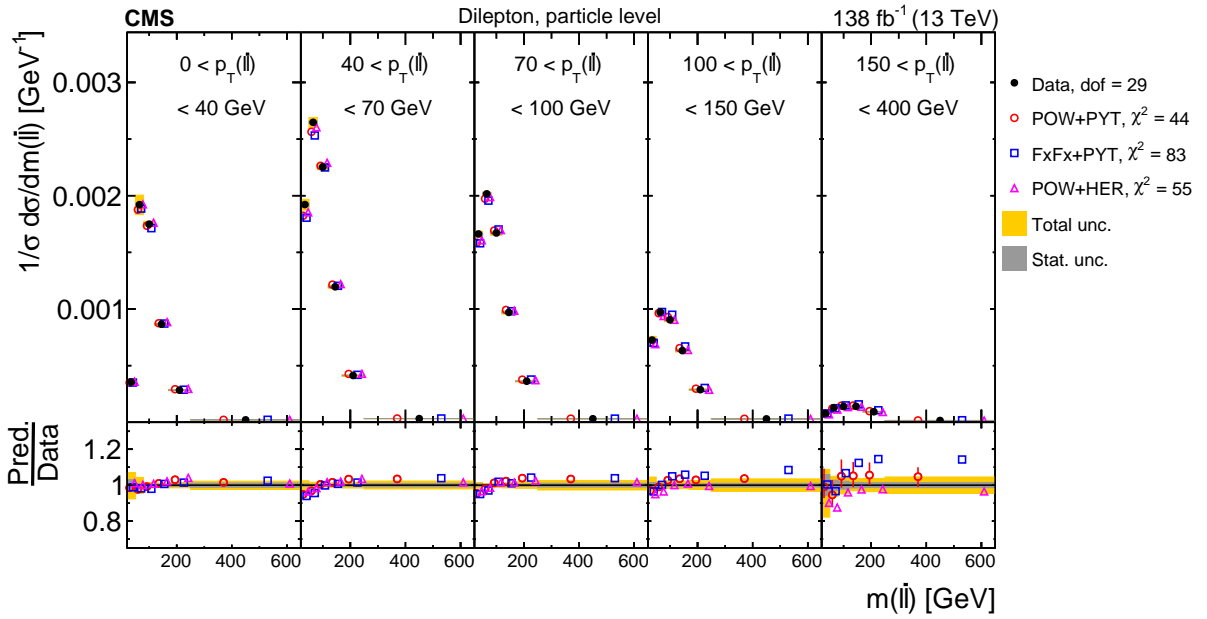
Figure 30: Normalized $[p_{\mathrm{T}}(\ell\bar{\ell}), m(\ell\bar{\ell})]$ cross sections are shown for data (filled circles) and various MC predictions (other points). Further details can be found in the caption of Fig. 24.

Table 5: The χ^2 values and dof of the measured normalized single-differential cross sections for lepton and b-jet kinematic observables at the particle level are shown with respect to the predictions of various MC generators. The χ^2 values are calculated taking only measurement uncertainties into account and excluding theory uncertainties. For POW+PYT, the χ^2 values including theory uncertainties are indicated with the brackets (w. unc.).

Cross section variables	dof	χ^2		
		POW+PYT (w. unc.)	FxFx+PYT	POW+HER
$p_T(\ell)$	11	28 (18)	51	18
$p_T(\ell)$ trailing$/p_T(\ell)$ leading	9	15 (11)	24	7
$p_T(\ell)/p_T(\bar{t})$	4	10 (9)	25	12
$p_T(b)$ leading	9	5 (4)	26	8
$p_T(b)$ trailing	6	6 (4)	24	7
$(p_T(b) + p_T(\bar{b}))/(p_T(t) + p_T(\bar{t}))$	3	19 (15)	27	18
$m(\ell\bar{\ell})$	11	23 (20)	27	23
$m(b\bar{b})$	6	15 (12)	15	14
$m(\ell\bar{\ell}b\bar{b})$	18	33 (18)	28	28
$p_T(\ell\bar{\ell})$	8	4 (3)	14	9
$|\eta(\ell\bar{\ell})|$	13	14 (9)	21	11
$[|\eta(\ell\bar{\ell})|,\, m(\ell\bar{\ell})]$	23	48 (28)	73	37
$[|\eta(\ell\bar{\ell})|,\, p_T(\ell\bar{\ell})]$	19	27 (14)	78	24
$[p_T(\ell\bar{\ell}),\, m(\ell\bar{\ell})]$	29	44 (37)	83	55

9.3 Results as a function of additional-jet multiplicity

In the final set of studies, we measure differential $t\bar{t}$ production cross sections as a function of the multiplicity of additional jets in the events. These investigations provide an exemplary testing ground for the understanding of perturbative QCD. In particular, additional jets provide a second hard kinematic scale in the events, competing with the $t\bar{t}$ invariant mass, and thus give rise to a multiscale situation that provides a challenge for the perturbative expansion [116]. The definitions of the cross sections are given in Section 6.1. Additional jets are measured at the particle level, and the top quark and antiquark are either measured at the parton level in the full phase space or at the particle level in a fiducial phase space. The cross sections are shown in Figs. 31–40. The upper and lower plots in the figures depict the cross sections at the parton and particle levels, respectively. The χ^2 values of model-to-data comparisons are listed in Tables 6–7 and the corresponding p-values in Tables 30–31.

We first discuss the additional-jet multiplicity N_{jet} distribution and its dependence on the minimum jet p_T requirement. This distribution provides a direct view of the amount of higher-order QCD radiation in $t\bar{t}$ events. Figure 31 shows the N_{jet} cross section distributions for minimum p_T values of 40 and 100 GeV, respectively. The data are compared to the same three MC models as discussed above. The POW+PYT MC provides a good description of the N_{jet} distribution for the lower p_T value, though for the higher p_T value it starts to overshoot the data at larger jet multiplicities $N_{jet} \geq 2$. The FxFx+PYT model exhibits a low accuracy, nearly independent of the p_T requirement. Its cross section prediction is too low for $N_{jet} = 0$ and too high for $N_{jet} = 1$, though it is reasonable for larger N_{jet}. The effect is underlined by large χ^2 values. The description of the data by POW+PYT and FxFx+PYT is consistent for the parton- and particle-level cross sections, but for POW+HER a different picture emerges. This model clearly predicts too many extra jets for the parton-level cross section, but describes the data well at the particle level in a fiducial phase space. The parton level is defined for the full phase space. However, there might be a larger contribution from extra jets in POW+HER from events that are predominantly outside the particle-level fiducial phase space for the top quark and antiquark.

Next we investigate the top quark and $t\bar{t}$ kinematics as a function of N_{jet}. This allows us to map the kinematic correlations to additional jets and to check whether description deficiencies seen, e.g. for the top quark transverse momentum $p_T(t)$ spectrum (Fig. 8), are associated with specific N_{jet} values. Figure 32 shows the $p_T(t)$ distributions. For POW+PYT, the effect of a harder $p_T(t)$ spectrum compared to that observed in data seems to be slightly enhanced in the lower two jet multiplicity bins $N_{jet} = 0, 1$, though a reasonable description is seen for higher multiplicities $N_{jet} > 1$. The FxFx+PYT model predicts harder $p_T(t)$ spectra, rather independent of N_{jet}. Among all considered predictions, POW+HER provides the best description of the $p_T(t)$ distributions at the particle level, but fails at the parton level, where its large excess at $N_{jet} > 1$ is accompanied by a $p_T(t)$ spectrum that falls too steeply. The distributions of $|y(t)|$ are illustrated in Fig. 33. The data prefer slightly less-central $|y(t)|$ distributions than the models, with weak dependence on N_{jet}. Figure 34 shows the $[N_{jet}, p_T(t\bar{t})]$ distributions. The two variables are correlated since additional QCD radiation in the event leads to nonzero values of $p_T(t\bar{t})$, as well as to values $N_{jet} \geq 1$. For low jet multiplicities, $N_{jet} = 0, 1$, the POW+PYT model provides a reasonable description of the measured $p_T(t\bar{t})$ spectrum, though for $N_{jet} > 1$ it predicts a rise of the cross section that is too steep over the first three $p_T(t\bar{t})$ ranges from 0 to 100 GeV. The ratio of the FxFx+PYT model to the data always exhibits a positive slope over the first three $p_T(t\bar{t})$ ranges, irrespectively of N_{jet}. The POW+HER prediction mostly follows the POW+PYT model, except at high $p_T(t\bar{t})$ where it is a bit lower.

The distributions of $m(t\bar{t})$ are shown in Fig. 35. The shapes of these distributions are fairly well

modeled by POW+PYT, for all N_{jet} ranges. The FxFx+PYT calculation clearly predicts much harder $m(t\bar{t})$ spectra for $N_{\text{jet}} = 1$. The POW+HER provides a fair description at the $t\bar{t}$ particle level, but fails again at the parton level, where it predicts a much softer $m(t\bar{t})$ distribution for $N_{\text{jet}} > 1$. Figure 36 displays the $|y(t\bar{t})|$ spectra. The shapes of these distributions are reasonably well described by the models, irrespectively of the N_{jet} range, but specific N_{jet}-dependent normalization problems remain for FxFx+PYT and POW+HER at the particle level. Figure 37 depicts the $\Delta\eta(t, \bar{t})$ distributions. The description by the models is poor, which is also indicated by the large χ^2 values with very small p-values. For the first two N_{jet} bins there is a clear trend for the models to predict rapidity separations between top quark and antiquark that are too small, while in the last bin the trend is slightly reversed.

Figures 38–40 show triple-differential cross sections as functions of N_{jet}, $m(t\bar{t})$, and $|y(t\bar{t})|$. These cross sections were one of the highlights of our previous analysis [39], where it was demonstrated that they can be used for a simultaneous extraction of the top quark pole mass, α_{S}, and the PDFs, with good precision. We measure the cross sections separately using two ($N_{\text{jet}} = 0$ and $N_{\text{jet}} \geq 1$), three ($N_{\text{jet}} = 0$, $N_{\text{jet}} = 1$, and $N_{\text{jet}} \geq 2$), and four ($N_{\text{jet}} = 0$, $N_{\text{jet}} = 1$, $N_{\text{jet}} = 2$ and $N_{\text{jet}} \geq 3$) bins of N_{jet} for the particle-level jets. These cross sections are denoted as $[N_{\text{jet}}^{0,1+}, m(t\bar{t}), |y(t\bar{t})|]$, $[N_{\text{jet}}^{0,1,2+}, m(t\bar{t}), |y(t\bar{t})|]$, and $[N_{\text{jet}}^{0,1,2,3+}, m(t\bar{t}), |y(t\bar{t})|]$, respectively. The $[N_{\text{jet}}^{0,1,2,3+}, m(t\bar{t}), |y(t\bar{t})|]$ cross sections are measured for the first time. A striking feature of the comparisons of the MC models to the data is a growing discrepancy when going from two to three and four bins of N_{jet}. The $[N_{\text{jet}}^{0,1,2,3+}, m(t\bar{t}), |y(t\bar{t})|]$ cross sections clearly exhibit the best power for distinguishing the models. Among all tested predictions, the POW+PYT model provides the overall best description. The FxFx+PYT calculation exhibits the same normalization problems versus N_{jet} that are visible in the N_{jet} spectrum (Fig. 31), coupled with a small trend to predict cross sections towards large $m(t\bar{t})$ that are too high, though the $|y(t\bar{t})|$ shapes are described reasonably well. The POW+HER model delivers a description at the particle level that is comparable to that of POW+PYT, but fails at the parton level where it overshoots the data for the $N_{\text{jet}} = 2$ and $N_{\text{jet}} > 2$ bins.

The comparisons of MC models and data can be summarized as follows. The POW+PYT calculation clearly provides the best description of the additional-jet multiplicity N_{jet} in $t\bar{t}$ events. The FxFx+PYT and POW+HER models fail, the former predicting too many events with $N_{\text{jet}} = 1$ and the latter too many events at the parton level in the full phase space with $N_{\text{jet}} > 1$. There are rather weak kinematic correlations of the top quark and $t\bar{t}$ rapidity spectra with N_{jet}, and the quality of the descriptions of the rapidity spectra by the models is rather independent of N_{jet}. As expected, there are larger kinematic correlations of top quark and $t\bar{t}$ transverse momenta or $t\bar{t}$ invariant mass with N_{jet}, showing harder spectra for larger N_{jet}. All models exhibit different level of discrepancies for these distributions that depend on the jet multiplicity. For instance, there is an indication that the problem of harder $p_{\text{T}}(t)$ distributions in the models is localized at small jet multiplicities. The theory-to-data χ^2 values indicate a rather poor description of the data by the nominal model predictions for many of the discussed distributions. The χ^2 values that include the prediction uncertainties for POW+PYT (see Tables 6–7) are significantly reduced, but the corresponding p-values remain too small for a reasonable description of several measured observables.
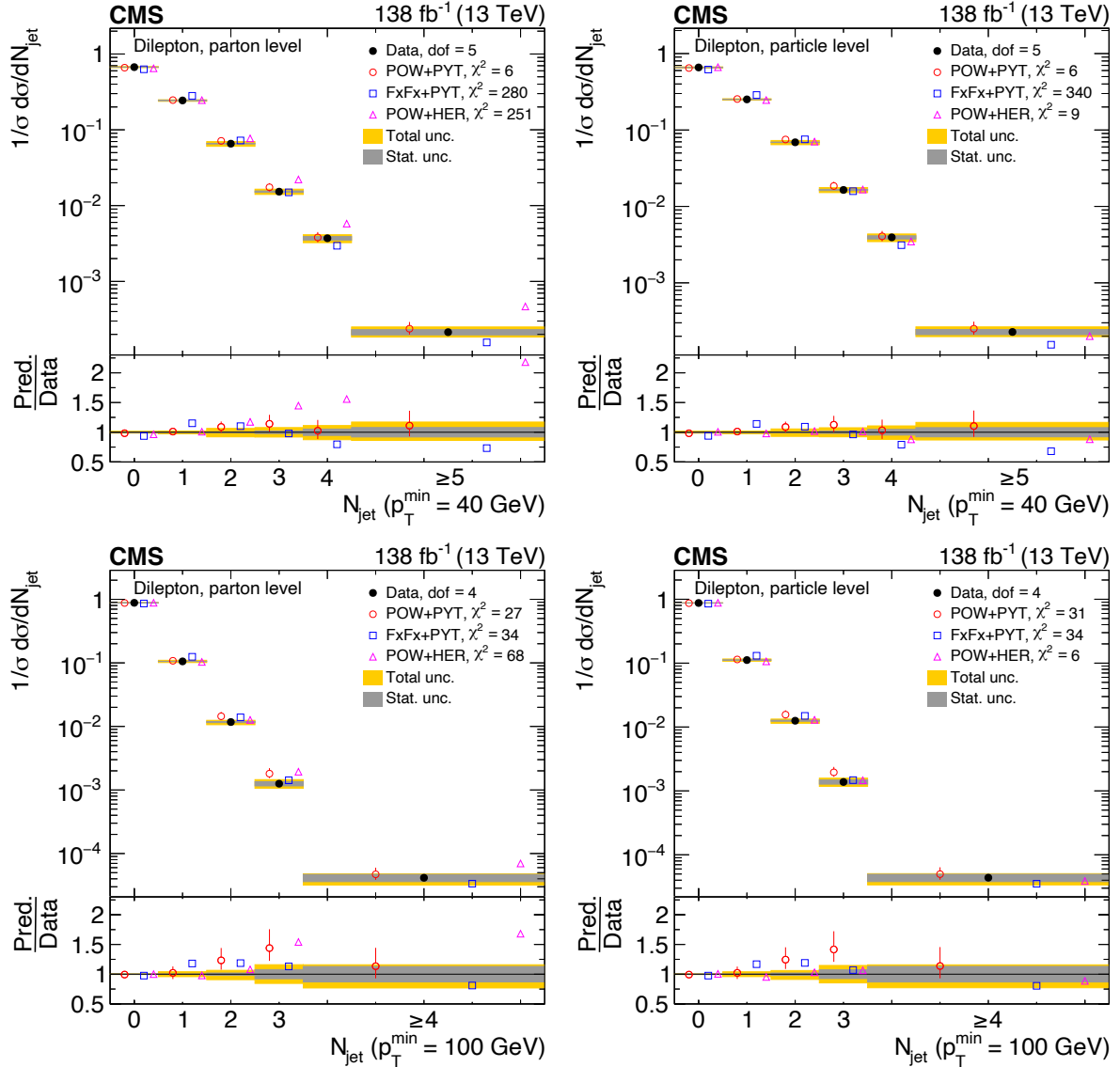
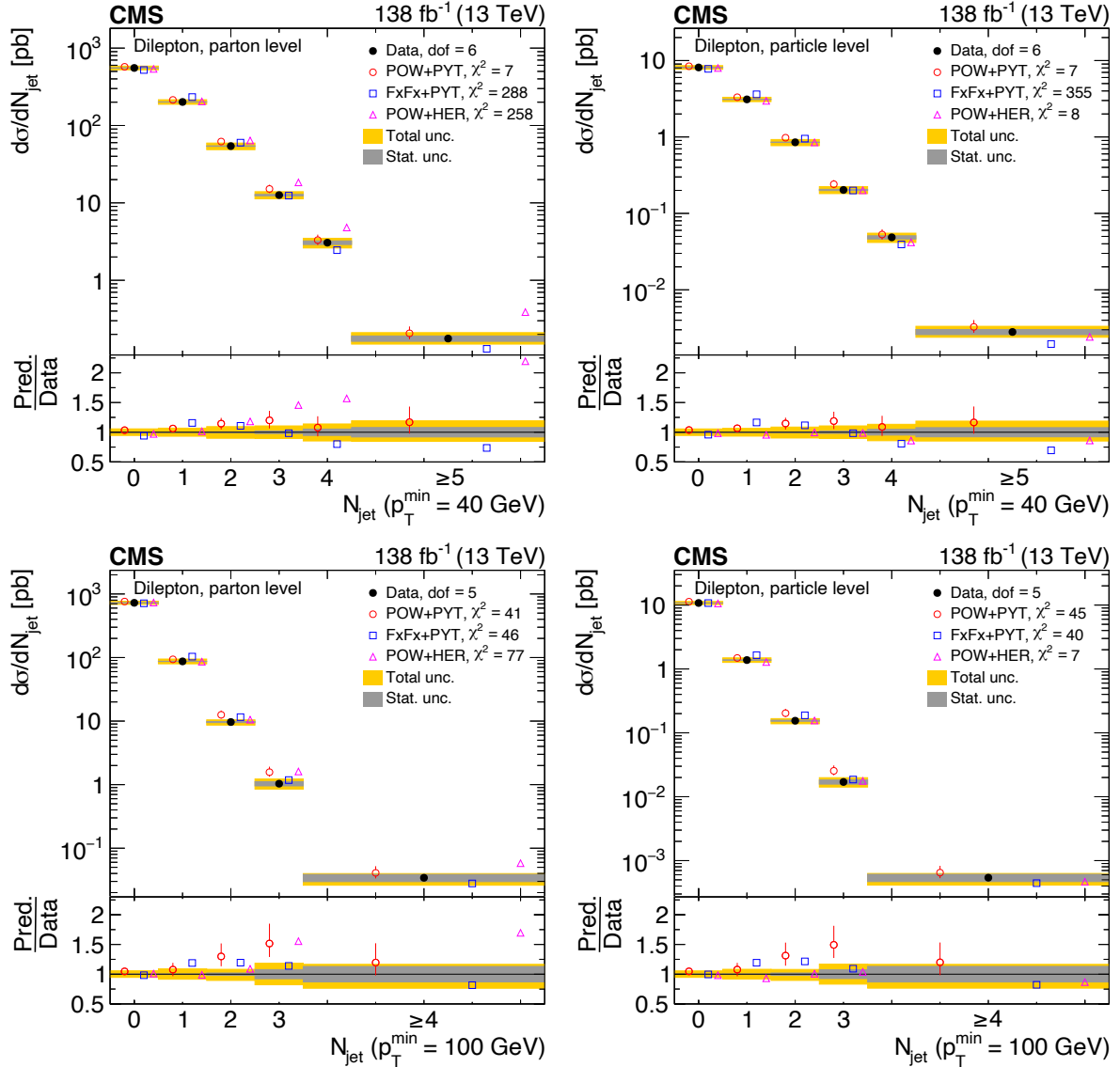Figure 31: Normalized differential $t\bar{t}$ production cross sections as a function of N_{jet}, for a minimum jet p_T of 40 GeV (upper) and 100 GeV (lower), measured at the parton level in the full phase space (left) and at the particle level in a fiducial phase space (right). The data are shown as filled circles with grey and yellow bands indicating the statistical and total uncertainties (statistical and systematic uncertainties added in quadrature), respectively. For each distribution, the number of degrees of freedom (dof) is also provided. The cross sections are compared to various MC predictions (other points). The estimated uncertainties in the POWHEG+PYTHIA 8 ('POW-PYT') simulation are represented by vertical bars on the corresponding points. For each MC model, a value of χ^2 is reported that takes into account the measurement uncertainties. The lower panel in each plot shows the ratios of the predictions to the data.
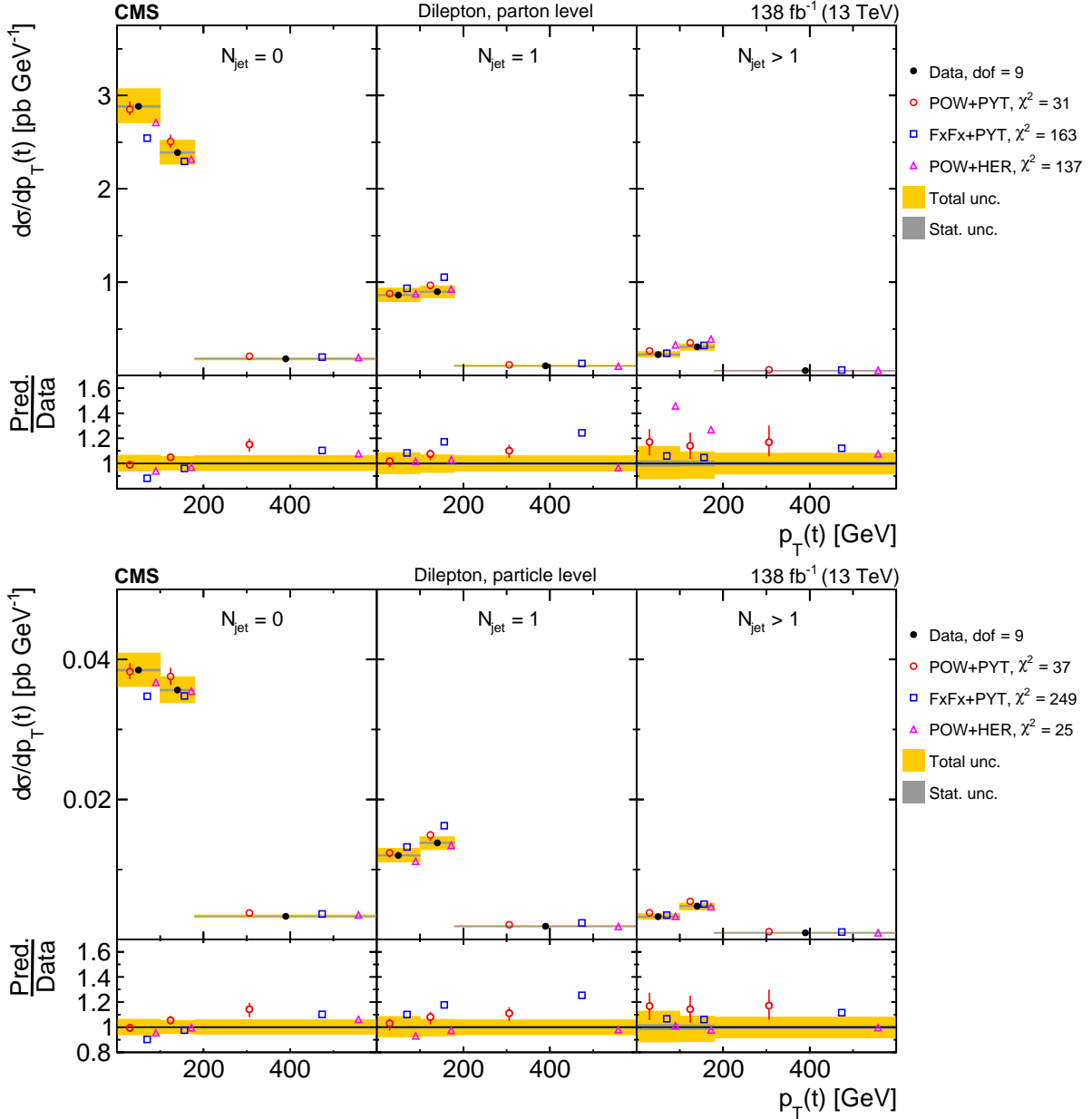
Figure 32: Normalized $[N_{jet}, p_T(t)]$ cross sections measured at the parton level in the full phase space (upper) and at the particle level in a fiducial phase space (lower). The data are shown as filled circles with grey and yellow bands indicating the statistical and total uncertainties (statistical and systematic uncertainties added in quadrature), respectively. For each distribution, the number of degrees of freedom (dof) is also provided. The cross sections are compared to various MC predictions (other points). The estimated uncertainties in the POWHEG+PYTHIA 8 ('POW-PYT') simulation are represented by vertical bars on the corresponding points. For each MC model, a value of χ^2 is reported that takes into account the measurement uncertainties. The lower panel in each plot shows the ratios of the predictions to the data.
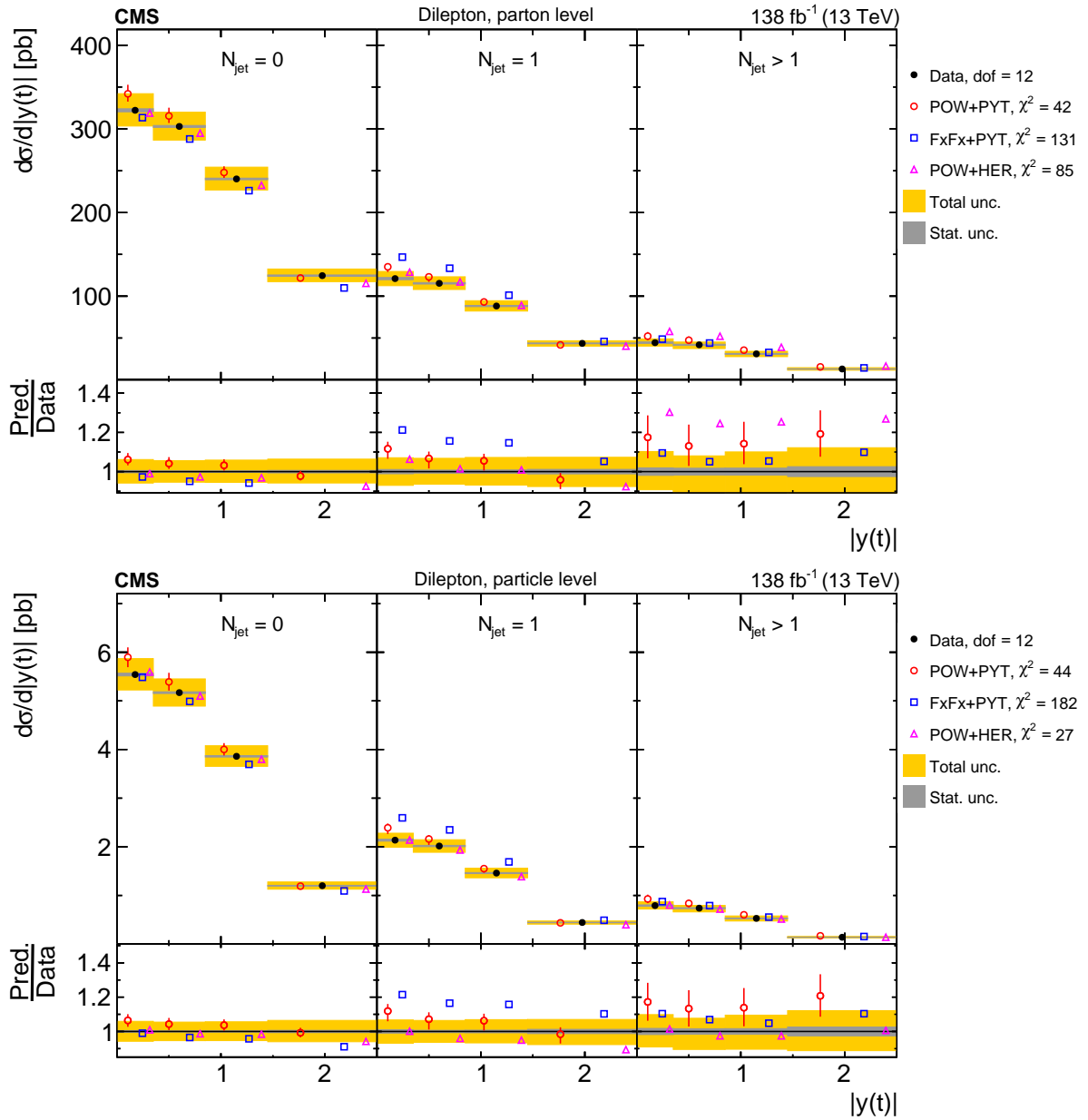
Figure 33: Normalized $[N_{\text{jet}}, |y(t)|]$ cross sections are shown for data (filled circles) and various MC predictions (other points). Further details can be found in the caption of Fig. 32.
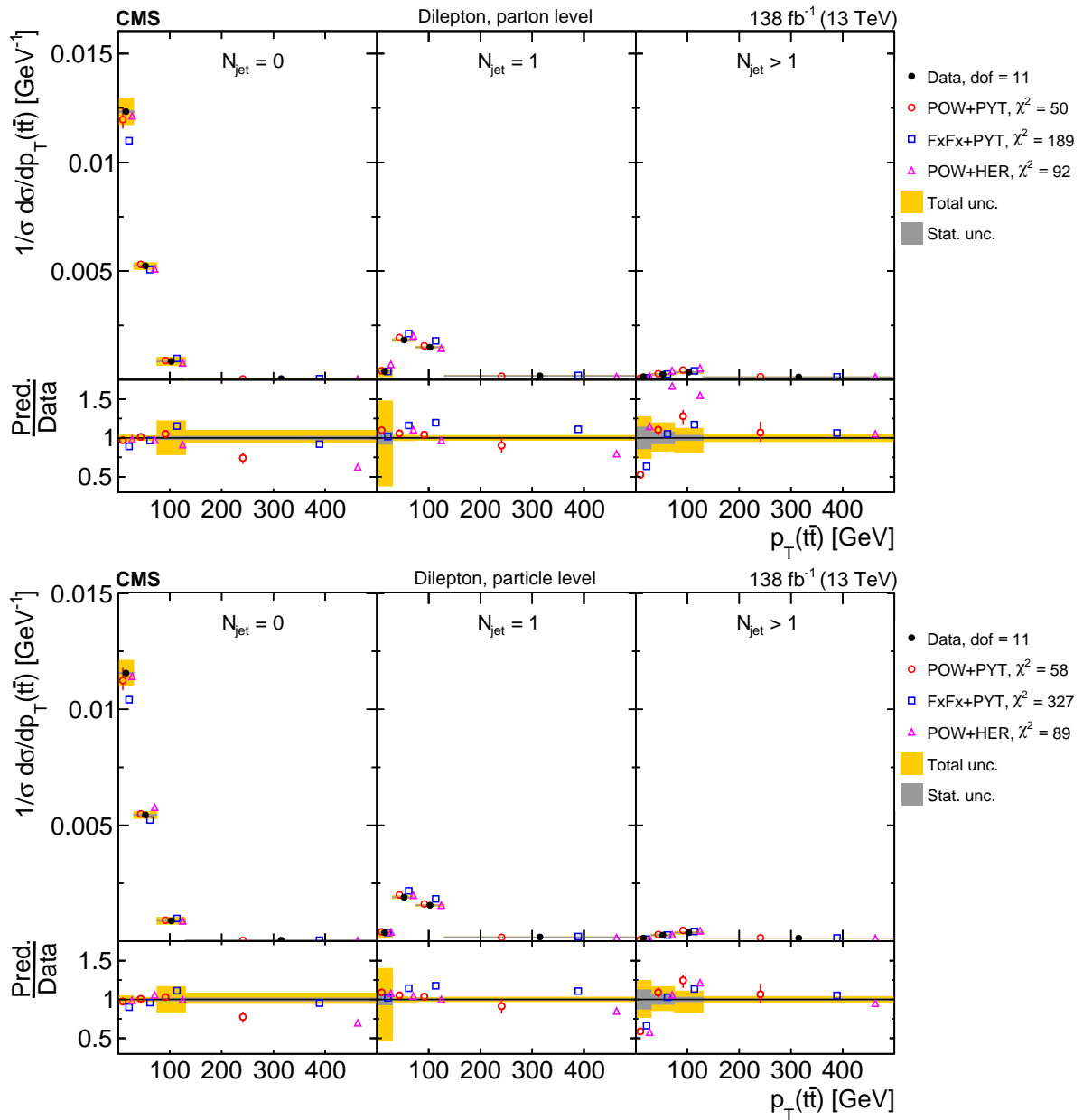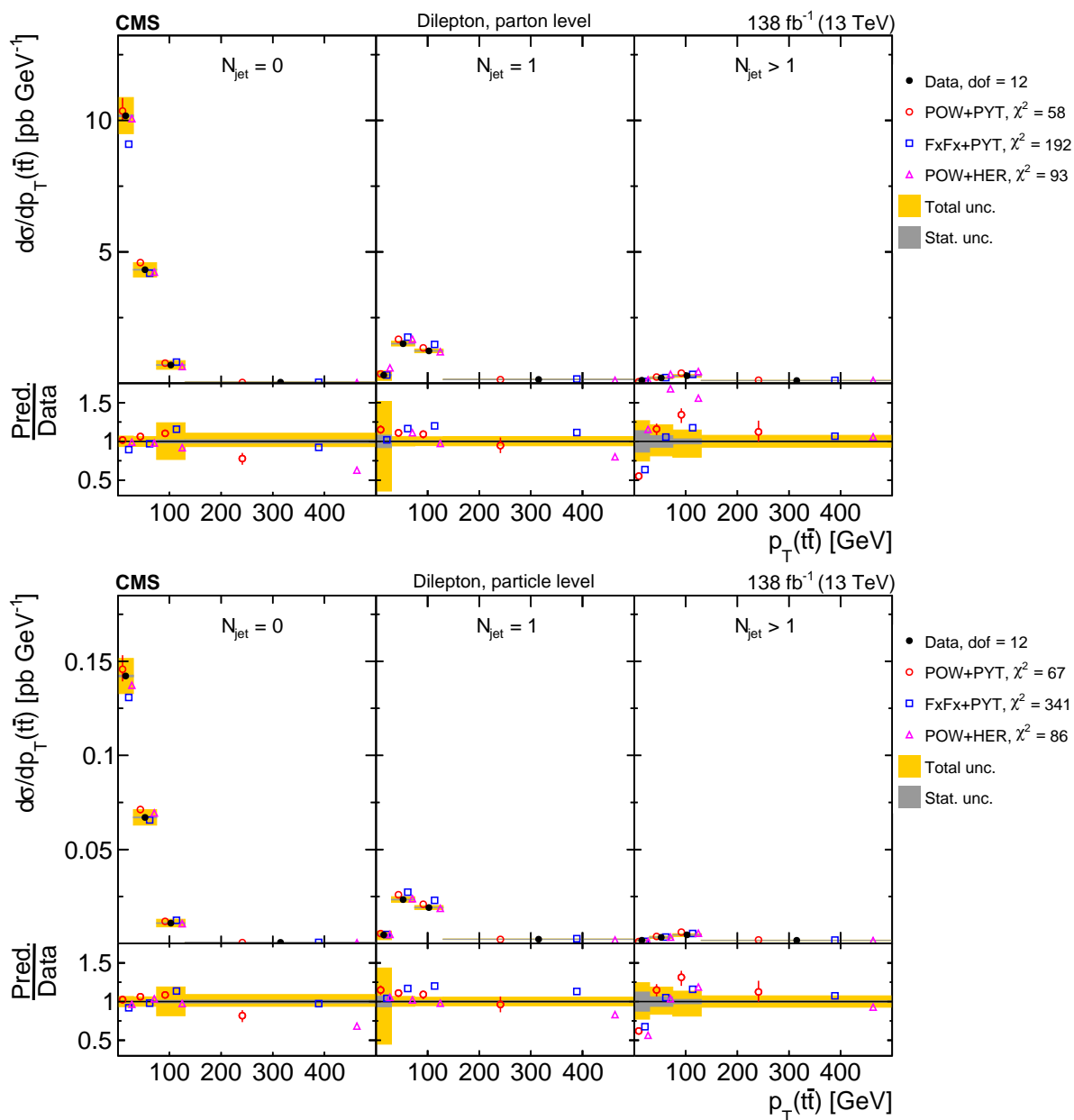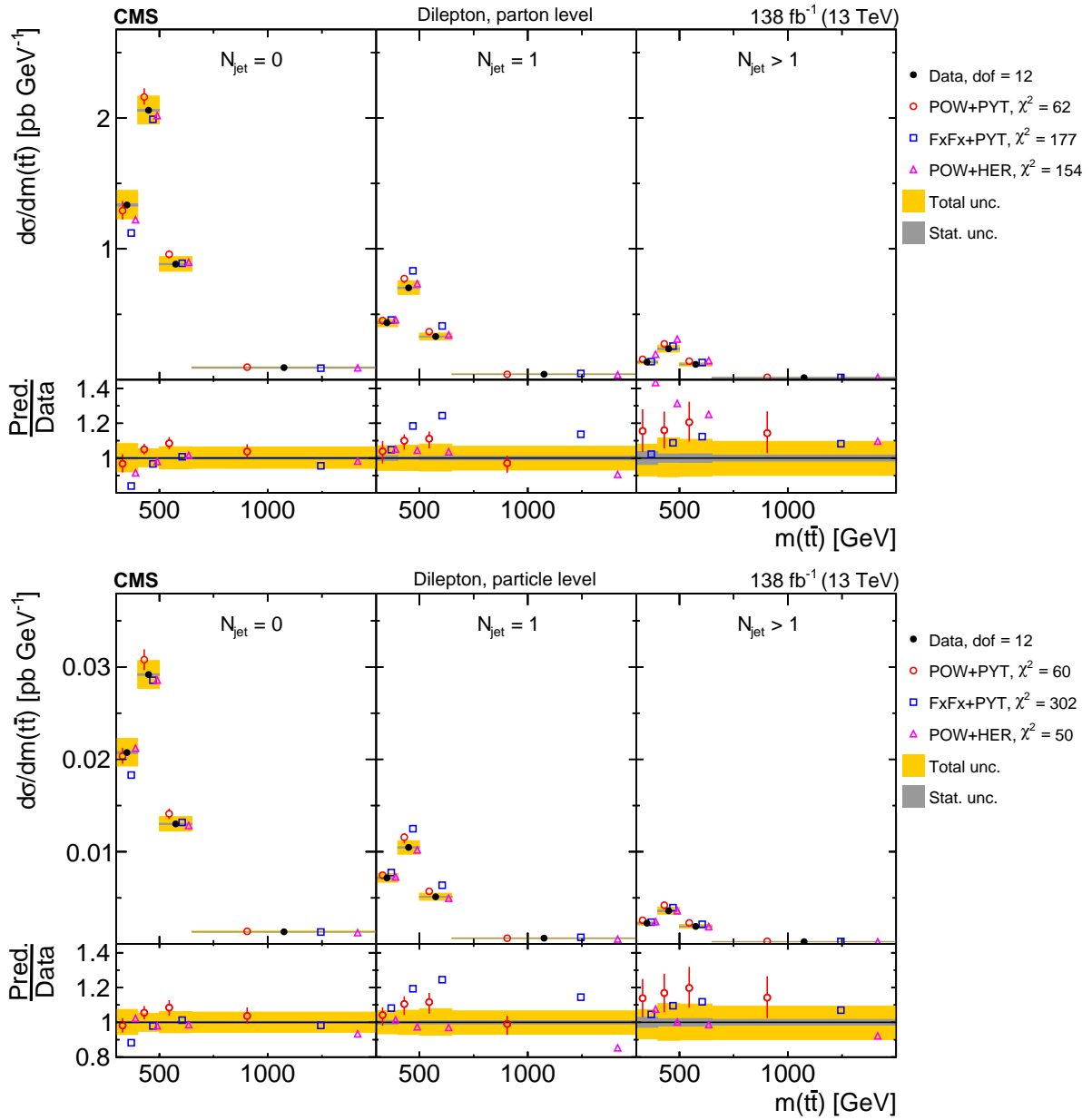
Figure 34: Normalized $[N_{\mathrm{jet}}, p_{\mathrm{T}}(t\bar{t})]$ cross sections are shown for data (filled circles) and various MC predictions (other points). Further details can be found in the caption of Fig. 32.
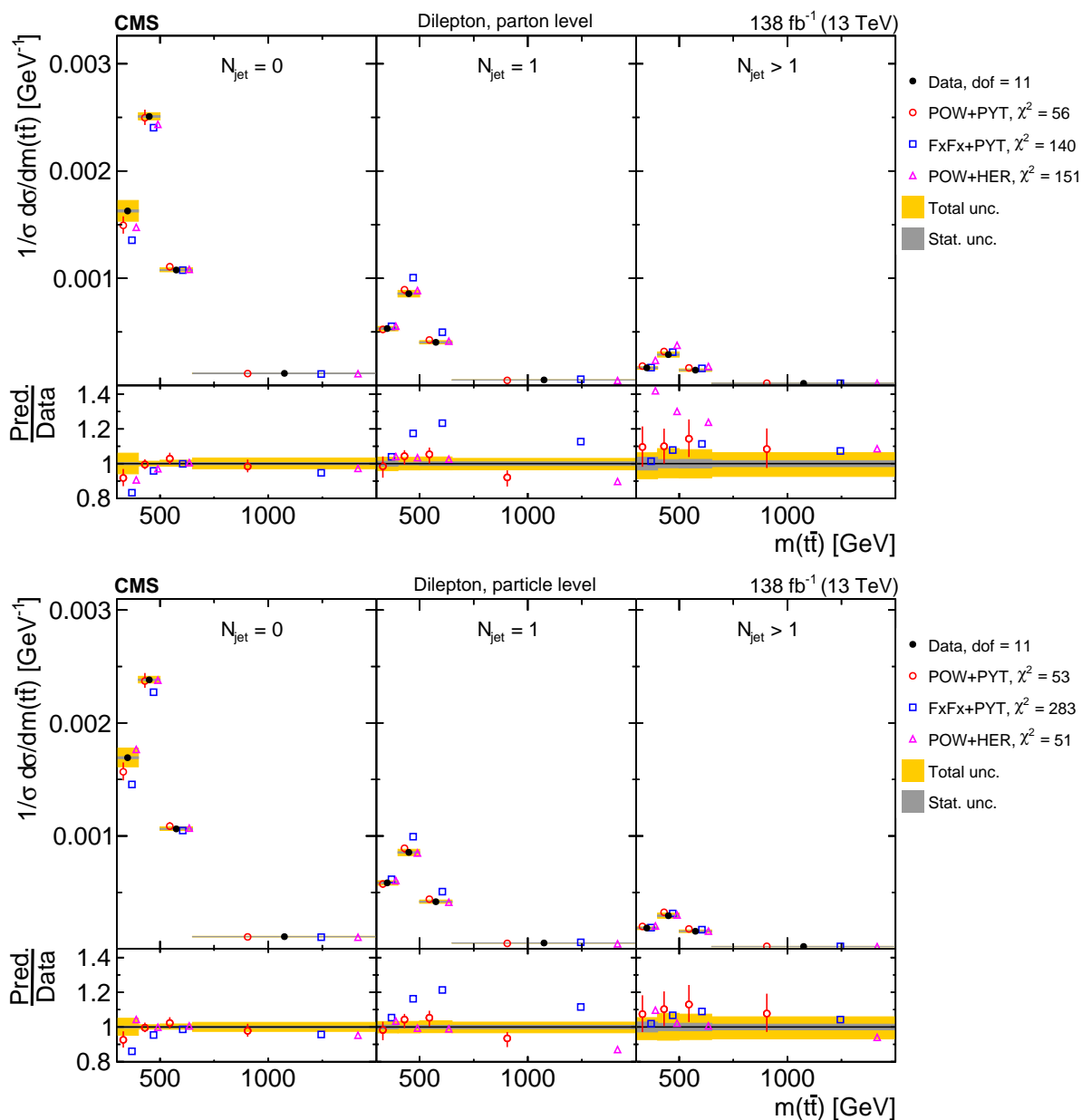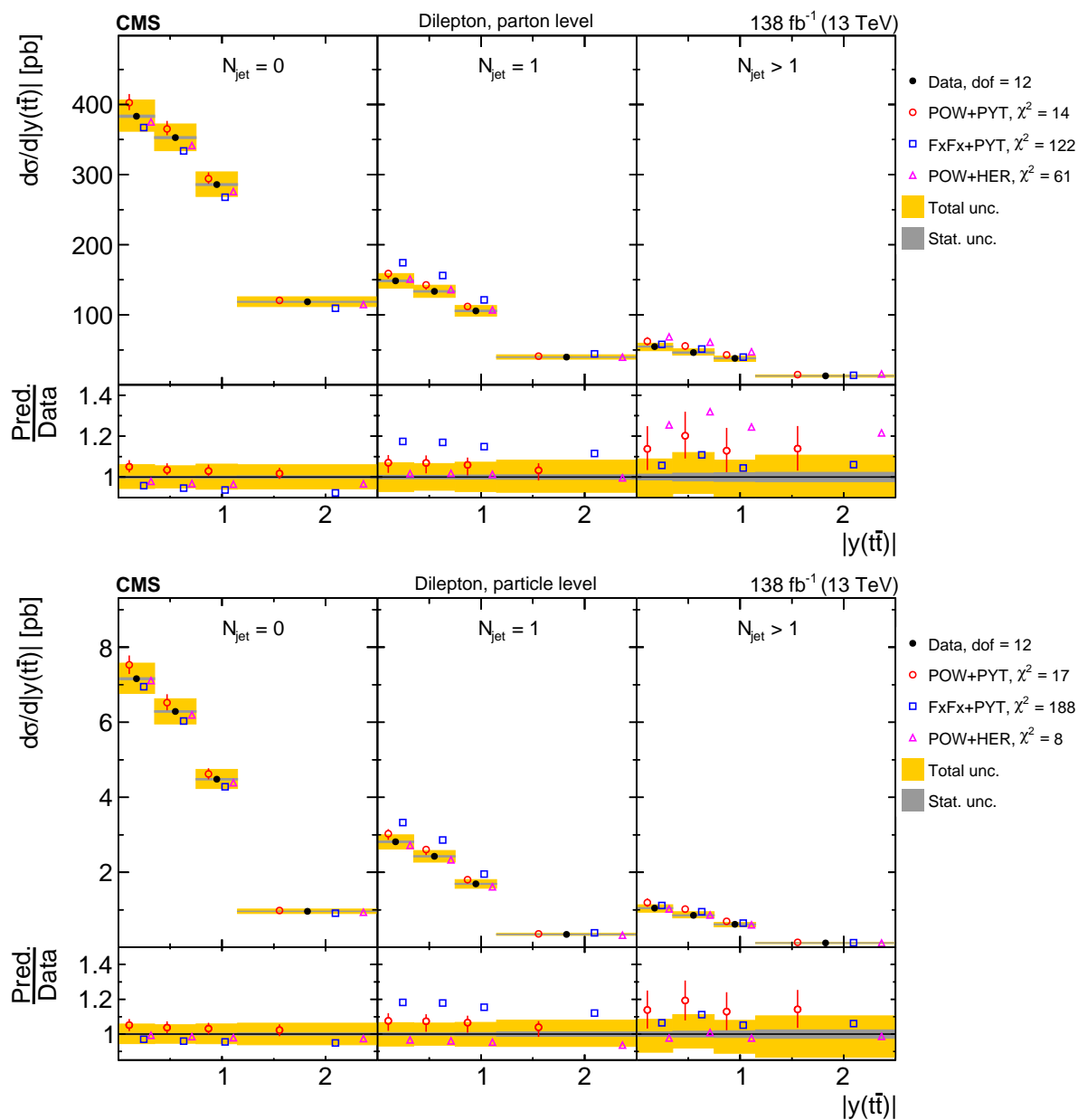
Figure 35: Normalized $[N_{jet}, m(t\bar{t})]$ cross sections are shown for data (filled circles) and various MC predictions (other points). Further details can be found in the caption of Fig. 32.
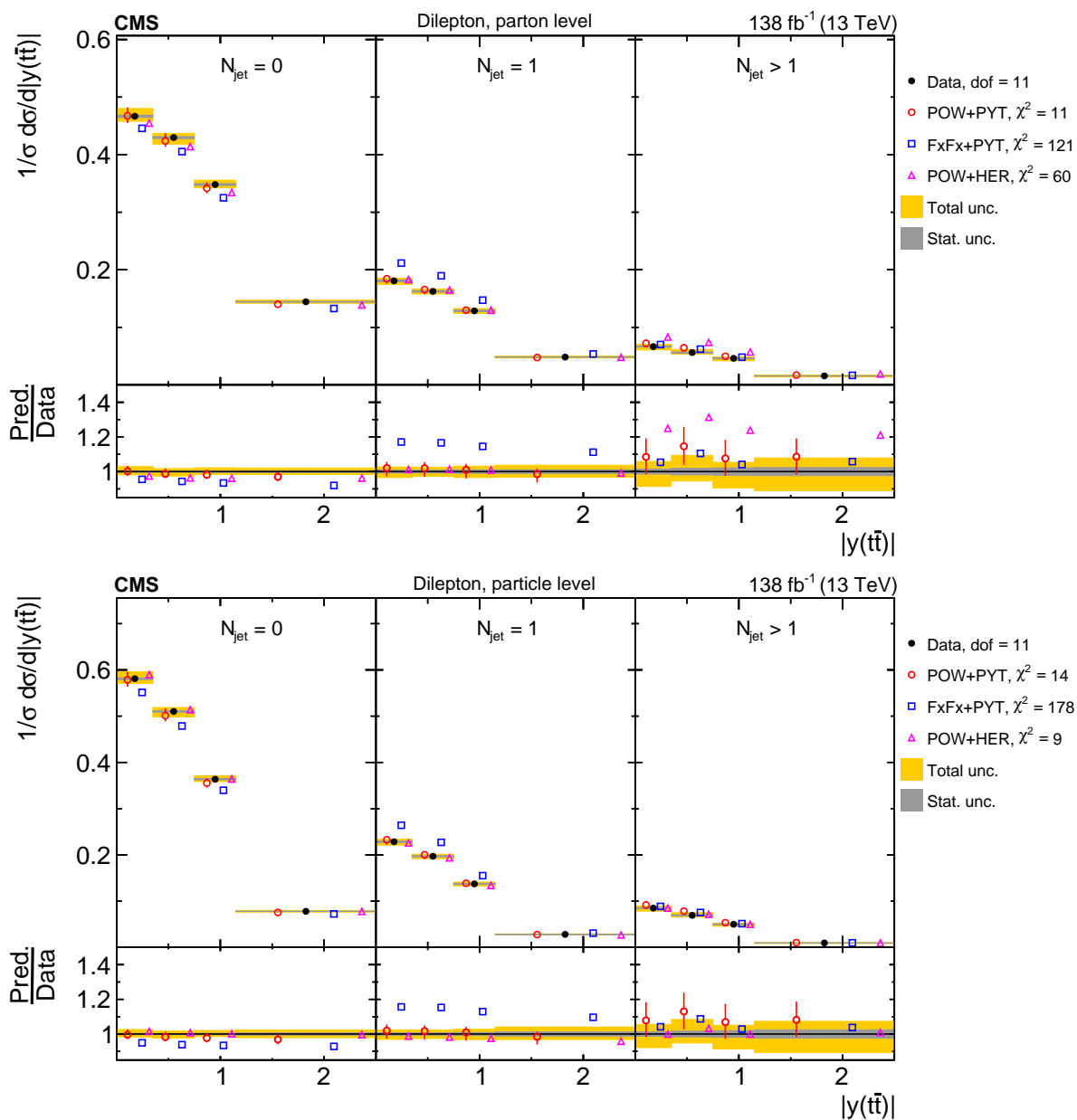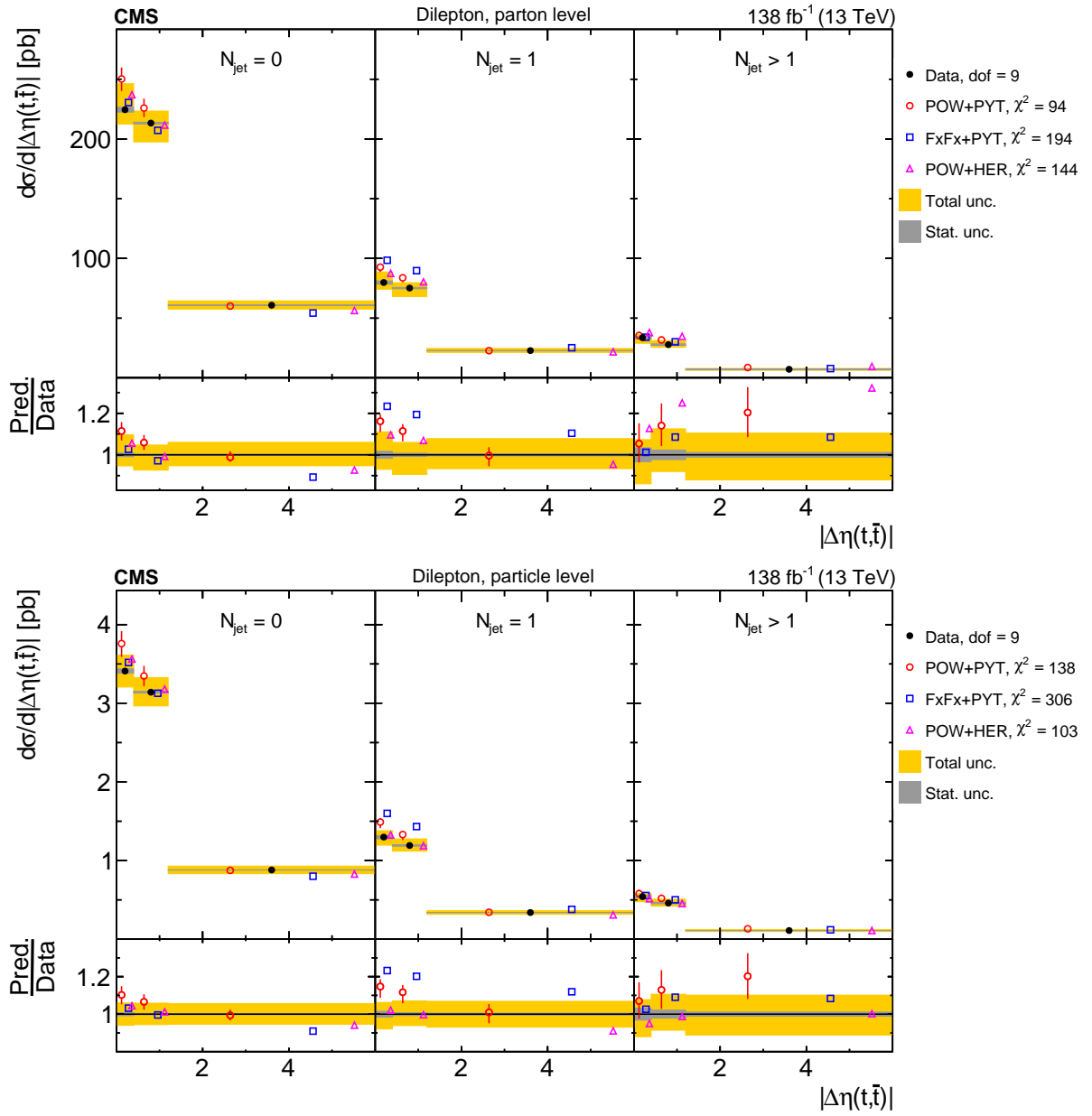
Figure 36: Normalized $[N_{\text{jet}}, |y(t\bar{t})|]$ cross sections are shown for data (filled circles) and various MC predictions (other points). Further details can be found in the caption of Fig. 32.
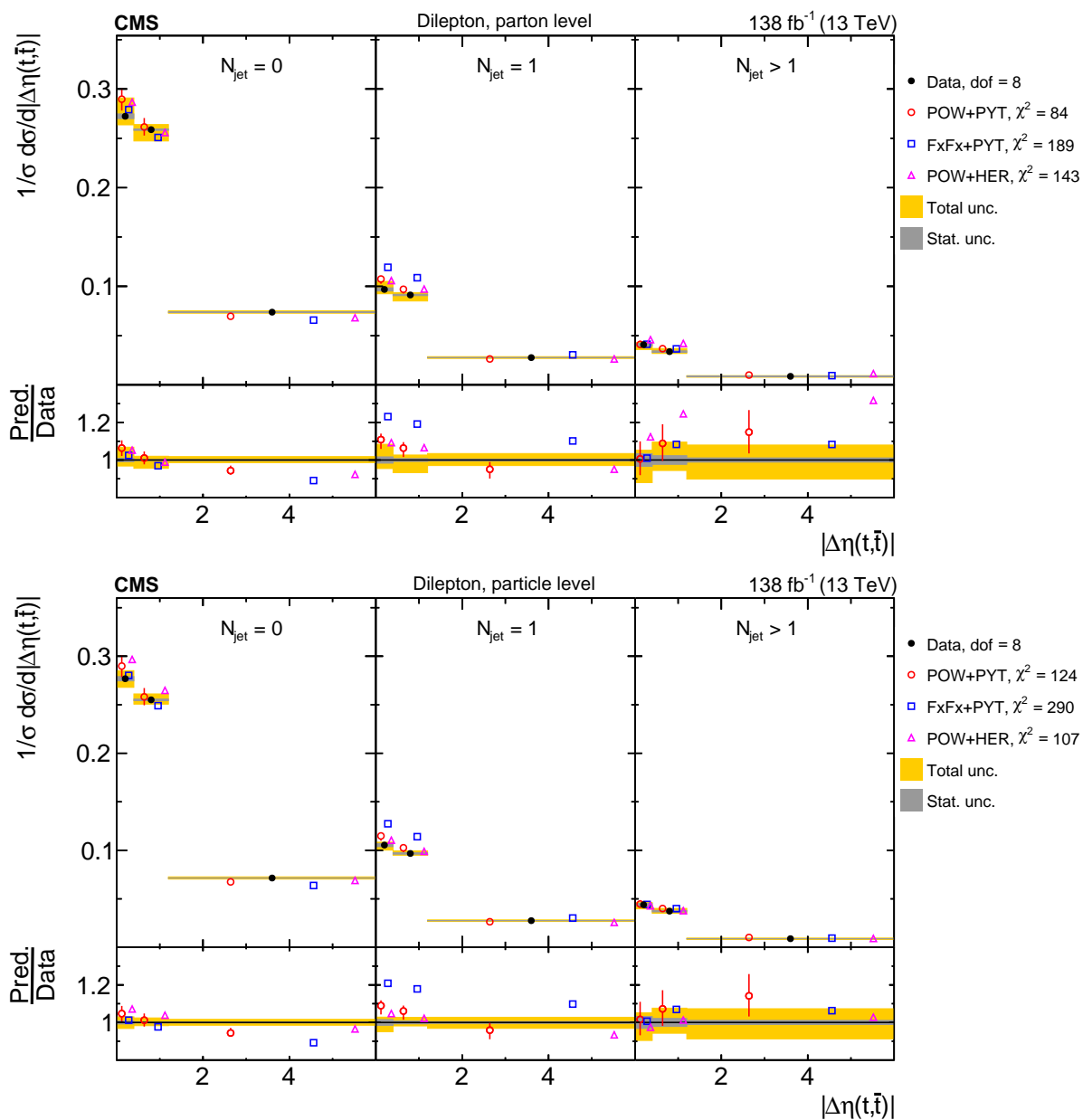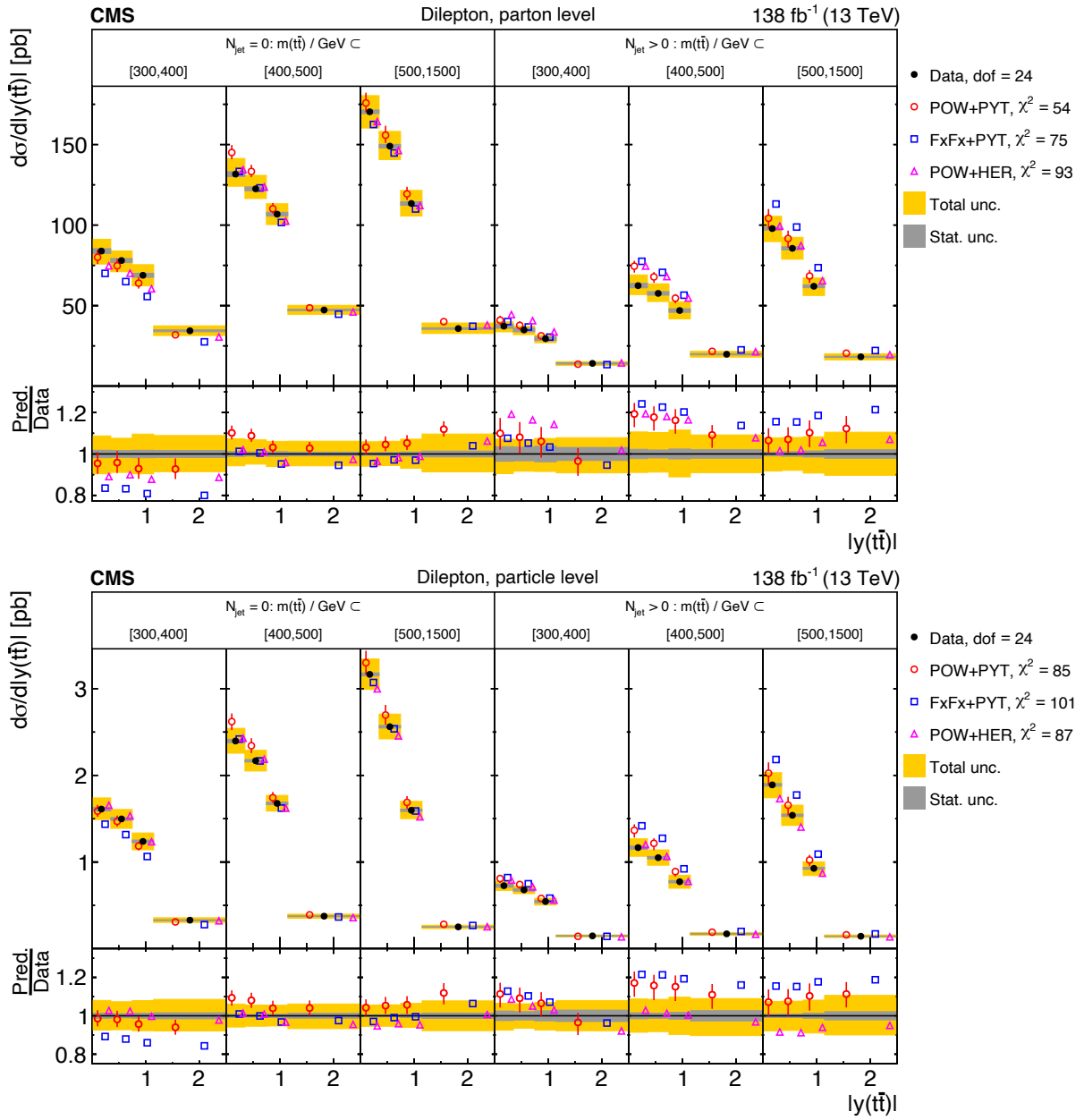
Figure 37: Normalized $[N_{jet}, |\Delta\eta(t,\bar{t})|]$ cross sections are shown for data (filled circles) and various MC predictions (other points). Further details can be found in the caption of Fig. 32.
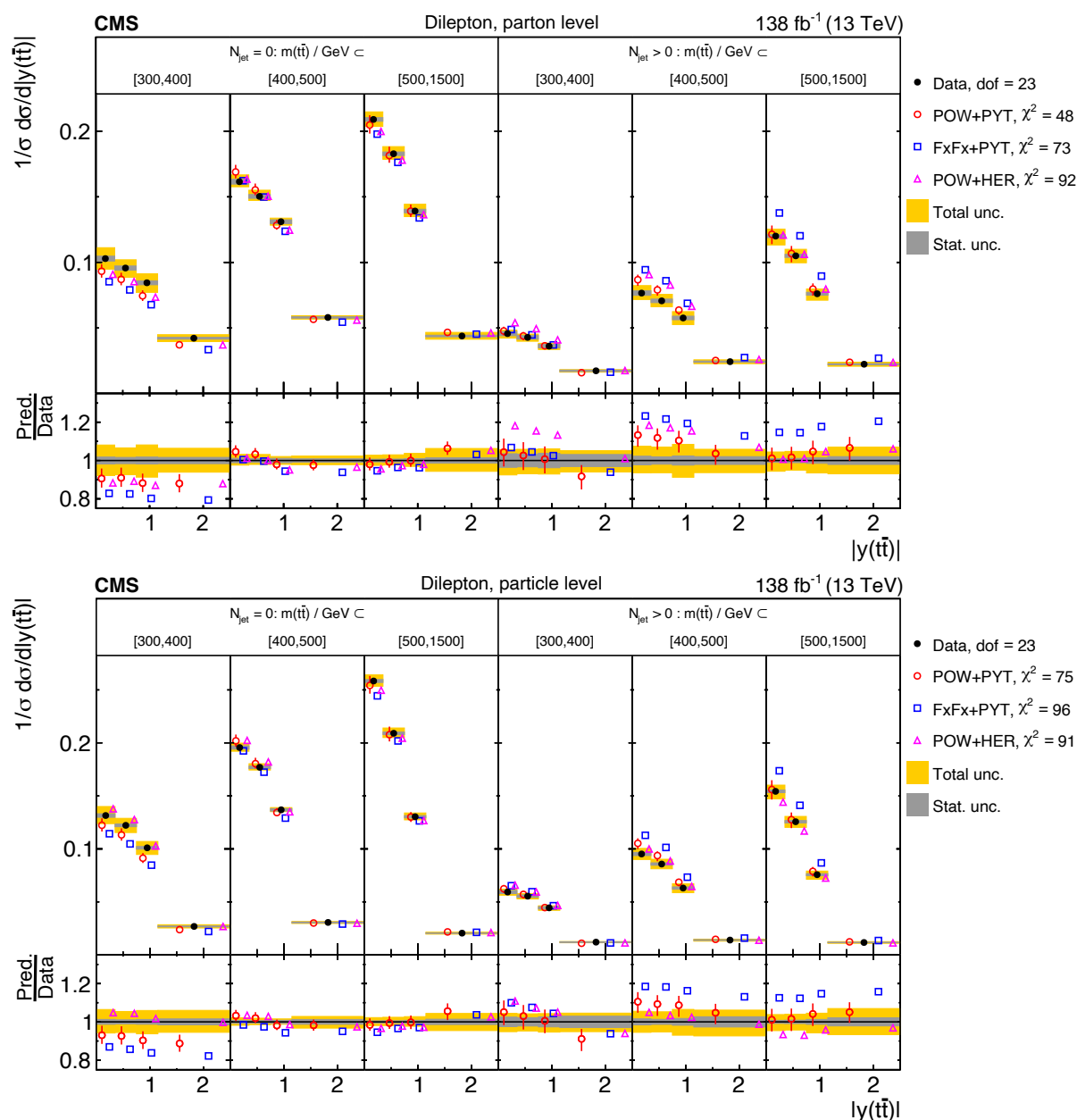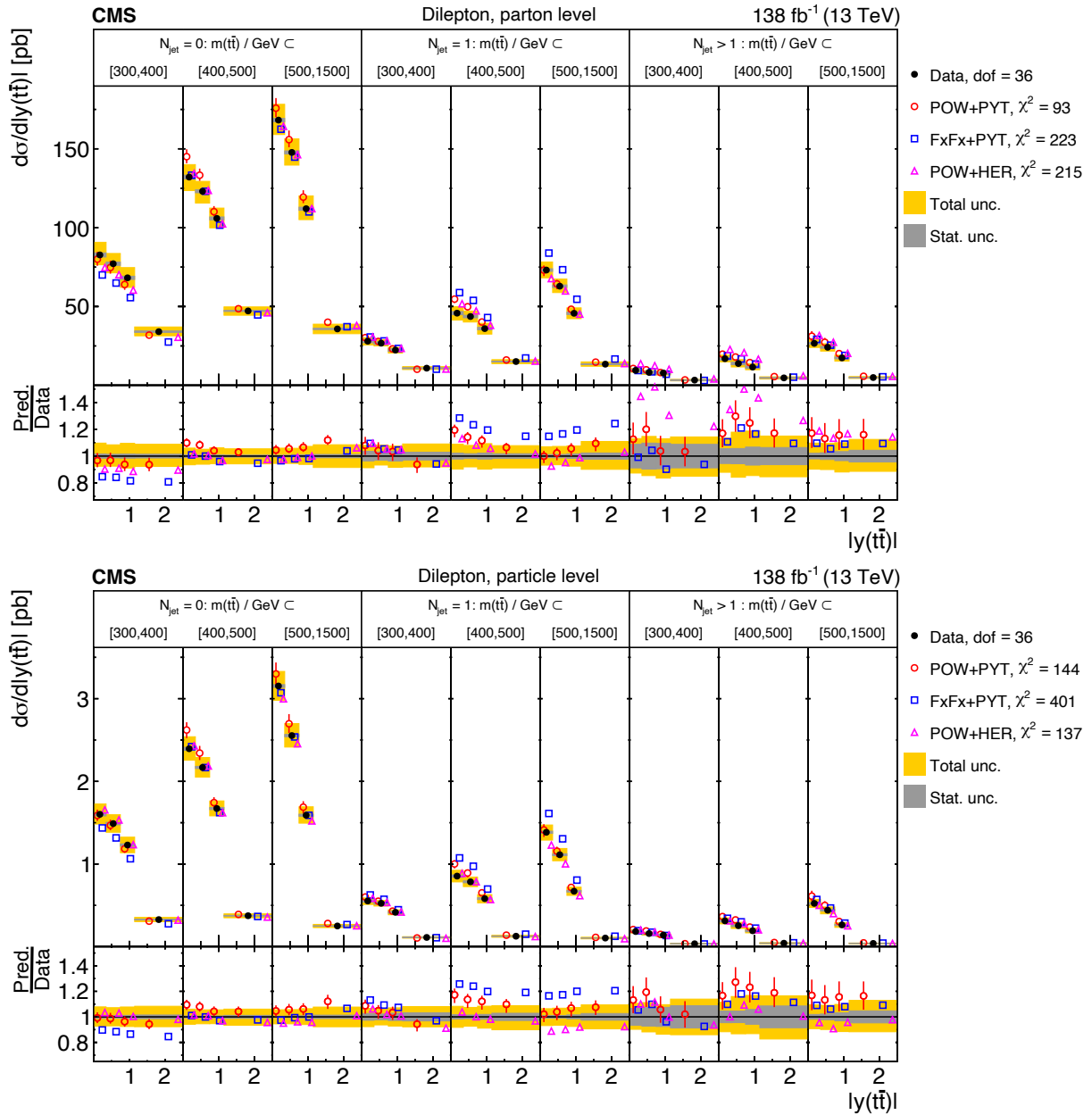
Figure 38: Normalized $[N_{\text{jet}}^{0,1+}, m(t\bar{t}), |y(t\bar{t})|]$ cross sections are shown for data (filled circles) and various MC predictions (other points). Further details can be found in the caption of Fig. 32.
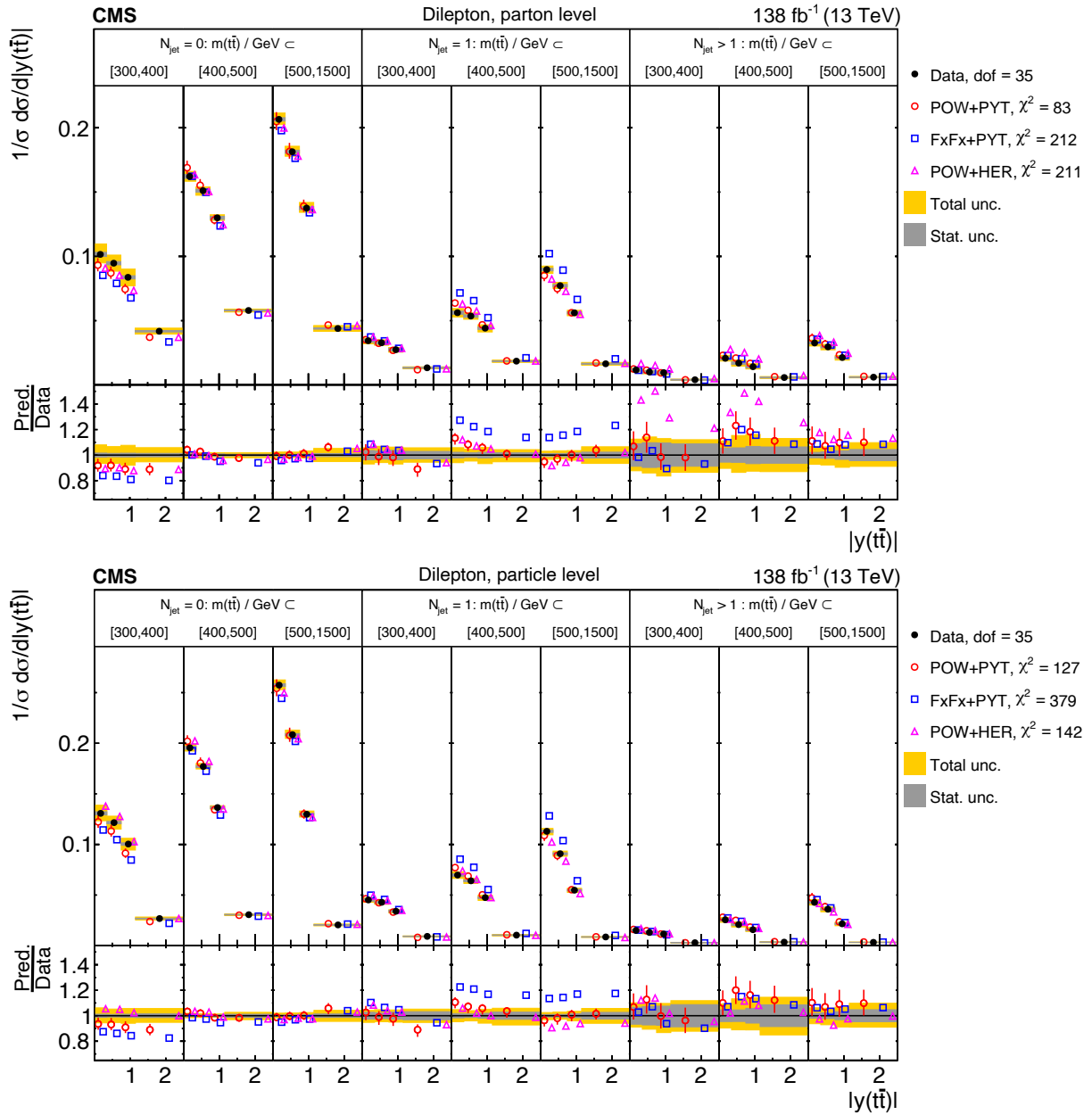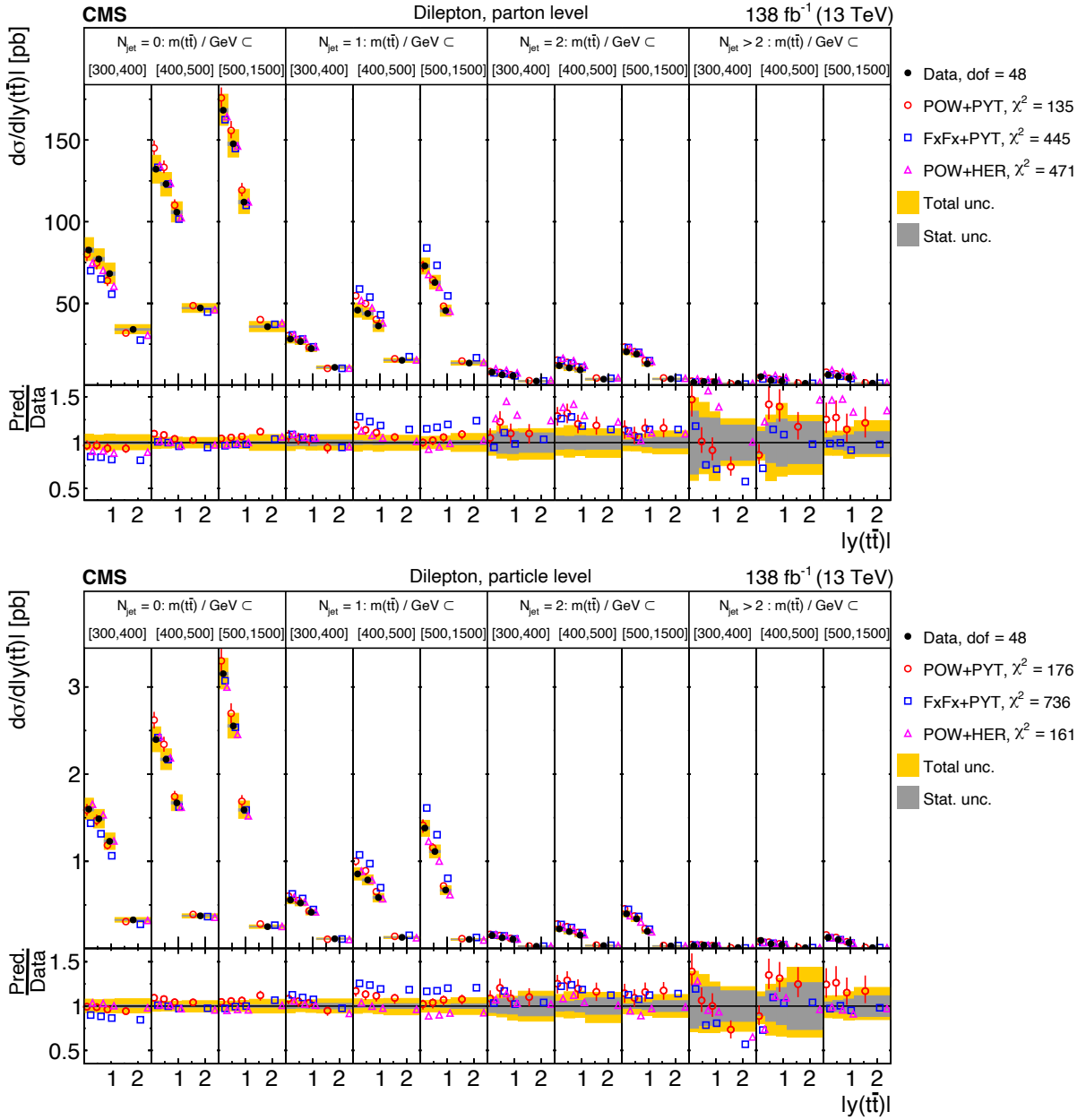
Figure 39: Normalized $[N_{jet}^{0,1,2+}, m(t\bar{t}), |y(t\bar{t})|]$ cross sections are shown for data (filled circles) and various MC predictions (other points). Further details can be found in the caption of Fig. 32.
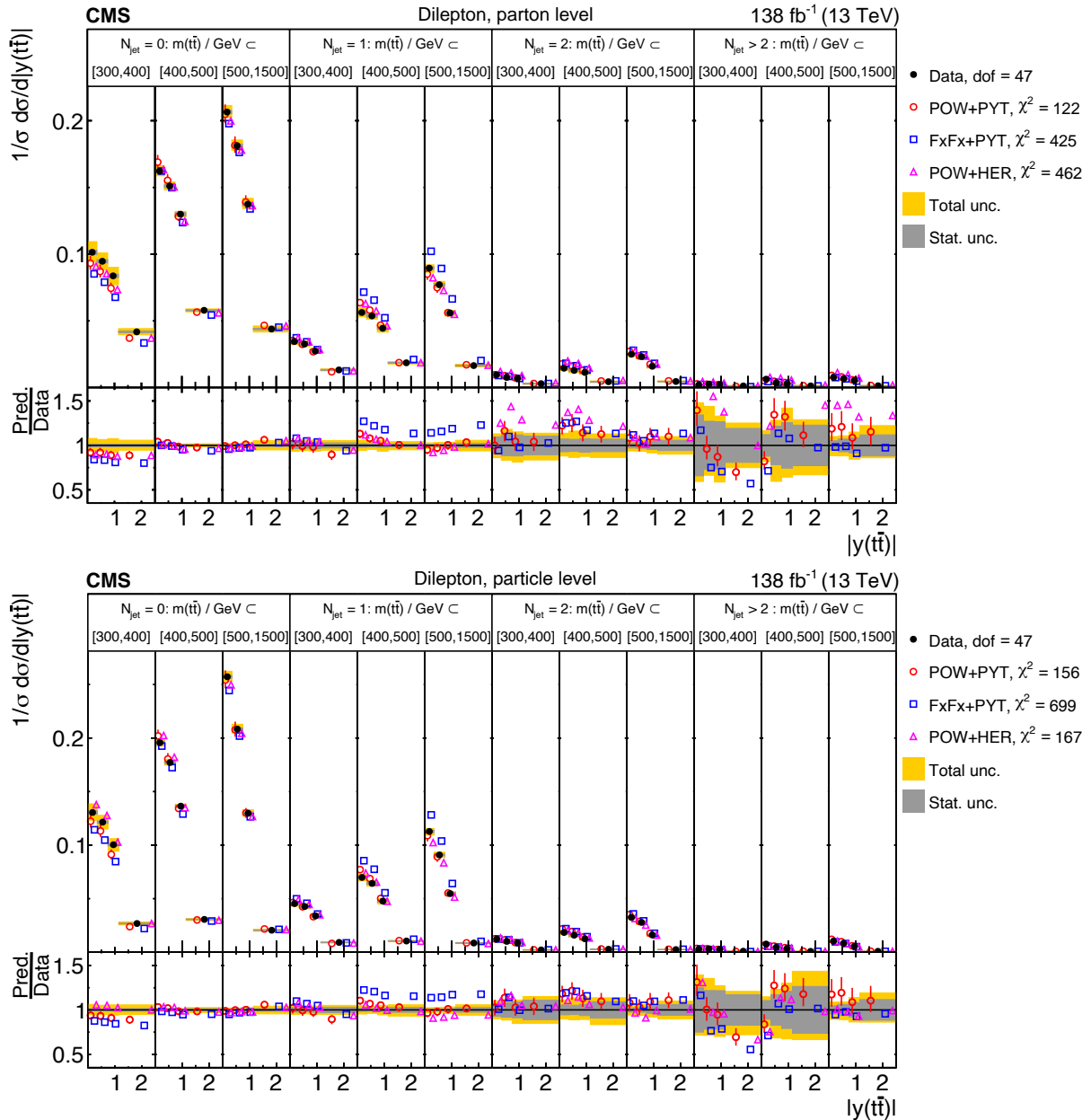
Figure 40: Normalized $[N_{jet}^{0,1,2,3+}, m(t\bar{t}), |y(t\bar{t})|]$ cross sections are shown for data (filled circles) and various MC predictions (other points). Further details can be found in the caption of Fig. 32.

Table 6: The χ^2 values and dof of the measured normalized differential cross sections as a function of the additional-jet multiplicity in the events, at the parton level of the top quark and antiquark, are shown with respect to the predictions of various MC generators. The χ^2 values are calculated taking only measurement uncertainties into account and excluding theory uncertainties. For POW+PYT, the χ^2 values including theory uncertainties are indicated with the brackets (w. unc.).

Cross section variables	dof	χ^2		
		POW+PYT (w. unc.)	FxFx+PYT	POW+HER
$N_{\text{jet}}(p_{\text{T}} > 40\,\text{GeV})$	5	6 (3)	280	251
$N_{\text{jet}}(p_{\text{T}} > 100\,\text{GeV})$	4	27 (8)	34	68
$[N_{\text{jet}}, p_{\text{T}}(\text{t})]$	8	22 (12)	161	124
$[N_{\text{jet}}, |y(\text{t})|]$	11	38 (29)	128	85
$[N_{\text{jet}}, p_{\text{T}}(\text{t}\bar{\text{t}})]$	11	50 (37)	189	92
$[N_{\text{jet}}, m(\text{t}\bar{\text{t}})]$	11	56 (41)	140	151
$[N_{\text{jet}}, |y(\text{t}\bar{\text{t}})|]$	11	11 (5)	121	60
$[N_{\text{jet}}, |\Delta\eta(\text{t},\bar{\text{t}})|]$	8	84 (37)	189	143
$[N_{\text{jet}}^{0,1+}, m(\text{t}\bar{\text{t}}), |y(\text{t}\bar{\text{t}})|]$	23	48 (35)	73	92
$[N_{\text{jet}}^{0,1,2+}, m(\text{t}\bar{\text{t}}), |y(\text{t}\bar{\text{t}})|]$	35	83 (57)	212	211
$[N_{\text{jet}}^{0,1,2,3+}, m(\text{t}\bar{\text{t}}), |y(\text{t}\bar{\text{t}})|]$	47	122 (84)	425	462

Table 7: The χ^2 values and dof of the measured normalized differential cross sections as a function of the additional-jet multiplicity in the events, at the particle level of the top quark and antiquark, are shown with respect to the predictions of various MC generators. The χ^2 values are calculated taking only measurement uncertainties into account and excluding theory uncertainties. For POW+PYT, the χ^2 values including theory uncertainties are indicated with the brackets (w. unc.).

Cross section variables	dof	χ^2		
		POW+PYT (w. unc.)	FxFx+PYT	POW+HER
$N_{\mathrm{jet}}(p_{\mathrm{T}} > 40\,\mathrm{GeV})$	5	6 (3)	340	9
$N_{\mathrm{jet}}(p_{\mathrm{T}} > 100\,\mathrm{GeV})$	4	31 (8)	34	6
$[N_{\mathrm{jet}},\, p_{\mathrm{T}}(\mathrm{t})]$	8	30 (13)	237	26
$[N_{\mathrm{jet}},\, |y(\mathrm{t})|]$	11	39 (24)	174	28
$[N_{\mathrm{jet}},\, p_{\mathrm{T}}(\mathrm{t\bar t})]$	11	58 (37)	327	89
$[N_{\mathrm{jet}},\, m(\mathrm{t\bar t})]$	11	53 (35)	283	51
$[N_{\mathrm{jet}},\, |y(\mathrm{t\bar t})|]$	11	14 (5)	178	9
$[N_{\mathrm{jet}},\, |\Delta\eta(\mathrm{t,\bar t})|]$	8	124 (41)	290	107
$[N_{\mathrm{jet}}^{0,1+},\, m(\mathrm{t\bar t}),\, |y(\mathrm{t\bar t})|]$	23	75 (45)	96	91
$[N_{\mathrm{jet}}^{0,1,2+},\, m(\mathrm{t\bar t}),\, |y(\mathrm{t\bar t})|]$	35	127 (69)	379	142
$[N_{\mathrm{jet}}^{0,1,2,3+},\, m(\mathrm{t\bar t}),\, |y(\mathrm{t\bar t})|]$	47	156 (94)	699	167

9.4 Comparisons to higher-order theoretical predictions

In this Section, the measured cross sections are compared to the following calculations of beyond-NLO precision in QCD:

- aN³LO: An approximate next-to-NNLO calculation [11, 12], based on the resummation of soft-gluon contributions at NNLL accuracy in the moment-space approach. This prediction is only available for the $p_T(t)$, $y(t)$, and $[|y(t)|, p_T(t)]$ cross sections. The renormalization and factorization scales are set to m_t for the $y(t)$ distributions and to m_T for $p_T(t)$ and $[|y(t)|, p_T(t)]$. Here, m_t denotes the top quark mass and m_T is defined as $m_T = \sqrt{m_t^2 + p_T(t)^2}$.

- MATRIX (NNLO): A prediction with full NNLO accuracy in QCD obtained with the MATRIX package [16, 117–123]. The dynamic scales are set to $H_T/4$, where H_T denotes the sum of the top quark and antiquark m_T values.

- STRIPPER (NNLO): A calculation with full NNLO precision in QCD using the STRIPPER framework [14, 17, 124–126]. The dynamic scales are set to $H_T/4$. For parton level cross sections as functions of the $t\bar{t}$ and top quark kinematic observables, the STRIPPER predictions are expected to be identical to the results obtained with MATRIX. The STRIPPER calculation also provides cross sections at NNLO accuracy for the process $pp \to t\bar{t} \to b\bar{b}\ell\bar{\ell}\nu\bar{\nu} + X$ [17], that can be compared to the particle level measurements obtained in this analysis as functions of the $t\bar{t}$, top quark, and lepton and b jet kinematic variables.

- MINNLOPS (NNLOPS): A prediction with full NNLO precision in QCD, complemented with parton showers and computed using the POWHEG-BOX-V2 [55]. These calculations are obtained using the MINNLOPS method [127–129], which supplements the MINLO prescription [130, 131] with the missing pieces to reach NNLO accuracy for inclusive observables. The μ_r for the two powers of α_S is set to $H_T/4$, and the scale of the modified logarithms is set to half of this value. Parton showering is simulated with PYTHIA 8, and includes the effects of underlying event and hadronization.

In all predictions, the top quark mass is set to $m_t = 172.5\,\text{GeV}$ and the NNPDF3.1 NNLO PDF set [52] is used. In the following, the calculations are collectively referred to as theoretical predictions.

The comparisons of the theoretical predictions, indicated by different symbols, to the measured normalized differential cross sections are shown in Figs. 41–63. The predictions from POW+PYT are also shown, serving as a reference for the description by the MC models, discussed in Sections 9.1 and 9.2. The χ^2 values of model-to-data comparisons are listed in Tables 8–12, and the corresponding p-values can be found in Tables 32–36. The values are provided considering only measurement uncertainties; for POW+PYT, additional values are presented, which include the full prediction uncertainties. Comparisons of the predictions to the measured absolute cross sections are provided in Appendix B.2. To illustrate the magnitude of the perturbative uncertainties, the beyond-NLO calculations are displayed with vertical bars constructed from the envelope of six μ_r and μ_f variations, following the procedure outlined in Section 8.2.

For the cross sections as functions of the $t\bar{t}$ and top quark kinematic observables at the parton and particle levels, shown in Figs. 41–56, the theoretical models provide descriptions of the data that are similar or improved in quality, compared to POW+PYT, with a few exceptions. For the

$p_T(t)$ and $p_T(\bar{t})$ distributions shown in Fig. 41, the MATRIX, STRIPPER, and MINNLOPS models provide a good description of the data, with no discernible trend towards a distribution that is harder, as exhibited by POW+PYT. For the $a\mathrm{N^3LO}$ calculation, some wiggles are visible in the distribution of the ratio to the data, leading to a rather poor χ^2. The STRIPPER model describes the data also at the particle level reasonably well. The theoretical models also provide a reasonable description of other measured cross sections related to top quark p_T, such as $p_T(t)/m(t\bar{t})$ (Fig. 45), and $[m(t\bar{t}), p_T(t)]$ (Fig. 48), clearly improving upon POW+PYT. For observables related to the top quark rapidity and the rapidity and mass of the $t\bar{t}$ system, the trends between data and theoretical calculations are mostly similar to those of POW+PYT. Exemplary cases are the rapidity spectra $y(t)$ and $y(\bar{t})$, depicted in Fig. 42, where the models exhibit rapidity distributions that are more central than what is observed in data, and the $[m(t\bar{t}), |y(t\bar{t})|]$ cross sections (Fig. 50), where the predictions overshoot the data in the high-$m(t\bar{t})$ region at large $y(t\bar{t})$.

Figures 43 and 44 present the cross sections as functions of $p_T(t\bar{t})$ and $|\Delta\phi(t,\bar{t})|$, which directly probe higher-order QCD effects. These effects are reflected in the large uncertainties of the theoretical predictions, as shown in the corresponding absolute cross section measurements in Figs. 101 and 102. The central predictions of these models fail to describe the data accurately. Similar observations can be made for the multi-differential cross sections involving these two kinematic variables.

Summarizing, the beyond-NLO theoretical predictions provide descriptions of the data that are of similar or improved quality, compared to POW+PYT, except for some of the kinematic distributions that are directly sensitive to higher-order QCD corrections.

For the differential cross sections as functions of lepton and b jet kinematic variables at the particle level, shown in Figs. 57–63, the STRIPPER calculation provides descriptions that are overall of similar quality compared to POW+PYT. One exception is the $m(b\bar{b})$ distribution, where STRIPPER clearly predicts too many events in the lowest mass bin.
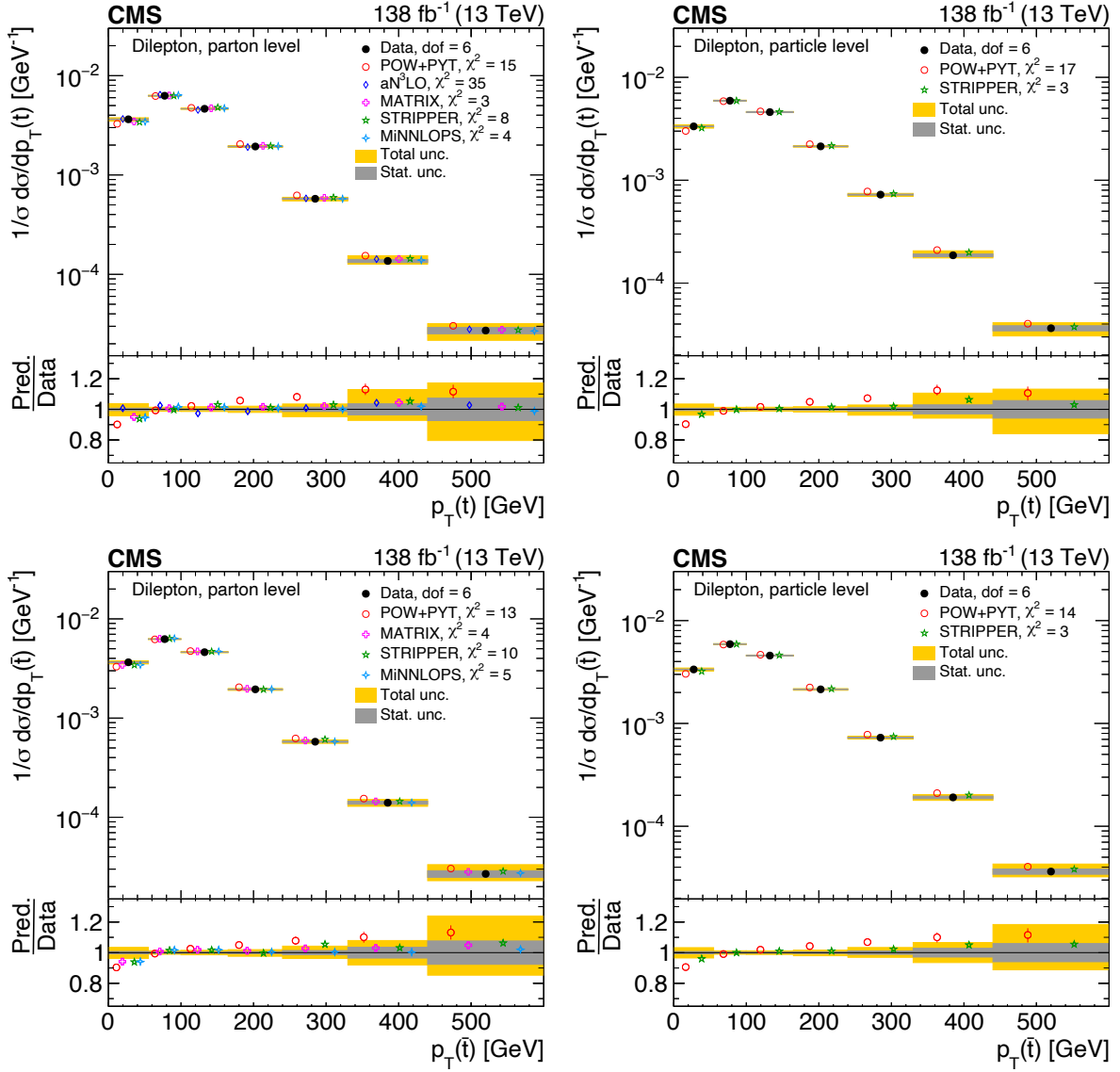
Figure 41: Normalized differential $t\bar{t}$ production cross sections as functions of $p_T(t)$ (upper) and $p_T(\bar{t})$ (lower), measured at the parton level in the full phase space (left) and at the particle level in a fiducial phase space (right). The data are shown as filled circles with grey and yellow bands indicating the statistical and total uncertainties (statistical and systematic uncertainties added in quadrature), respectively. For each distribution, the number of degrees of freedom (dof) is also provided. The cross sections are compared to predictions from the POWHEG+PYTHIA 8 ('POW-PYT', open circles) simulation and various theoretical predictions with beyond-NLO precision (other points). The estimated uncertainties in the POW+PYT model are represented by vertical bars on the corresponding points. For each model, a value of χ^2 is reported that takes into account the measurement uncertainties. The lower panel in each plot shows the ratios of the predictions to the data.

Figure 42: Normalized differential $t\bar{t}$ production cross sections as functions of $y(t)$ (upper) and $y(\bar{t})$ (lower) are shown for data (filled circles), POWHEG+PYTHIA 8 ('POW-PYT', open circles) simulation, and various theoretical predictions with beyond-NLO precision (other points). Further details can be found in the caption of Fig. 41.
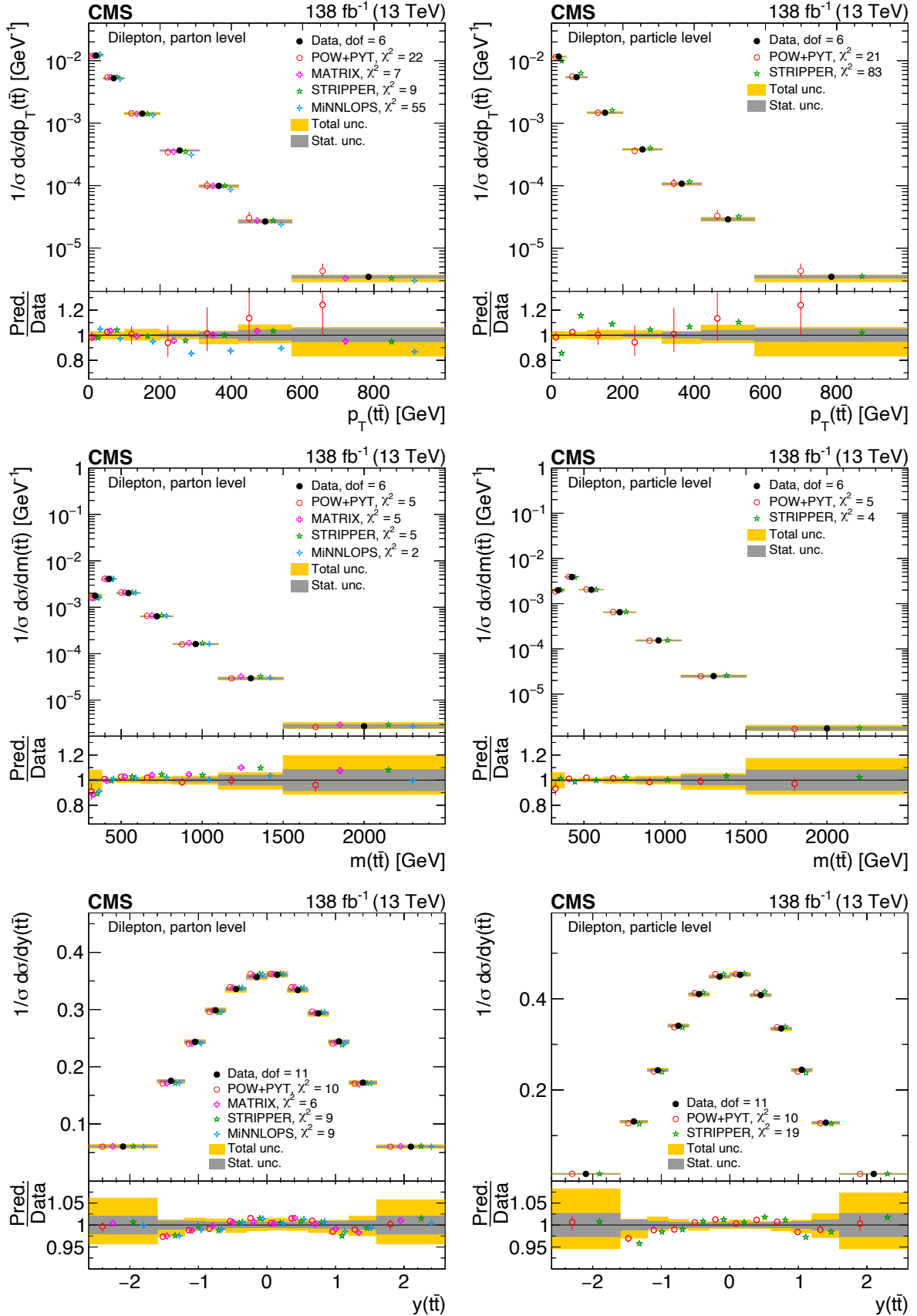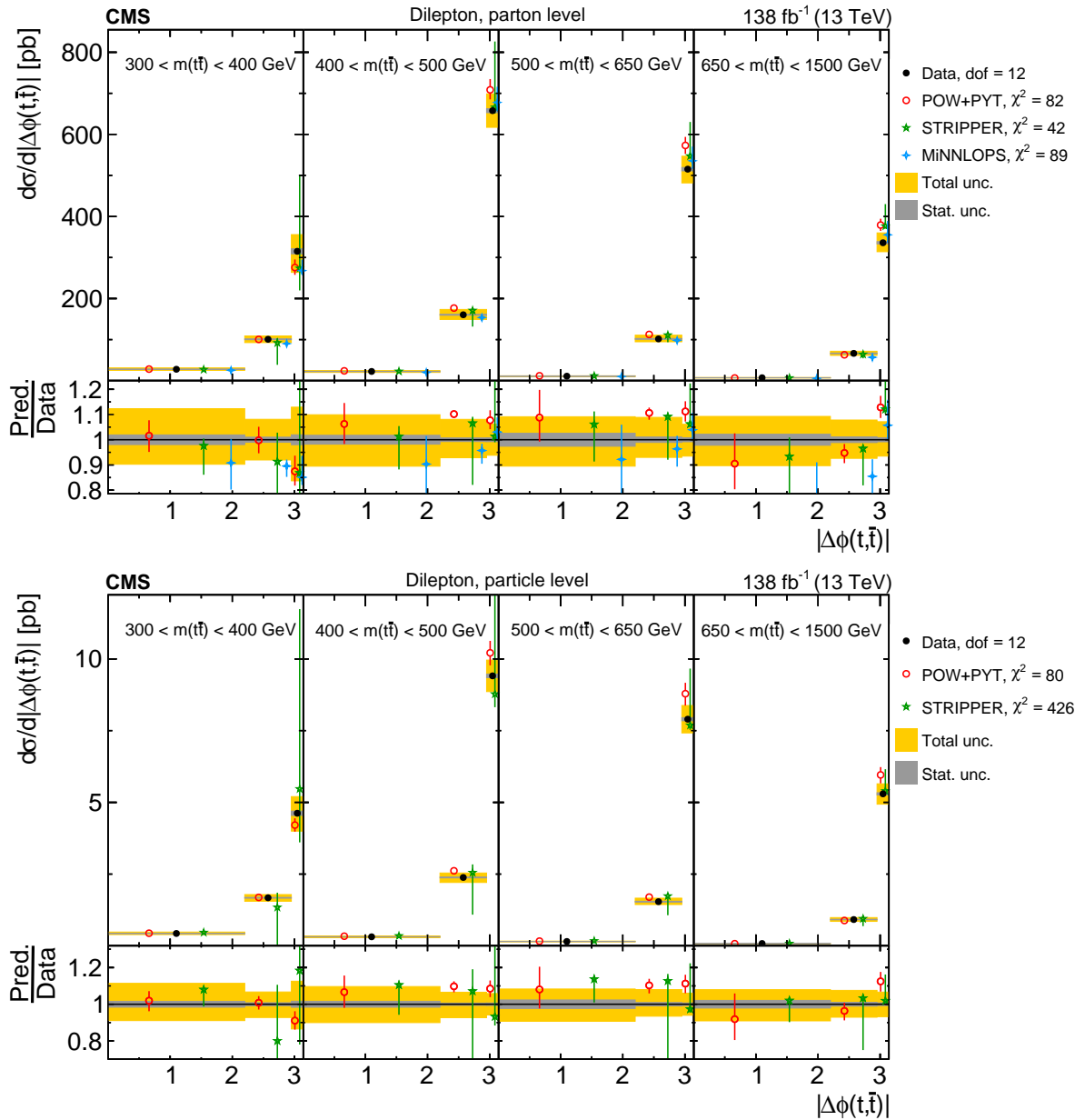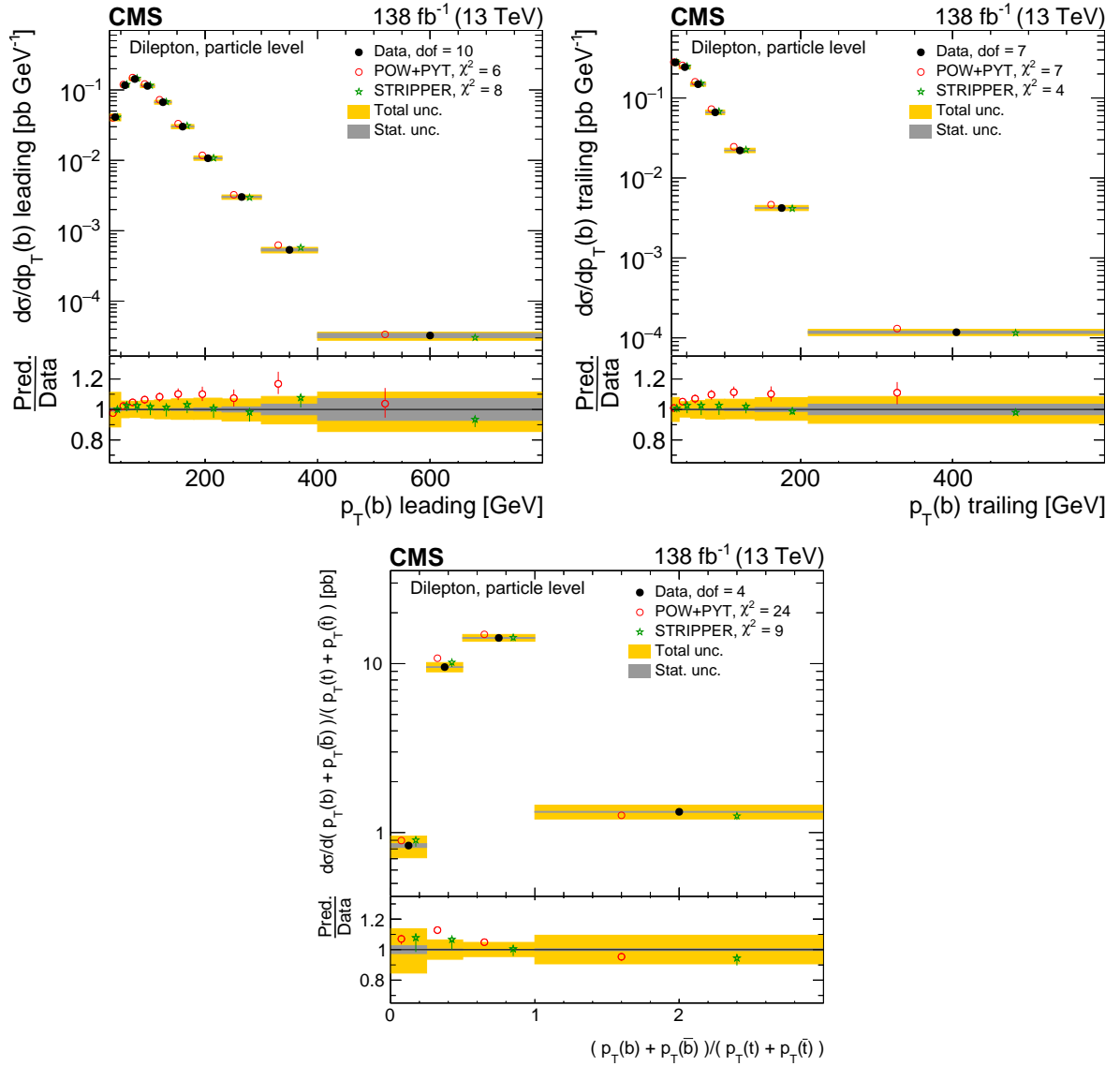
Figure 43: Normalized differential $t\bar{t}$ production cross sections as functions of $p_T(t\bar{t})$ (upper), $m(t\bar{t})$ (middle), and $y(t\bar{t})$ (lower) are shown for data (filled circles), POWHEG+PYTHIA 8 ('POW-PYT', open circles) simulation, and various theoretical predictions with beyond-NLO precision (other points). Further details can be found in the caption of Fig. 41.
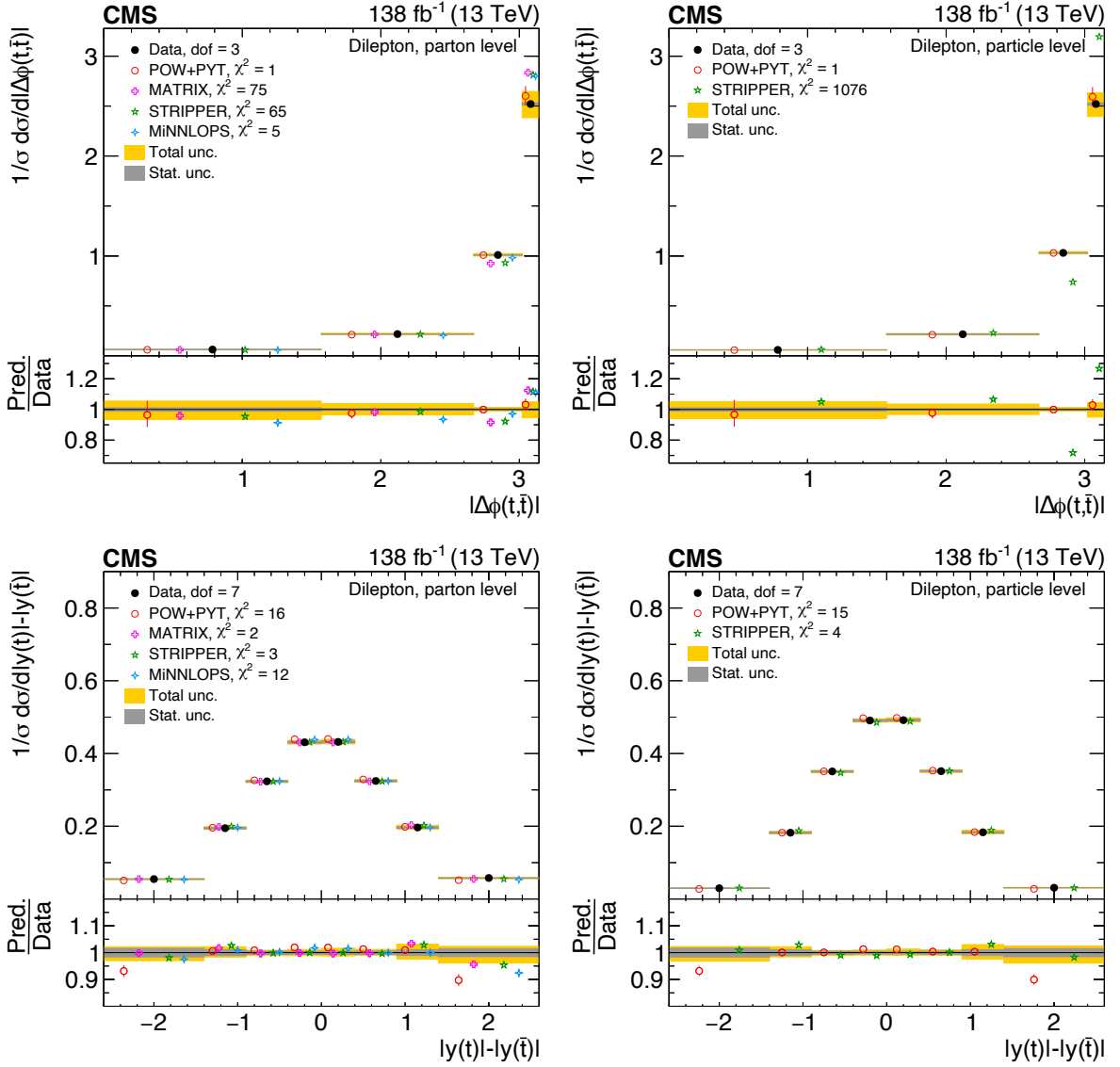
Figure 44: Normalized differential $t\bar{t}$ production cross sections as functions of $|\Delta\phi(t,\bar{t})|$ (upper) and $|y(t)| - |y(\bar{t})|$ (lower) are shown for data (filled circles), POWHEG+PYTHIA 8 ('POW-PYT', open circles) simulation, and various theoretical predictions with beyond-NLO precision (other points). Further details can be found in the caption of Fig. 41.
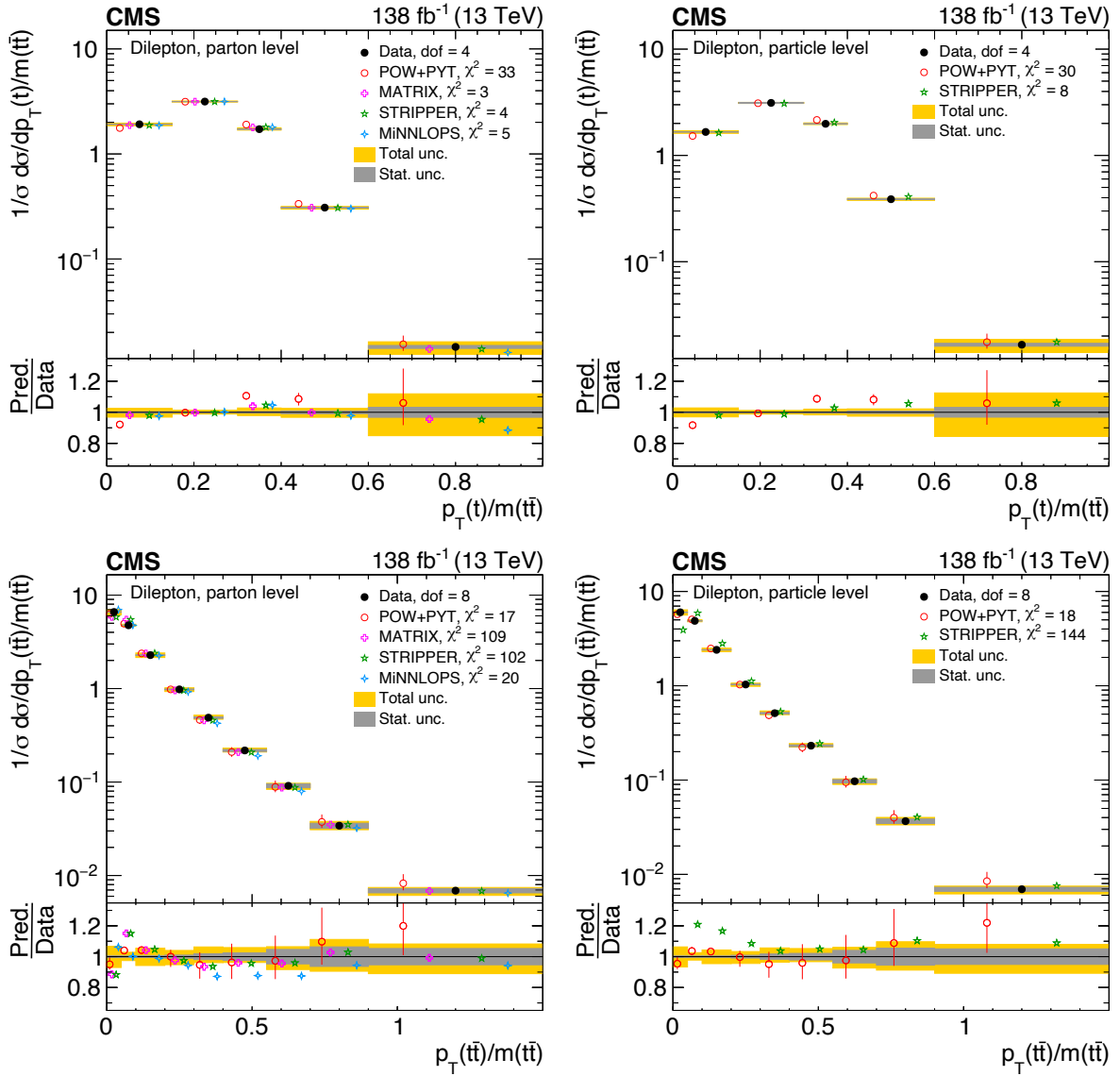
Figure 45: Normalized differential $t\bar{t}$ production cross sections as functions of $p_{\mathrm{T}}(t)/m(t\bar{t})$ (upper) and $p_{\mathrm{T}}(t\bar{t})/m(t\bar{t})$ (lower) are shown for data (filled circles), POWHEG+PYTHIA 8 ('POW-PYT', open circles) simulation, and various theoretical predictions with beyond-NLO precision (other points). Further details can be found in the caption of Fig. 41.
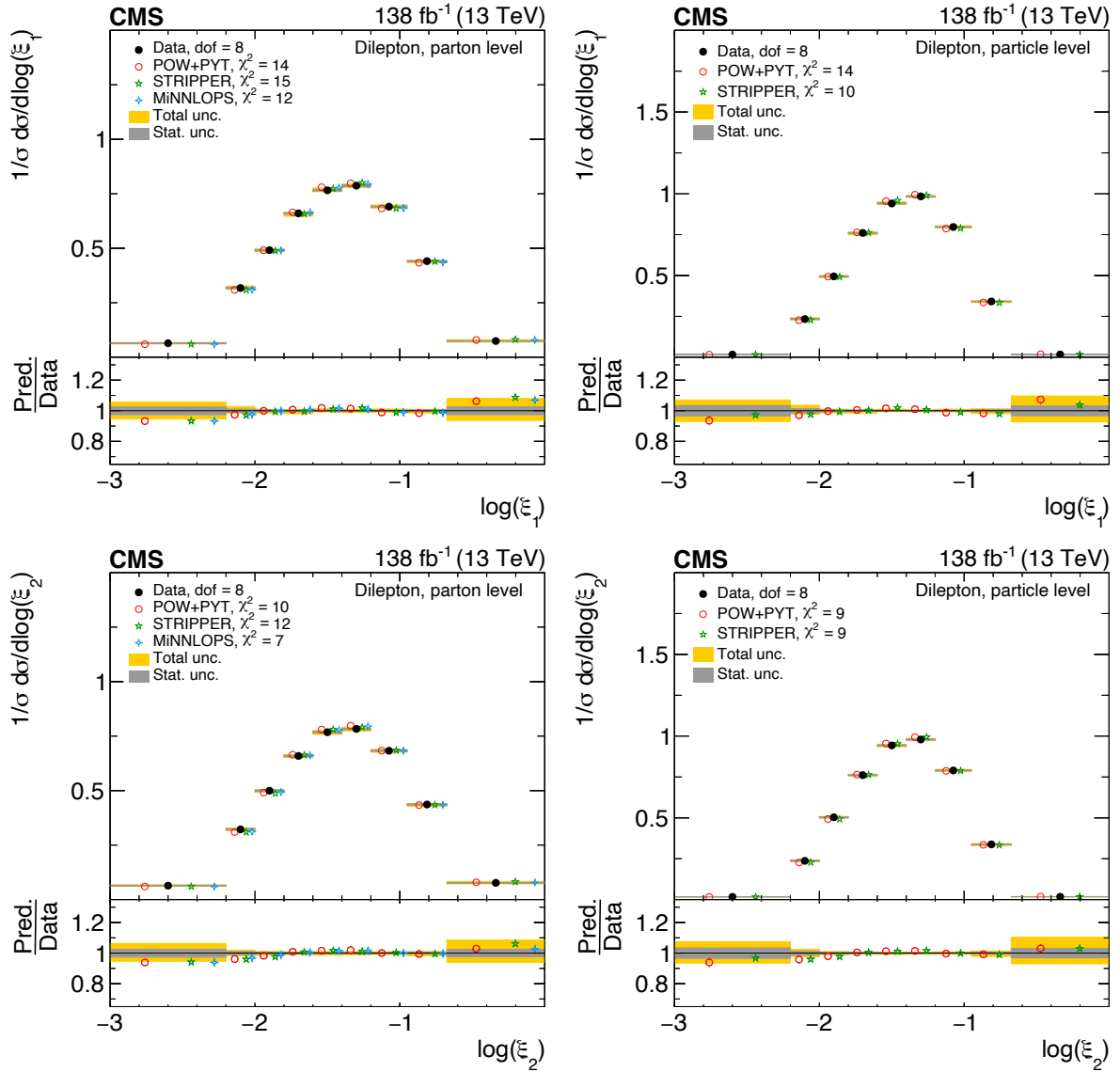
Figure 46: Normalized differential $t\bar{t}$ production cross sections as functions of $\log(\xi_1)$ (upper) and $\log(\xi_2)$ (lower) are shown for data (filled circles), POWHEG+PYTHIA 8 ('POW-PYT', open circles) simulation, and STRIPPER NNLO calculation (stars). Further details can be found in the caption of Fig. 41.
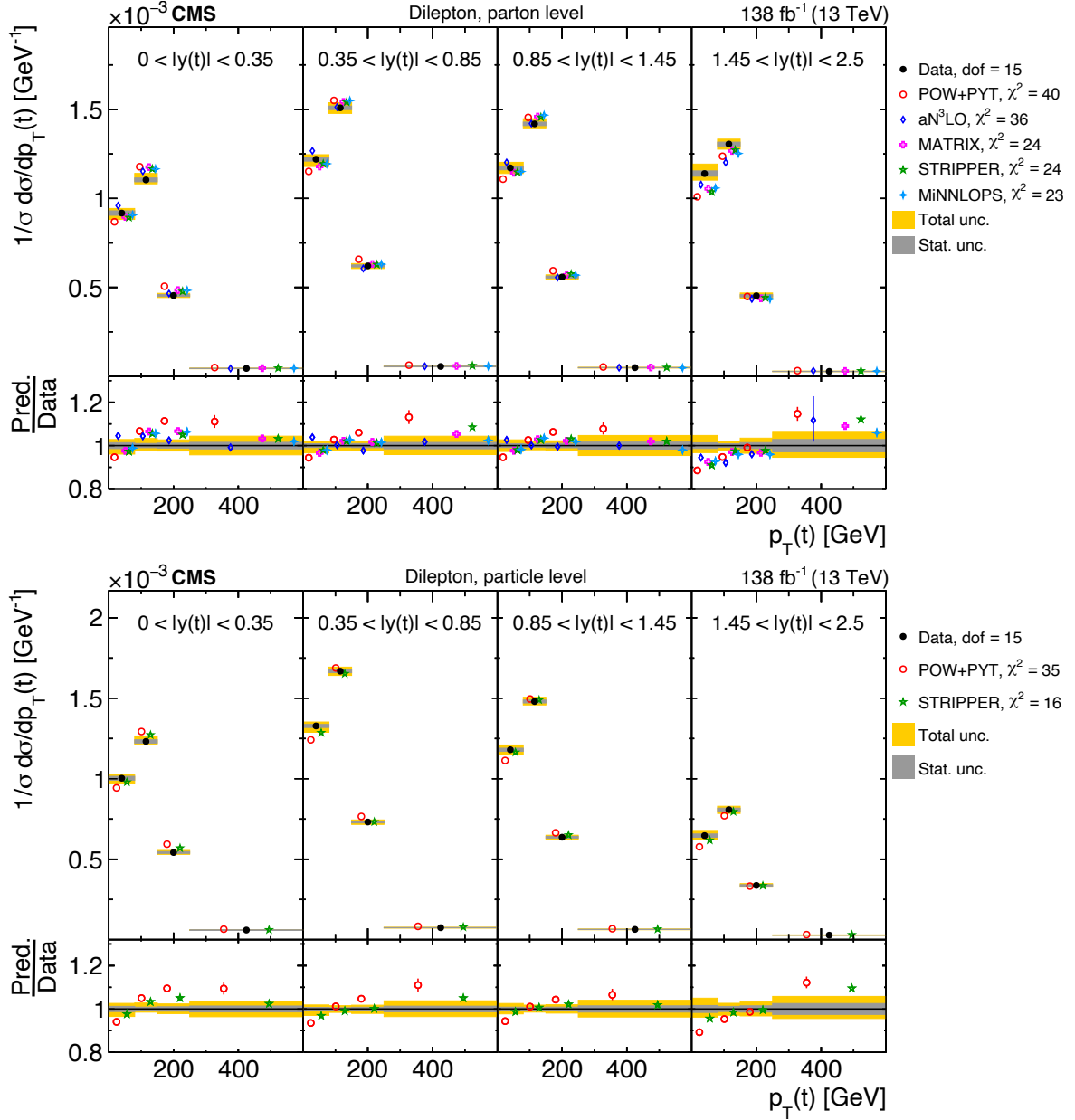
Figure 47: Normalized $[|y(t)|, p_T(t)]$ cross sections measured at the parton level in the full phase space (upper) and at the particle level in a fiducial phase space (lower). The data are shown as filled circles with grey and yellow bands indicating the statistical and total uncertainties (statistical and systematic uncertainties added in quadrature), respectively. For each distribution, the number of degrees of freedom (dof) is also provided. The cross sections are compared to predictions from the POWHEG+PYTHIA 8 ('POW-PYT', open circles) simulation and various theoretical predictions with beyond-NLO precision (other points). The estimated uncertainties in the POW+PYT model are represented by vertical bars on the corresponding points. For each model, a value of χ^2 is reported that takes into account the measurement uncertainties. The lower panel in each plot shows the ratios of the predictions to the data.

Figure 48:   Normalized $[m(t\bar{t}), p_T(t)]$ cross sections are shown for data (filled circles), POWHEG+PYTHIA 8 ('POW-PYT', open circles) simulation, and various theoretical predictions with beyond-NLO precision (other points). Further details can be found in the caption of Fig. 47.
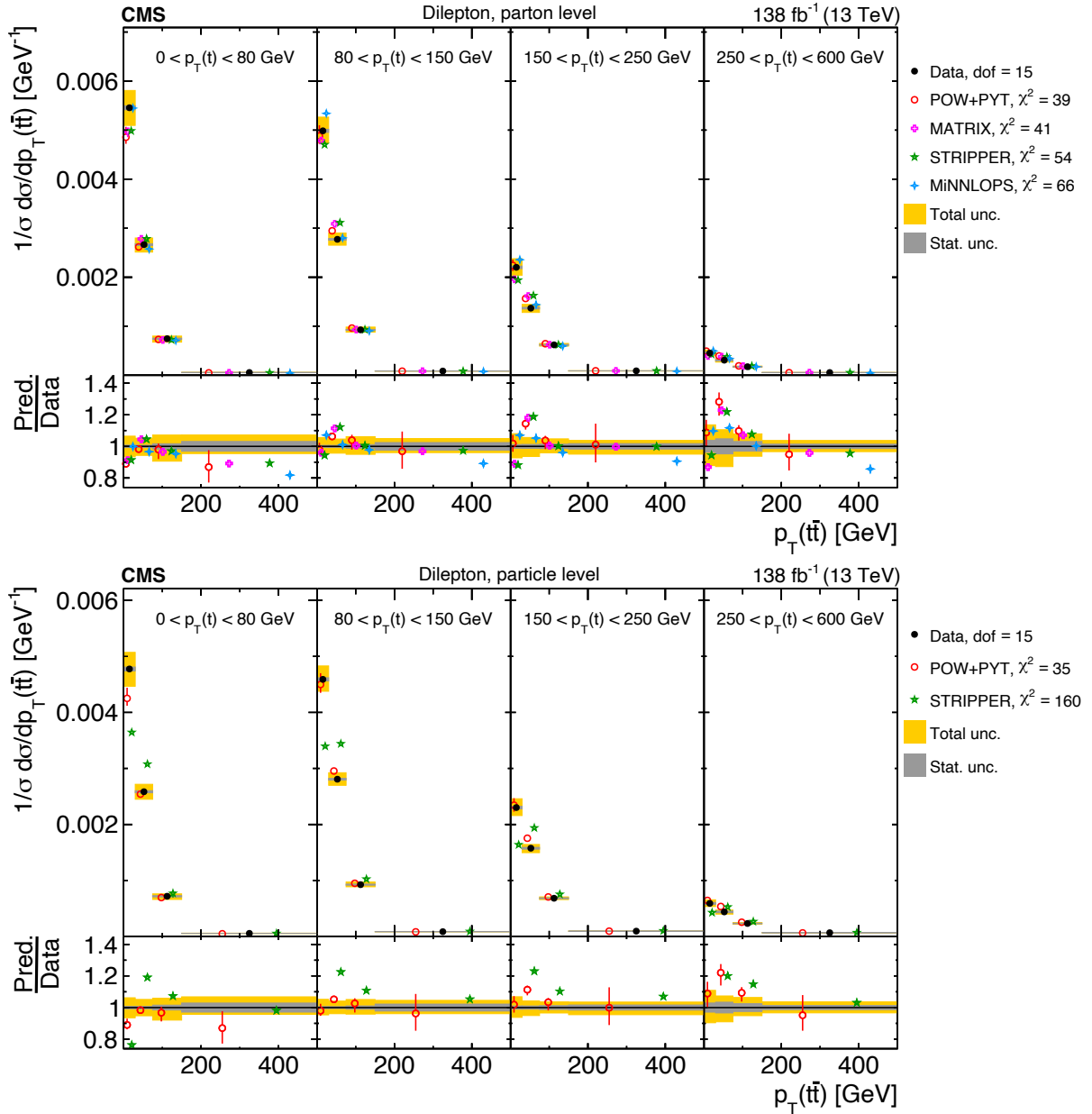
Figure 49: Normalized $[p_T(t), p_T(t\bar{t})]$ cross sections are shown for data (filled circles), POWHEG+PYTHIA 8 ('POW-PYT', open circles) simulation, and various theoretical predictions with beyond-NLO precision (other points). Further details can be found in the caption of Fig. 47.
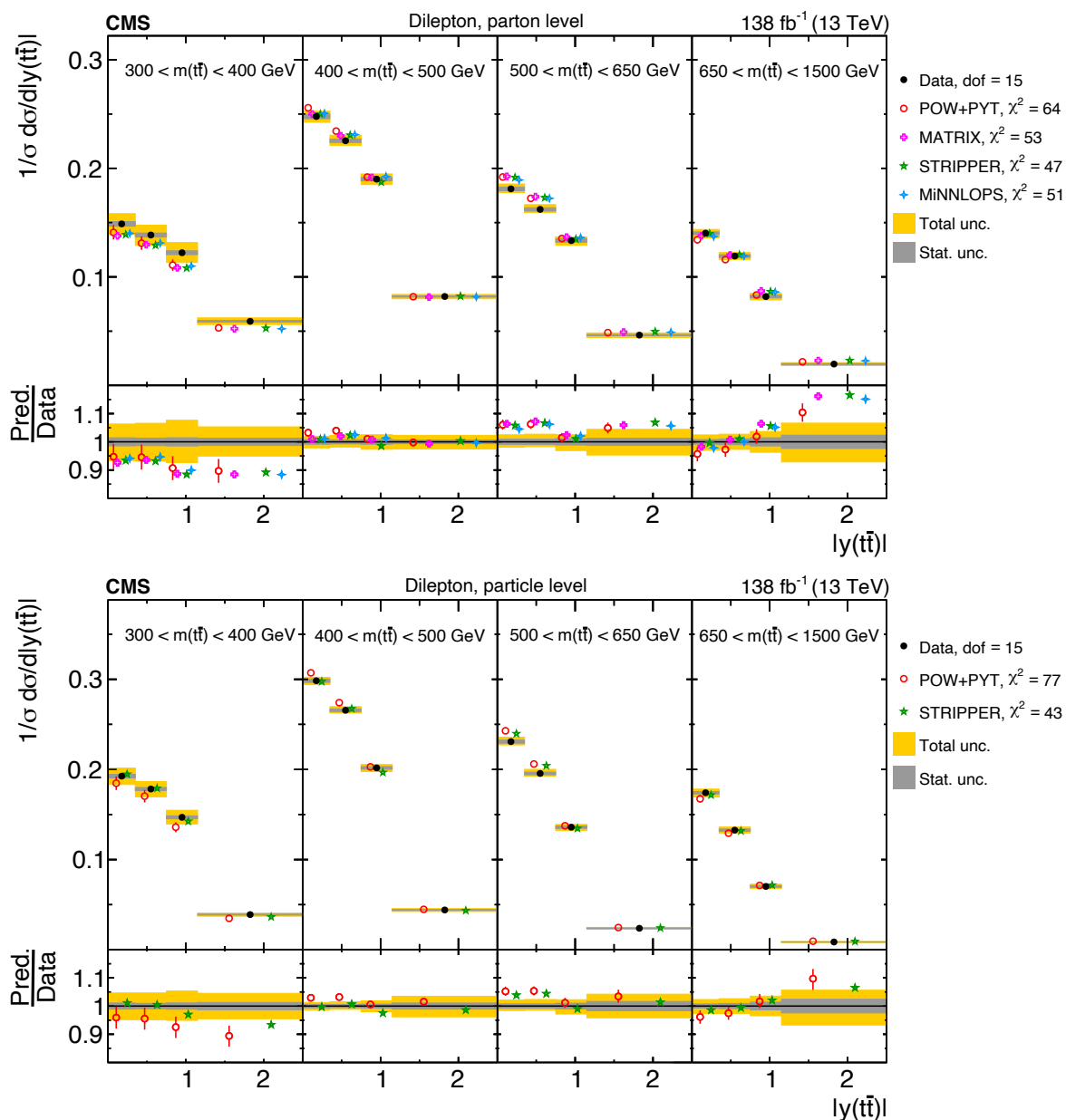
Figure 50: Normalized $[m(t\bar{t}), |y(t\bar{t})|]$ cross sections are shown for data (filled circles), POWHEG+PYTHIA 8 ('POW-PYT', open circles) simulation, and various theoretical predictions with beyond-NLO precision (other points). Further details can be found in the caption of Fig. 47.
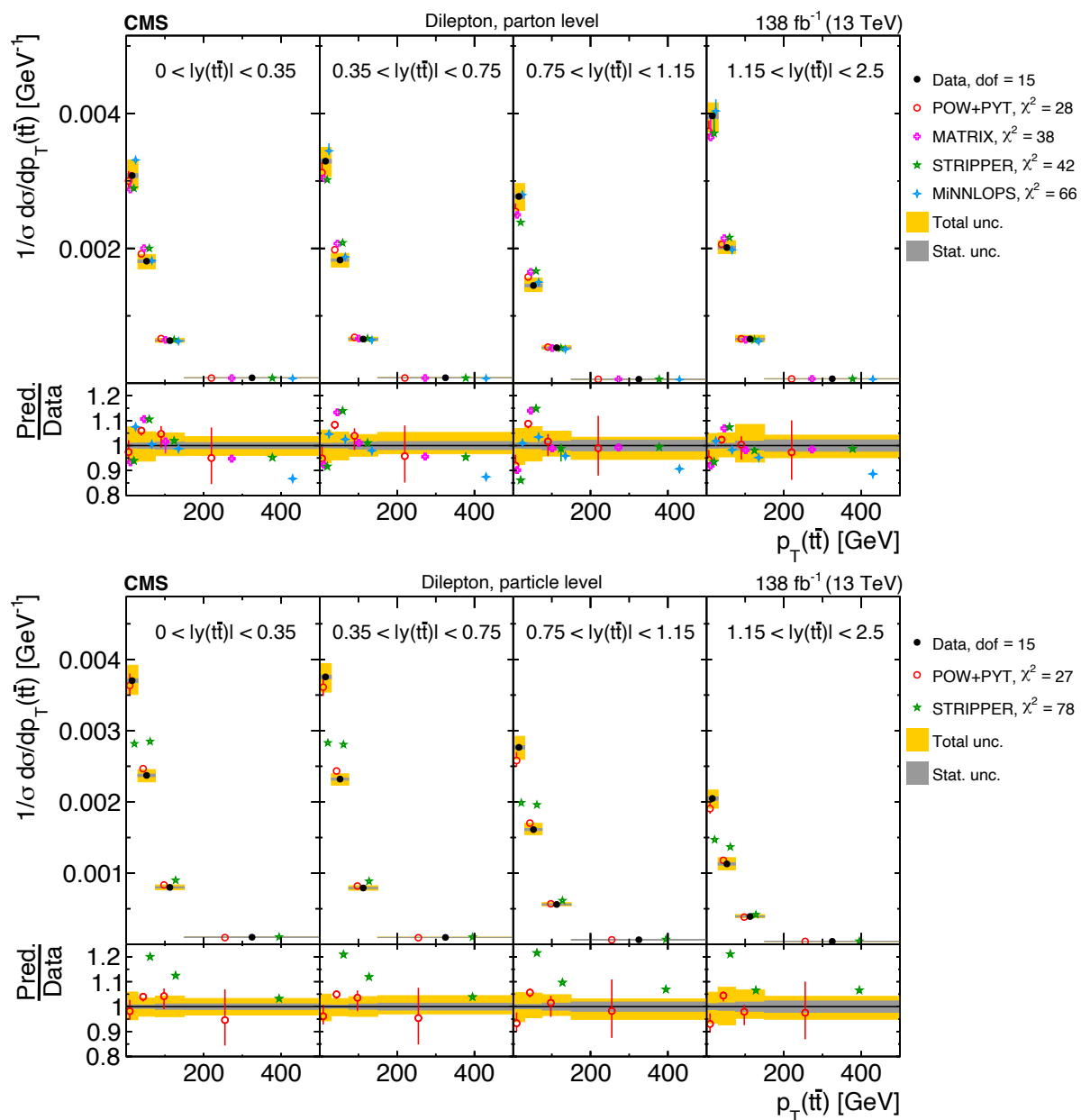
Figure 51: Normalized $[|y(t\bar{t})|, p_T(t\bar{t})]$ cross sections are shown for data (filled circles), POWHEG+PYTHIA 8 ('POW-PYT', open circles) simulation, and various theoretical predictions with beyond-NLO precision (other points). Further details can be found in the caption of Fig. 47.
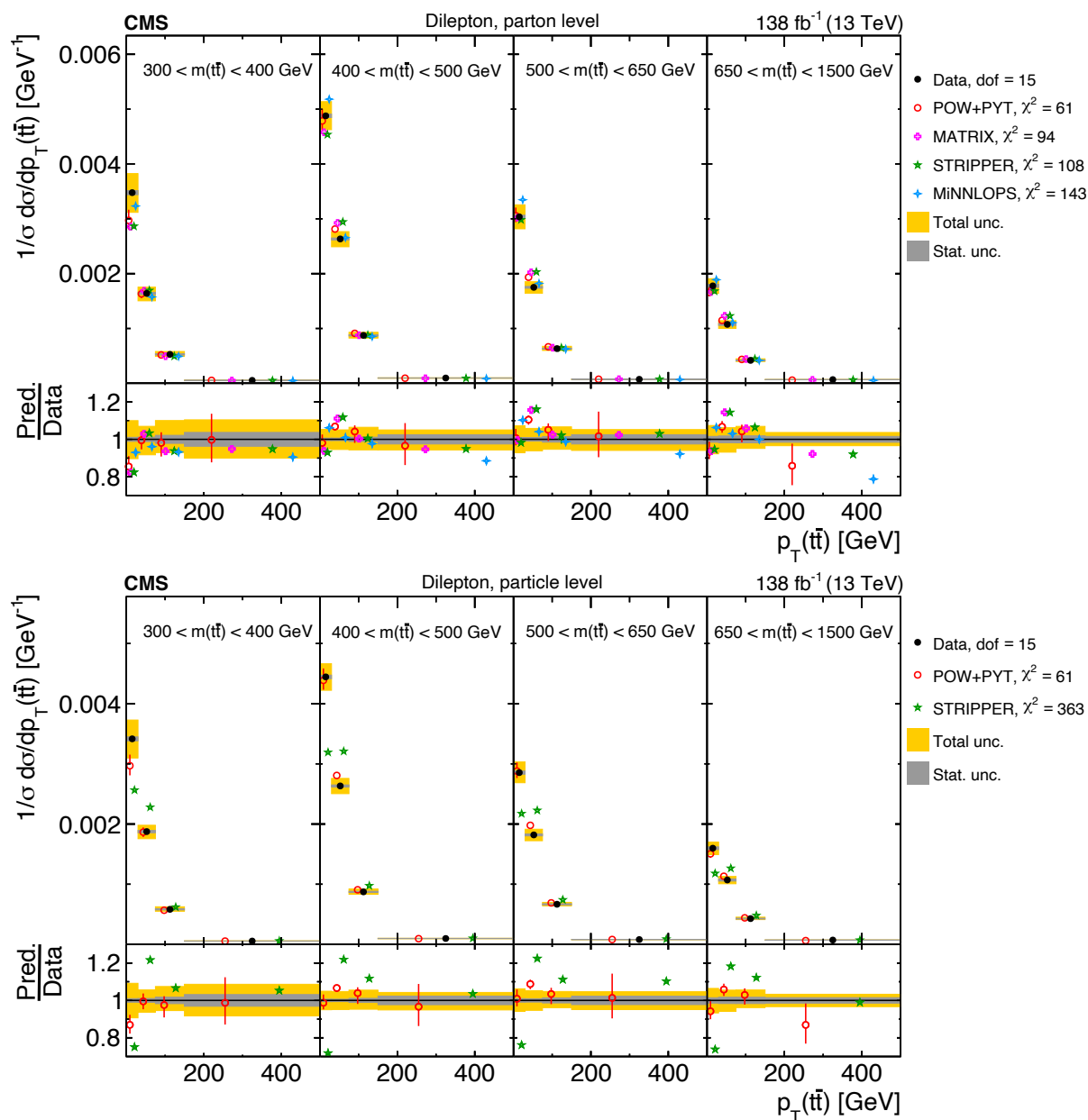
Figure 52: Normalized $[m(t\bar{t}), p_T(t\bar{t})]$ cross sections are shown for data (filled circles), POWHEG+PYTHIA 8 ('POW-PYT', open circles) simulation, and various theoretical predictions with beyond-NLO precision (other points). Further details can be found in the caption of Fig. 47.
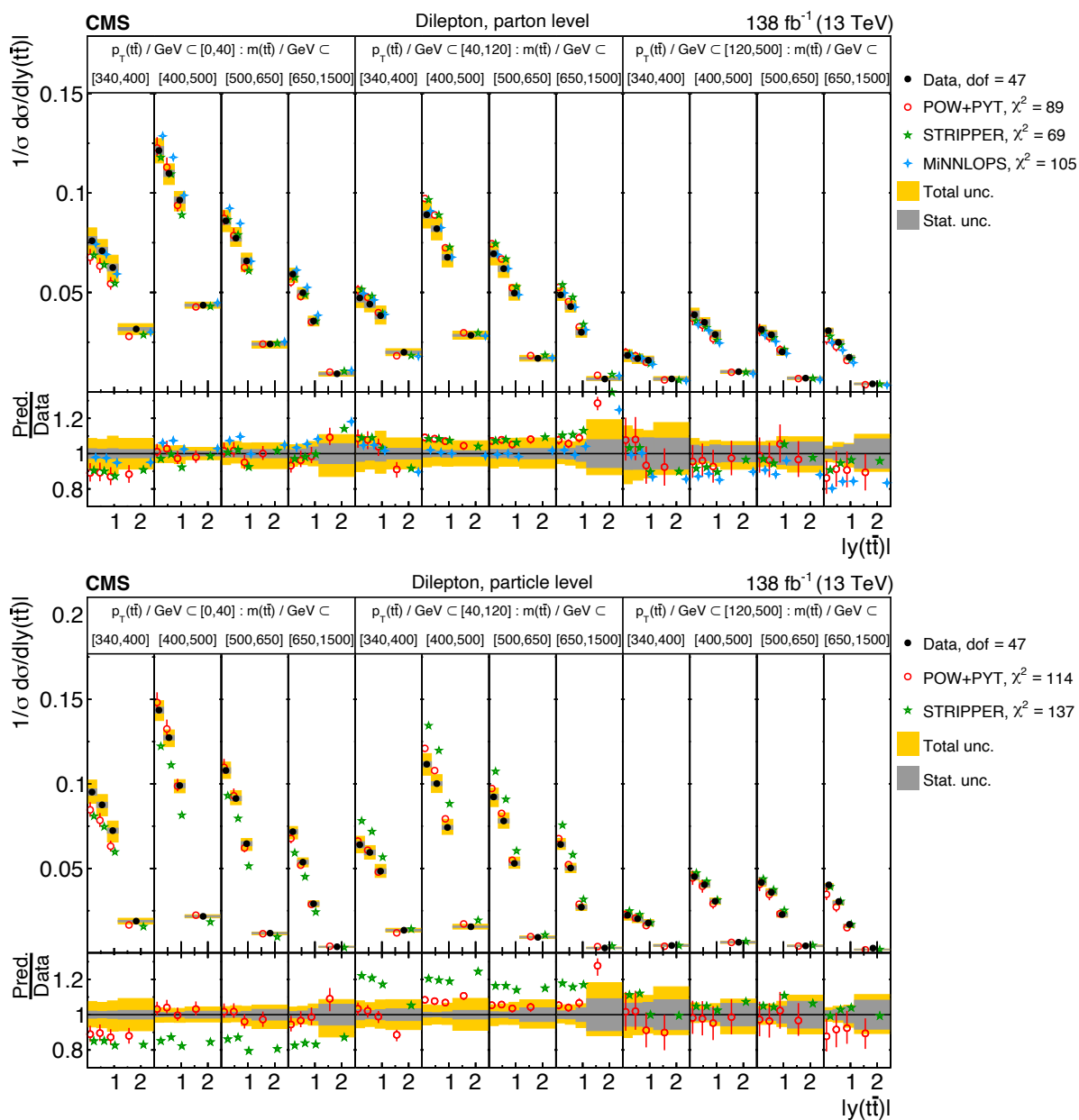
Figure 53: Normalized $[p_T(t\bar{t}), m(t\bar{t}), |y(t\bar{t})|]$ cross sections are shown for data (filled circles), POWHEG+PYTHIA 8 ('POW-PYT', open circles) simulation, and various theoretical predictions with beyond-NLO precision (other points). Further details can be found in the caption of Fig. 47.
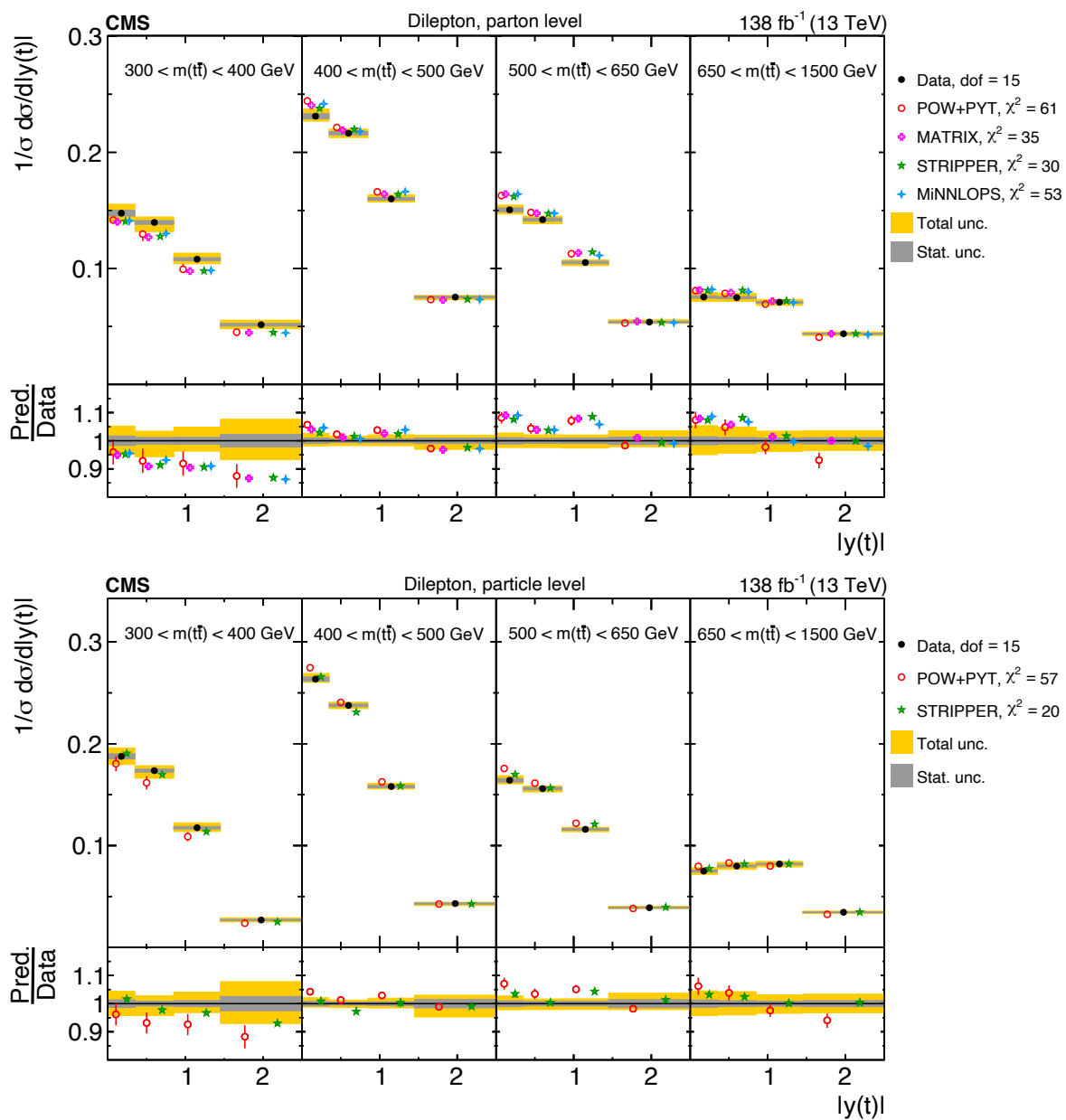
Figure 54: Normalized $[m(t\bar{t}), |y(t)|]$ cross sections are shown for data (filled circles), POWHEG+PYTHIA 8 ('POW-PYT', open circles) simulation, and various theoretical predictions with beyond-NLO precision (other points). Further details can be found in the caption of Fig. 47.
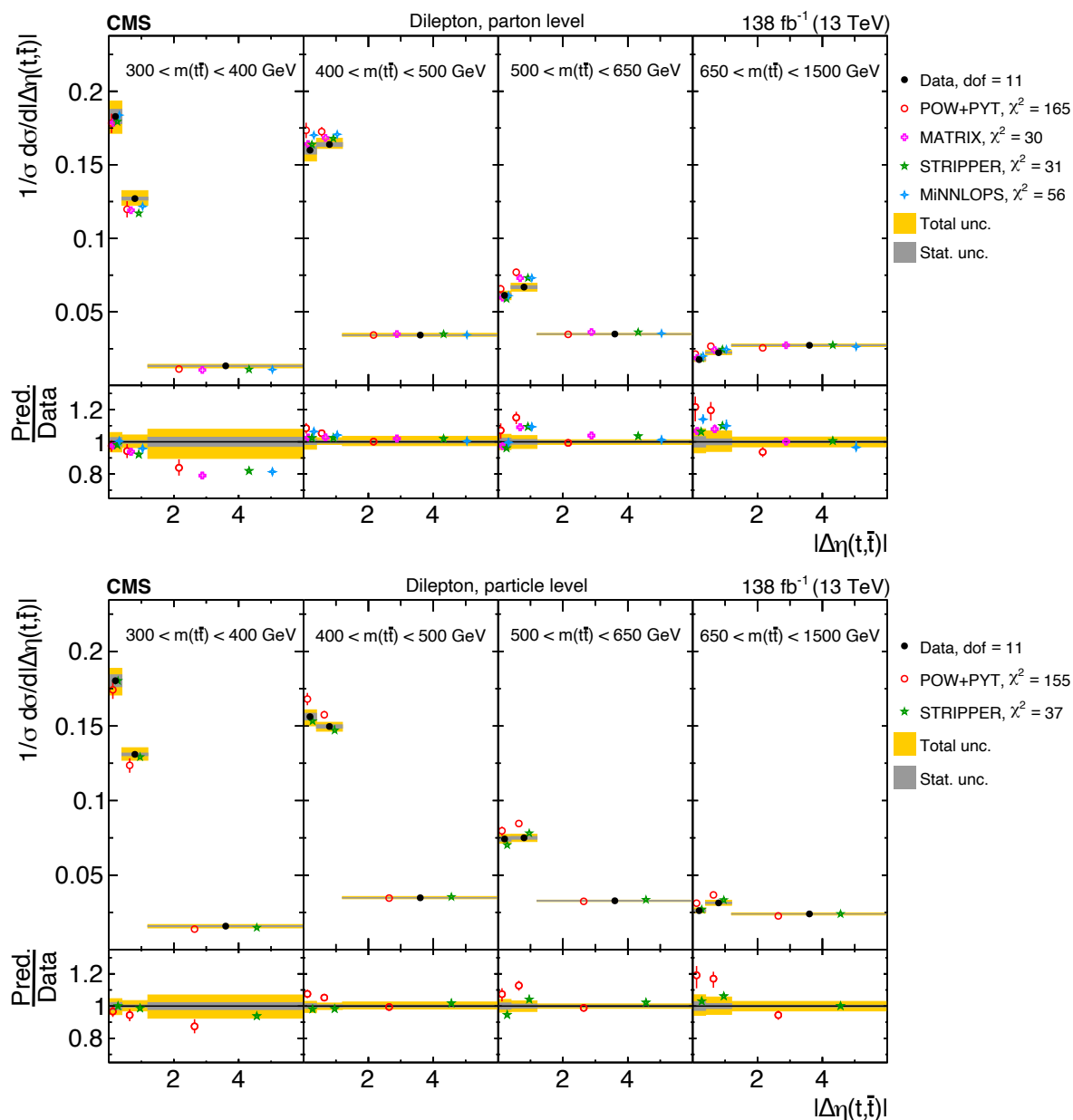
Figure 55: Normalized $[m(t\bar{t}), |\Delta\eta(t,\bar{t})|]$ cross sections are shown for data (filled circles), POWHEG+PYTHIA 8 ('POW-PYT', open circles) simulation, and various theoretical predictions with beyond-NLO precision (other points). Further details can be found in the caption of Fig. 47.
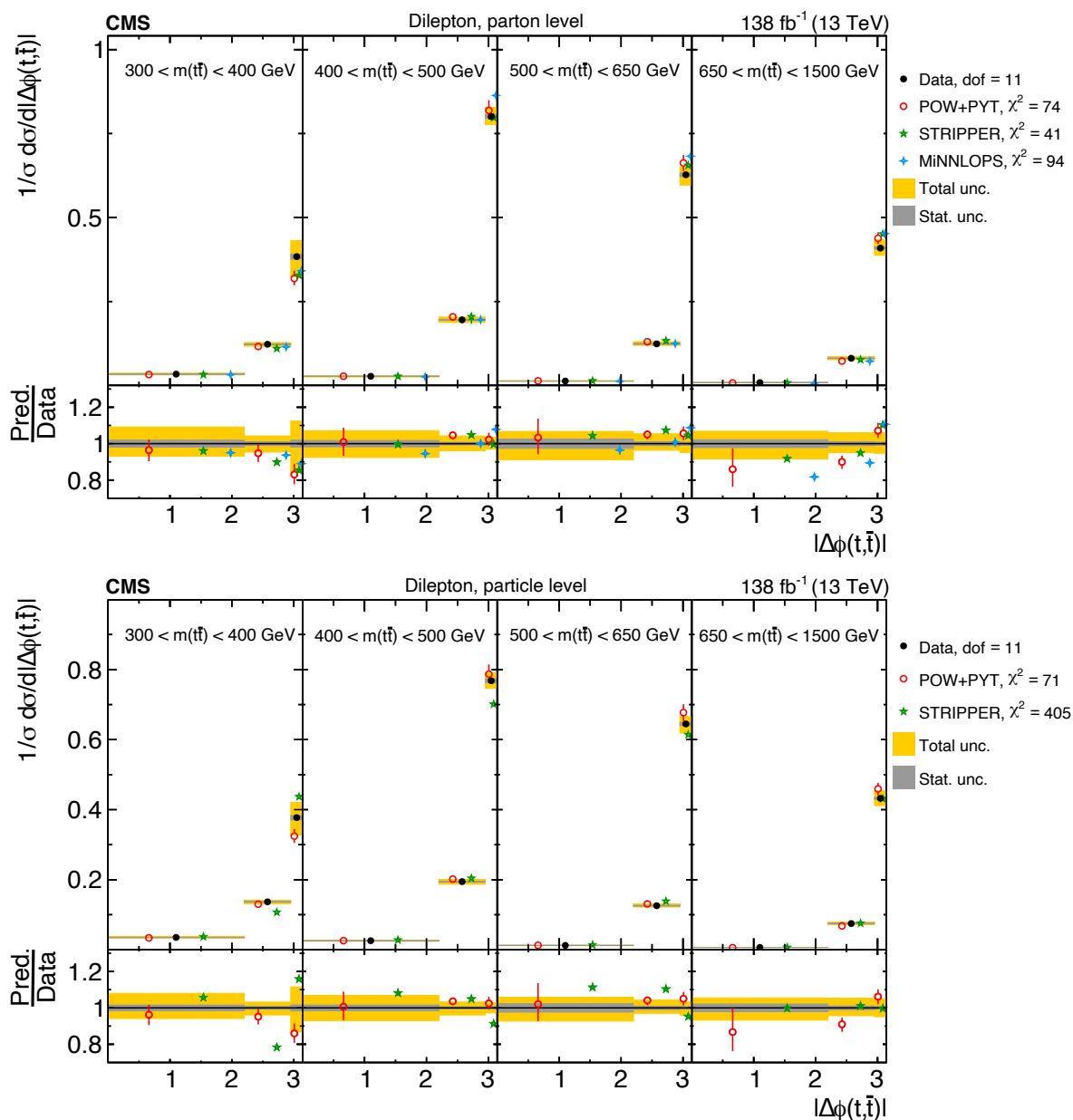
Figure 56: Normalized $[m(t\bar{t}), |\Delta\phi(t,\bar{t})|]$ cross sections are shown for data (filled circles), POWHEG+PYTHIA 8 ('POW-PYT', open circles) simulation, and various theoretical predictions with beyond-NLO precision (other points). Further details can be found in the caption of Fig. 47.
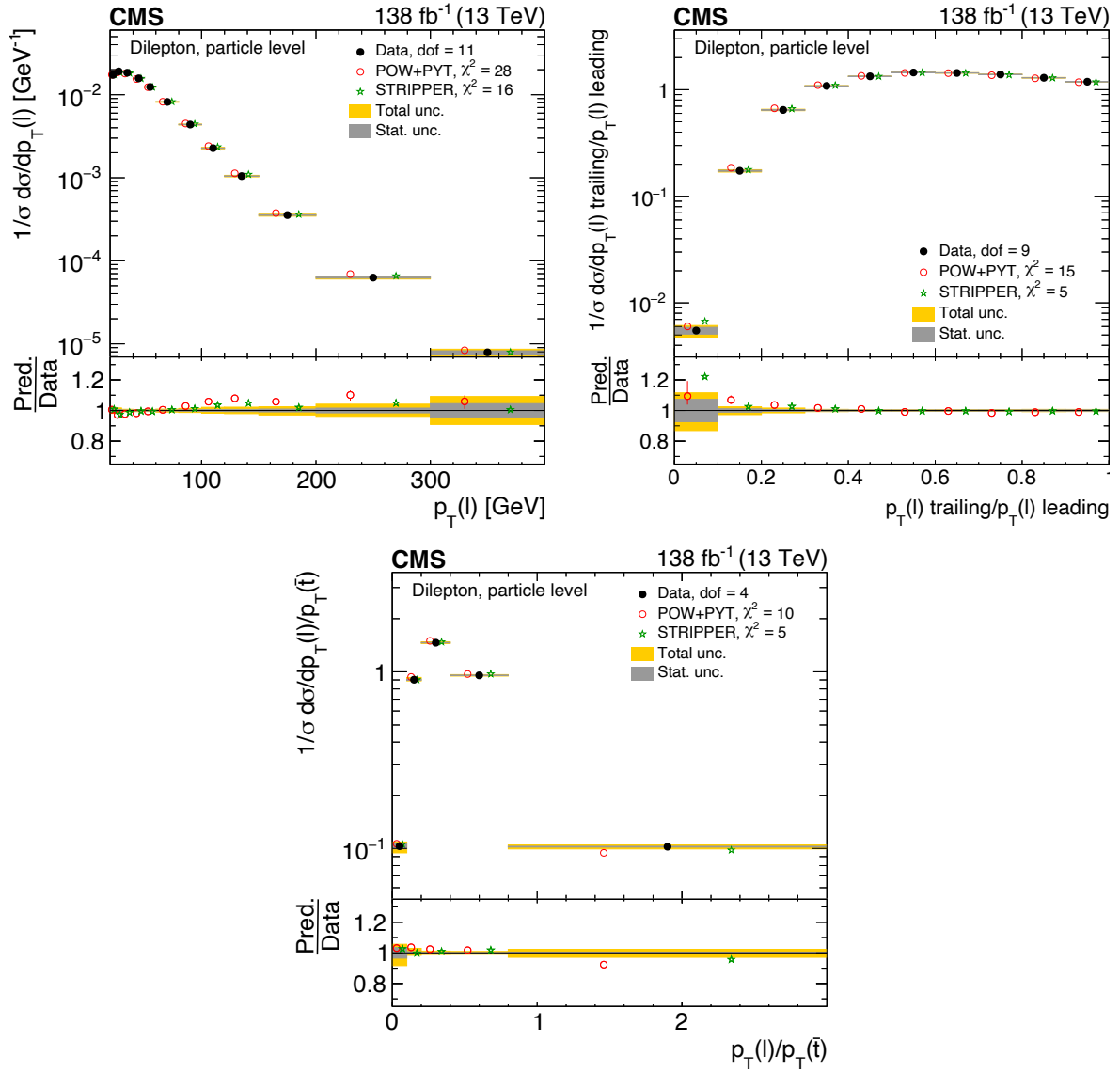
Figure 57: Normalized differential $t\bar{t}$ production cross sections as functions of p_T of the lepton (upper left), of the ratio of the trailing and leading lepton p_T (upper right), and of the ratio of lepton and top antiquark p_T (lower middle), measured at the particle level in a fiducial phase space. The data are shown as filled circles with grey and yellow bands indicating the statistical and total uncertainties (statistical and systematic uncertainties added in quadrature), respectively. For each distribution, the number of degrees of freedom (dof) is also provided. The cross sections are compared to predictions from the POWHEG+PYTHIA 8 ('POW-PYT', open circles) simulation and STRIPPER NNLO calculation (stars). The estimated uncertainties in the POW+PYT model are represented by vertical bars on the corresponding points. For each model, a value of χ^2 is reported that takes into account the measurement uncertainties. The lower panel in each plot shows the ratios of the predictions to the data.

Figure 58: Normalized differential $t\bar{t}$ production cross sections as functions of the p_T of the leading (upper left) and trailing (upper right) b jet, and $(p_T(b) + p_T(\bar{b}))/(p_T(t) + p_T(\bar{t}))$ (lower) are shown for data (filled circles), POWHEG+PYTHIA 8 ('POW-PYT', open circles) simulation, and STRIPPER NNLO calculation (stars). Further details can be found in the caption of Fig. 57.
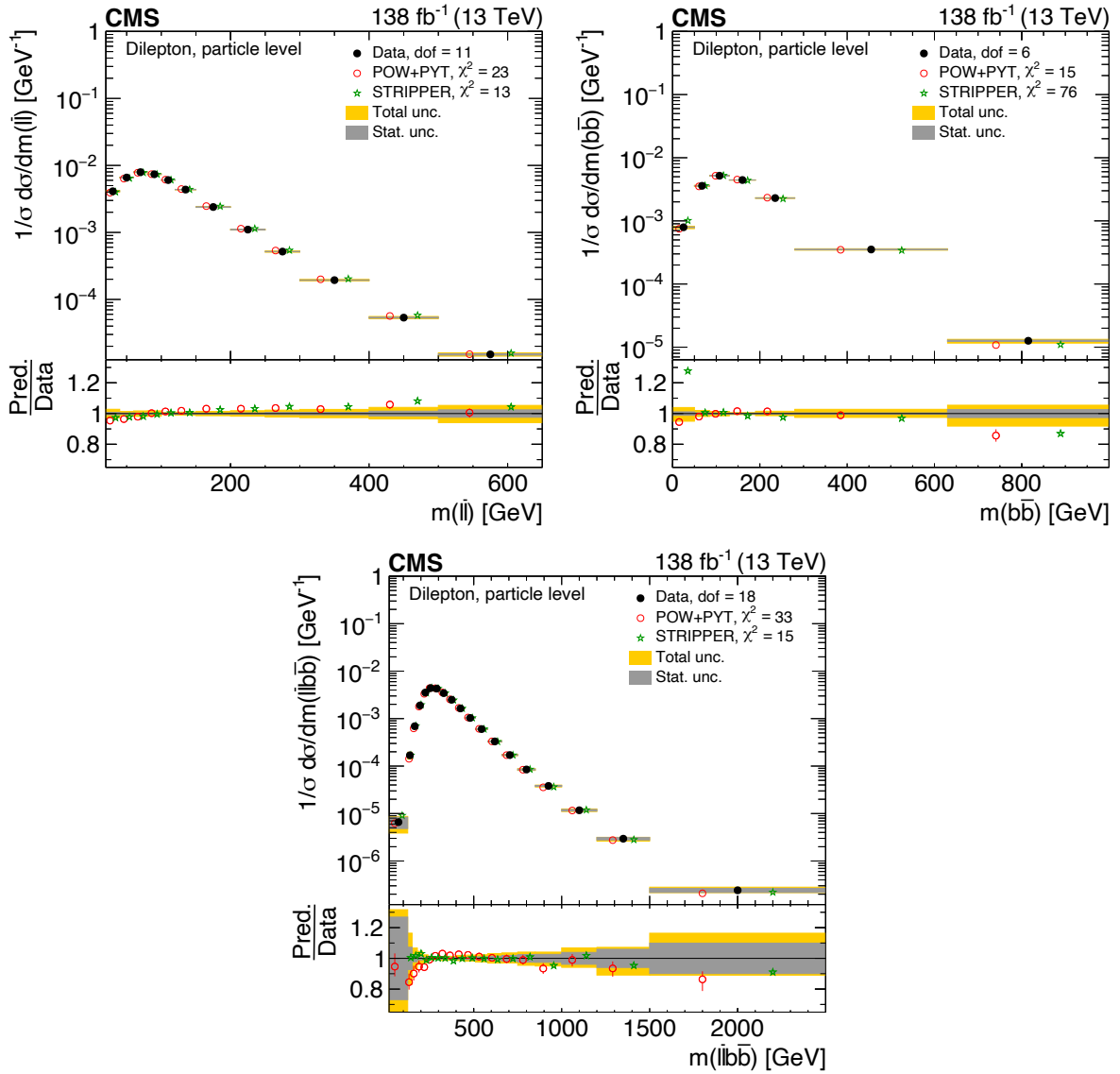
Figure 59: Normalized differential $t\bar{t}$ production cross sections as functions of $m(\ell\bar{\ell})$ (upper left), $m(b\bar{b})$ (upper right), and $m(\ell\bar{\ell}b\bar{b})$ (lower) are shown for data (filled circles), POWHEG+PYTHIA 8 ('POW-PYT', open circles) simulation, and STRIPPER NNLO calculation (stars). Further details can be found in the caption of Fig. 57.
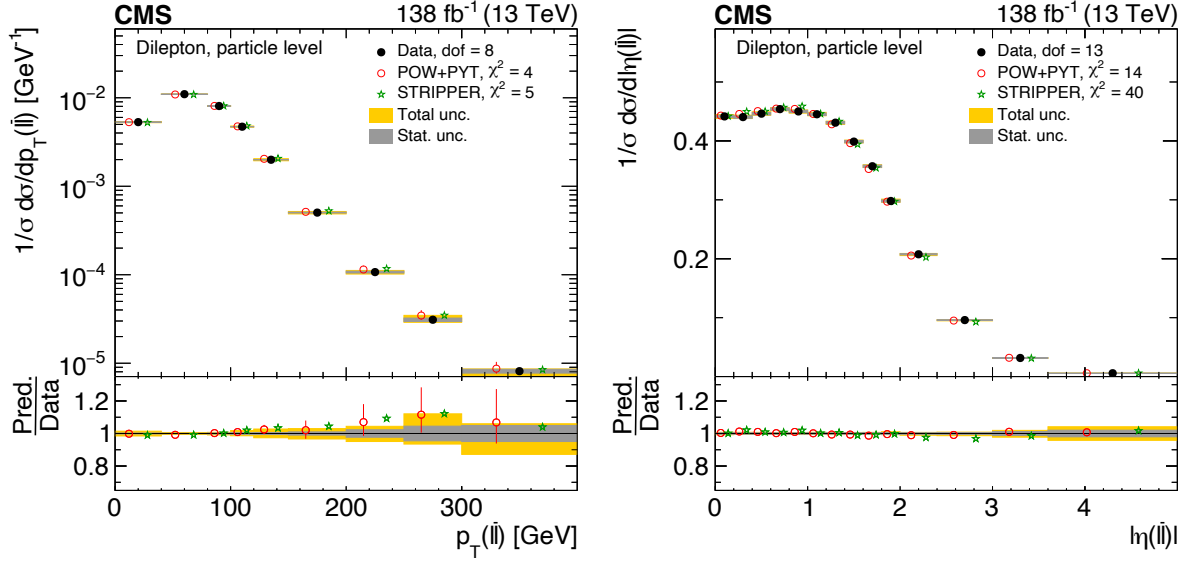
Figure 60: Normalized differential $t\bar{t}$ production cross sections as functions of $p_{\mathrm{T}}(\ell\bar{\ell})$ (left) and $|\eta(\ell\bar{\ell})|$ (right) are shown for data (filled circles), POWHEG+PYTHIA 8 ('POW-PYT', open circles) simulation, and STRIPPER NNLO calculation (stars). Further details can be found in the caption of Fig. 57.
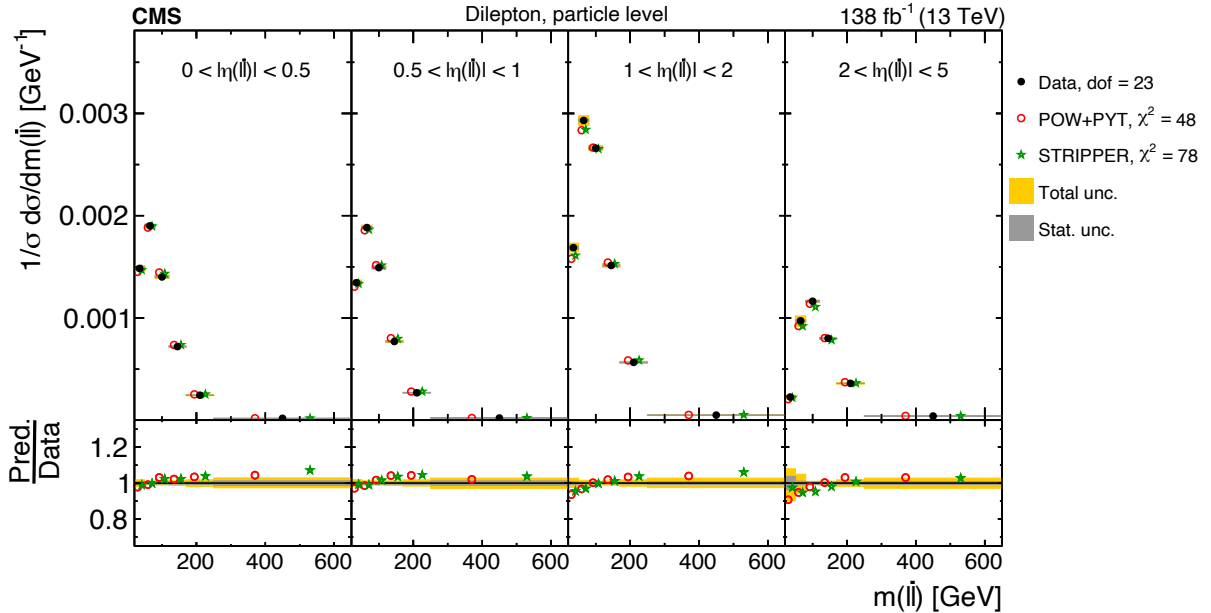
Figure 61: Normalized $[|\eta(\ell\bar{\ell})|, m(\ell\bar{\ell})]$ cross sections are shown for data (filled circles), POWHEG+PYTHIA 8 ('POW-PYT', open circles) simulation, and STRIPPER NNLO calculation (stars). Further details can be found in the caption of Fig. 57.
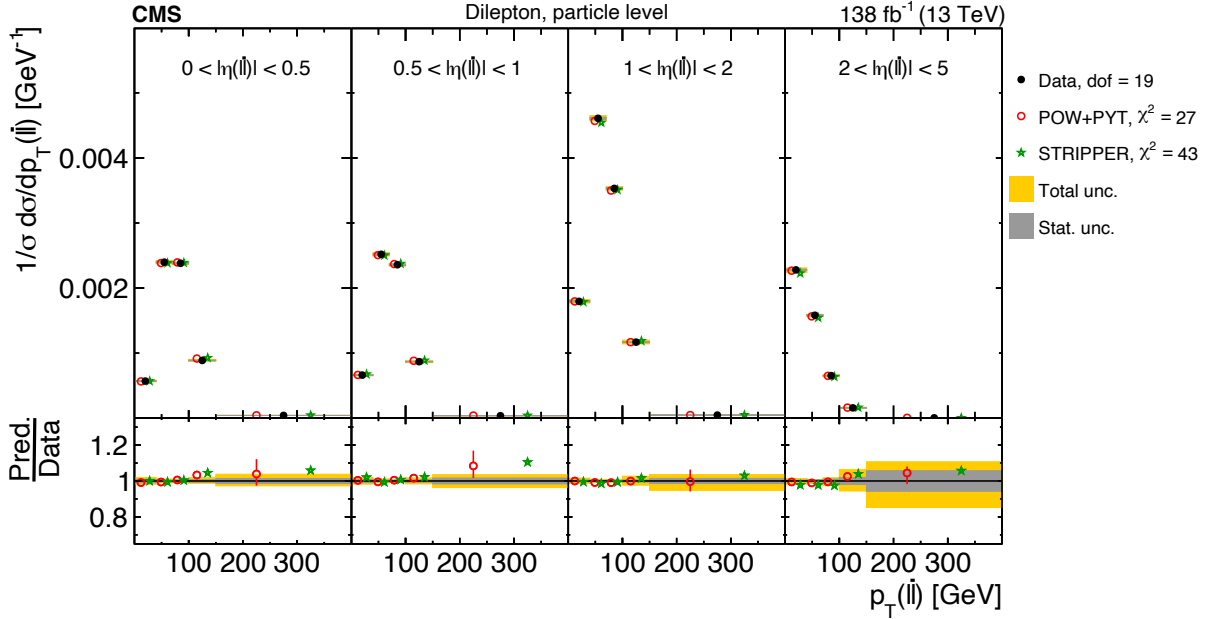
Figure 62: Normalized $[|\eta(\ell\bar\ell)|, p_T(\ell\bar\ell)]$ cross sections are shown for data (filled circles), POWHEG+PYTHIA 8 ('POW-PYT', open circles) simulation, and STRIPPER NNLO calculation (stars). Further details can be found in the caption of Fig. 57.
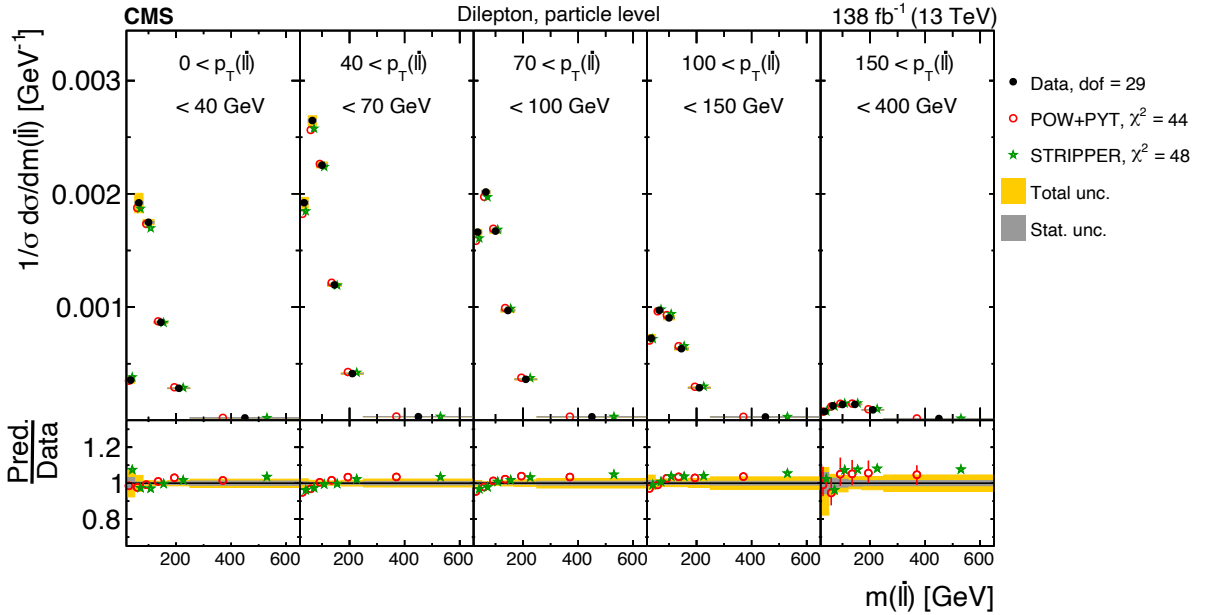
Figure 63: Normalized $[p_T(\ell\bar\ell), m(\ell\bar\ell)]$ cross sections are shown for data (filled circles), POWHEG+PYTHIA 8 ('POW-PYT', open circles) simulation, and STRIPPER NNLO calculation (stars). Further details can be found in the caption of Fig. 57.

Table 8: The χ^2 values and dof of the measured normalized single-differential cross sections for $t\bar{t}$ and top quark kinematic observables at the parton level are shown with respect to the POWHEG+PYTHIA 8 ('POW-PYT') simulation and various theoretical predictions with beyond-NLO precision. The χ^2 values are calculated taking only measurement uncertainties into account and excluding theory uncertainties. For POW+PYT, the χ^2 values including theory uncertainties are indicated with the brackets (w. unc.).

Cross section variables	dof	χ^2				
		POW+PYT (w. unc.)	$a\mathrm{N^3LO}$	MATRIX	STRIPPER	MiNNLOPS
$p_\mathrm{T}(\mathrm{t})$	6	15 (11)	35	3	8	4
$p_\mathrm{T}(\bar{\mathrm{t}})$	6	13 (9)	—	4	10	5
$y(\mathrm{t})$	9	23 (20)	23	16	17	15
$y(\bar{\mathrm{t}})$	9	28 (25)	—	15	25	23
$p_\mathrm{T}(\mathrm{t}\bar{\mathrm{t}})$	6	22 (7)	—	7	9	55
$y(\mathrm{t}\bar{\mathrm{t}})$	11	10 (8)	—	6	9	9
$m(\mathrm{t}\bar{\mathrm{t}})$	6	5 (3)	—	5	5	2
$|\Delta\phi(\mathrm{t},\bar{\mathrm{t}})|$	3	1 (0)	—	75	65	5
$|y(\mathrm{t})|-|y(\bar{\mathrm{t}})|$	7	16 (9)	—	2	3	12
$p_\mathrm{T}(\mathrm{t})/m(\mathrm{t}\bar{\mathrm{t}})$	4	33 (20)	—	3	4	5
$p_\mathrm{T}(\mathrm{t}\bar{\mathrm{t}})/m(\mathrm{t}\bar{\mathrm{t}})$	8	17 (6)	—	109	102	20
$\log(\xi_1)$	8	14 (10)	—	—	15	12
$\log(\xi_2)$	8	10 (7)	—	—	12	7

Table 9: The χ^2 values and dof of the measured normalized single-differential cross sections for t$\bar{\text{t}}$ and top quark kinematic observables at the particle level are shown with respect to the POWHEG+PYTHIA 8 ('POW-PYT') simulation and the STRIPPER NNLO calculation. The χ^2 values are calculated taking only measurement uncertainties into account and excluding theory uncertainties. For POW+PYT, the χ^2 values including theory uncertainties are indicated with the brackets (w. unc.).

Cross section variables	dof	χ^2	
		POW+PYT (w. unc.)	STRIPPER
$p_{\text{T}}(\text{t})$	6	17 (12)	3
$p_{\text{T}}(\bar{\text{t}})$	6	14 (9)	3
$y(\text{t})$	9	19 (16)	11
$y(\bar{\text{t}})$	9	24 (20)	10
$p_{\text{T}}(\text{t}\bar{\text{t}})$	6	21 (7)	83
$y(\text{t}\bar{\text{t}})$	11	10 (7)	19
$m(\text{t}\bar{\text{t}})$	6	5 (3)	4
$|\Delta\phi(\text{t},\bar{\text{t}})|$	3	1 (0)	1076
$|y(\text{t})| - |y(\bar{\text{t}})|$	7	15 (10)	4
$p_{\text{T}}(\text{t})/m(\text{t}\bar{\text{t}})$	4	30 (20)	8
$p_{\text{T}}(\text{t}\bar{\text{t}})/m(\text{t}\bar{\text{t}})$	8	18 (7)	144
$\log(\xi_1)$	8	14 (9)	10
$\log(\xi_2)$	8	9 (6)	9

Table 10: The χ^2 values and dof of the measured normalized multi-differential cross sections for $t\bar{t}$ and top quark kinematic observables at the parton level are shown with respect to the POWHEG+PYTHIA 8 ('POW-PYT') simulation and various theoretical predictions with beyond-NLO precision. The χ^2 values are calculated taking only measurement uncertainties into account and excluding theory uncertainties. For POW+PYT, the χ^2 values including theory uncertainties are indicated with the brackets (w. unc.).

Cross section	dof	χ^2				
variables		POW+PYT (w. unc.)	aN^{3}LO	MATRIX	STRIPPER	MiNNLOPS
$[\lvert y(\mathrm{t})\rvert, p_{\mathrm{T}}(\mathrm{t})]$	15	40 (31)	36	24	24	23
$[m(\mathrm{t}\bar{\mathrm{t}}), p_{\mathrm{T}}(\mathrm{t})]$	8	83 (35)	—	14	16	15
$[p_{\mathrm{T}}(\mathrm{t}), p_{\mathrm{T}}(\mathrm{t}\bar{\mathrm{t}})]$	15	39 (21)	—	41	54	66
$[m(\mathrm{t}\bar{\mathrm{t}}), \lvert y(\mathrm{t}\bar{\mathrm{t}})\rvert]$	15	64 (42)	—	53	47	51
$[\lvert y(\mathrm{t}\bar{\mathrm{t}})\rvert, p_{\mathrm{T}}(\mathrm{t}\bar{\mathrm{t}})]$	15	28 (15)	—	38	42	66
$[m(\mathrm{t}\bar{\mathrm{t}}), p_{\mathrm{T}}(\mathrm{t}\bar{\mathrm{t}})]$	15	61 (43)	—	94	108	143
$[p_{\mathrm{T}}(\mathrm{t}\bar{\mathrm{t}}), m(\mathrm{t}\bar{\mathrm{t}}), \lvert y(\mathrm{t}\bar{\mathrm{t}})\rvert]$	47	89 (64)	—	—	69	105
$[m(\mathrm{t}\bar{\mathrm{t}}), \lvert y(\mathrm{t})\rvert]$	15	61 (37)	—	35	30	53
$[m(\mathrm{t}\bar{\mathrm{t}}), \lvert \Delta\eta(\mathrm{t},\bar{\mathrm{t}})\rvert]$	11	165 (31)	—	30	31	56
$[m(\mathrm{t}\bar{\mathrm{t}}), \lvert \Delta\phi(\mathrm{t},\bar{\mathrm{t}})\rvert]$	11	74 (47)	—	—	41	94

Table 11: The χ^2 values and dof of the measured normalized multi-differential cross sections for $t\bar{t}$ and top quark kinematic observables at the particle level are shown with respect to the POWHEG+PYTHIA 8 ('POW-PYT') simulation and the STRIPPER NNLO calculation. The χ^2 values are calculated taking only measurement uncertainties into account and excluding theory uncertainties. For POW+PYT, the χ^2 values including theory uncertainties are indicated with the brackets (w. unc.).

Cross section variables	dof	χ^2	
		POW+PYT (w. unc.)	STRIPPER
$[\lvert y(\mathrm{t})\rvert,\ p_{\mathrm{T}}(\mathrm{t})]$	15	35 (25)	16
$[m(t\bar{t}),\ p_{\mathrm{T}}(\mathrm{t})]$	8	86 (36)	18
$[p_{\mathrm{T}}(\mathrm{t}),\ p_{\mathrm{T}}(t\bar{t})]$	15	35 (19)	160
$[m(t\bar{t}),\ \lvert y(t\bar{t})\rvert]$	15	77 (40)	43
$[\lvert y(t\bar{t})\rvert,\ p_{\mathrm{T}}(t\bar{t})]$	15	27 (18)	78
$[m(t\bar{t}),\ p_{\mathrm{T}}(t\bar{t})]$	15	61 (36)	363
$[p_{\mathrm{T}}(t\bar{t}),\ m(t\bar{t}),\ \lvert y(t\bar{t})\rvert]$	47	114 (68)	137
$[m(t\bar{t}),\ \lvert y(\mathrm{t})\rvert]$	15	57 (26)	20
$[m(t\bar{t}),\ \lvert\Delta\eta(\mathrm{t},\bar{\mathrm{t}})\rvert]$	11	155 (30)	37
$[m(t\bar{t}),\ \lvert\Delta\phi(\mathrm{t},\bar{\mathrm{t}})\rvert]$	11	71 (42)	405

Table 12: The χ^2 values and dof of the measured normalized single-differential cross sections for lepton and b-jet kinematic observables at the particle level are shown with respect to the POWHEG+PYTHIA 8 ('POW-PYT') simulation and the STRIPPER NNLO calculation. The χ^2 values are calculated taking only measurement uncertainties into account and excluding theory uncertainties. For POW+PYT, the χ^2 values including theory uncertainties are indicated with the brackets (w. unc.).

Cross section variables	dof	χ^2	
		POW+PYT (w. unc.)	STRIPPER
$p_T(\ell)$	11	28 (18)	16
$p_T(\ell)$ trailing$/p_T(\ell)$ leading	9	15 (11)	5
$p_T(\ell)/p_T(\bar{t})$	4	10 (9)	5
$p_T(b)$ leading	9	5 (4)	7
$p_T(b)$ trailing	6	6 (4)	3
$(p_T(b) + p_T(\bar{b}))/(p_T(t) + p_T(\bar{t}))$	3	19 (15)	8
$m(\ell\bar{\ell})$	11	23 (20)	13
$m(b\bar{b})$	6	15 (12)	76
$m(\ell\bar{\ell}b\bar{b})$	18	33 (18)	15
$p_T(\ell\bar{\ell})$	8	4 (3)	5
$|\eta(\ell\bar{\ell})|$	13	14 (9)	40
$[|\eta(\ell\bar{\ell})|, m(\ell\bar{\ell})]$	23	48 (28)	78
$[|\eta(\ell\bar{\ell})|, p_T(\ell\bar{\ell})]$	19	27 (14)	43
$[p_T(\ell\bar{\ell}), m(\ell\bar{\ell})]$	29	44 (37)	48

9.5 Comparisons to POWHEG+PYTHIA 8 predictions using different PDFs

In this subsection the sensitivity of the measured differential $t\bar{t}$ production cross sections to the PDFs is assessed. The $t\bar{t}$ production at the LHC is known to be particularly sensitive to the gluon density at higher proton momentum fractions x. In the previous CMS analyses [28, 39], systematic investigations were performed in which different sets of $t\bar{t}$ kinematic spectra were included in PDF fits and their impact evaluated. A particularly large sensitivity was observed in Ref. [28] for the $[m(t\bar{t}), |y(t\bar{t})|]$ cross sections measured at $\sqrt{s} = 8\,\text{TeV}$, leading to a strong constraint on the gluon density at x values around 0.3. In the present analysis, the PDF sensitivity is assessed by comparing kinematic spectra of the top quark or the $t\bar{t}$ system with the POWHEG+PYTHIA 8 predictions, evaluated with a number of different PDF sets: NNPDF3.1 [52], CT14 [132], ABMP16 [133], MMHT2014 [134], and HERAPDF2.0 [135]. For the NNPDF3.1 PDFs, both the NNLO (used in the nominal simulation) and NLO variants are studied, while only the NLO versions are taken for all other sets. The PDFs differ in the input data and methodologies that were used to extract them, as discussed elsewhere [136, 137].

Figure 64 shows the measured normalized single-differential cross sections, defined at the parton level, as functions of $p_\text{T}(t)$, $y(t)$, $m(t\bar{t})$, and $y(t\bar{t})$, and compared to the predictions obtained with different PDF sets. Most of the PDFs provide a similar description of the data, except HERAPDF2.0 NLO that describes the $p_\text{T}(t)$ distribution well but exhibits clear shape deviations for the other spectra, leading to large χ^2 values. In Fig. 65, the $\log(\xi_1)$, $\log(\xi_2)$, and $[m(t\bar{t}), |y(t\bar{t})|]$ cross section distributions are shown. As discussed above, in the LO QCD picture the $\log(\xi_1)$ and $\log(\xi_2)$ variables represent the proton momentum fractions carried by the two partons entering the hard interaction. The HERAPDF2.0 NLO prediction undershoots the data near the smallest and largest values of these observables, which may give a hint of a possibly wrong x dependence of the gluon density in this PDF set. For $[m(t\bar{t}), |y(t\bar{t})|]$, all PDFs again provide data descriptions of similar quality, except HERAPDF2.0 NLO, that predicts too few events towards large $m(t\bar{t})$ and $y(t\bar{t})$ values. The particularly large χ^2 for HERAPDF2.0 NLO for this distribution indicates an enhanced PDF sensitivity for this double-differential cross section. Summarizing, the differential spectra of the top quark and the $t\bar{t}$ system show some sensitivity to the PDFs and, therefore, it will be useful to include the corresponding data in future global PDF fits.
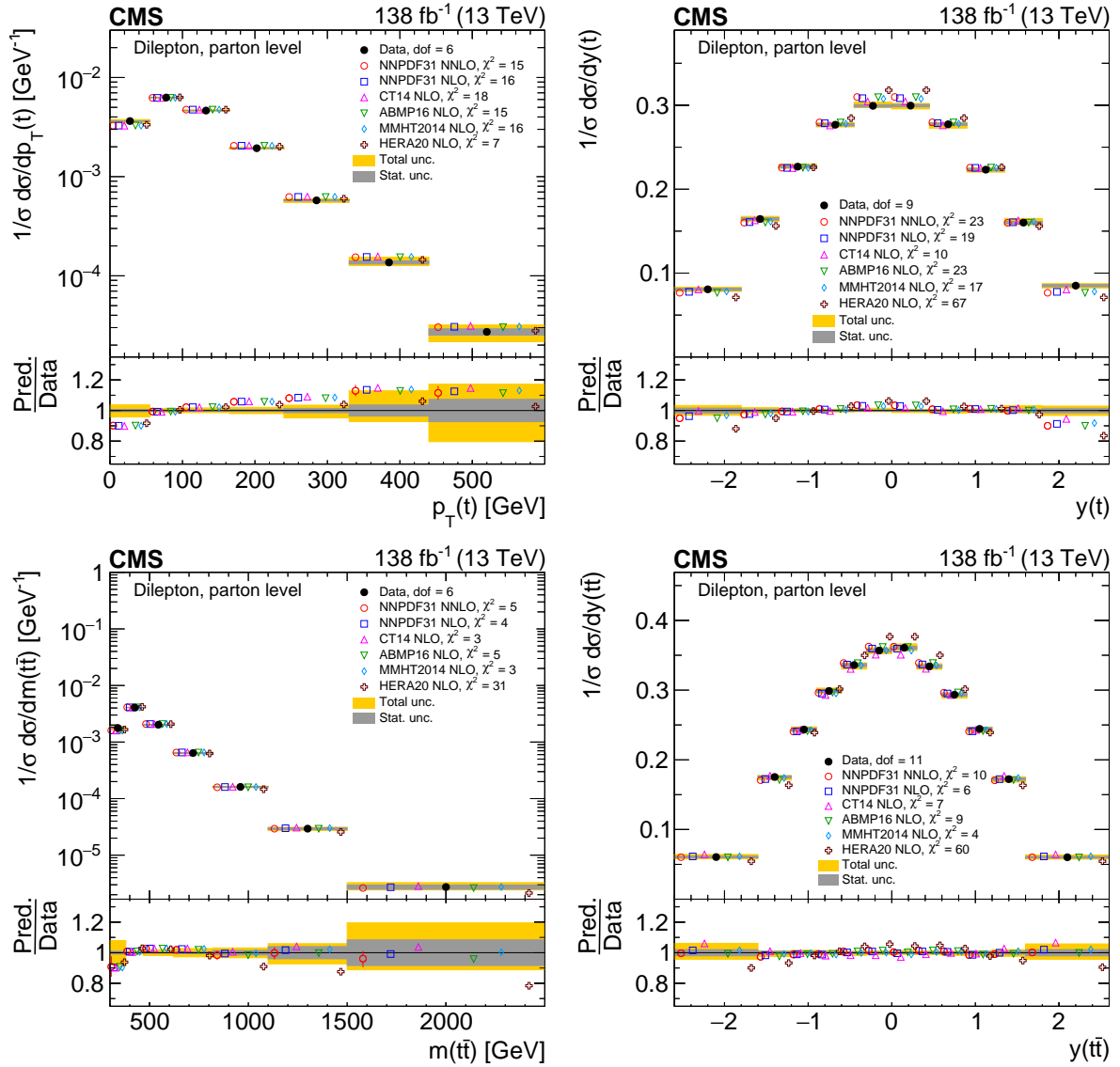
Figure 64: Normalized differential $t\bar{t}$ production cross sections as functions of $p_T(t)$ (upper left), $y(t)$ (upper right), $m(t\bar{t})$ (lower left), and $y(t\bar{t})$ (lower right), measured at the parton level in the full phase space. The data are shown as filled circles with grey and yellow bands indicating the statistical and total uncertainties (statistical and systematic uncertainties added in quadrature), respectively. For each distribution, the number of degrees of freedom (dof) is also provided. The cross sections are compared to predictions from the POWHEG+PYTHIA 8 ('POW-PYT') simulation with various PDF sets. The nominal prediction (open circles) uses the PDF set NNPDF3.1 at NNLO accuracy, assuming a top quark mass value of 172.5 GeV and $\alpha_S = 0.118$. The alternative PDF sets (other points) constitute NNPDF3.1, CT14, ABMP16, MMHT2014, and HERAPDF2.0 at NLO accuracy and assume the same values for the top quark mass and α_S as the nominal NNPDF3.1 NNLO PDF set. The estimated uncertainties in the nominal prediction are represented by vertical bars on the corresponding points. For each PDF set, a value of χ^2 is reported that takes into account the measurement uncertainties. The lower panel in each plot shows the ratios of the predictions to the data.
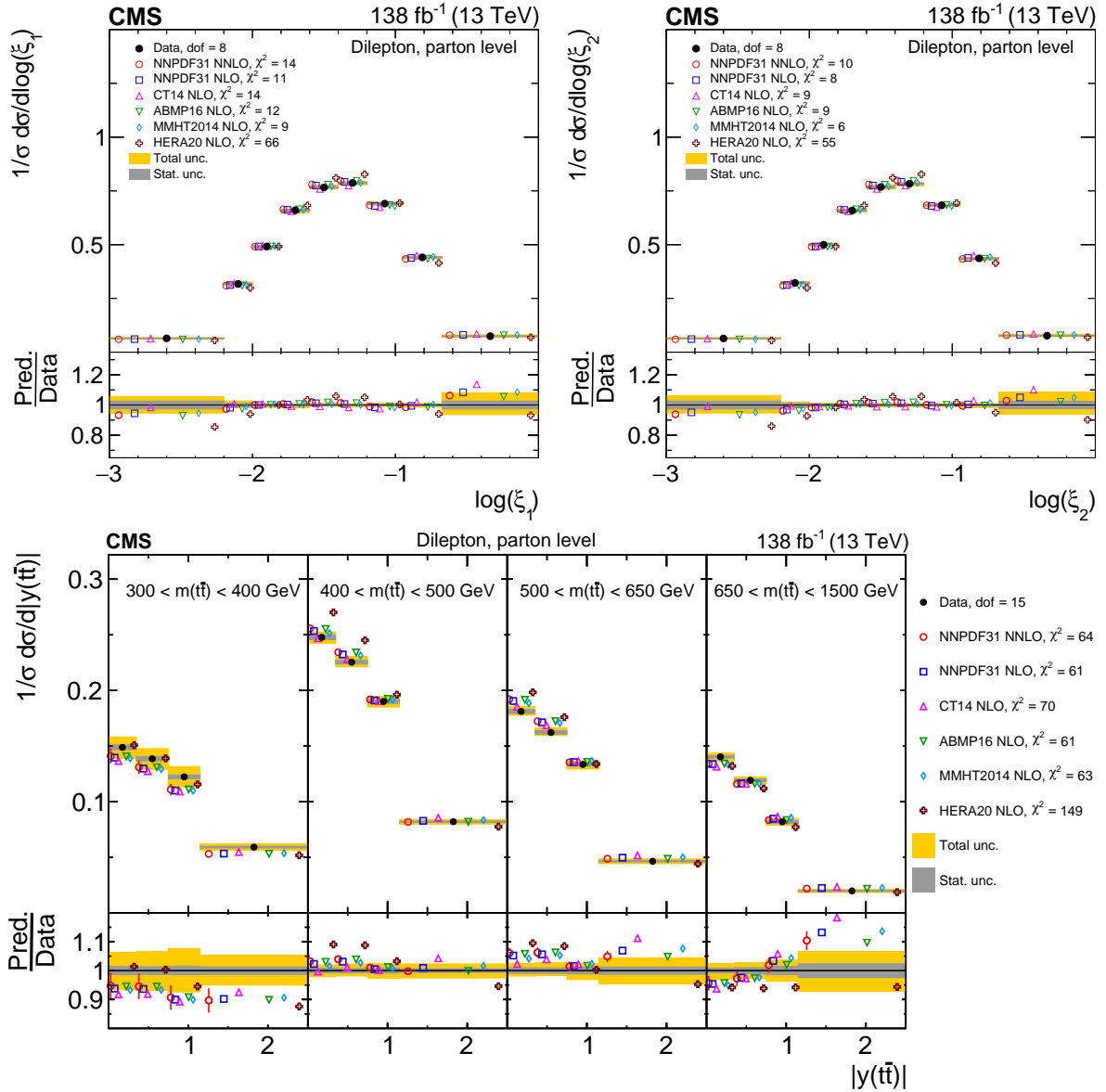
Figure 65: Normalized $\log(\xi_1)$ (upper left), $\log(\xi_2)$ (upper right), and $[m(t\bar{t}), |y(t\bar{t})|]$ (lower) cross sections are shown for data (filled circles) and predictions from the POWHEG+PYTHIA 8 ('POW-PYT') simulation with various PDF sets (other points). Further details can be found in the caption of Fig. 64.

10 Summary

A measurement of differential top quark pair ($t\bar{t}$) production cross sections in proton-proton collisions at $\sqrt{s} = 13\,\text{TeV}$ was presented, performed with events containing two oppositely charged leptons (electrons or muons). The data used in this analysis were recorded in the years 2016 through 2018 with the CMS detector at the LHC and correspond to an integrated luminosity of $138\,\text{fb}^{-1}$. Differential cross sections are measured as functions of kinematical observables of the $t\bar{t}$ system, the top quark and antiquark and their decay products, and the total number of additional jets in the event not originating from the $t\bar{t}$ decay. The measurements are performed as functions of single observables, or simultaneously as functions of two or three kinematic variables. The differential cross sections are defined both with particle-level objects in a fiducial phase space close to that of the detector acceptance and with parton-level top quarks in the full phase space. Overall, both the statistical and the systematic uncertainties in the measurements are improved by a factor of about two compared to the previous analyses [38, 39] which are based on the 2016 data set.

Predictions of several next-to-leading-order (NLO) Monte Carlo (MC) event generators that differ in the hard matrix element, parton shower, and hadronization models were compared to the data. The predictions of these MC models, without taking theoretical uncertainties into account, generally fail to describe many of the measured cross sections in their full kinematic range. The predicted transverse momentum p_T distributions of the top quark and antiquark are harder than observed in the data, and the rapidity distributions are more central. The invariant mass and rapidity distributions of the $t\bar{t}$ system are reasonably well described by the models overall. The predictions for the $t\bar{t}$ transverse momentum distribution differ from the data even more than the top quark and antiquark distributions do; none of them provides a good description of the data. Double- and triple-differential cross sections show large model-to-data discrepancies, for instance the effect of a harder top quark p_T spectrum $p_\text{T}(\text{t})$ in the models is pronounced at high $m(t\bar{t})$. Differential cross sections as functions of kinematic observables of the leptons and b jets originating from the decay of the top quark and antiquark are measured with high precision. Overall, the observed trends for these objects follow those for the top quarks and antiquarks, with the models predicting harder p_T spectra than seen in the data. For the leptons, this effect is somewhat enhanced and furthermore the dilepton invariant mass spectrum is harder in the models than in the data. The distribution of the multiplicity of additional jets in $t\bar{t}$ events shows varying level of agreement between data and the models. When considered as a function of jet multiplicity, the evolution of the shapes of $t\bar{t}$, top quark and antiquark kinematic distributions is different for the models and for data. There is an indication that the trend of harder $p_\text{T}(\text{t})$ distributions in the models is localized at small jet multiplicities.

Selected kinematic distributions were also compared to a variety of theoretical predictions beyond NLO precision. For observables of the top quark and the $t\bar{t}$ system, these predictions provide descriptions of the data that are of similar or improved quality, compared to the MC model best describing each variable, except for some of the kinematic spectra that are directly sensitive to higher-order QCD effects. For observables associated with the leptons and b jets, the quality of the tested next-to-NLO model is on average comparable to but not better than that of the NLO MC models. Comparing several kinematic distributions of the top quark and the $t\bar{t}$ system to NLO MC models using various parton distribution function (PDF) sets, clear differences are observed which indicate a sensitivity to PDFs that could be exploited in future PDF fits.

For each distribution, the quality of the description of the data by the models has been assessed with a χ^2 test statistic. When only the measurement uncertainties are taken into account

in the calculation (i.e. neglecting the uncertainties on the predictions), the p-values obtained from the χ^2 tests are in general close to zero, pointing to a poor description of the data by the nominal models. For the POWHEG+PYTHIA 8 model, additional χ^2 values have been evaluated including the uncertainties on the prediction. This inclusion often leads to substantially reduced χ^2 values with reasonable p-values. However, for several distributions, and in particular for a larger fraction of the multi-differential distributions, the observed differences between data and simulation still remain significant, providing important input for future theoretical predictions.

Acknowledgments

References

[1] Particle Data Group Collaboration, "Review of Particle Physics", *PTEP* **2022** (2022) 083C01, `doi:10.1093/ptep/ptac097`.

[2] D. Atwood, A. Kagan, and T. G. Rizzo, "Constraining anomalous top quark couplings at the Tevatron", *Phys. Rev. D* **52** (1995) 6264, `doi:10.1103/PhysRevD.52.6264`, `arXiv:hep-ph/9407408`.

[3] P. Langacker, "The physics of heavy Z' gauge bosons", *Rev. Mod. Phys.* **81** (2009) 1199, `doi:10.1103/RevModPhys.81.1199`, `arXiv:0801.1345`.

[4] C. Englert, A. Freitas, M. Spira, and P. M. Zerwas, "Constraining the intrinsic structure of top-quarks", *Phys. Lett. B* **721** (2013) 261, `doi:10.1016/j.physletb.2013.03.017`, `arXiv:1210.2570`.

[5] ATLAS Collaboration, "Measurement of spin correlation in top-antitop quark events and search for top squark pair production in pp collisions at $\sqrt{s} = 8$ TeV using the ATLAS detector", *Phys. Rev. Lett.* **114** (2015) 142001, `doi:10.1103/PhysRevLett.114.142001`, `arXiv:1412.4742`.

[6] A. Albert et al., "Towards the next generation of simplified Dark Matter models", *Phys. Dark Univ.* **16** (2017) 49, `doi:10.1016/j.dark.2017.02.002`, `arXiv:1607.06680`.

[7] CMS Collaboration, "Search for dark matter particles produced in association with a top quark pair at $\sqrt{s} = 13$ TeV", *Phys. Rev. Lett.* **122** (2019) 011803, `doi:10.1103/PhysRevLett.122.011803`, `arXiv:1807.06522`.

[8] CMS Collaboration, "Search for heavy Higgs bosons decaying to a top quark pair in proton-proton collisions at $\sqrt{s} = 13$ TeV", *JHEP* **04** (2020) 171, `doi:10.1007/JHEP04(2020)171`, `arXiv:1908.01115`. [Erratum: JHEP 03, 187 (2022)].

[9] T. Biekötter et al., "Possible indications for new Higgs bosons in the reach of the LHC: N2HDM and NMSSM interpretations", *Eur. Phys. J. C* **82** (2022) 178, `doi:10.1140/epjc/s10052-022-10099-1`, `arXiv:2109.01128`.

[10] A. Anuar et al., "ALP-ine quests at the LHC: hunting axion-like particles via peaks and dips in $t\bar{t}$ production", 4, 2024. `arXiv:2404.19014`.

[11] N. Kidonakis, "NNNLO soft-gluon corrections for the top-quark p_T and rapidity distributions", *Phys. Rev. D* **91** (2015) 031501, `doi:10.1103/PhysRevD.91.031501`, `arXiv:1411.2633`.

[12] N. Kidonakis, "Top-quark double-differential distributions at approximate N^{3}LO", *Phys. Rev. D* **101** (2020) 074006, `doi:10.1103/PhysRevD.101.074006`, `arXiv:1912.10362`.

[13] M. Czakon, D. Heymes, and A. Mitov, "High-precision differential predictions for top-quark pairs at the LHC", *Phys. Rev. Lett.* **116** (2016) 082003, `doi:10.1103/PhysRevLett.116.082003`, `arXiv:1511.00549`.

[14] M. Czakon et al., "Top-pair production at the LHC through NNLO QCD and NLO EW", *JHEP* **10** (2017) 186, `doi:10.1007/JHEP10(2017)186`, `arXiv:1705.04105`.

[15] M. Czakon et al., "Resummation for (boosted) top-quark pair production at NNLO+NNLL' in QCD", *JHEP* **05** (2018) 149, `doi:10.1007/JHEP05(2018)149`, `arXiv:1803.07623`.

[16] S. Catani et al., "Top-quark pair production at the LHC: Fully differential QCD predictions at NNLO", *JHEP* **07** (2019) 100, `doi:10.1007/JHEP07(2019)100`, `arXiv:1906.06535`.

[17] M. Czakon, A. Mitov, and R. Poncelet, "NNLO QCD corrections to leptonic observables in top-quark pair production and decay", *JHEP* **05** (2021) 212, `doi:10.1007/JHEP05(2021)212`, `arXiv:2008.11133`.

[18] ATLAS Collaboration, "Measurements of top quark pair relative differential cross sections with ATLAS in pp collisions at $\sqrt{s} = 7\,\text{TeV}$", *Eur. Phys. J. C* **73** (2013) 2261, `doi:10.1140/epjc/s10052-012-2261-1`, `arXiv:1207.5644`.

[19] CMS Collaboration, "Measurement of differential top-quark pair production cross sections in pp collisions at $\sqrt{s} = 7\,\text{TeV}$", *Eur. Phys. J. C* **73** (2013) 2339, `doi:10.1140/epjc/s10052-013-2339-4`, `arXiv:1211.2220`.

[20] ATLAS Collaboration, "Measurements of normalized differential cross sections for $t\bar{t}$ production in pp collisions at $\sqrt{s} = 7\,\text{TeV}$ using the ATLAS detector", *Phys. Rev. D* **90** (2014) 072004, `doi:10.1103/PhysRevD.90.072004`, `arXiv:1407.0371`.

[21] ATLAS Collaboration, "Differential top-antitop cross section measurements as a function of observables constructed from final-state particles using pp collisions at $\sqrt{s} = 7\,\text{TeV}$ in the ATLAS detector", *JHEP* **06** (2015) 100, `doi:10.1007/JHEP06(2015)100`, `arXiv:1502.05923`.

[22] ATLAS Collaboration, "Measurement of top quark pair differential cross sections in the dilepton channel in pp collisions at $\sqrt{s} = 7$ and $8\,\text{TeV}$ with ATLAS", *Phys. Rev. D* **94** (2016) 092003, `doi:10.1103/PhysRevD.94.092003`, `arXiv:1607.07281`.

[23] CMS Collaboration, "Measurement of the differential cross section for top quark pair production in pp collisions at $\sqrt{s} = 8\,\text{TeV}$", *Eur. Phys. J. C* **75** (2015) 542, `doi:10.1140/epjc/s10052-015-3709-x`, `arXiv:1505.04480`.

[24] ATLAS Collaboration, "Measurements of top-quark pair differential cross sections in the lepton+jets channel in pp collisions at $\sqrt{s} = 8$ TeV using the ATLAS detector", *Eur. Phys. J. C* **76** (2016) 538, `doi:10.1140/epjc/s10052-016-4366-4`, `arXiv:1511.04716`.

[25] ATLAS Collaboration, "Measurement of the differential cross section of highly boosted top quarks as a function of their transverse momentum in $\sqrt{s} = 8$ TeV proton-proton collisions using the ATLAS detector", *Phys. Rev. D* **93** (2016) 032009, `doi:10.1103/PhysRevD.93.032009`, `arXiv:1510.03818`.

[26] CMS Collaboration, "Measurement of the $t\bar{t}$ production cross section in the all-jets final state in pp collisions at $\sqrt{s} = 8$ TeV", *Eur. Phys. J. C* **76** (2016) 128, `doi:10.1140/epjc/s10052-016-3956-5`, `arXiv:1509.06076`.

[27] CMS Collaboration, "Measurement of the integrated and differential $t\bar{t}$ production cross sections for high-p_T top quarks in pp collisions at $\sqrt{s} = 8$ TeV", *Phys. Rev. D* **94** (2016) 072002, `doi:10.1103/PhysRevD.94.072002`, `arXiv:1605.00116`.

[28] CMS Collaboration, "Measurement of double-differential cross sections for top quark pair production in pp collisions at $\sqrt{s} = 8$ TeV and impact on parton distribution functions", *Eur. Phys. J. C* **77** (2017) 459, `doi:10.1140/epjc/s10052-017-4984-5`, `arXiv:1703.01630`.

[29] ATLAS Collaboration, "Measurement of the top-quark mass in $t\bar{t} + 1$-jet events collected with the ATLAS detector in pp collisions at $\sqrt{s} = 8$ TeV", *JHEP* **11** (2019) 150, `doi:10.1007/JHEP11(2019)150`, `arXiv:1905.02302`.

[30] CMS Collaboration, "Measurement of differential cross sections for top quark pair production using the lepton+jets final state in proton-proton collisions at 13 TeV", *Phys. Rev. D* **95** (2017) 092001, `doi:10.1103/PhysRevD.95.092001`, `arXiv:1610.04191`.

[31] ATLAS Collaboration, "Measurement of jet activity produced in top-quark events with an electron, a muon and two b-tagged jets in the final state in pp collisions at $\sqrt{s} = 13$ TeV with the ATLAS detector", *Eur. Phys. J. C* **77** (2017) 220, `doi:10.1140/epjc/s10052-017-4766-0`, `arXiv:1610.09978`.

[32] ATLAS Collaboration, "Measurements of top-quark pair differential cross sections in the eμ channel in pp collisions at $\sqrt{s} = 13$ TeV using the ATLAS detector", *Eur. Phys. J. C* **77** (2017) 292, `doi:10.1140/epjc/s10052-017-4821-x`, `arXiv:1612.05220`.

[33] ATLAS Collaboration, "Measurements of top-quark pair differential cross sections in the lepton+jets channel in pp collisions at $\sqrt{s} = 13$ TeV using the ATLAS detector", *JHEP* **11** (2017) 191, `doi:10.1007/JHEP11(2017)191`, `arXiv:1708.00727`.

[34] CMS Collaboration, "Measurement of normalized differential $t\bar{t}$ cross sections in the dilepton channel from pp collisions at $\sqrt{s} = 13$ TeV", *JHEP* **04** (2018) 060, `doi:10.1007/JHEP04(2018)060`, `arXiv:1708.07638`.

[35] ATLAS Collaboration, "Measurements of $t\bar{t}$ differential cross-sections of highly boosted top quarks decaying to all-hadronic final states in pp collisions at $\sqrt{s} = 13$ TeV using the ATLAS detector", *Phys. Rev. D* **98** (2018) 012003, `doi:10.1103/PhysRevD.98.012003`, `arXiv:1801.02052`.

[36] ATLAS Collaboration, "Measurements of differential cross sections of top quark pair production in association with jets in pp collisions at $\sqrt{s} = 13$ TeV using the ATLAS detector", *JHEP* **10** (2018) 159, `doi:10.1007/JHEP10(2018)159`, `arXiv:1802.06572`.

[37] CMS Collaboration, "Measurement of differential cross sections for the production of top quark pairs and of additional jets in lepton+jets events from pp collisions at $\sqrt{s} = 13$ TeV", *Phys. Rev. D* **97** (2018) 112003, `doi:10.1103/PhysRevD.97.112003`, `arXiv:1803.08856`.

[38] CMS Collaboration, "Measurements of $t\bar{t}$ differential cross sections in proton-proton collisions at $\sqrt{s} = 13$ TeV using events containing two leptons", *JHEP* **02** (2019) 149, `doi:10.1007/JHEP02(2019)149`, `arXiv:1811.06625`.

[39] CMS Collaboration, "Measurement of $t\bar{t}$ normalised multi-differential cross sections in pp collisions at $\sqrt{s} = 13$ TeV, and simultaneous determination of the strong coupling strength, top quark pole mass, and parton distribution functions", *Eur. Phys. J. C* **80** (2020) 658, `doi:10.1140/epjc/s10052-020-7917-7`, `arXiv:1904.05237`.

[40] ATLAS Collaboration, "Measurements of top-quark pair differential and double-differential cross sections in the ℓ+jets channel with pp collisions at $\sqrt{s} = 13$ TeV using the ATLAS detector", *Eur. Phys. J. C* **79** (2019) 1028, `doi:10.1140/epjc/s10052-019-7525-6`, `arXiv:1908.07305`. [Erratum: `doi:10.1140/epjc/s10052-020-08541-3`].

[41] ATLAS Collaboration, "Measurement of the $t\bar{t}$ production cross section and lepton differential distributions in eμ dilepton events from pp collisions at $\sqrt{s} = 13$ TeV with the ATLAS detector", *Eur. Phys. J. C* **80** (2020) 528, `doi:10.1140/epjc/s10052-020-7907-9`, `arXiv:1910.08819`.

[42] ATLAS Collaboration, "Measurements of top-quark pair single- and double-differential cross sections in the all-hadronic channel in pp collisions at $\sqrt{s} = 13$ TeV using the ATLAS detector", *JHEP* **01** (2021) 033, `doi:10.1007/JHEP01(2021)033`, `arXiv:2006.09274`.

[43] CMS Collaboration, "Measurement of differential $t\bar{t}$ production cross sections using top quarks at large transverse momenta in pp collisions at $\sqrt{s} = 13$ TeV", *Phys. Rev. D* **103** (2021) 052008, `doi:10.1103/PhysRevD.103.052008`, `arXiv:2008.07860`.

[44] CMS Collaboration, "Measurement of differential $t\bar{t}$ production cross sections in the full kinematic range using lepton+jets events from proton-proton collisions at $\sqrt{s} = 13$ TeV", *Phys. Rev. D* **104** (2021) 092013, `doi:10.1103/PhysRevD.104.092013`, `arXiv:2108.02803`.

[45] ATLAS Collaboration, "Measurements of differential cross sections in top-quark pair events with a high transverse momentum top quark and limits on beyond the standard model contributions to top-quark pair production with the atlas detector at $\sqrt{s} = 13$ TeV", *JHEP* **06** (2022) 063, `doi:10.1007/JHEP06(2022)063`, `arXiv:2202.12134`.

[46] ATLAS Collaboration, "Differential $t\bar{t}$ cross-section measurements using boosted top quarks in the all-hadronic final state with 139 fb^{-1} of ATLAS data", *JHEP* **04** (2023) 080, `doi:10.1007/JHEP04(2023)080`, `arXiv:2205.02817`.

[47] ATLAS Collaboration, "Inclusive and differential cross sections for dilepton $t\bar{t}$ production measured in $\sqrt{s} = 13$ TeV pp collisions with the ATLAS detector", *JHEP* **07** (2023) 141, `doi:10.1007/JHEP07(2023)141`, `arXiv:2303.15340`.

[48] "HEPData record for this analysis", 2023. `doi:10.17182/hepdata.127702`.

[49] CMS Collaboration, "The CMS trigger system", *JINST* **12** (2017) P01020, `doi:10.1088/1748-0221/12/01/P01020`, `arXiv:1609.02366`.

[50] CMS Collaboration, "The CMS experiment at the CERN LHC", *JINST* **3** (2008) S08004, `doi:10.1088/1748-0221/3/08/S08004`.

[51] NNPDF Collaboration, "Unbiased global determination of parton distributions and their uncertainties at NNLO and LO", *Nucl. Phys. B* **855** (2012) 153, `doi:10.1016/j.nuclphysb.2011.09.024`, `arXiv:1107.2652`.

[52] NNPDF Collaboration, "Parton distributions from high-precision collider data", *Eur. Phys. J. C* **77** (2017) 663, `doi:10.1140/epjc/s10052-017-5199-5`, `arXiv:1706.00428`.

[53] P. Nason, "A new method for combining NLO QCD with shower Monte Carlo algorithms", *JHEP* **11** (2004) 040, `doi:10.1088/1126-6708/2004/11/040`, `arXiv:hep-ph/0409146`.

[54] S. Frixione, P. Nason, and C. Oleari, "Matching NLO QCD computations with parton shower simulations: the POWHEG method", *JHEP* **11** (2007) 070, `doi:10.1088/1126-6708/2007/11/070`, `arXiv:0709.2092`.

[55] S. Alioli, P. Nason, C. Oleari, and E. Re, "A general framework for implementing NLO calculations in shower Monte Carlo programs: the POWHEG BOX", *JHEP* **06** (2010) 043, `doi:10.1007/JHEP06(2010)043`, `arXiv:1002.2581`.

[56] S. Frixione, P. Nason, and G. Ridolfi, "A positive-weight next-to-leading-order Monte Carlo for heavy flavour hadroproduction", *JHEP* **09** (2007) 126, `doi:10.1088/1126-6708/2007/09/126`, `arXiv:0707.3088`.

[57] CMS Collaboration, "Extraction and validation of a new set of CMS PYTHIA8 tunes from underlying-event measurements", *Eur. Phys. J. C* **80** (2020) 4, `doi:10.1140/epjc/s10052-019-7499-4`, `arXiv:1903.12179`.

[58] T. Sjöstrand et al., "An introduction to PYTHIA 8.2", *Comput. Phys. Commun.* **191** (2015) 159, `doi:10.1016/j.cpc.2015.01.024`, `arXiv:1410.3012`.

[59] J. Alwall et al., "The automated computation of tree-level and next-to-leading order differential cross sections, and their matching to parton shower simulations", *JHEP* **07** (2014) 079, `doi:10.1007/JHEP07(2014)079`, `arXiv:1405.0301`.

[60] R. Frederix and S. Frixione, "Merging meets matching in MC@NLO", *JHEP* **12** (2012) 061, `doi:10.1007/JHEP12(2012)061`, `arXiv:1209.6215`.

[61] CMS Collaboration, "Investigations of the impact of the parton shower tuning in PYTHIA in the modelling of $t\bar{t}$ at $\sqrt{s} = 8$ and 13 TeV", CMS Physics Analysis Summary CMS-PAS-TOP-16-021, 2016.

[62] P. Artoisenet, R. Frederix, O. Mattelaer, and R. Rietkerk, "Automatic spin-entangled decays of heavy resonances in Monte Carlo simulations", *JHEP* **03** (2013) 015, `doi:10.1007/JHEP03(2013)015`, `arXiv:1212.3460`.

[63] J. Bellm et al., "HERWIG 7.0/HERWIG++ 3.0 release note", *Eur. Phys. J. C* **76** (2016) 196, `doi:10.1140/epjc/s10052-016-4018-8`, `arXiv:1512.01178`.

[64] CMS Collaboration, "Development and validation of HERWIG 7 tunes from CMS underlying-event measurements", *Eur. Phys. J. C* **81** (2021) 312, `doi:10.1140/epjc/s10052-021-08949-5`, `arXiv:2011.03422`.

[65] S. Alioli, P. Nason, C. Oleari, and E. Re, "NLO single-top production matched with shower in POWHEG: *s*- and *t*-channel contributions", *JHEP* **09** (2009) 111, `doi:10.1088/1126-6708/2009/09/111`, `arXiv:0907.4076`. [Erratum: `doi:10.1007/JHEP02(2010)011`].

[66] R. Frederix, E. Re, and P. Torrielli, "Single-top *t*-channel hadroproduction in the four-flavour scheme with POWHEG and aMC@NLO", *JHEP* **09** (2012) 130, `doi:10.1007/JHEP09(2012)130`, `arXiv:1207.5391`.

[67] E. Re, "Single-top Wt-channel production matched with parton showers using the POWHEG method", *Eur. Phys. J. C* **71** (2011) 1547, `doi:10.1140/epjc/s10052-011-1547-z`, `arXiv:1009.2450`.

[68] CMS Collaboration, "Event generator tunes obtained from underlying event and multiparton scattering measurements", *Eur. Phys. J. C* **76** (2016) 155, `doi:10.1140/epjc/s10052-016-3988-x`, `arXiv:1512.00815`.

[69] P. Skands, S. Carrazza, and J. Rojo, "Tuning PYTHIA 8.1: the Monash 2013 Tune", *Eur. Phys. J. C* **74** (2014) 3024, `doi:10.1140/epjc/s10052-014-3024-y`, `arXiv:1404.5630`.

[70] NNPDF Collaboration, "Parton distributions for the LHC Run II", *JHEP* **04** (2015) 040, `doi:10.1007/JHEP04(2015)040`, `arXiv:1410.8849`.

[71] M. L. Mangano, M. Moretti, F. Piccinini, and M. Treccani, "Matching matrix elements and shower evolution for top-quark production in hadronic collisions", *JHEP* **01** (2007) 013, `doi:10.1088/1126-6708/2007/01/013`, `arXiv:hep-ex/0611129`.

[72] S. Mrenna and P. Richardson, "Matching matrix elements and parton showers with HERWIG and PYTHIA", *JHEP* **05** (2004) 040, `doi:10.1088/1126-6708/2004/05/040`, `arXiv:hep-ph/0312274`.

[73] P. Kant et al., "HatHor for single top-quark production: Updated predictions and uncertainty estimates for single top-quark production in hadronic collisions", *Comput. Phys. Commun.* **191** (2015) 74, `doi:10.1016/j.cpc.2015.02.001`, `arXiv:1406.4403`.

[74] N. Kidonakis, "Two-loop soft anomalous dimensions for single top quark associated production with W^- or H^-", *Phys. Rev. D* **82** (2010) 054018, `doi:10.1103/PhysRevD.82.054018`, `arXiv:hep-ph/1005.4451`.

[75] Y. Li and F. Petriello, "Combining QCD and electroweak corrections to dilepton production in FEWZ", *Phys. Rev. D* **86** (2012) 094034, `doi:10.1103/PhysRevD.86.094034`, `arXiv:1208.5967`.

[76] J. M. Campbell, R. K. Ellis, and C. Williams, "Vector boson pair production at the LHC", *JHEP* **07** (2011) 018, `doi:10.1007/JHEP07(2011)018`, `arXiv:1105.0020`.

[77] M. Czakon and A. Mitov, "TOP++: a program for the calculation of the top-pair cross section at hadron colliders", *Comput. Phys. Commun.* **185** (2014) 2930, `doi:10.1016/j.cpc.2014.06.021`, `arXiv:1112.5675`.

[78] M. Cacciari et al., "Top-pair production at hadron colliders with next-to-next-to-leading logarithmic soft-gluon resummation", *Phys. Lett. B* **710** (2012) 612, `doi:10.1016/j.physletb.2012.03.013`, `arXiv:1111.5869`.

[79] P. Bärnreuther, M. Czakon, and A. Mitov, "Percent level precision physics at the Tevatron: first genuine NNLO QCD corrections to $q\overline{q} \to t\overline{t} + X$", *Phys. Rev. Lett.* **109** (2012) 132001, `doi:10.1103/PhysRevLett.109.132001`, `arXiv:1204.5201`.

[80] M. Czakon and A. Mitov, "NNLO corrections to top-pair production at hadron colliders: the all-fermionic scattering channels", *JHEP* **12** (2012) 054, `doi:10.1007/JHEP12(2012)054`, `arXiv:1207.0236`.

[81] M. Czakon and A. Mitov, "NNLO corrections to top-pair production at hadron colliders: the quark-gluon reaction", *JHEP* **01** (2013) 080, `doi:10.1007/JHEP01(2013)080`, `arXiv:1210.6832`.

[82] M. Beneke, P. Falgari, S. Klein, and C. Schwinn, "Hadronic top-quark pair production with NNLL threshold resummation", *Nucl. Phys. B* **855** (2012) 695, `doi:10.1016/j.nuclphysb.2011.10.021`, `arXiv:1109.1536`.

[83] M. Czakon, P. Fiedler, and A. Mitov, "Total top-quark pair-production cross section at hadron colliders through $\mathcal{O}(\alpha_s^4)$", *Phys. Rev. Lett.* **110** (2013) 252004, `doi:10.1103/PhysRevLett.110.252004`, `arXiv:1303.6254`.

[84] GEANT4 Collaboration, "GEANT4—a simulation toolkit", *Nucl. Instrum. Meth. A* **506** (2003) 250, `doi:10.1016/S0168-9002(03)01368-8`.

[85] ATLAS Collaboration, "Measurement of the inelastic proton-proton cross section at $\sqrt{s} = 13$ TeV with the ATLAS detector at the LHC", *Phys. Rev. Lett.* **117** (2016) 182002, `doi:10.1103/PhysRevLett.117.182002`, `arXiv:1606.02625`.

[86] CMS Collaboration, "Particle-flow reconstruction and global event description with the CMS detector", *JINST* **12** (2017) P10003, `doi:10.1088/1748-0221/12/10/P10003`, `arXiv:1706.04965`.

[87] CMS Collaboration, "Technical proposal for the Phase-II upgrade of the Compact Muon Solenoid", CMS Technical Proposal CERN-LHCC-2015-010, CMS-TDR-15-02, 2015.

[88] CMS Collaboration, "Electron and photon reconstruction and identification with the CMS experiment at the CERN LHC", *JINST* **16** (2021) P05014, `doi:10.1088/1748-0221/16/05/P05014`, `arXiv:2012.06888`.

[89] CMS Collaboration, "Performance of the CMS muon detector and muon reconstruction with proton-proton collisions at $\sqrt{s} = 13$ TeV", *JINST* **13** (2018) P06015, `doi:10.1088/1748-0221/13/06/P06015`, `arXiv:1804.04528`.

[90] M. Cacciari, G. P. Salam, and G. Soyez, "The anti-k_T jet clustering algorithm", *JHEP* **04** (2008) 063, `doi:10.1088/1126-6708/2008/04/063`, `arXiv:0802.1189`.

[91] M. Cacciari, G. P. Salam, and G. Soyez, "FastJet user manual", *Eur. Phys. J. C* **72** (2012) 1896, `doi:10.1140/epjc/s10052-012-1896-2`, `arXiv:1111.6097`.

[92] CMS Collaboration, "Jet energy scale and resolution in the CMS experiment in pp collisions at 8 TeV", *JINST* **12** (2017) P02014, `doi:10.1088/1748-0221/12/02/P02014`, `arXiv:1607.03663`.

[93] CMS Collaboration, "Identification of heavy-flavour jets with the CMS detector in pp collisions at 13 TeV", *JINST* **13** (2018) P05011, `doi:10.1088/1748-0221/13/05/P05011`, `arXiv:1712.07158`.

[94] CMS Collaboration, "A Deep Neural Network for simultaneous estimation of b jet energy and resolution", *Comput. Softw. Big Sci.* **4** (2020) 10, `doi:10.1007/s41781-020-00041-z`, `arXiv:1912.06046`.

[95] CMS Collaboration, "Performance of missing transverse momentum reconstruction in proton-proton collisions at $\sqrt{s} = 13$ TeV using the CMS detector", *JINST* **14** (2019) P07004, `doi:10.1088/1748-0221/14/07/P07004`, `arXiv:1903.06078`.

[96] D. Bertolini, P. Harris, M. Low, and N. Tran, "Pileup per particle identification", *JHEP* **10** (2014) 59, `doi:10.1007/JHEP10(2014)059`, `arXiv:1407.6013`.

[97] I. Korol, "Measurement of Double Differential $t\bar{t}$ Production Cross Sections with the CMS Detector". PhD thesis, Universität Hamburg, 2016. `doi:10.3204/DESY-THESIS-2016-011`.

[98] R. J. Barlow and C. Beeston, "Fitting using finite Monte Carlo samples", *Comput. Phys. Commun.* **77** (1993) 219, `doi:10.1016/0010-4655(93)90005-W`.

[99] R. Brun and F. Rademakers, "ROOT: An object oriented data analysis framework", *Nucl. Instrum. Meth. A* **389** (1997) 81, `doi:10.1016/S0168-9002(97)00048-X`.

[100] S. Schmitt, "TUnfold: an algorithm for correcting migration effects in high energy physics", *JINST* **7** (2012) T10003, `doi:10.1088/1748-0221/7/10/T10003`, `arXiv:1205.6201`.

[101] A. N. Tikhonov, "Solution of incorrectly formulated problems and the regularization method", *Sov. Math. Dokl.* **4** (1963) 1035.

[102] S. Schmitt, "Data unfolding methods in high energy physics", *Eur. Phys. J. Web Conf.* **137** (2017) 11008, `doi:10.1051/epjconf/201713711008`, `arXiv:1611.01927`.

[103] CMS Collaboration, "Object definitions for top quark analyses at the particle level", CMS Note CERN-CMS-NOTE-2017-004, 2017.

[104] M. Cacciari, G. P. Salam, and G. Soyez, "The catchment area of jets", *JHEP* **04** (2008) 005, `doi:10.1088/1126-6708/2008/04/005`, `arXiv:0802.1188`.

[105] CMS Collaboration, "Precision luminosity measurement in proton-proton collisions at $\sqrt{s} = 13$ TeV in 2015 and 2016 at CMS", *Eur. Phys. J. C* **81** (2021) 800, `doi:10.1140/epjc/s10052-021-09538-2`, `arXiv:2104.01927`.

[106] CMS Collaboration, "CMS Luminosity measurement for the 2017 data-taking period at $\sqrt{s} = 13$ TeV", CMS Physics Analysis Summary CMS-PAS-LUM-17-004, 2018.

[107] CMS Collaboration, "CMS Luminosity measurement for the 2018 data-taking period at $\sqrt{s} = 13\,\text{TeV}$", CMS Physics Analysis Summary CMS-PAS-LUM-18-002, 2019.

[108] CMS Collaboration, "Measurement of the Drell-Yan cross section in pp collisions at $\sqrt{s} = 7\,\text{TeV}$", *JHEP* **10** (2011) 007, `doi:10.1007/JHEP10(2011)007`, `arXiv:1108.0566`.

[109] CMS Collaboration, "Measurement of the top quark pair production cross section in proton-proton collisions at $\sqrt{s} = 13\,\text{TeV}$", *Phys. Rev. Lett.* **116** (2016) 052002, `doi:10.1103/PhysRevLett.116.052002`, `arXiv:1510.05302`.

[110] CMS Collaboration, "Measurement of the Higgs boson production rate in association with top quarks in final states with electrons, muons, and hadronically decaying tau leptons at $\sqrt{s} = 13\,\text{TeV}$", *Eur. Phys. J. C* **81** (2021) 378, `doi:10.1140/epjc/s10052-021-09014-x`, `arXiv:2011.03652`.

[111] S. Argyropoulos and T. Sjöstrand, "Effects of color reconnection on $t\bar{t}$ final states at the LHC", *JHEP* **11** (2014) 043, `doi:10.1007/JHEP11(2014)043`, `arXiv:1407.6653`.

[112] J. R. Christiansen and P. Z. Skands, "String formation beyond leading colour", *JHEP* **08** (2015) 003, `doi:10.1007/JHEP08(2015)003`, `arXiv:1505.01681`.

[113] M. Bähr et al., "HERWIG++ physics and manual", *Eur. Phys. J. C* **58** (2008) 639, `doi:10.1140/epjc/s10052-008-0798-9`, `arXiv:0803.0883`.

[114] CMS Collaboration, "Running of the top quark mass from proton-proton collisions at $\sqrt{s} = 13\text{TeV}$", *Phys. Lett. B* **803** (2020) 135263, `doi:10.1016/j.physletb.2020.135263`, `arXiv:1909.09193`.

[115] T. Chwalek and F. Déliot, "Top quark asymmetries", *Universe* **8** (2022) 622, `doi:10.3390/universe8120622`.

[116] M. Diehl, "Theory uncertainties", in *Data analysis in high energy physics: A practical guide to statistical methods*, O. Behnke, K. Kröninger, T. Schörner-Sadenius, and G. Schott, eds., p. 297. 2013. `doi:10.1002/9783527653416.ch9`.

[117] M. Grazzini, S. Kallweit, and M. Wiesemann, "Fully differential NNLO computations with MATRIX", *Eur. Phys. J. C* **78** (2018) 537, `doi:10.1140/epjc/s10052-018-5771-7`, `arXiv:1711.06631`.

[118] S. Catani et al., "Top-quark pair hadroproduction at next-to-next-to-leading order in QCD", *Phys. Rev. D* **99** (2019) 051501, `doi:10.1103/PhysRevD.99.051501`, `arXiv:1901.04005`.

[119] F. Buccioni et al., "OpenLoops 2", *Eur. Phys. J. C* **79** (2019) 866, `doi:10.1140/epjc/s10052-019-7306-2`, `arXiv:1907.13071`.

[120] F. Cascioli, P. Maierhofer, and S. Pozzorini, "Scattering amplitudes with Open Loops", *Phys. Rev. Lett.* **108** (2012) 111601, `doi:10.1103/PhysRevLett.108.111601`, `arXiv:1111.5206`.

[121] A. Denner, S. Dittmaier, and L. Hofer, "Collier: a fortran-based Complex One-Loop LIbrary in Extended Regularizations", *Comput. Phys. Commun.* **212** (2017) 220, `doi:10.1016/j.cpc.2016.10.013`, `arXiv:1604.06792`.

[122] S. Catani et al., "Vector boson production at hadron colliders: hard-collinear coefficients at the NNLO", *Eur. Phys. J. C* **72** (2012) 2195, `doi:10.1140/epjc/s10052-012-2195-7`, `arXiv:1209.0158`.

[123] S. Catani and M. Grazzini, "An NNLO subtraction formalism in hadron collisions and its application to Higgs boson production at the LHC", *Phys. Rev. Lett.* **98** (2007) 222002, `doi:10.1103/PhysRevLett.98.222002`, `arXiv:hep-ph/0703012`.

[124] M. Czakon, "A novel subtraction scheme for double-real radiation at NNLO", *Phys. Lett. B* **693** (2010) 259, `doi:10.1016/j.physletb.2010.08.036`, `arXiv:1005.0274`.

[125] M. Czakon and D. Heymes, "Four-dimensional formulation of the sector-improved residue subtraction scheme", *Nucl. Phys. B* **890** (2014) 152, `doi:10.1016/j.nuclphysb.2014.11.006`, `arXiv:1408.2500`.

[126] M. Czakon, "Double-real radiation in hadronic top quark pair production as a proof of a certain concept", *Nucl. Phys. B* **849** (2011) 250, `doi:10.1016/j.nuclphysb.2011.03.020`, `arXiv:1101.0642`.

[127] P. F. Monni et al., "MiNNLO$_{PS}$: a new method to match NNLO QCD to parton showers", *JHEP* **05** (2020) 143, `doi:10.1007/JHEP05(2020)143`, `arXiv:1908.06987`.

[128] P. F. Monni, E. Re, and M. Wiesemann, "MiNNLO$_{PS}$: optimizing $2 \to 1$ hadronic processes", *Eur. Phys. J. C* **80** (2020) 1075, `doi:10.1140/epjc/s10052-020-08658-5`, `arXiv:2006.04133`.

[129] J. Mazzitelli et al., "Top-pair production at the LHC with MiNNLO$_{PS}$", *JHEP* **04** (2022) 079, `doi:10.1007/JHEP04(2022)079`, `arXiv:2112.12135`.

[130] K. Hamilton, P. Nason, and G. Zanderighi, "MINLO: Multi-scale improved NLO", *JHEP* **10** (2012) 155, `doi:10.1007/JHEP10(2012)155`, `arXiv:1206.3572`.

[131] K. Hamilton, P. Nason, C. Oleari, and G. Zanderighi, "Merging H/W/Z + 0 and 1 jet at NLO with no merging scale: a path to parton shower + NNLO matching", *JHEP* **05** (2013) 082, `doi:10.1007/JHEP05(2013)082`, `arXiv:1212.4504`.

[132] S. Dulat et al., "New parton distribution functions from a global analysis of quantum chromodynamics", *Phys. Rev. D* **93** (2016) 033006, `doi:10.1103/PhysRevD.93.033006`, `arXiv:1506.07443`.

[133] S. Alekhin, J. Blümlein, and S. Moch, "NLO PDFs from the ABMP16 fit", *Eur. Phys. J. C* **78** (2018) 477, `doi:10.1140/epjc/s10052-018-5947-1`, `arXiv:1803.07537`.

[134] L. A. Harland-Lang, A. D. Martin, P. Motylinski, and R. S. Thorne, "Parton distributions in the LHC era: MMHT 2014 PDFs", *Eur. Phys. J. C* **75** (2015) 204, `doi:10.1140/epjc/s10052-015-3397-6`, `arXiv:1412.3989`.

[135] H1 and ZEUS Collaborations, "Combination of measurements of inclusive deep inelastic e$^{\pm}$p scattering cross sections and QCD analysis of HERA data", *Eur. Phys. J. C* **75** (2015) 580, `doi:10.1140/epjc/s10052-015-3710-4`, `arXiv:1506.06042`.

[136] J. Butterworth et al., "PDF4LHC recommendations for LHC Run II", *J. Phys. G* **43** (2016) 023001, `doi:10.1088/0954-3899/43/2/023001`, `arXiv:1510.03865`.

[137] A. Accardi et al., "A critical appraisal and evaluation of modern PDFs", *Eur. Phys. J. C* **76** (2016) 471, `doi:10.1140/epjc/s10052-016-4285-4`, `arXiv:1603.08906`.

A   Definition of χ^2 for theory-to-data comparisons

We define here the χ^2 values for the theory-to-data comparisons shown in Section 9 and Appendix B. The standard χ^2 values are calculated taking the measurement uncertainties into account, but ignoring the uncertainties in the predictions:

$$\chi^2 = \mathbf{R}_N^T \mathbf{Cov}_N^{-1} \mathbf{R}_N, \tag{2}$$

where N denotes the number of bins of the respective cross section distribution and $\mathbf{R}_N$ the vector of differences of the measured cross sections and the corresponding predictions. The covariance matrix $\mathbf{Cov}$ is calculated as:

$$\mathbf{Cov} = \mathbf{Cov}^{\text{unf}} + \mathbf{Cov}^{\text{syst}}, \tag{3}$$

where $\mathbf{Cov}^{\text{unf}}$ and $\mathbf{Cov}^{\text{syst}}$ are the covariance matrices representing the statistical uncertainties from the unfolding, and the systematic uncertainties, respectively. The systematic covariance matrix $\mathbf{Cov}^{\text{syst}}$ is calculated as

$$\mathbf{Cov}_{ij}^{\text{syst}} = \sum_{k,l} \frac{1}{N_k} C_{j,k,l} C_{i,k,l}, \quad 1 \le i \le N, \quad 1 \le j \le N. \tag{4}$$

Here, $C_{i,k,l}$ denotes the signed systematic shift of the measurement in the ith bin arising from variation l of source k and N_k is the number of variations for source k. The sums run over all sources of systematic uncertainties and all their corresponding variations. Most of the systematic uncertainty sources in this analysis consist of positive and negative variations and thus have $N_k = 2$, though one model uncertainty (namely, the model of color reconnection) consists of more than two variations, a property that is accounted for in Eq. (4). For the POW+PYT model, additional χ^2 values are provided including the uncertainties in the predictions. This is achieved by adding the covariance matrix of the predictions, $\mathbf{Cov}^{\text{pred}}$, calculated analogously to Eq. (4), to $\mathbf{Cov}$.

For normalized cross sections the χ^2 values are calculated as

$$\chi^2 = \mathbf{R}_{N-1}^T \mathbf{Cov}_{N-1}^{-1} \mathbf{R}_{N-1}, \tag{5}$$

where $\mathbf{R}_{N-1}$ is the column vector of the residuals calculated as the difference of the measured normalized cross sections and the corresponding predictions and discarding one of the N bins, and $\mathbf{Cov}_{N-1}$ is the $(N-1) \times (N-1)$ submatrix obtained from the full covariance matrix by discarding the corresponding row and column. The matrix $\mathbf{Cov}_{N-1}$ obtained in this way is invertible, while the original covariance matrix $\mathbf{Cov}$ is singular because for normalized cross sections one degree of freedom is lost.

B Results for absolute cross sections

Absolute differential cross sections corresponding to the normalized ones discussed in Section 9 are presented in the following, together with tables listing χ^2 values of all prediction-to-data comparisons.

B.1 Comparisons to MC simulations

The absolute differential cross sections comparing data to predictions based on MC simulations are shown in Figs. 66–98, and the corresponding χ^2 values are presented in Tables 13–19. The p-values of the χ^2 tests are provided in Tables 37–43. The measurements are compared to the three MC simulations introduced in Section 3: POWHEG+PYTHIA 8 (POW+PYT), MG5_aMC@NLO[FxFx]+PYTHIA 8 (FxFx+PYT), and POWHEG+HERWIG 7 (POW+HER). As detailed in Section 3, the POWHEG+PYTHIA 8 simulation is normalized to the cross section calculated at NNLO+NNLL. Comparing the absolute cross sections to the normalized ones presented in Section 9, two effects are visible. Firstly, the uncertainties in the measured absolute cross sections are considerably larger than those of the corresponding normalized ones, which can be attributed to bin-to-bin correlated global normalization uncertainties. Secondly, the absolute total cross section obtained by integrating over the spectra of the three MC models is within 5% of that calculated from the data, indicating a reasonable agreement.
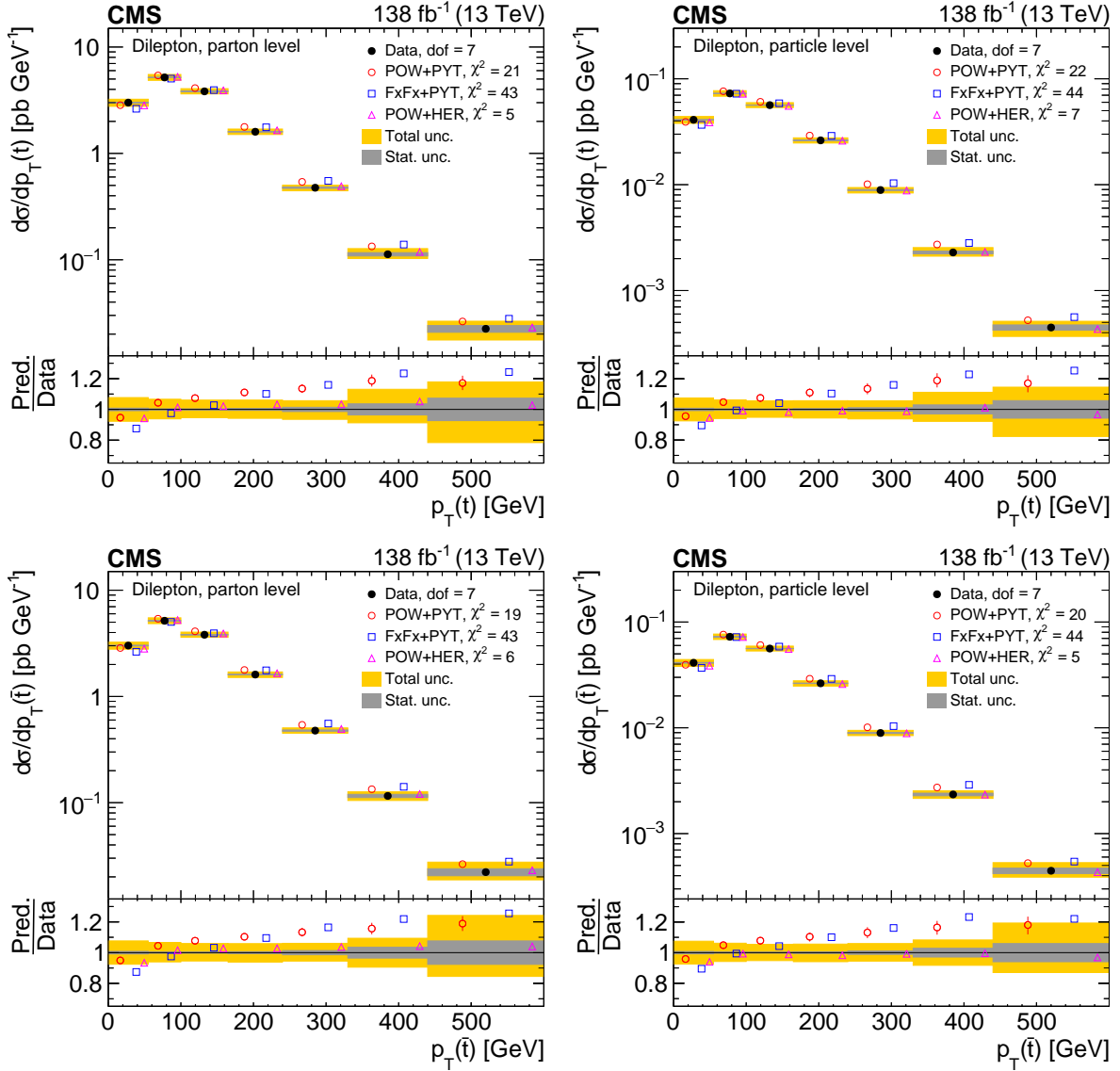
Figure 66: Absolute differential $t\bar{t}$ production cross sections as functions of $p_{\mathrm{T}}(t)$ (upper) and $p_{\mathrm{T}}(\bar{t})$ (lower), measured at the parton level in the full phase space (left) and at the particle level in a fiducial phase space (right). The data are shown as filled circles with grey and yellow bands indicating the statistical and total uncertainties (statistical and systematic uncertainties added in quadrature), respectively. For each distribution, the number of degrees of freedom (dof) is also provided. The cross sections are compared to various MC predictions (other points). The estimated uncertainties in the POWHEG+PYTHIA 8 ('POW-PYT') simulation are represented by vertical bars on the corresponding points. For each MC model, a value of χ^2 is reported that takes into account the measurement uncertainties. The lower panel in each plot shows the ratios of the predictions to the data.

Figure 67: Absolute differential t$\bar{\text{t}}$ production cross sections as functions of $y(\text{t})$ (upper) and $y(\bar{\text{t}})$ (lower) are shown for data (filled circles) and various MC predictions (other points). Further details can be found in the caption of Fig. 66.
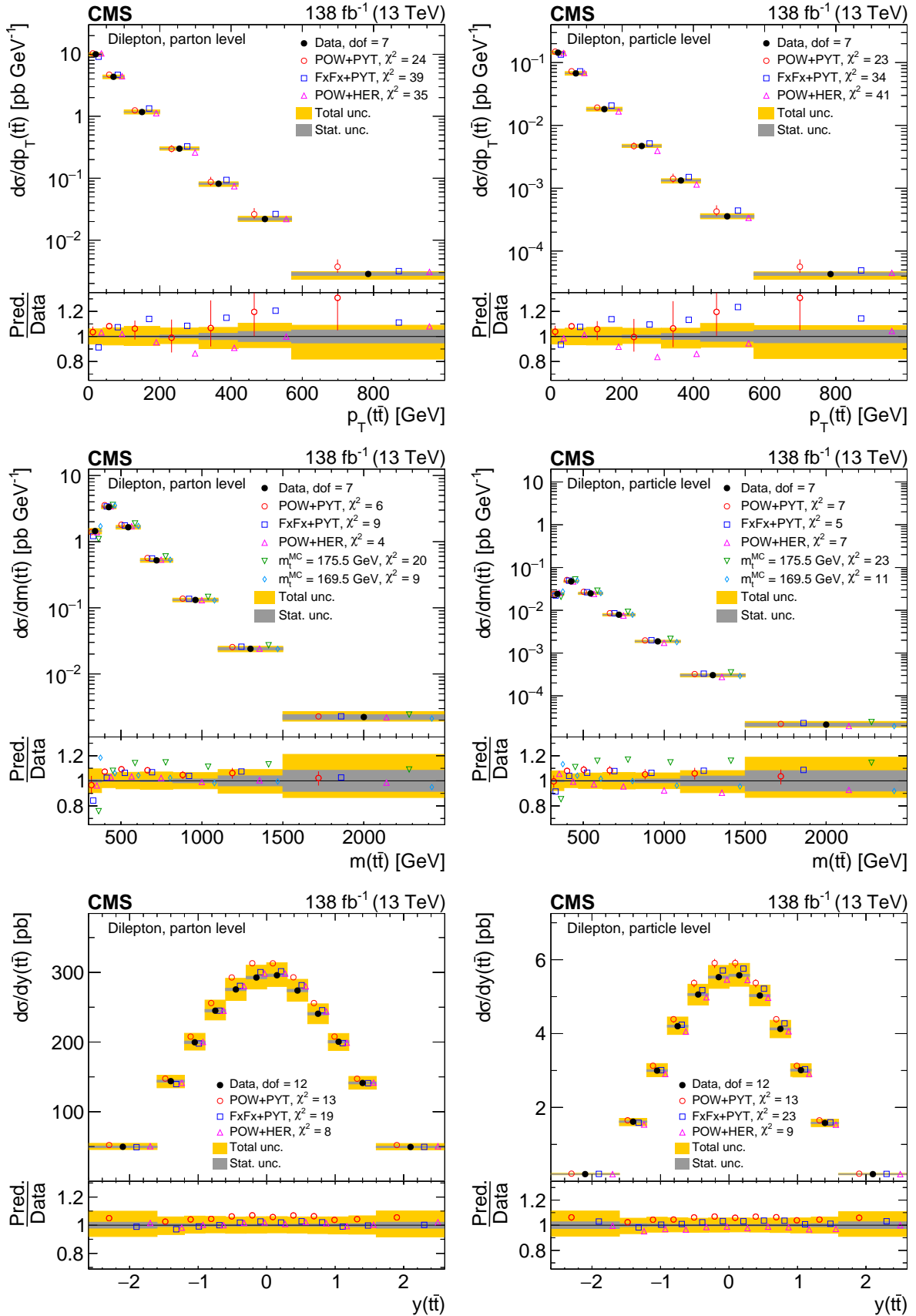
Figure 68: Absolute differential $t\bar{t}$ production cross sections as functions of $p_{\mathrm{T}}(t\bar{t})$ (upper), $m(t\bar{t})$ (middle) and $y(t\bar{t})$ (lower) are shown for data (filled circles) and various MC predictions (other points). Further details can be found in the caption of Fig. 66.
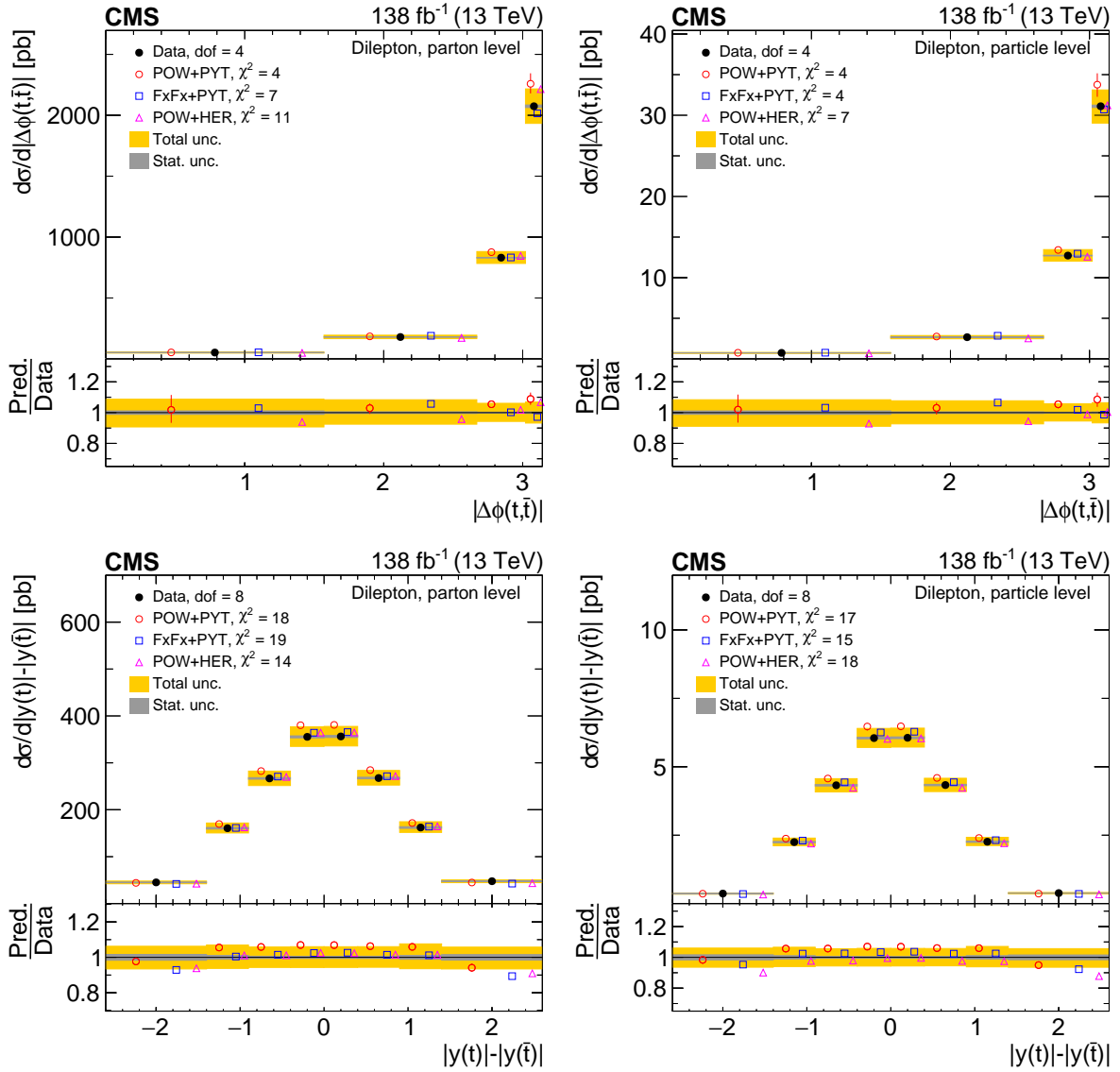
Figure 69: Absolute differential t$\bar{\text{t}}$ production cross sections as functions of $|\Delta\phi(\text{t},\bar{\text{t}})|$ (upper) and $|y(\text{t})| - |y(\bar{\text{t}})|$ (lower) are shown for the data (filled circles) and various MC predictions (other points). Further details can be found in the caption of Fig. 66.
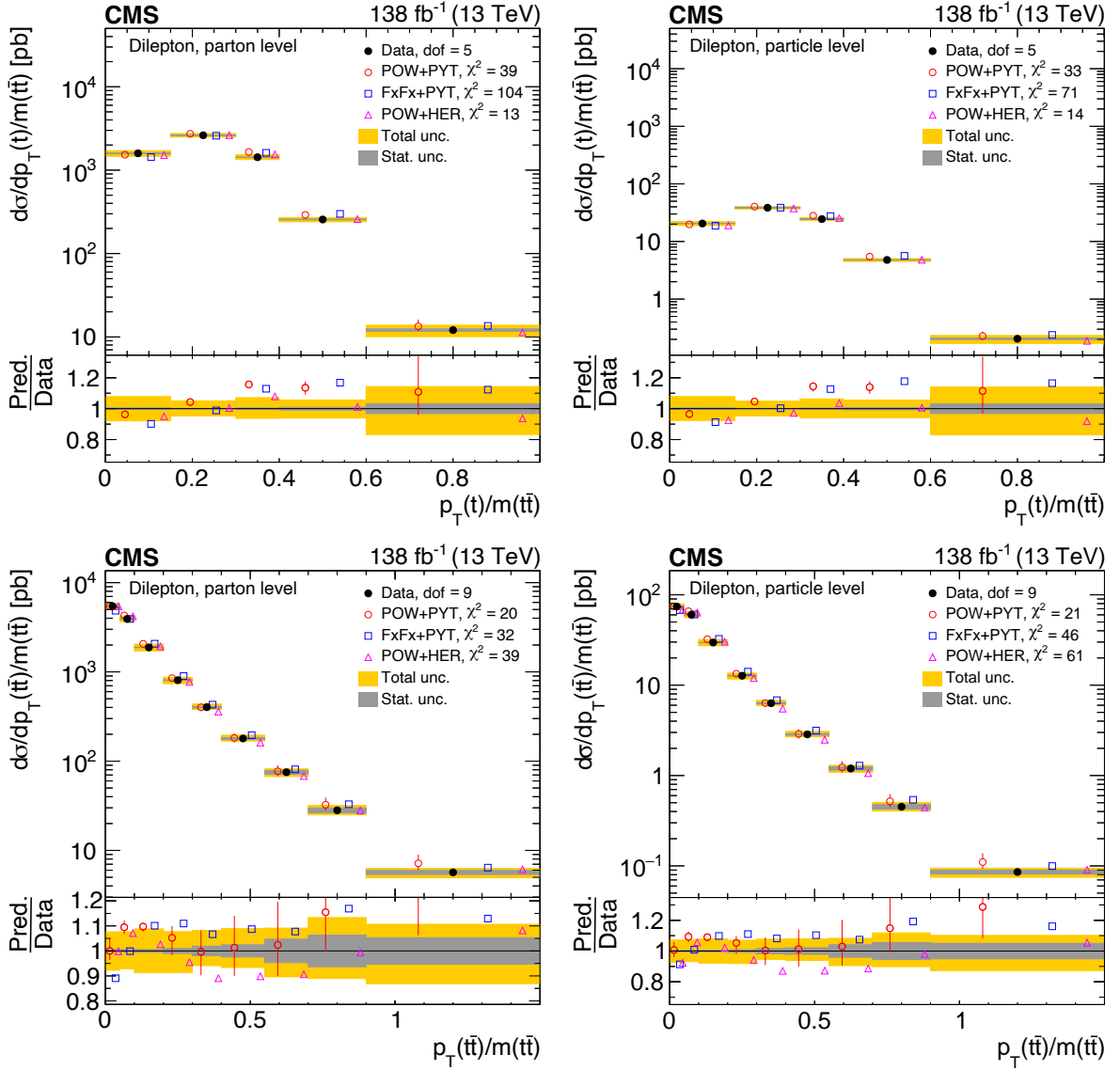
Figure 70: Absolute differential $t\bar{t}$ production cross sections as functions of $p_T(t)/m(t\bar{t})$ (upper) and $p_T(t\bar{t})/m(t\bar{t})$ (lower) are shown for the data (filled circles) and various MC predictions (other points). Further details can be found in the caption of Fig. 66.
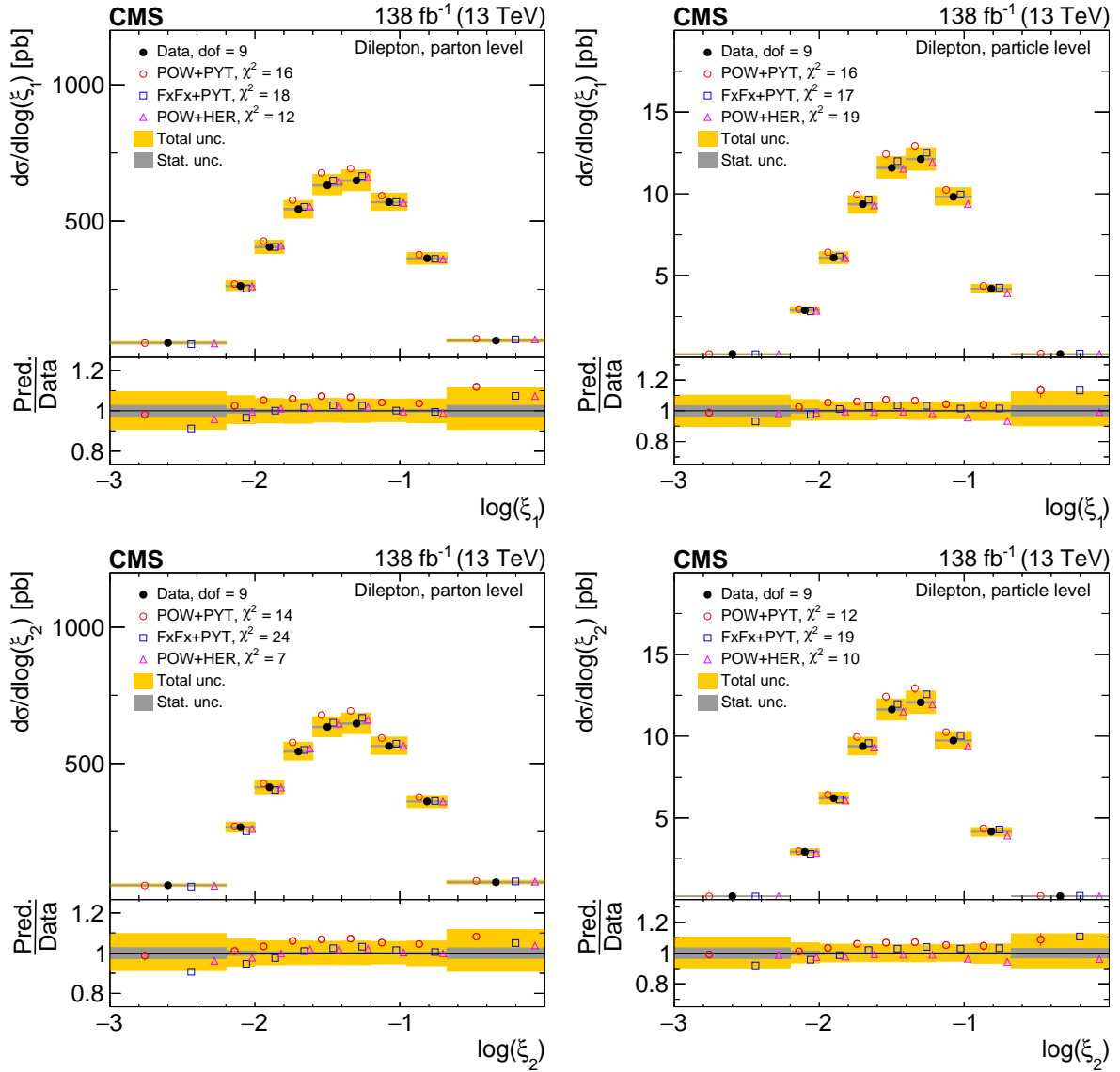
Figure 71: Absolute differential $t\bar{t}$ production cross sections as functions of $\log(\xi_1)$ (upper) and $\log(\xi_2)$ (lower) are shown for the data (filled circles) and various MC predictions (other points). Further details can be found in the caption of Fig. 66.
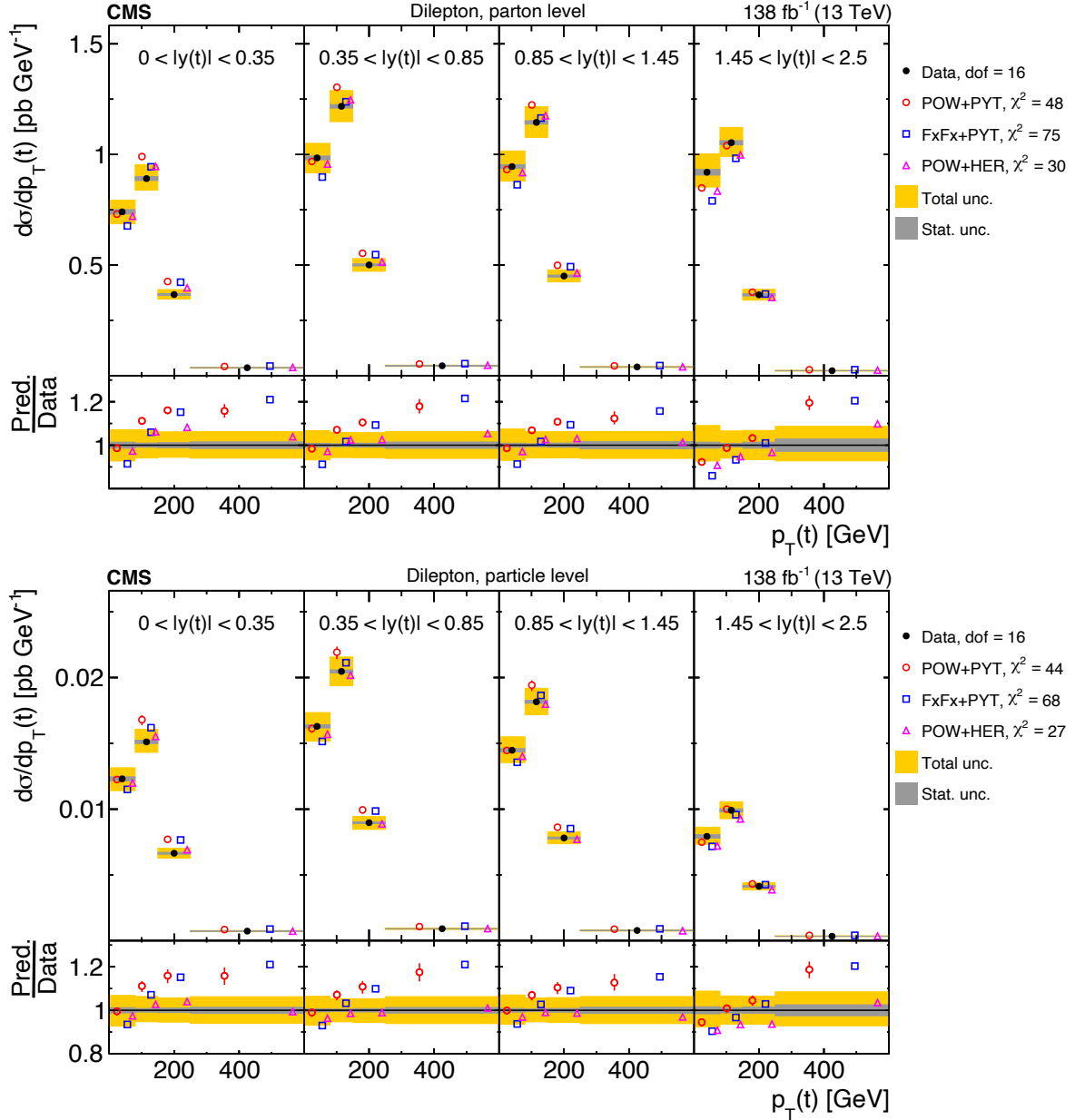
Figure 72: Absolute $[|y(t)|, p_T(t)]$ cross sections measured at the parton level in the full phase space (upper) and at the particle level in a fiducial phase space (lower). The data are shown as filled circles with grey and yellow bands indicating the statistical and total uncertainties (statistical and systematic uncertainties added in quadrature), respectively. For each distribution, the number of degrees of freedom (dof) is also provided. The cross sections are compared to various MC predictions (other points). The estimated uncertainties in the POWHEG+PYTHIA 8 ('POW-PYT') simulation are represented by vertical bars on the corresponding points. For each MC model, a value of χ^2 is reported that takes into account the measurement uncertainties. The lower panel in each plot shows the ratios of the predictions to the data.

Figure 73: Absolute $[m(t\bar{t}), p_{T}(t)]$ cross sections are shown for data (filled circles) and various MC predictions (other points). Further details can be found in the caption of Fig. 72.
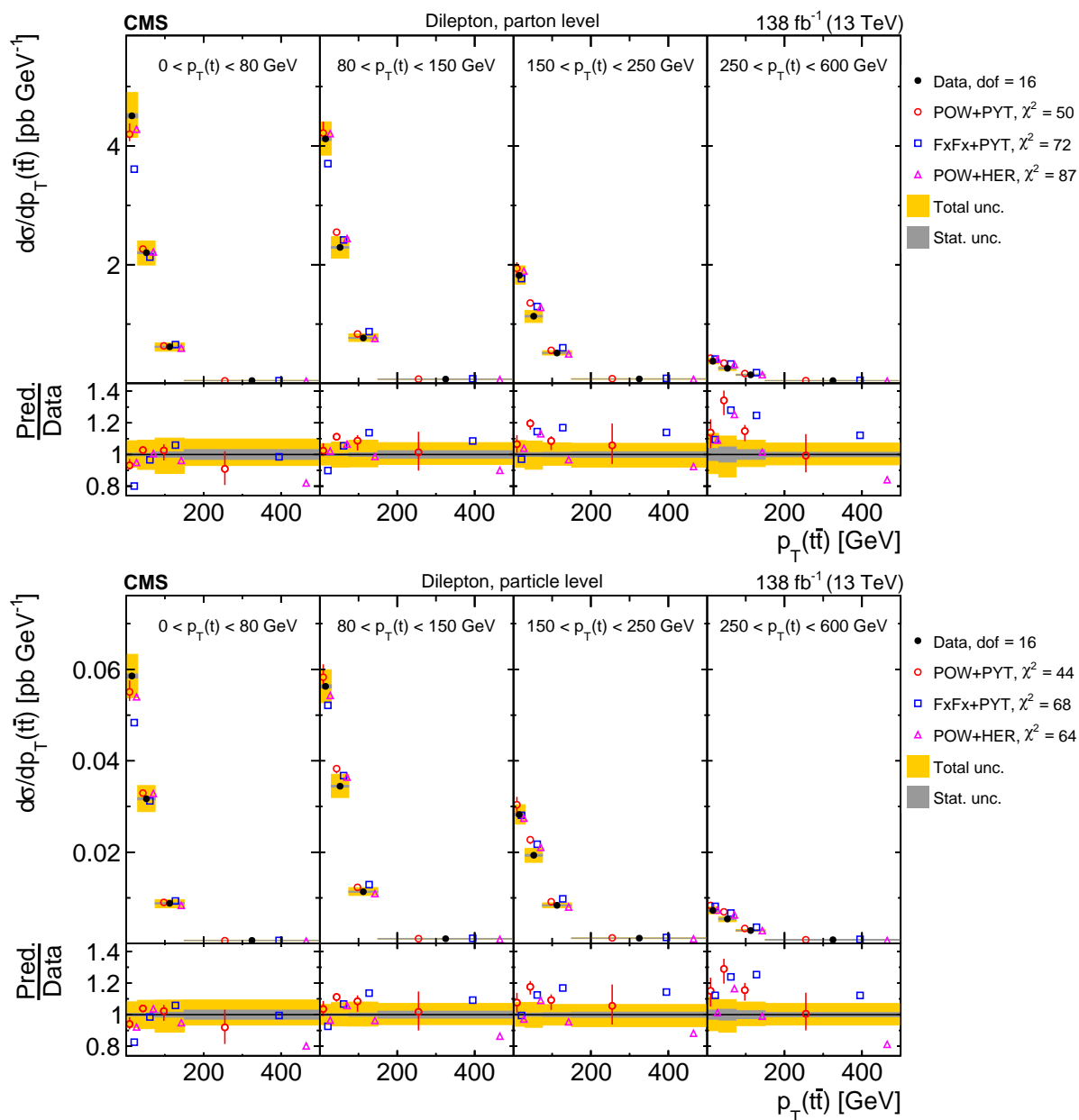
Figure 74: Absolute $[p_T(t), p_T(t\bar{t})]$ cross sections are shown for data (filled circles) and various MC predictions (other points). Further details can be found in the caption of Fig. 72.
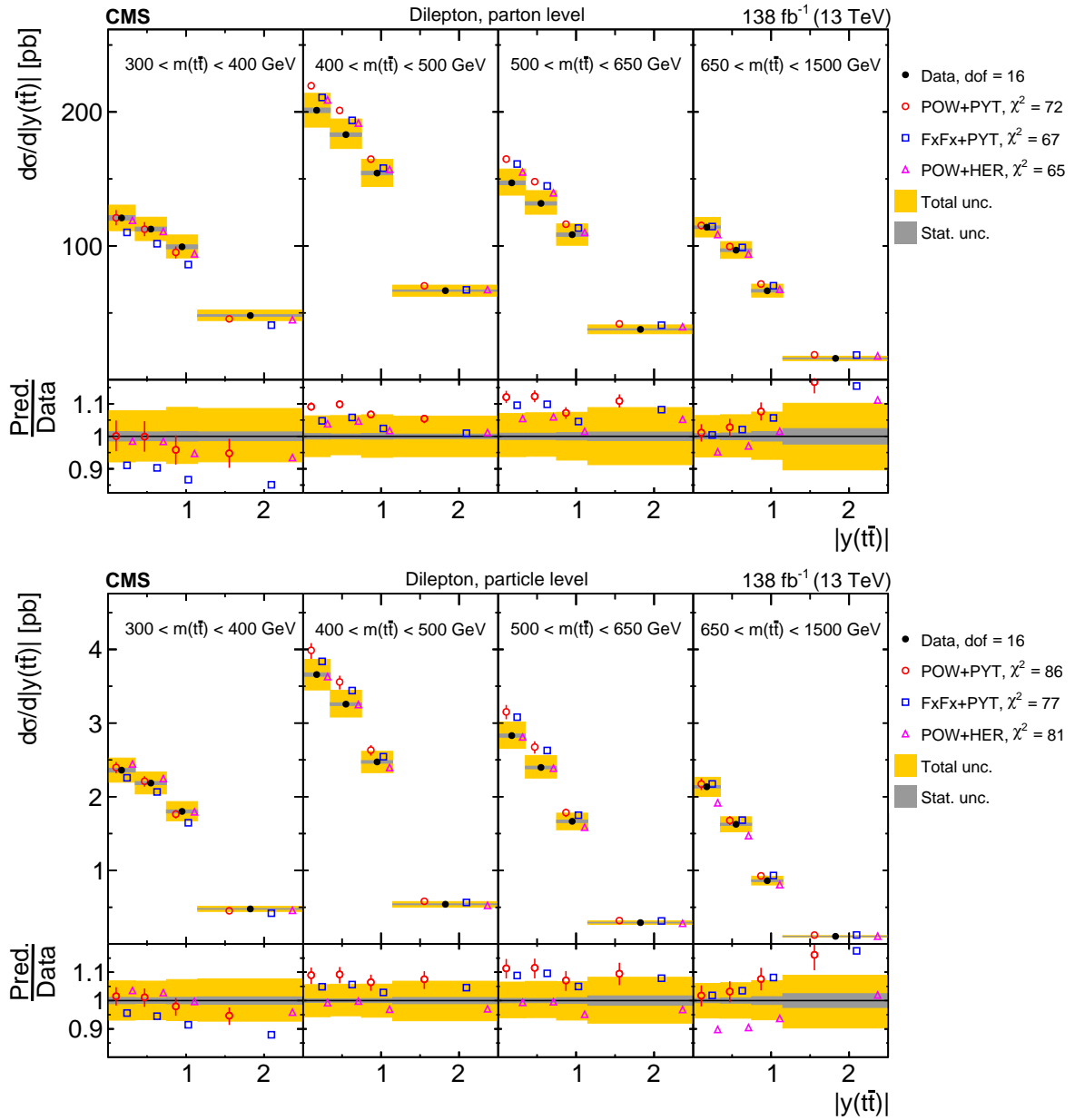
Figure 75: Absolute $[m(t\bar{t}), |y(t\bar{t})|]$ cross sections are shown for data (filled circles) and various MC predictions (other points). Further details can be found in the caption of Fig. 72.
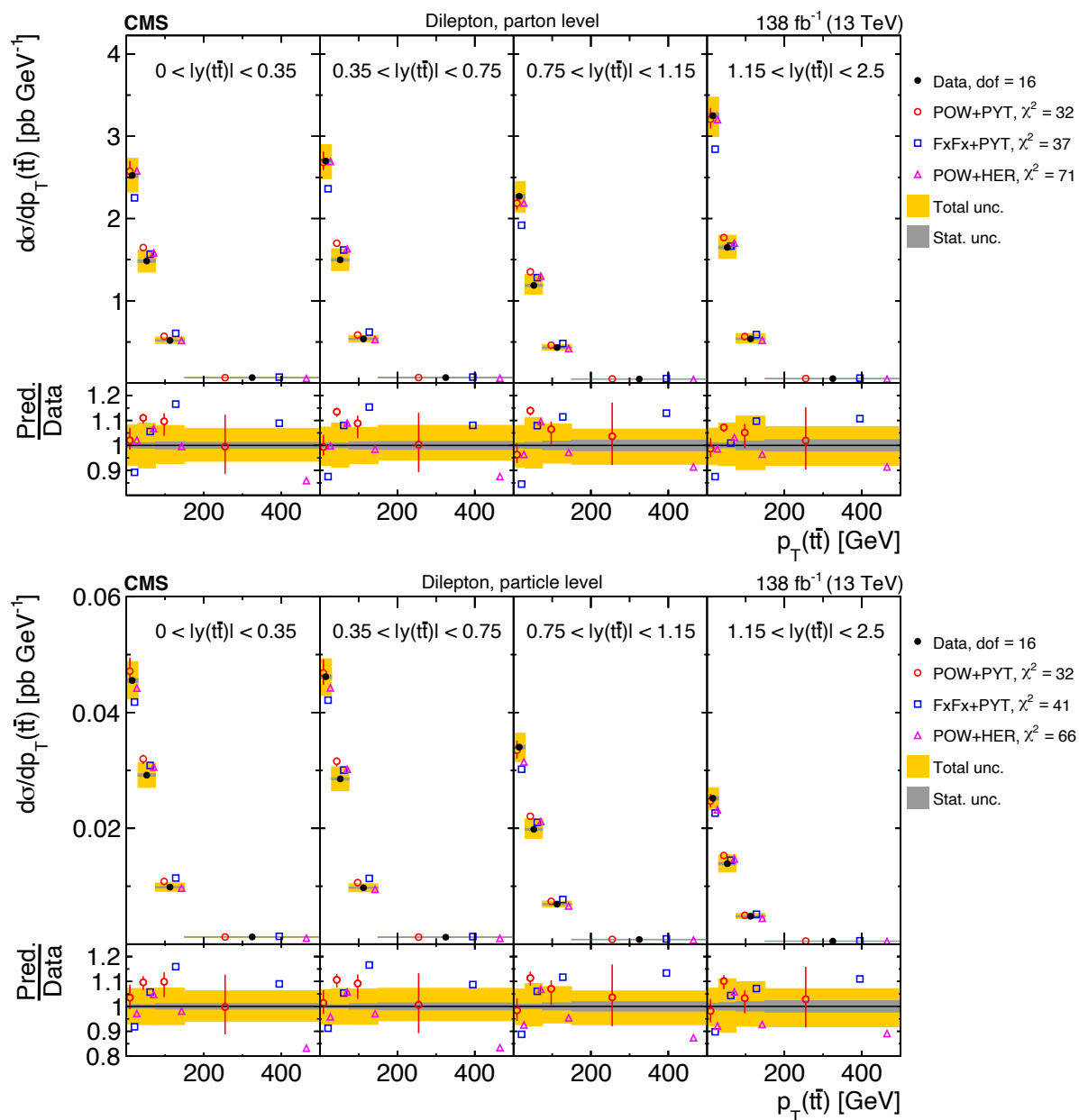
Figure 76: Absolute $[|y(t\bar{t})|, p_T(t\bar{t})]$ cross sections are shown for data (filled circles) and various MC predictions (other points). Further details can be found in the caption of Fig. 72.
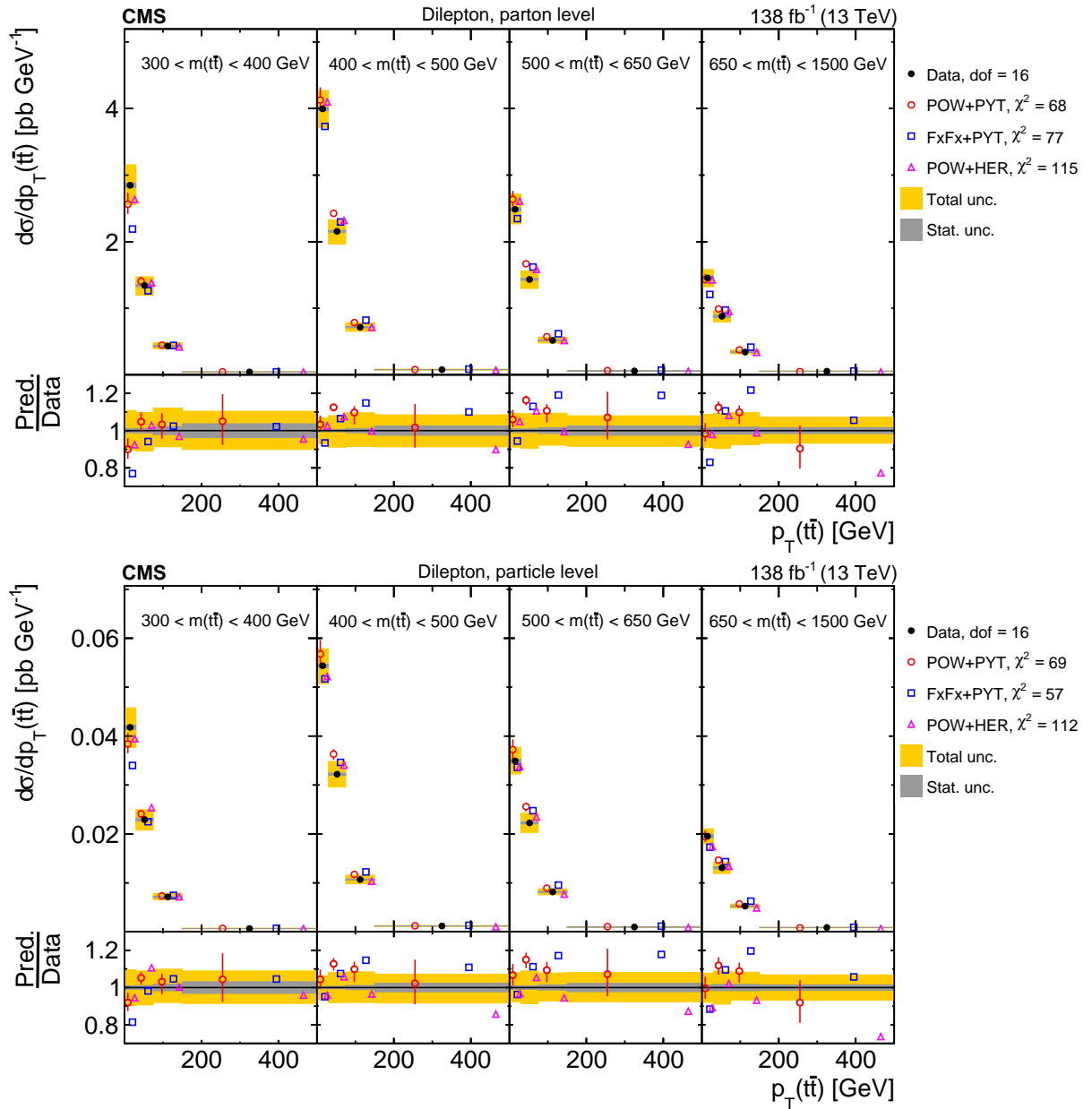
Figure 77: Absolute $[m(t\bar{t}), p_{T}(t\bar{t})]$ cross sections are shown for data (filled circles) and various MC predictions (other points). Further details can be found in the caption of Fig. 72.
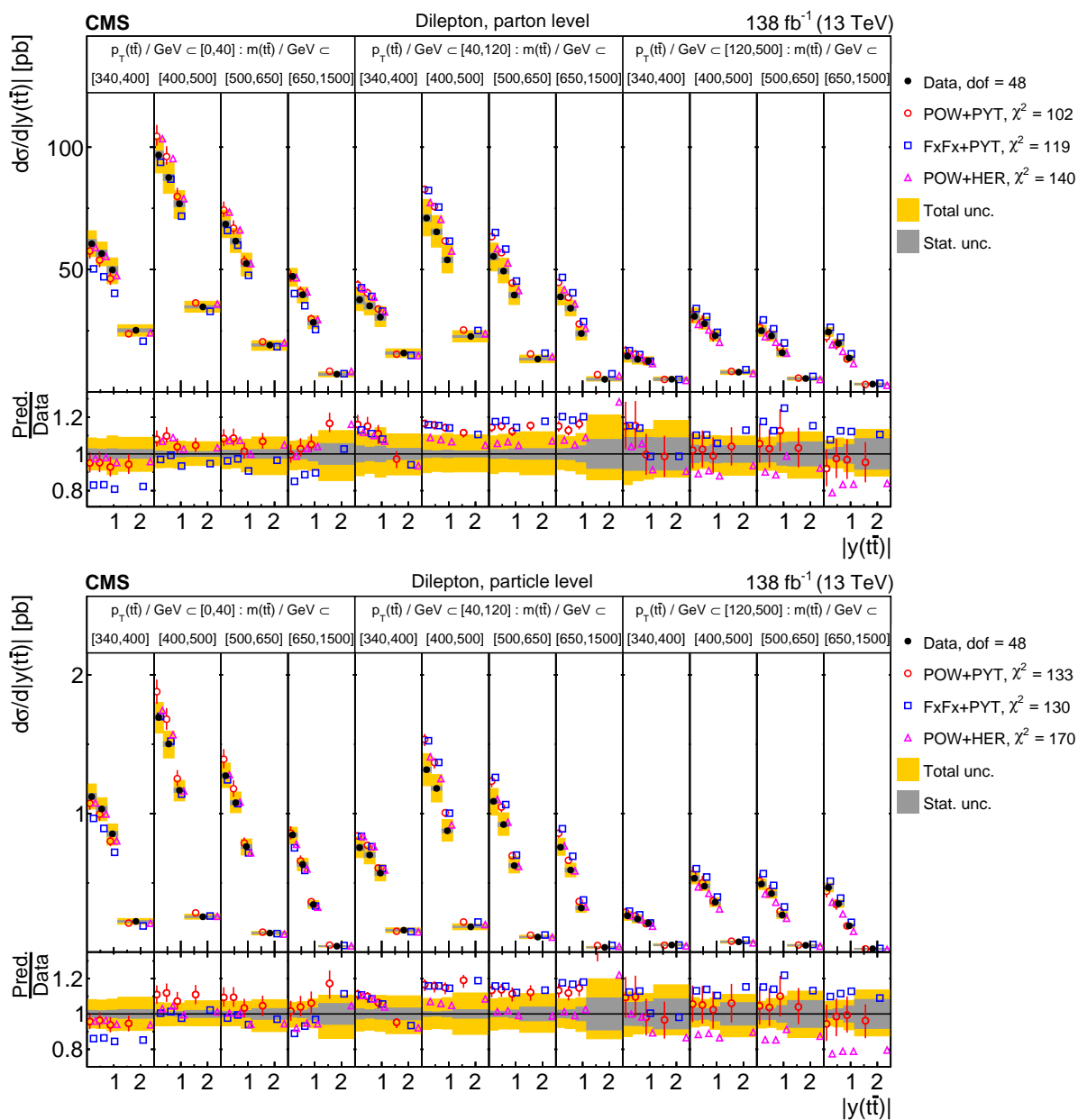
Figure 78: Absolute $[p_T(t\bar{t}),\ m(t\bar{t}),\ |y(t\bar{t})|]$ cross sections are shown for data (filled circles) and various MC predictions (other points). Further details can be found in the caption of Fig. 72.
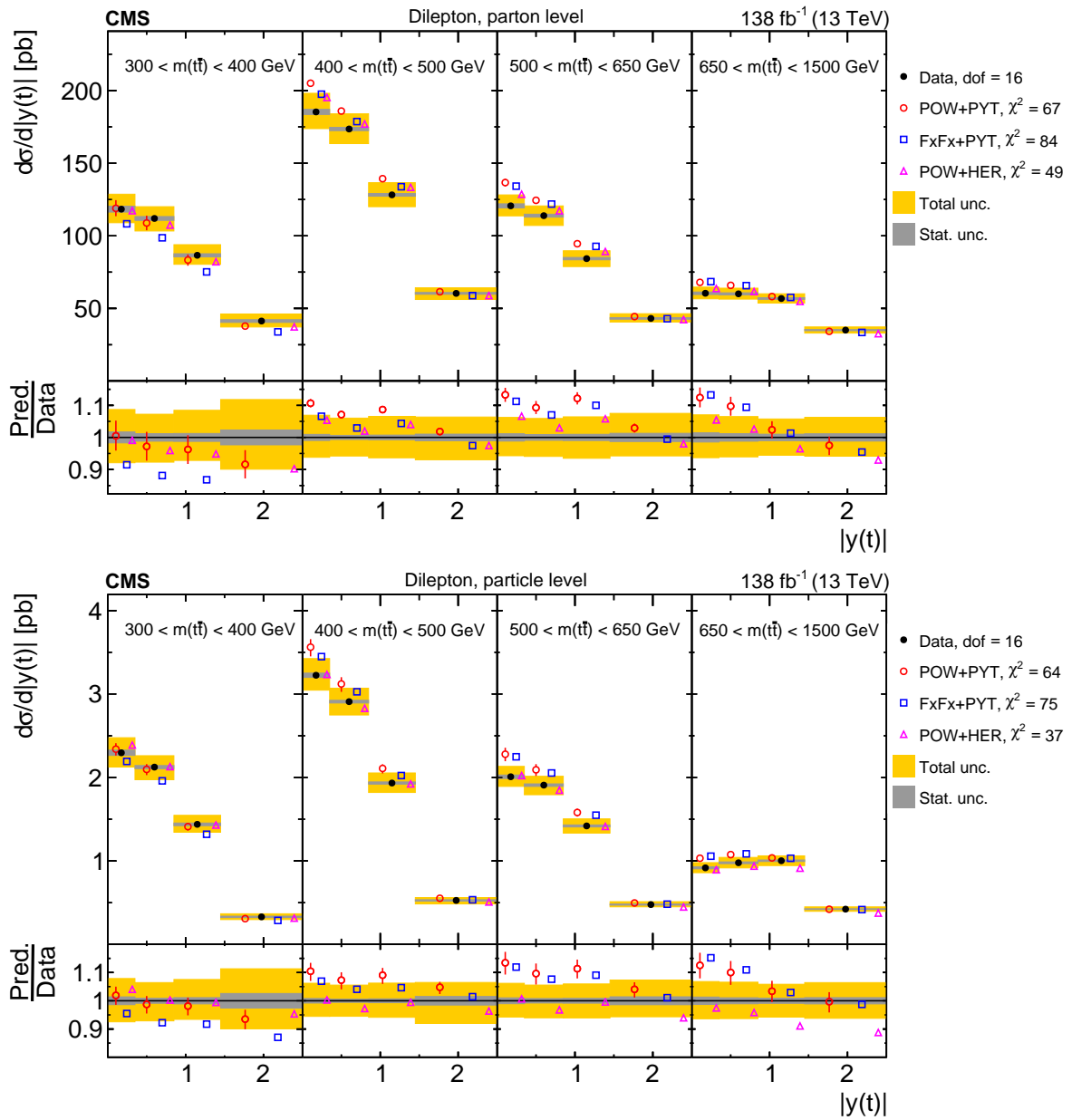
Figure 79: Absolute $[m(t\bar{t}), |y(t)|]$ cross sections are shown for data (filled circles) and various MC predictions (other points). Further details can be found in the caption of Fig. 72.
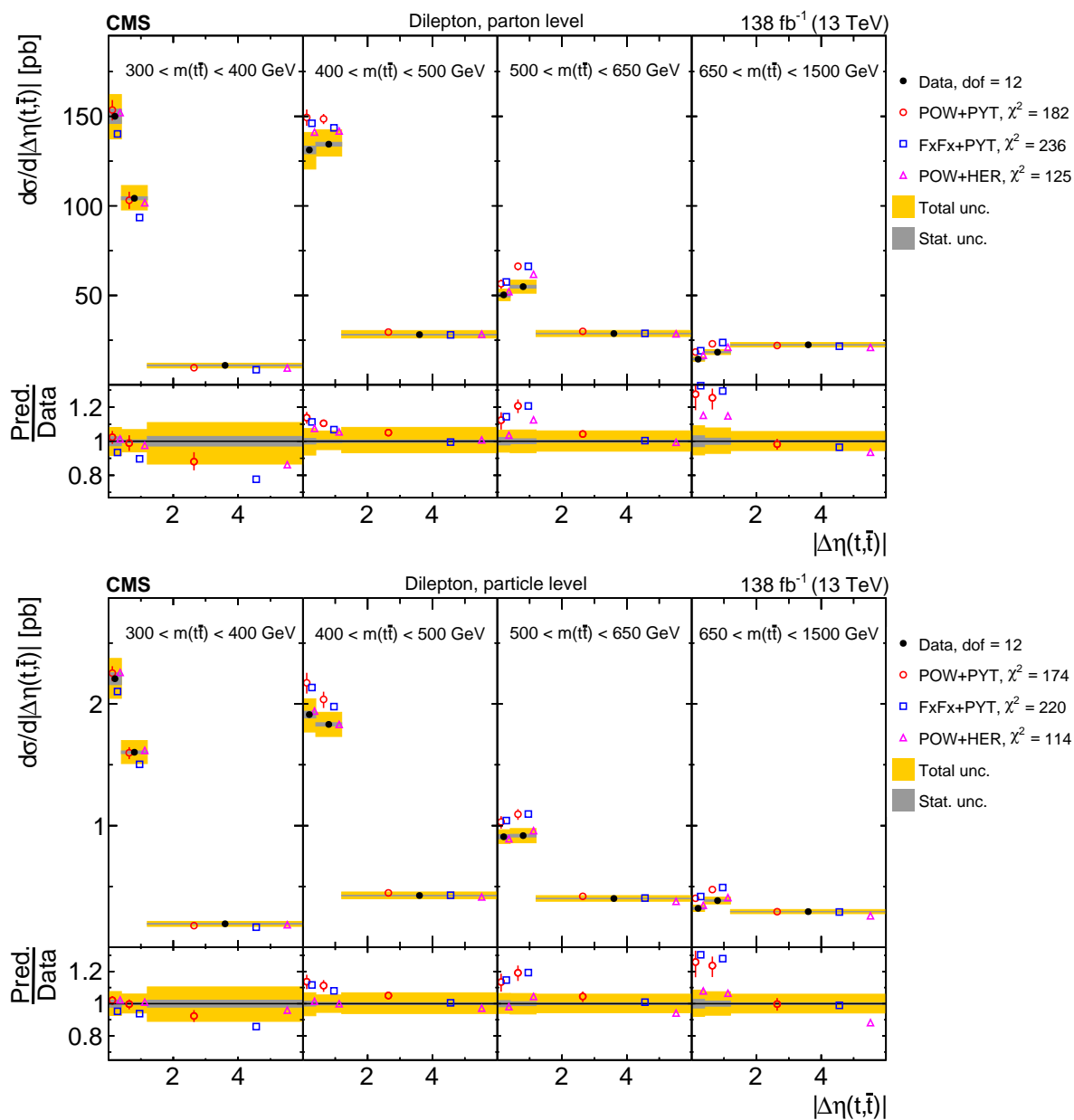
Figure 80: Absolute $[m(t\bar{t}),\ |\Delta\eta(t,\bar{t})|]$ cross sections are shown for data (filled circles) and various MC predictions (other points). Further details can be found in the caption of Fig. 72.
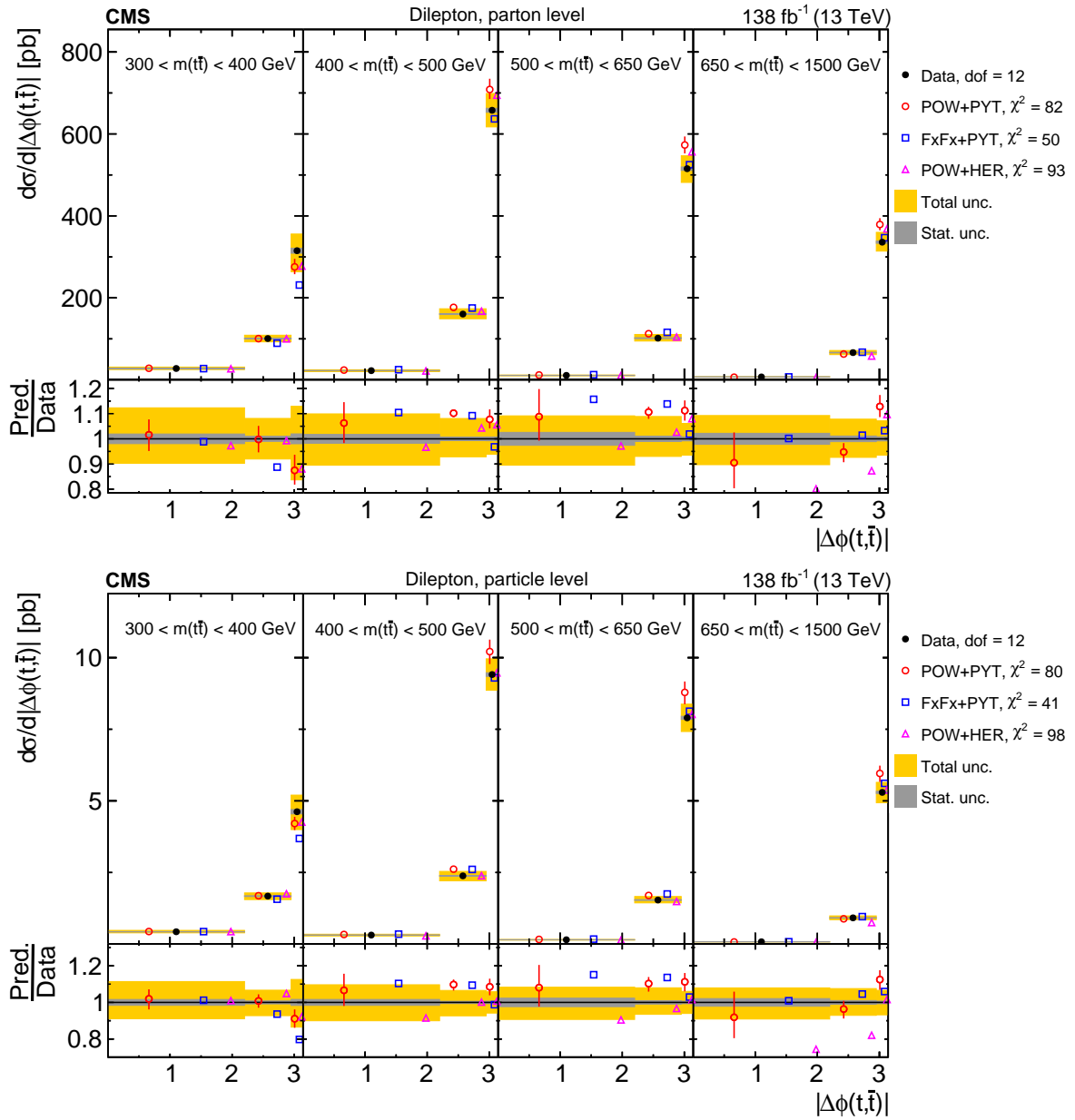
Figure 81: Absolute $[m(t\bar{t}), |\Delta\phi(t,\bar{t})|]$ cross sections are shown for data (filled circles) and various MC predictions (other points). Further details can be found in the caption of Fig. 72.
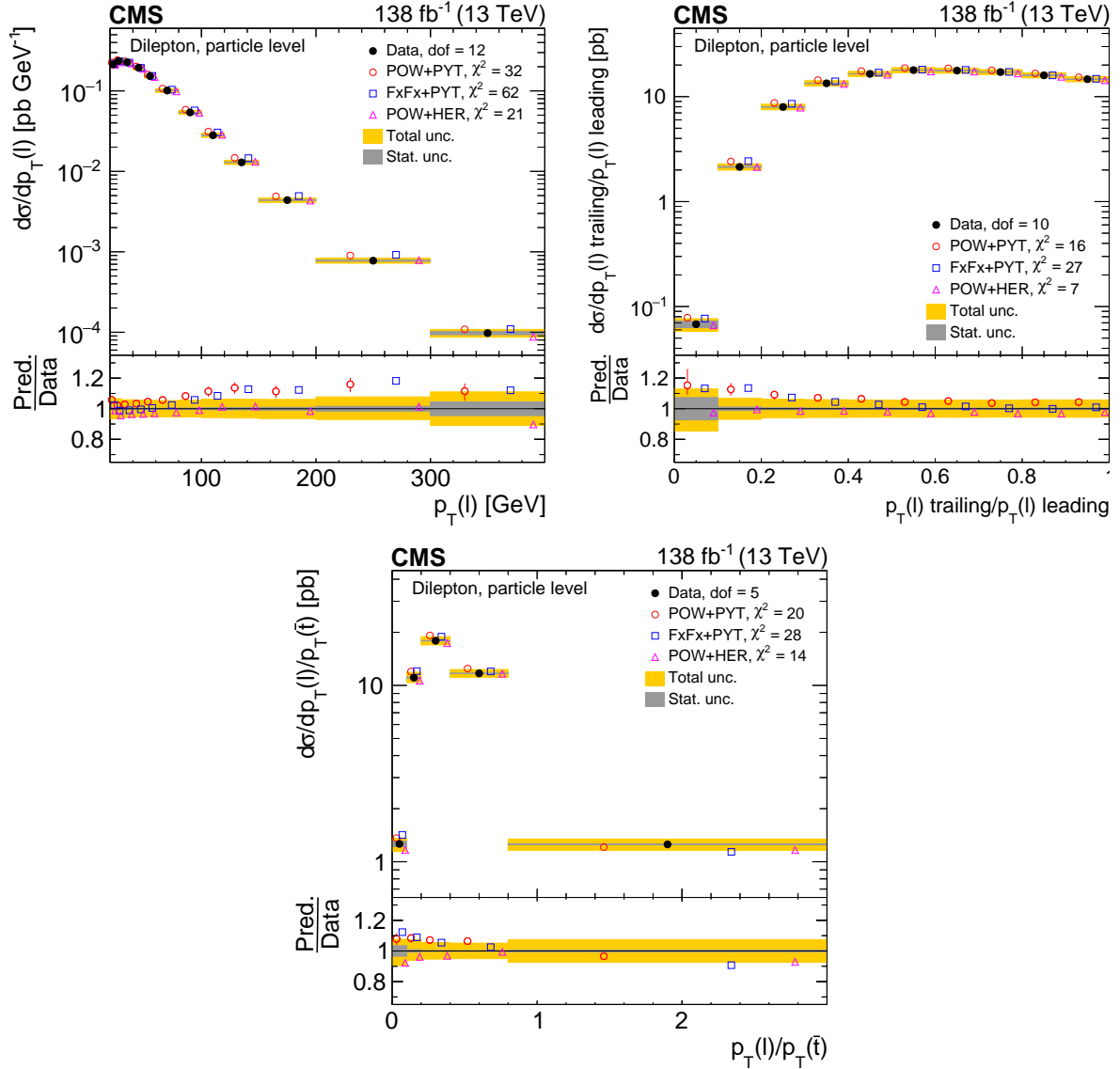
Figure 82: Absolute differential $t\bar{t}$ production cross sections as a function of p_T of the lepton (upper left), of the ratio of the trailing and leading lepton p_T (upper right), and of the ratio of lepton and top antiquark p_T (lower middle), measured at the particle level in a fiducial phase space. The data are shown as filled circles with grey and yellow bands indicating the statistical and total uncertainties (statistical and systematic uncertainties added in quadrature), respectively. For each distribution, the number of degrees of freedom (dof) is also provided. The cross sections are compared to various MC predictions (other points). The estimated uncertainties in the POWHEG+PYTHIA 8 ('POW-PYT') simulation are represented by vertical bars on the corresponding points. For each MC model, a value of χ^2 is reported that takes into account the measurement uncertainties. The lower panel in each plot shows the ratios of the predictions to the data.

Figure 83: Absolute differential $t\bar{t}$ production cross sections as functions of the p_T of the leading (upper left) and trailing (upper right) b jet, and $(p_T(b) + p_T(\bar{b}))/(p_T(t) + p_T(\bar{t}))$ (lower). Further details can be found in the caption of Fig. 82.
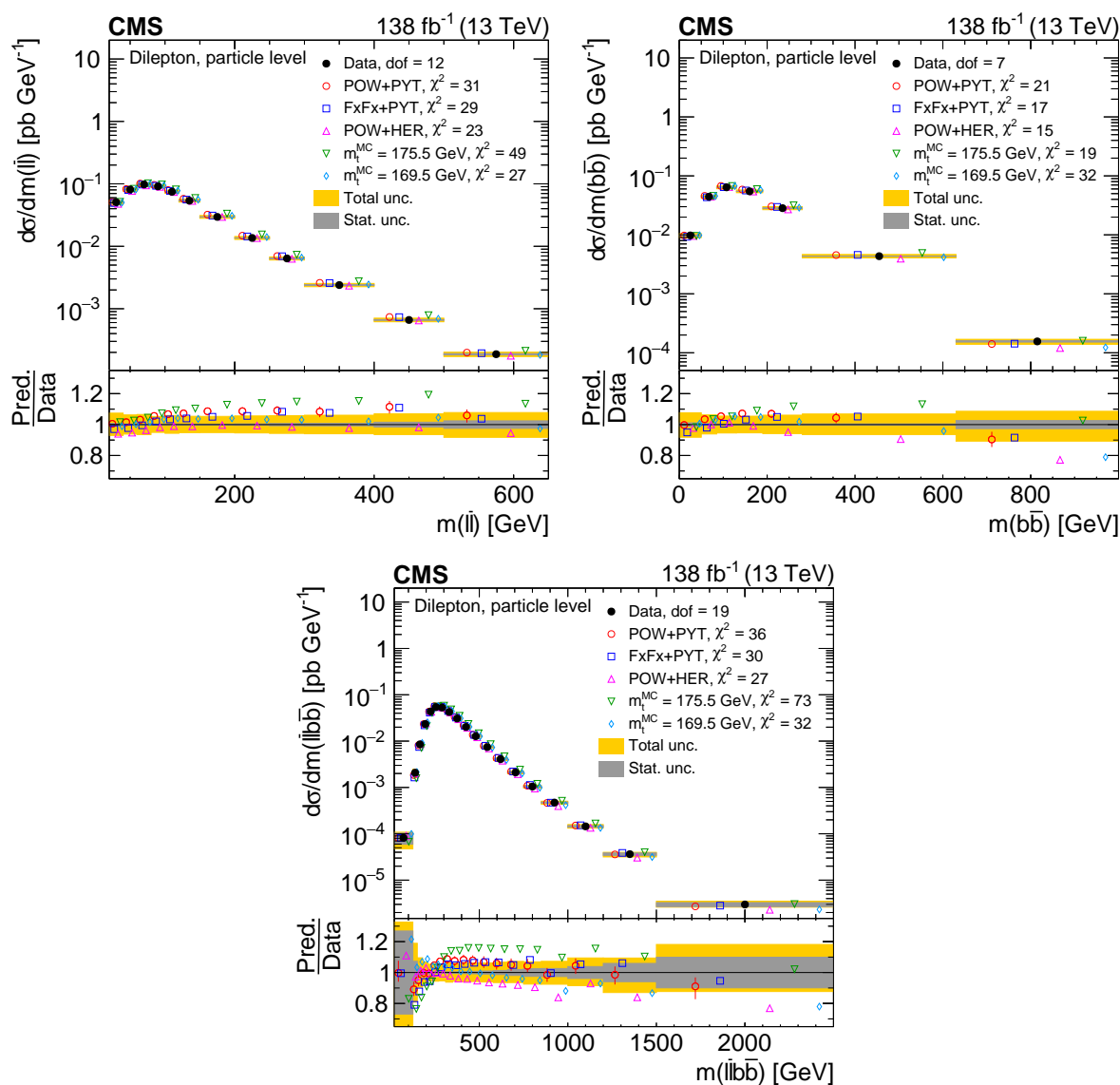
Figure 84: Absolute differential $t\bar{t}$ production cross sections as functions of $m(\ell\bar{\ell})$ (upper left), $m(b\bar{b})$ (upper right) and $m(\ell\bar{\ell}b\bar{b})$ (lower) are shown for data (filled circles) and various MC predictions (other points). Further details can be found in the caption of Fig. 82.
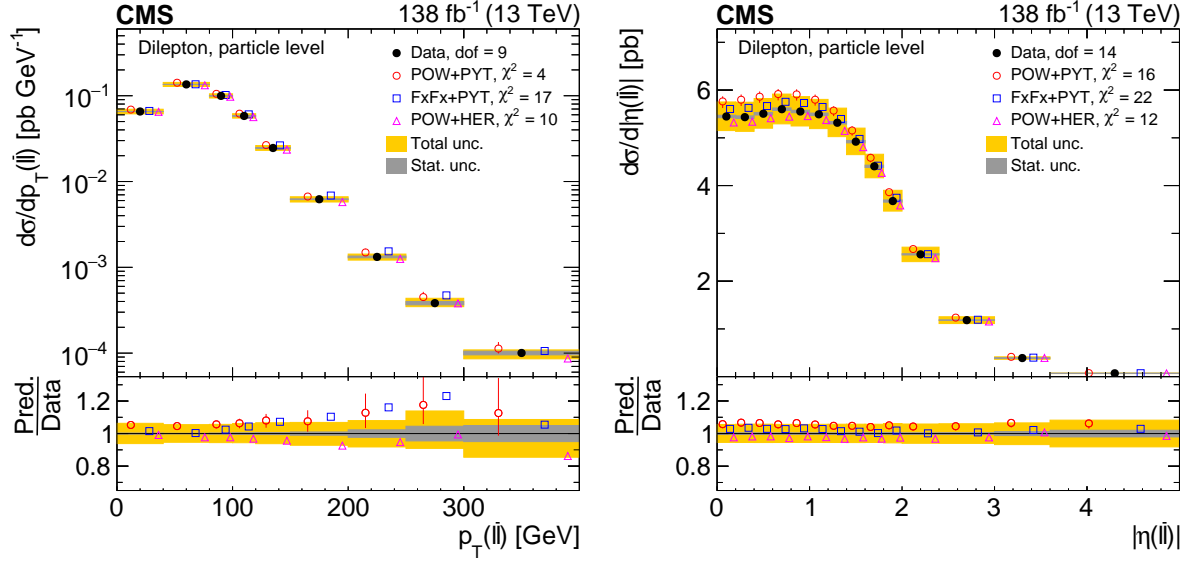
Figure 85: Absolute differential $t\bar{t}$ production cross sections as functions of $p_\mathrm{T}(\ell\bar{\ell})$ (left) and $|\eta(\ell\bar{\ell})|$ (right) are shown for data (filled circles) and various MC predictions (other points). Further details can be found in the caption of Fig. 82.
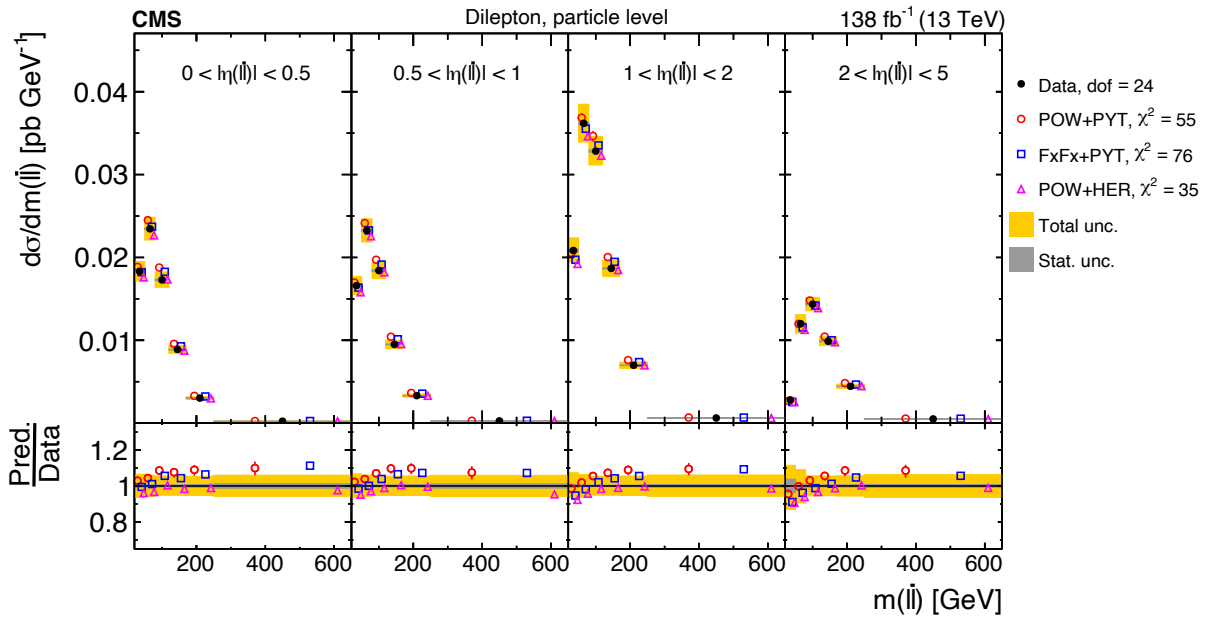
Figure 86: Absolute $[|\eta(\ell\bar{\ell})|, m(\ell\bar{\ell})]$ cross sections are shown for data (filled circles) and various MC predictions (other points). Further details can be found in the caption of Fig. 82.
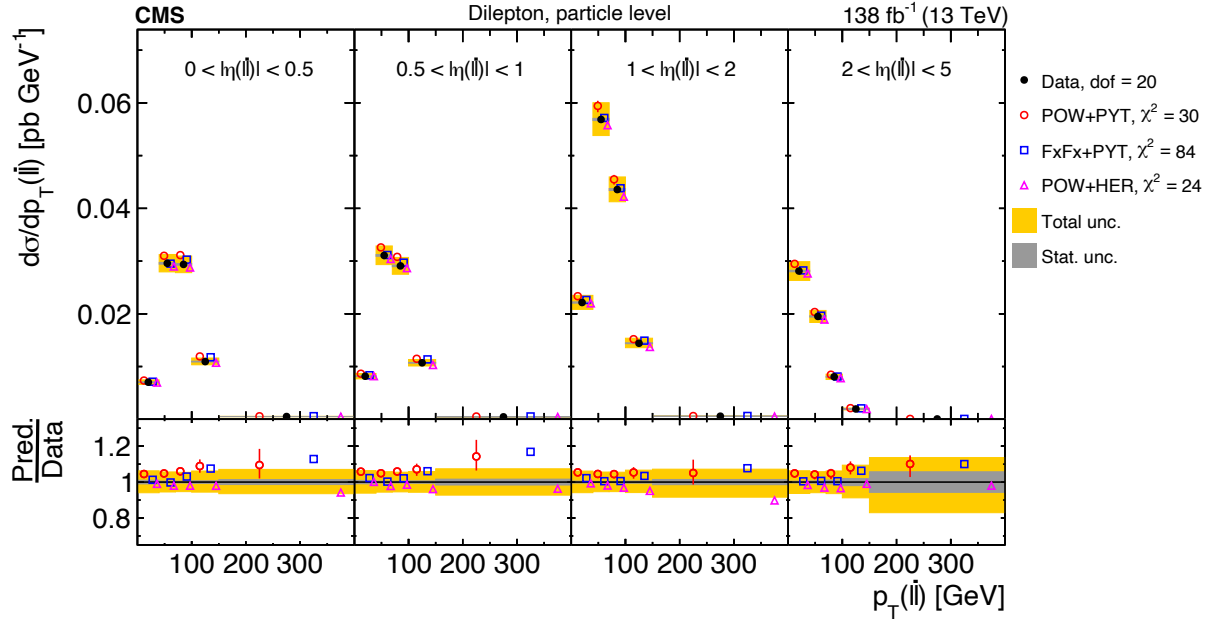
Figure 87: Absolute $[|\eta(\ell\bar{\ell})|,\ p_{\mathrm{T}}(\ell\bar{\ell})]$ cross sections are shown for data (filled circles) and various MC predictions (other points). Further details can be found in the caption of Fig. 82.
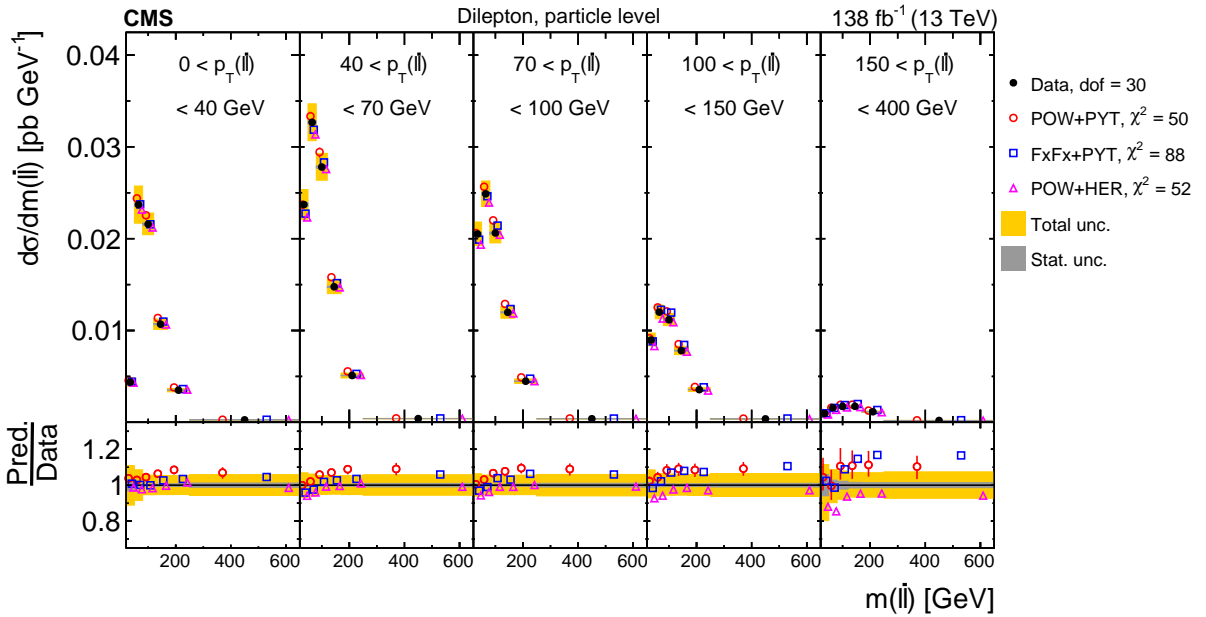
Figure 88: Absolute $[p_{\mathrm{T}}(\ell\bar{\ell}),\ m(\ell\bar{\ell})]$ cross sections are shown for data (filled circles) and various MC predictions (other points). Further details can be found in the caption of Fig. 82.

Figure 89: Absolute differential $t\bar{t}$ production cross sections as a function of N_{jet}, for a minimum jet p_T of 40 GeV (upper) and 100 GeV (lower), measured at the parton level in the full phase space (left) and at the particle level in a fiducial phase space (right). The data are shown as filled circles with grey and yellow bands indicating the statistical and total uncertainties (statistical and systematic uncertainties added in quadrature), respectively. For each distribution, the number of degrees of freedom (dof) is also provided. The cross sections are compared to various MC predictions (other points). The estimated uncertainties in the POWHEG+PYTHIA 8 ('POW-PYT') simulation are represented by vertical bars on the corresponding points. For each MC model, a value of χ^2 is reported that takes into account the measurement uncertainties. The lower panel in each plot shows the ratios of the predictions to the data.

Figure 90: Absolute $[N_{jet}, p_T(t)]$ cross sections measured at the parton level in the full phase space (upper) and at the particle level in a fiducial phase space (lower). The data are shown as filled circles with grey and yellow bands indicating the statistical and total (sum in quadrature of statistical and systematic) uncertainties, respectively. For each distribution, the number of degrees of freedom (dof) is also provided. The cross sections are compared to various MC predictions (other points). The estimated uncertainties in the POWHEG+PYTHIA 8 ('POW-PYT') simulation are represented by vertical bars on the corresponding points. For each MC model, a value of χ^2 is reported that takes into account the measurement uncertainties. The lower panel in each plot shows the ratios of the predictions to the data.

Figure 91: Absolute $[N_{\text{jet}}, |y(t)|]$ cross sections are shown for data (filled circles) and various MC predictions (other points). Further details can be found in the caption of Fig. 90.

Figure 92: Absolute $[N_{\text{jet}}, p_{\text{T}}(t\bar{t})]$ cross sections are shown for data (filled circles) and various MC predictions (other points). Further details can be found in the caption of Fig. 90.

Figure 93: Absolute $[N_{\mathrm{jet}}, m(t\bar{t})]$ cross sections are shown for data (filled circles) and various MC predictions (other points). Further details can be found in the caption of Fig. 90.

Figure 94: Absolute $[N_{jet}, |y(t\bar{t})|]$ cross sections are shown for data (filled circles) and various MC predictions (other points). Further details can be found in the caption of Fig. 90.

Figure 95: Absolute $[N_{\text{jet}}, |\Delta\eta(t,\bar{t})|]$ cross sections are shown for data (filled circles) and various MC predictions (other points). Further details can be found in the caption of Fig. 90.

Figure 96: Absolute $[N_{\text{jet}}^{0,1+}, m(t\bar{t}), |y(t\bar{t})|]$ cross sections are shown for data (filled circles) and various MC predictions (other points). Further details can be found in the caption of Fig. 90.

Figure 97: Absolute $[N_{\mathrm{jet}}^{0,1,2+}, m(t\bar{t}), |y(t\bar{t})|]$ cross sections are shown for data (filled circles) and various MC predictions (other points). Further details can be found in the caption of Fig. 90.

Figure 98: Absolute $[N_{jet}^{0,1,2,3+}, m(t\bar{t}), |y(t\bar{t})|]$ cross sections are shown for data (filled circles) and various MC predictions (other points). Further details can be found in the caption of Fig. 90.

Table 13: The χ^2 values and dof of the measured absolute single-differential cross sections for $t\bar{t}$ and top quark kinematic observables at the parton level are shown with respect to the predictions of various MC generators. The χ^2 values are calculated taking only measurement uncertainties into account and excluding theory uncertainties. For POW+PYT, the χ^2 values including theory uncertainties are indicated with the brackets (w. unc.).

Cross section variables	dof	χ^2		
		POW+PYT (w. unc.)	FxFx+PYT	POW+HER
$p_\mathrm{T}(t)$	7	21 (13)	43	5
$p_\mathrm{T}(\bar{t})$	7	19 (12)	43	6
$y(t)$	10	28 (24)	34	21
$y(\bar{t})$	10	33 (28)	40	25
$p_\mathrm{T}(t\bar{t})$	7	24 (8)	39	35
$y(t\bar{t})$	12	13 (9)	19	8
$m(t\bar{t})$	7	6 (4)	9	4
$|\Delta\phi(t,\bar{t})|$	4	4 (2)	7	11
$|y(t)| - |y(\bar{t})|$	8	18 (10)	19	14
$p_\mathrm{T}(t)/m(t\bar{t})$	5	39 (21)	104	13
$p_\mathrm{T}(t\bar{t})/m(t\bar{t})$	9	20 (7)	32	39
$\log(\xi_1)$	9	16 (12)	18	12
$\log(\xi_2)$	9	14 (9)	24	7

Table 14: The χ^2 values and dof of the measured absolute single-differential cross sections for t$\bar{\text{t}}$ and top quark kinematic observables at the particle level are shown with respect to the predictions of various MC generators. The χ^2 values are calculated taking only measurement uncertainties into account and excluding theory uncertainties. For POW+PYT, the χ^2 values including theory uncertainties are indicated with the brackets (w. unc.).

Cross section variables	dof	χ^2		
		POW+PYT (w. unc.)	FxFx+PYT	POW+HER
$p_T(t)$	7	22 (13)	44	7
$p_T(\bar{t})$	7	20 (12)	44	5
$y(t)$	10	24 (18)	32	19
$y(\bar{t})$	10	28 (23)	32	26
$p_T(t\bar{t})$	7	23 (8)	34	41
$y(t\bar{t})$	12	13 (8)	23	9
$m(t\bar{t})$	7	7 (4)	5	7
$|\Delta\phi(t,\bar{t})|$	4	4 (1)	4	7
$|y(t)| - |y(\bar{t})|$	8	17 (11)	15	18
$p_T(t)/m(t\bar{t})$	5	33 (23)	71	14
$p_T(t\bar{t})/m(t\bar{t})$	9	21 (7)	46	61
$\log(\xi_1)$	9	16 (10)	17	19
$\log(\xi_2)$	9	12 (7)	19	10

Table 15: The χ^2 values and dof of the measured absolute multi-differential cross sections for $t\bar{t}$ and top quark kinematic observables at the parton level are shown with respect to the predictions of various MC generators. The χ^2 values are calculated taking only measurement uncertainties into account and excluding theory uncertainties. For POW+PYT, the χ^2 values including theory uncertainties are indicated with the brackets (w. unc.).

Cross section variables	dof	χ^2 POW+PYT (w. unc.)	FxFx+PYT	POW+HER
$[|y(t)|,\ p_T(t)]$	16	48 (36)	75	30
$[m(t\bar{t}),\ p_T(t)]$	9	93 (36)	156	42
$[p_T(t),\ p_T(t\bar{t})]$	16	50 (25)	72	87
$[m(t\bar{t}),\ |y(t\bar{t})|]$	16	72 (46)	67	65
$[|y(t\bar{t})|,\ p_T(t\bar{t})]$	16	32 (17)	37	71
$[m(t\bar{t}),\ p_T(t\bar{t})]$	16	68 (47)	77	115
$[p_T(t\bar{t}),\ m(t\bar{t}),\ |y(t\bar{t})|]$	48	102 (71)	119	140
$[m(t\bar{t}),\ |y(t)|]$	16	67 (39)	84	49
$[m(t\bar{t}),\ |\Delta\eta(t,\bar{t})|]$	12	182 (34)	236	125
$[m(t\bar{t}),\ |\Delta\phi(t,\bar{t})|]$	12	82 (51)	50	93

Table 16: The χ^2 values and dof of the measured absolute multi-differential cross sections for $t\bar{t}$ and top quark kinematic observables at the particle level are shown with respect to the predictions of various MC generators. The χ^2 values are calculated taking only measurement uncertainties into account and excluding theory uncertainties. For POW+PYT, the χ^2 values including theory uncertainties are indicated with the brackets (w. unc.).

Cross section variables	dof	χ^2 POW+PYT (w. unc.)	FxFx+PYT	POW+HER
$[|y(t)|,\ p_T(t)]$	16	44 (28)	68	27
$[m(t\bar{t}),\ p_T(t)]$	9	103 (37)	151	46
$[p_T(t),\ p_T(t\bar{t})]$	16	44 (21)	68	64
$[m(t\bar{t}),\ |y(t\bar{t})|]$	16	86 (41)	77	81
$[|y(t\bar{t})|,\ p_T(t\bar{t})]$	16	32 (19)	41	66
$[m(t\bar{t}),\ p_T(t\bar{t})]$	16	69 (37)	57	112
$[p_T(t\bar{t}),\ m(t\bar{t}),\ |y(t\bar{t})|]$	48	133 (69)	130	170
$[m(t\bar{t}),\ |y(t)|]$	16	64 (27)	75	37
$[m(t\bar{t}),\ |\Delta\eta(t,\bar{t})|]$	12	174 (32)	220	114
$[m(t\bar{t}),\ |\Delta\phi(t,\bar{t})|]$	12	80 (44)	41	98

Table 17: The χ^2 values and dof of the measured absolute single-differential cross sections for lepton and b-jet kinematic observables at the particle level are shown with respect to the predictions of various MC generators. The χ^2 values are calculated taking only measurement uncertainties into account and excluding theory uncertainties. For POW+PYT, the χ^2 values including theory uncertainties are indicated with the brackets (w. unc.).

Cross section variables	dof	χ^2		
		POW+PYT (w. unc.)	FxFx+PYT	POW+HER
$p_{\mathrm{T}}(\ell)$	12	32 (19)	62	21
$p_{\mathrm{T}}(\ell)$ trailing$/p_{\mathrm{T}}(\ell)$ leading	10	16 (11)	27	7
$p_{\mathrm{T}}(\ell)/p_{\mathrm{T}}(\bar{\mathrm{t}})$	5	20 (17)	28	14
$p_{\mathrm{T}}(\mathrm{b})$ leading	10	6 (5)	31	8
$p_{\mathrm{T}}(\mathrm{b})$ trailing	7	7 (5)	26	7
$(p_{\mathrm{T}}(\mathrm{b}) + p_{\mathrm{T}}(\overline{\mathrm{b}}))/(p_{\mathrm{T}}(\mathrm{t}) + p_{\mathrm{T}}(\bar{\mathrm{t}}))$	4	24 (19)	30	21
$m(\ell\bar{\ell})$	12	31 (25)	29	23
$m(\mathrm{b}\overline{\mathrm{b}})$	7	21 (16)	17	15
$m(\ell\bar{\ell}\mathrm{b}\overline{\mathrm{b}})$	19	36 (19)	30	27
$p_{\mathrm{T}}(\ell\bar{\ell})$	9	4 (3)	17	10
$|\eta(\ell\bar{\ell})|$	14	16 (10)	22	12
$[|\eta(\ell\bar{\ell})|, m(\ell\bar{\ell})]$	24	55 (29)	76	35
$[|\eta(\ell\bar{\ell})|, p_{\mathrm{T}}(\ell\bar{\ell})]$	20	30 (15)	84	24
$[p_{\mathrm{T}}(\ell\bar{\ell}), m(\ell\bar{\ell})]$	30	50 (39)	88	52

Table 18: The χ^2 values and dof of the measured absolute differential cross sections as a function of the additional-jet multiplicity in the events, at the parton level of the top quark and antiquark, are shown with respect to the predictions of various MC generators. The χ^2 values are calculated taking only measurement uncertainties into account and excluding theory uncertainties. For POW+PYT, the χ^2 values including theory uncertainties are indicated with the brackets (w. unc.).

Cross section variables	dof	χ^2		
		POW+PYT (w. unc.)	FxFx+PYT	POW+HER
$N_{\mathrm{jet}}(p_{\mathrm{T}} > 40\,\mathrm{GeV})$	6	7 (5)	288	258
$N_{\mathrm{jet}}(p_{\mathrm{T}} > 100\,\mathrm{GeV})$	5	41 (11)	46	77
$[N_{\mathrm{jet}}, p_{\mathrm{T}}(\mathrm{t})]$	9	31 (17)	163	137
$[N_{\mathrm{jet}}, |y(\mathrm{t})|]$	12	42 (32)	131	85
$[N_{\mathrm{jet}}, p_{\mathrm{T}}(\mathrm{t\bar{t}})]$	12	58 (43)	192	93
$[N_{\mathrm{jet}}, m(\mathrm{t\bar{t}})]$	12	62 (48)	177	154
$[N_{\mathrm{jet}}, |y(\mathrm{t\bar{t}})|]$	12	14 (7)	122	61
$[N_{\mathrm{jet}}, |\Delta\eta(\mathrm{t},\bar{\mathrm{t}})|]$	9	94 (40)	194	144
$[N_{\mathrm{jet}}^{0,1+}, m(\mathrm{t\bar{t}}), |y(\mathrm{t\bar{t}})|]$	24	54 (39)	75	93
$[N_{\mathrm{jet}}^{0,1,2+}, m(\mathrm{t\bar{t}}), |y(\mathrm{t\bar{t}})|]$	36	93 (63)	223	215
$[N_{\mathrm{jet}}^{0,1,2,3+}, m(\mathrm{t\bar{t}}), |y(\mathrm{t\bar{t}})|]$	48	135 (92)	445	471

Table 19: The χ^2 values and dof of the measured absolute differential cross sections as a function of the additional-jet multiplicity in the events, at the particle level of the top quark and antiquark, are shown with respect to the predictions of various MC generators. The χ^2 values are calculated taking only measurement uncertainties into account and excluding theory uncertainties. For POW+PYT, the χ^2 values including theory uncertainties are indicated with the brackets (w. unc.).

Cross section	dof	χ^2		
variables		POW+PYT (w. unc.)	FxFx+PYT	POW+HER
$N_{\mathrm{jet}}(p_{\mathrm{T}} > 40\,\mathrm{GeV})$	6	7 (4)	355	8
$N_{\mathrm{jet}}(p_{\mathrm{T}} > 100\,\mathrm{GeV})$	5	45 (11)	40	7
$[N_{\mathrm{jet}},\, p_{\mathrm{T}}(\mathrm{t})]$	9	37 (15)	249	25
$[N_{\mathrm{jet}},\, |y(\mathrm{t})|]$	12	44 (26)	182	27
$[N_{\mathrm{jet}},\, p_{\mathrm{T}}(\mathrm{t\bar{t}})]$	12	67 (41)	341	86
$[N_{\mathrm{jet}},\, m(\mathrm{t\bar{t}})]$	12	60 (40)	302	50
$[N_{\mathrm{jet}},\, |y(\mathrm{t\bar{t}})|]$	12	17 (6)	188	8
$[N_{\mathrm{jet}},\, |\Delta\eta(\mathrm{t},\bar{\mathrm{t}})|]$	9	138 (43)	306	103
$[N_{\mathrm{jet}}^{0,1+},\, m(\mathrm{t\bar{t}}),\, |y(\mathrm{t\bar{t}})|]$	24	85 (46)	101	87
$[N_{\mathrm{jet}}^{0,1,2+},\, m(\mathrm{t\bar{t}}),\, |y(\mathrm{t\bar{t}})|]$	36	144 (71)	401	137
$[N_{\mathrm{jet}}^{0,1,2,3+},\, m(\mathrm{t\bar{t}}),\, |y(\mathrm{t\bar{t}})|]$	48	176 (97)	736	161

B.2 Comparisons to higher-order theoretical predictions

The absolute differential cross sections comparing data to theoretical predictions of beyond-NLO precision are shown in Figs. 99–121, and the corresponding χ^2 values are given in Tables 20–24. The p-values of the χ^2 tests are presented in Tables 44–48. The theoretical calculations are those discussed in Section 9.4: aN^{3}LO, STRIPPER (NNLO), MATRIX (NNLO), and MINNLOPS (NNLOPS). Comparing the absolute cross sections to the normalized ones in Section 9.4, one can see a similar level of agreement between data and predictions. We conclude that the calculations provide overall reasonable predictions of the total normalization of the data.
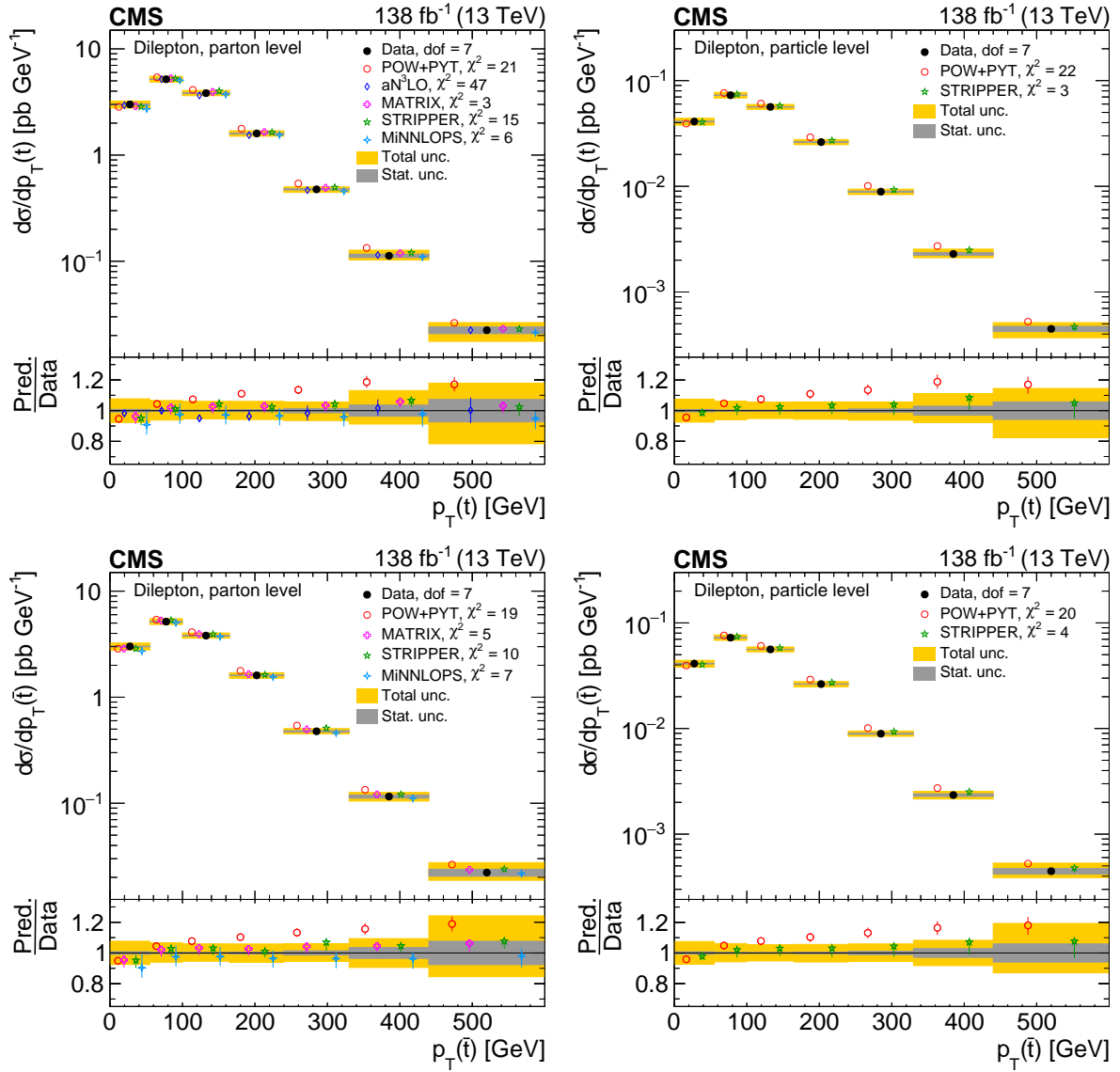
Figure 99: Absolute differential $t\bar{t}$ production cross sections as functions of $p_T(t)$ (upper) and $p_T(\bar{t})$ (lower), measured at the parton level in the full phase space (left) and at the particle level in a fiducial phase space (right). The data are shown as filled circles with grey and yellow bands indicating the statistical and total uncertainties (statistical and systematic uncertainties added in quadrature), respectively. For each distribution, the number of degrees of freedom (dof) is also provided. The cross sections are compared to predictions from the POWHEG+PYTHIA 8 ('POW-PYT', open circles) simulation and various theoretical predictions with beyond-NLO precision (other points). The estimated uncertainties in the predictions are represented by vertical bars on the corresponding points. For each model, a value of χ^2 is reported that takes into account the measurement uncertainties. The lower panel in each plot shows the ratios of the predictions to the data.

Figure 100: Absolute differential $t\bar{t}$ production cross sections as functions of $y(t)$ (upper) and $y(\bar{t})$ (lower) are shown for data (filled circles), POWHEG+PYTHIA 8 ('POW-PYT', open circles) simulation, and various theoretical predictions with beyond-NLO precision (other points). Further details can be found in the caption of Fig. 99.
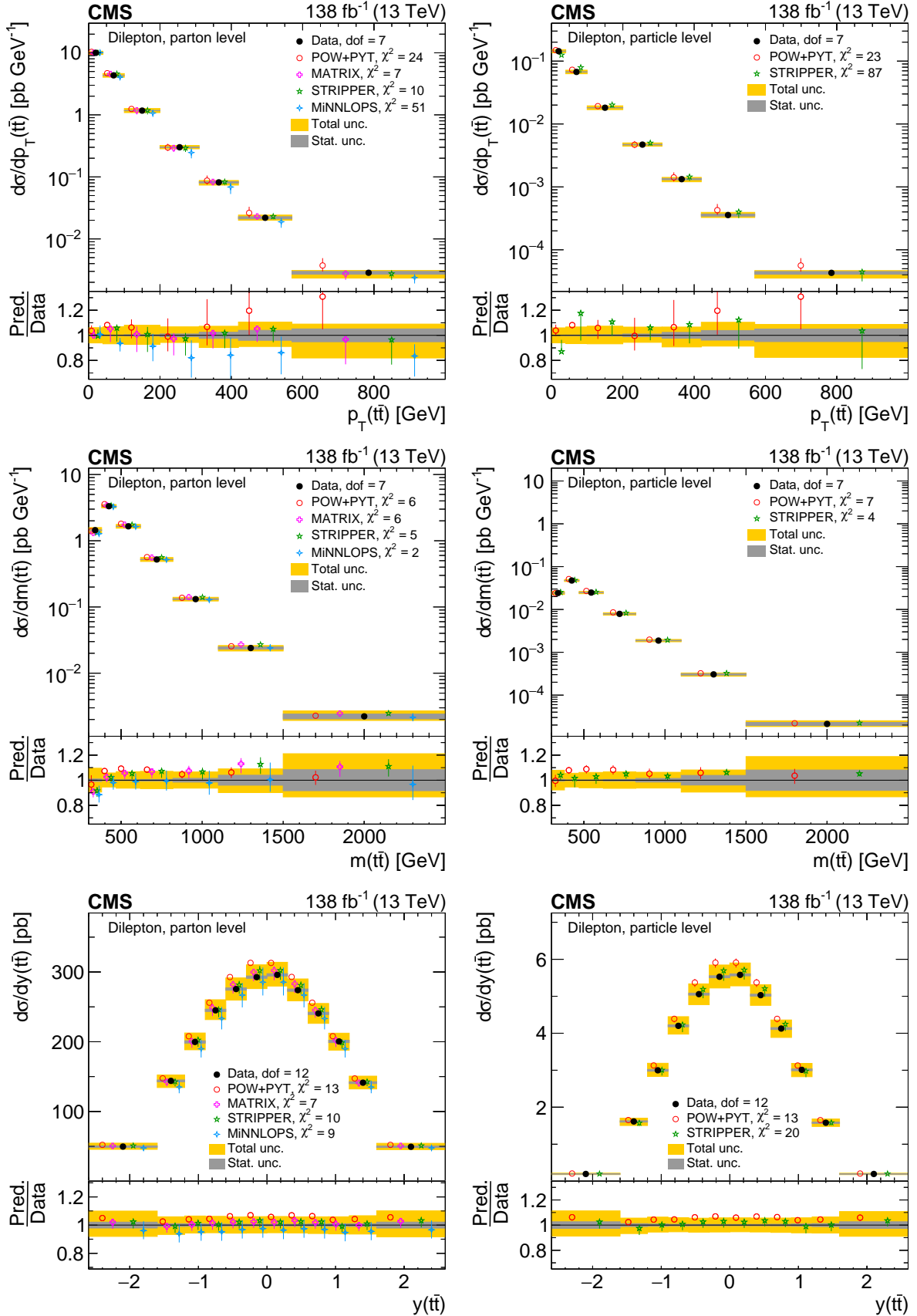
Figure 101: Absolute differential $t\bar{t}$ production cross sections as functions of $p_\mathrm{T}(t\bar{t})$ (upper), $m(t\bar{t})$ (middle), and $y(t\bar{t})$ (lower) are shown for data (filled circles), POWHEG+PYTHIA 8 ('POW-PYT', open circles) simulation, and various theoretical predictions with beyond-NLO precision (other points). Further details can be found in the caption of Fig. 99.
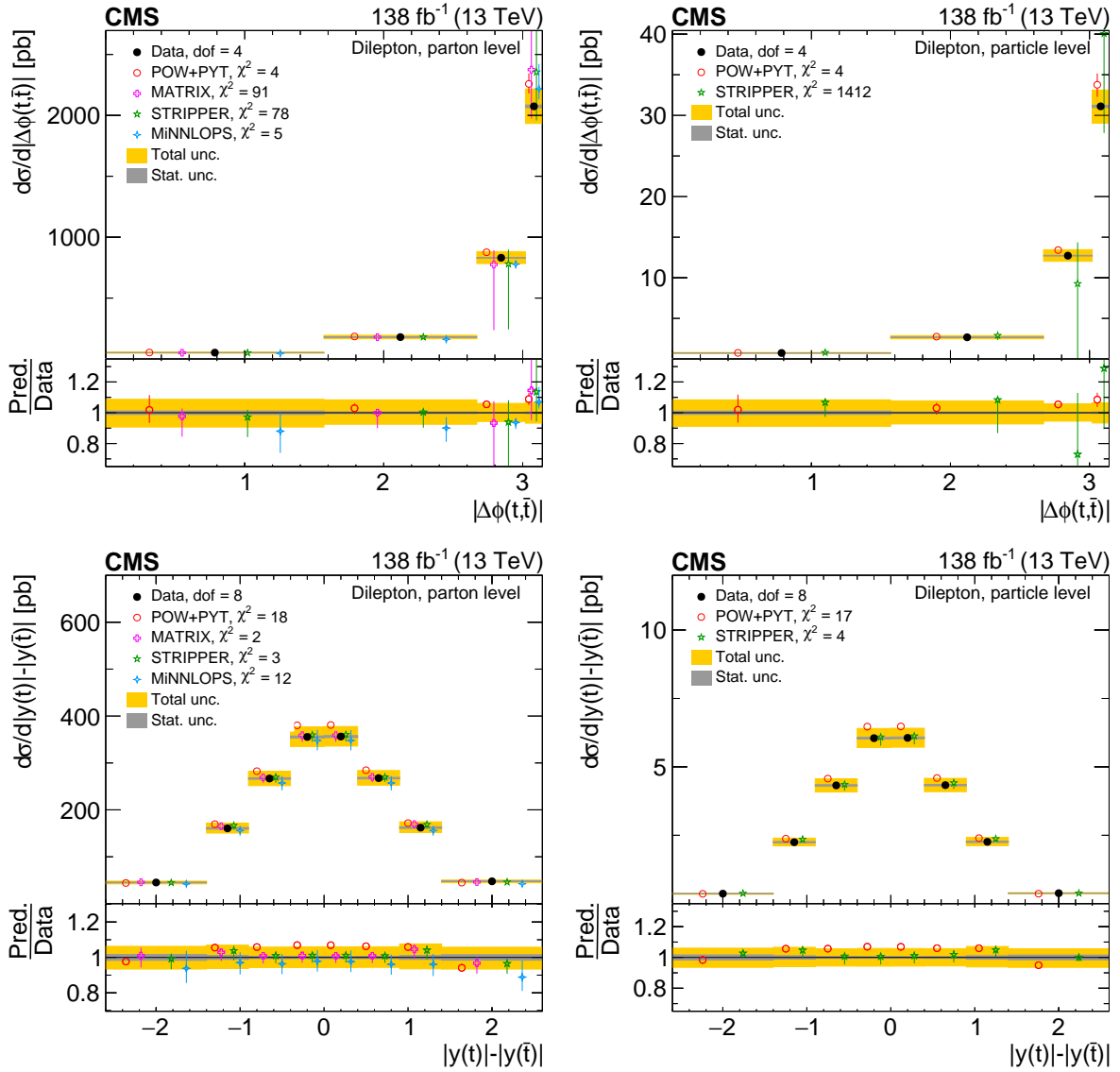
Figure 102: Absolute differential $t\bar{t}$ production cross sections as functions of $|\Delta\phi(t,\bar{t})|$ (upper) and $|y(t)| - |y(\bar{t})|$ (lower) are shown for data (filled circles), POWHEG+PYTHIA 8 ('POW-PYT', open circles) simulation, and various theoretical predictions with beyond-NLO precision (other points). Further details can be found in the caption of Fig. 99.
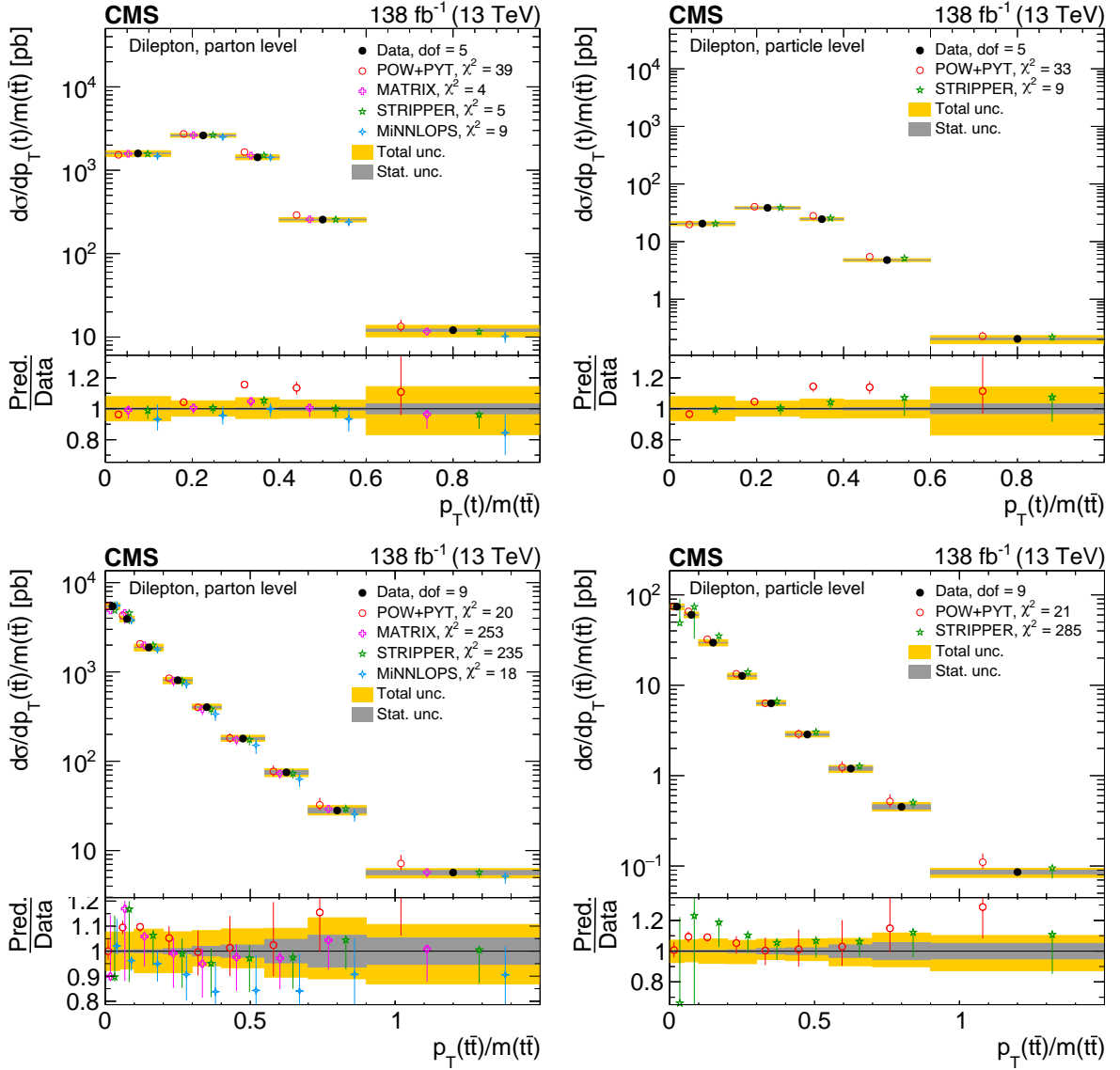
Figure 103: Absolute differential $t\bar{t}$ production cross sections as functions of $p_T(t)/m(t\bar{t})$ (upper) and $p_T(t\bar{t})/m(t\bar{t})$ (lower) are shown for data (filled circles), POWHEG+PYTHIA 8 ('POW-PYT', open circles) simulation, and various theoretical predictions with beyond-NLO precision (other points). Further details can be found in the caption of Fig. 99.
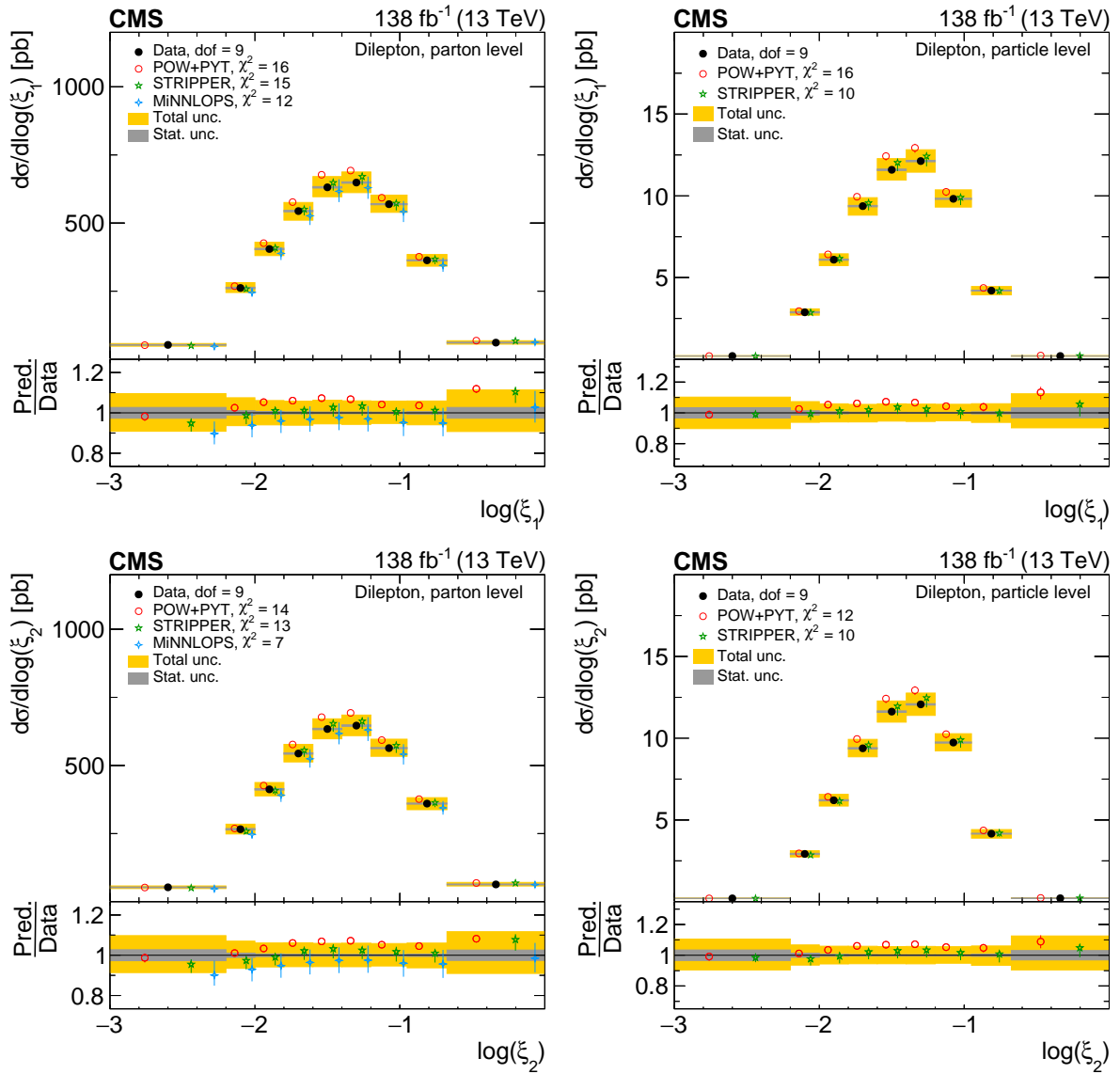
Figure 104: Absolute differential $t\bar{t}$ production cross sections as functions of $\log(\xi_1)$ (upper) and $\log(\xi_2)$ (lower) are shown for data (filled circles), POWHEG+PYTHIA 8 ('POW-PYT', open circles) simulation, and STRIPPER NNLO calculation (stars). Further details can be found in the caption of Fig. 99.
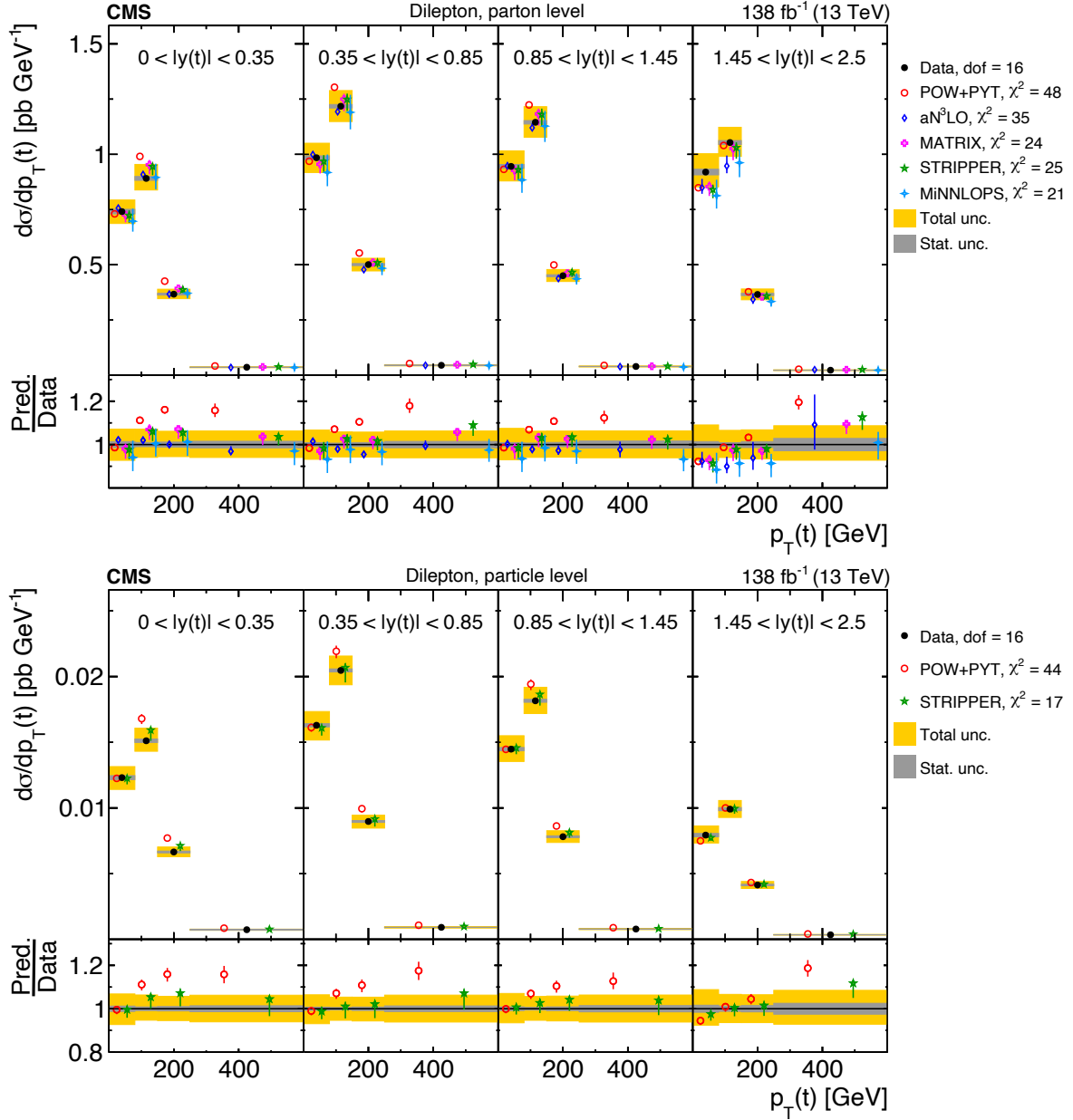
Figure 105: Absolute $[|y(\mathrm{t})|, p_\mathrm{T}(\mathrm{t})]$ cross sections measured at the parton level in the full phase space (upper) and at the particle level in a fiducial phase space (lower). The data are shown as filled circles with grey and yellow bands indicating the statistical and total uncertainties (statistical and systematic uncertainties added in quadrature), respectively. For each distribution, the number of degrees of freedom (dof) is also provided. The cross sections are compared to predictions from the POWHEG+PYTHIA 8 ('POW-PYT', open circles) simulation and various theoretical predictions with beyond-NLO precision (other points). The estimated uncertainties in the predictions are represented by vertical bars on the corresponding points. For each model, a value of χ^2 is reported that takes into account the measurement uncertainties. The lower panel in each plot shows the ratios of the predictions to the data.

Figure 106: Absolute $[m(t\bar{t}), p_T(t)]$ cross sections are shown for data (filled circles), POWHEG+PYTHIA 8 ('POW-PYT', open circles) simulation, and various theoretical predictions with beyond-NLO precision (other points). Further details can be found in the caption of Fig. 105.
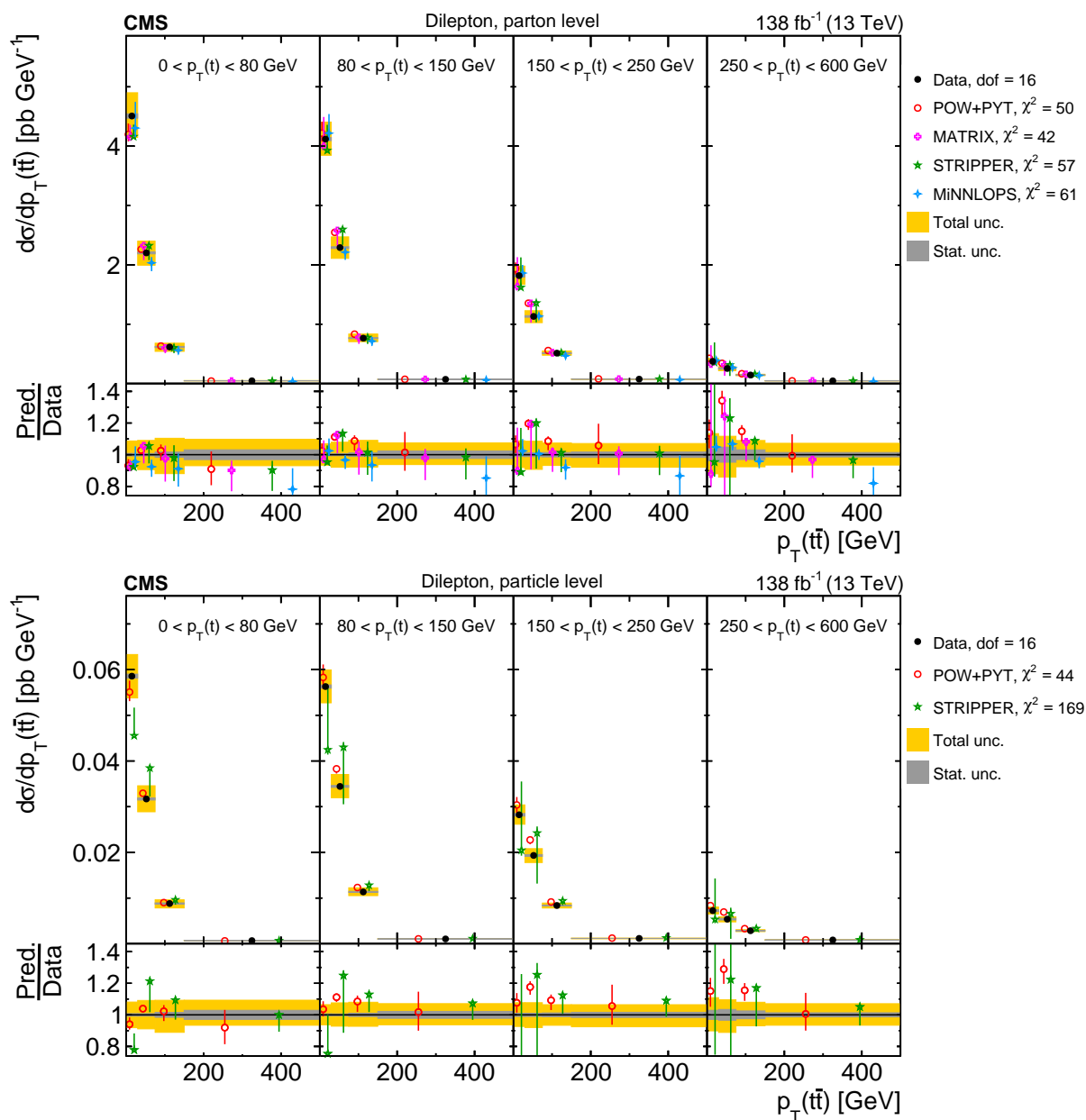
Figure 107: Absolute $[p_T(t), p_T(t\bar{t})]$ cross sections are shown for data (filled circles), POWHEG+PYTHIA 8 ('POW-PYT', open circles) simulation, and various theoretical predictions with beyond-NLO precision (other points). Further details can be found in the caption of Fig. 105.
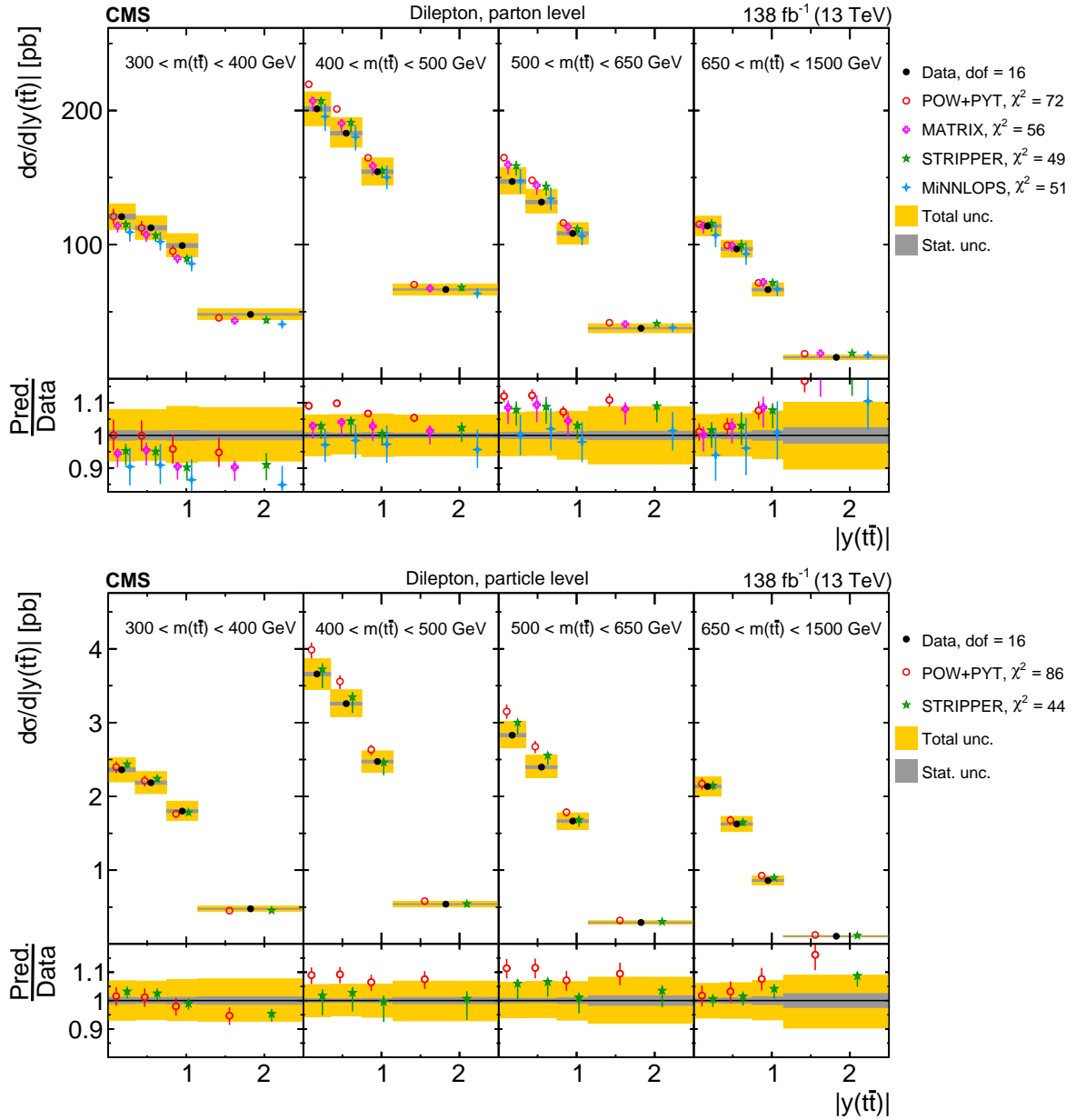
Figure 108: Absolute $[m(t\bar{t}), |y(t\bar{t})|]$ cross sections are shown for data (filled circles), POWHEG+PYTHIA 8 ('POW-PYT', open circles) simulation, and various theoretical predictions with beyond-NLO precision (other points). Further details can be found in the caption of Fig. 105.
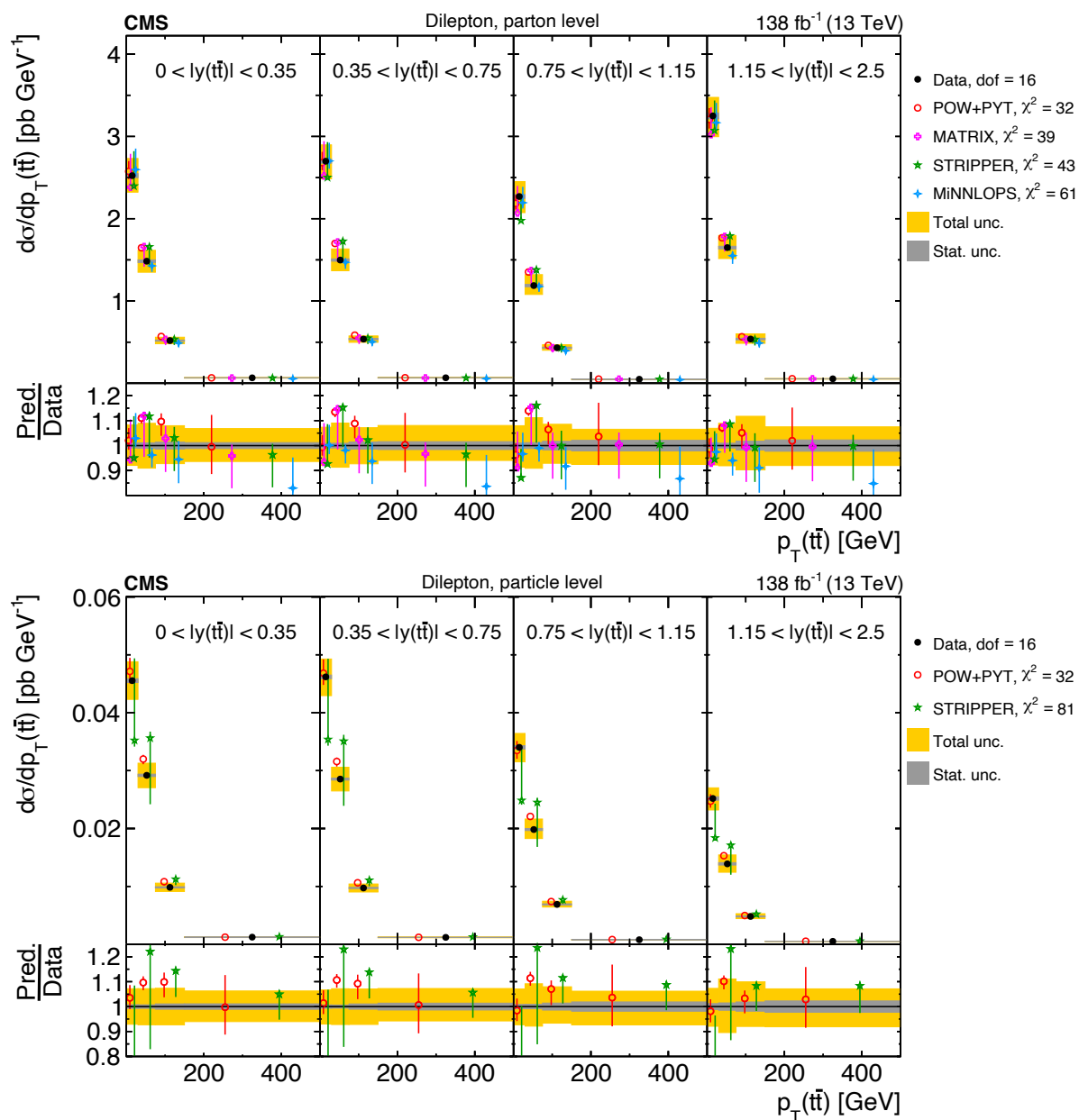
Figure 109:   Absolute $[|y(t\bar{t})|, p_{\mathrm{T}}(t\bar{t})]$ cross sections are shown for data (filled circles), POWHEG+PYTHIA 8 ('POW-PYT', open circles) simulation, and various theoretical predictions with beyond-NLO precision (other points). Further details can be found in the caption of Fig. 105.
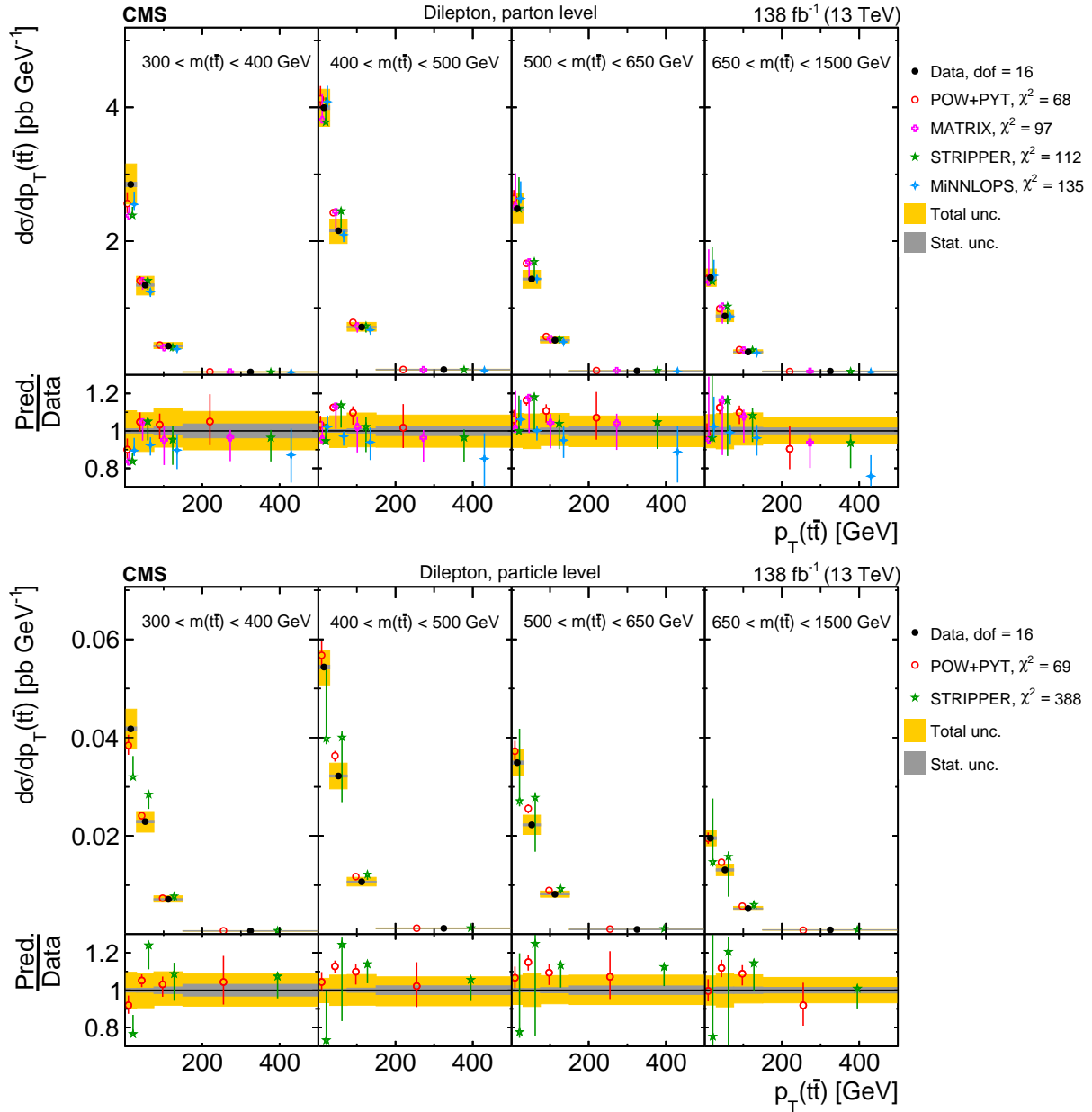
Figure 110: Absolute $[m(t\bar{t}), p_\mathrm{T}(t\bar{t})]$ cross sections are shown for data (filled circles), POWHEG+PYTHIA 8 ('POW-PYT', open circles) simulation, and various theoretical predictions with beyond-NLO precision (other points). Further details can be found in the caption of Fig. 105.
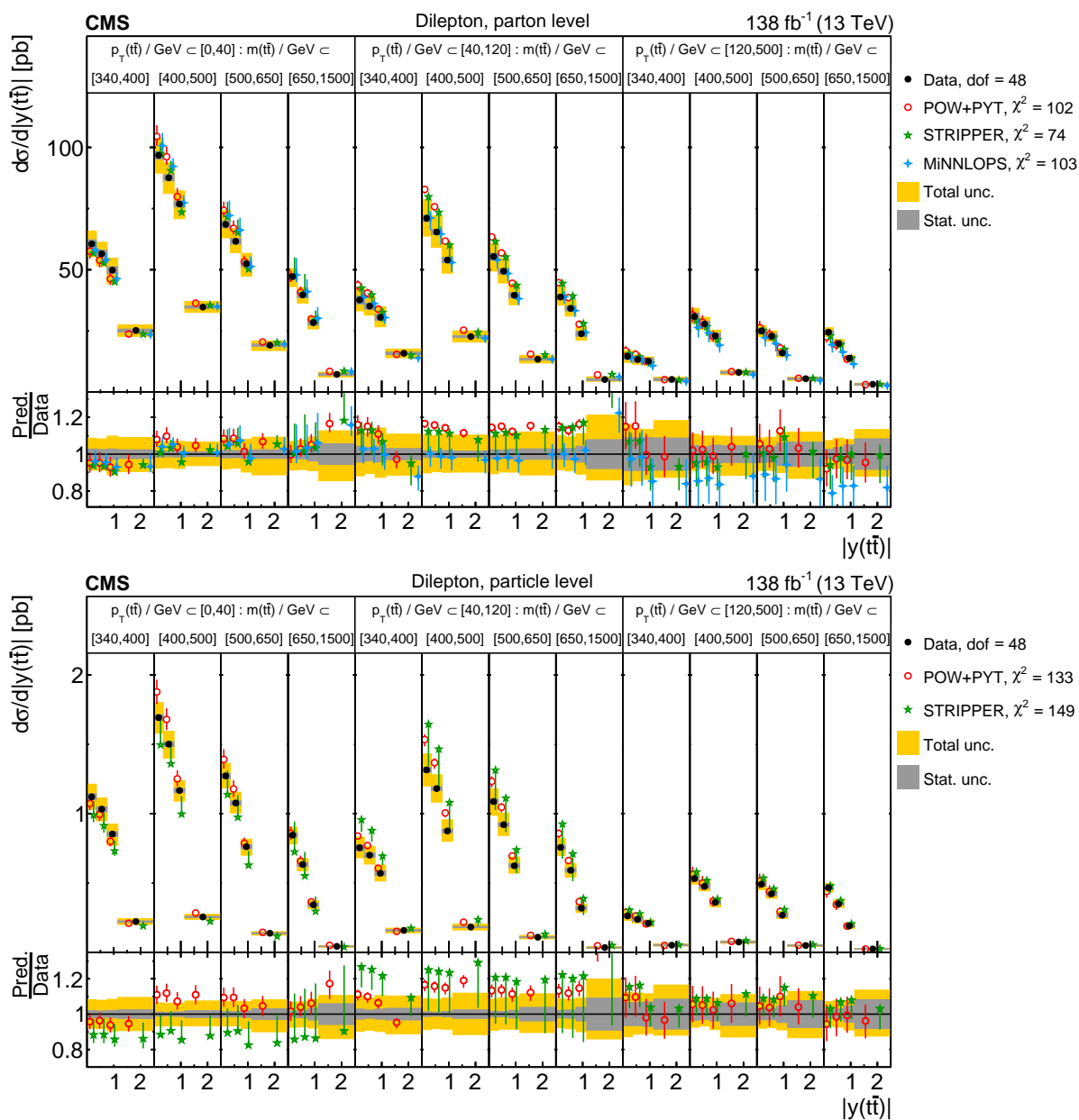
Figure 111: Absolute $[p_T(t\bar{t}), m(t\bar{t}), |y(t\bar{t})|]$ cross sections are shown for data (filled circles), POWHEG+PYTHIA 8 ('POW-PYT', open circles) simulation, and various theoretical predictions with beyond-NLO precision (other points). Further details can be found in the caption of Fig. 105.
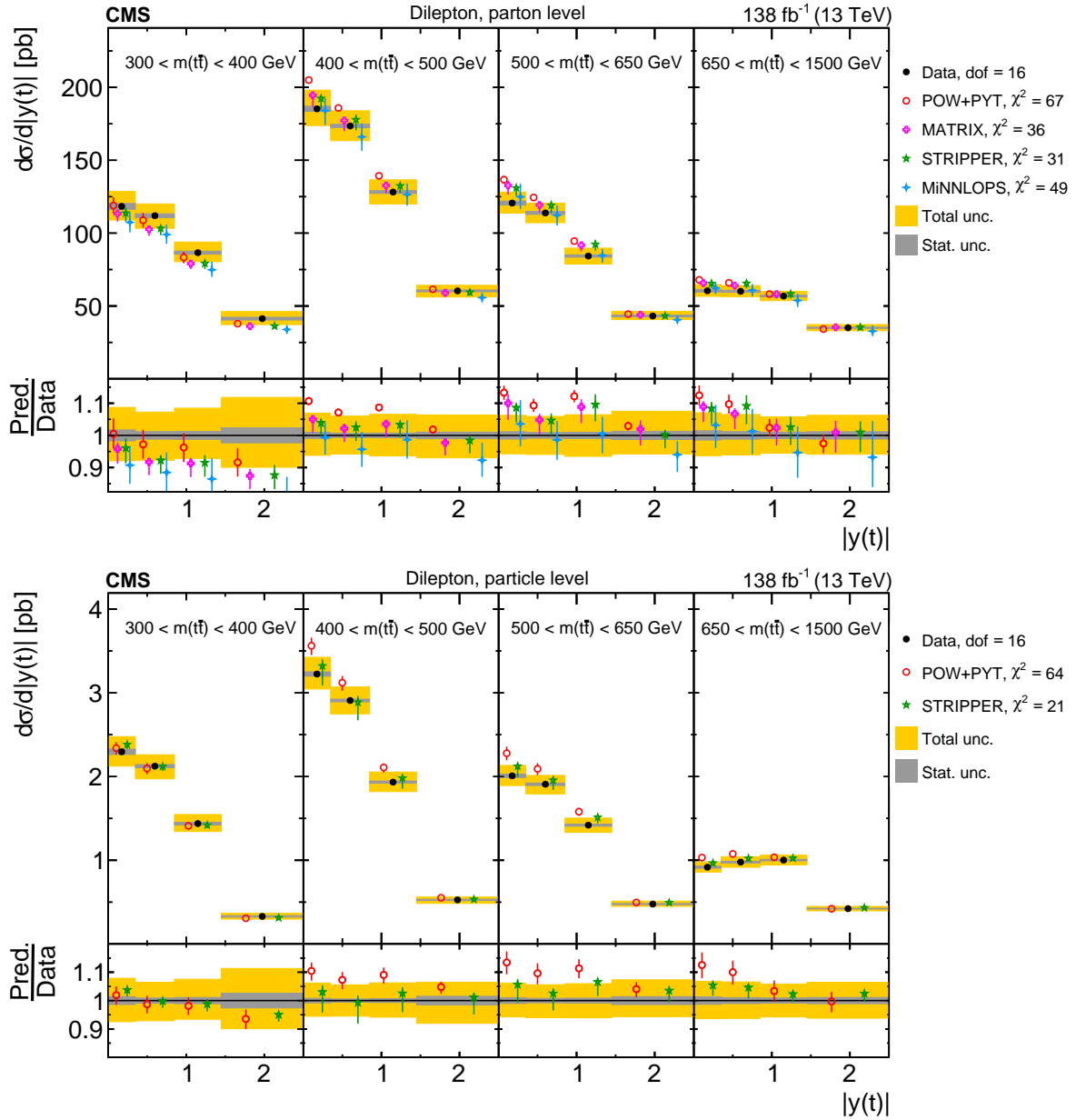
Figure 112: Absolute $[m(t\bar{t}), |y(t)|]$ cross sections are shown for data (filled circles), POWHEG+PYTHIA 8 ('POW-PYT', open circles) simulation, and various theoretical predictions with beyond-NLO precision (other points). Further details can be found in the caption of Fig. 105.
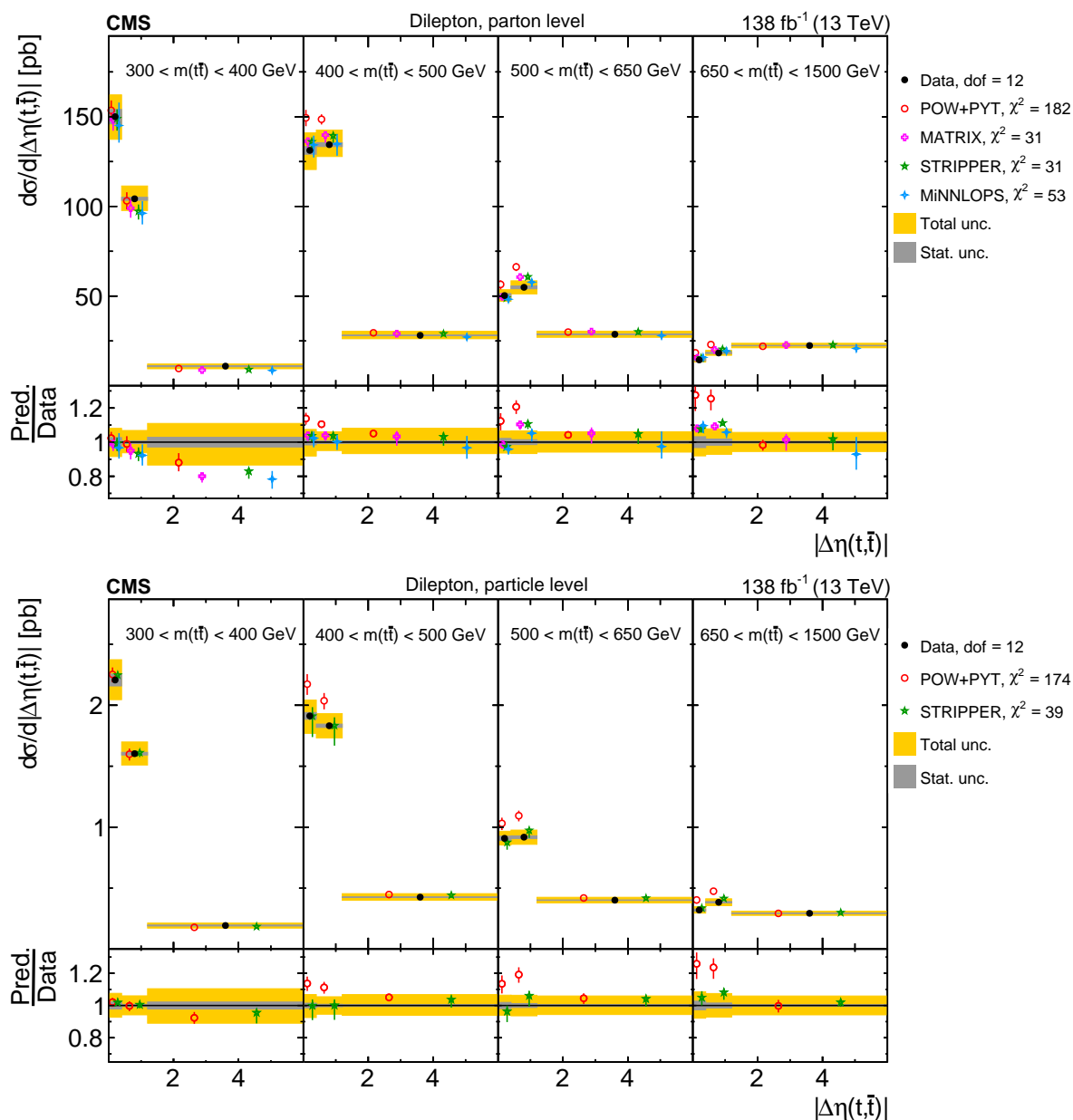
Figure 113: Absolute $[m(t\bar{t}), |\Delta\eta(t,\bar{t})|]$ cross sections are shown for data (filled circles), POWHEG+PYTHIA 8 ('POW-PYT', open circles) simulation, and various theoretical predictions with beyond-NLO precision (other points). Further details can be found in the caption of Fig. 105.

Figure 114: Absolute $[m(t\bar{t}), |\Delta\phi(t,\bar{t})|]$ cross sections are shown for data (filled circles), POWHEG+PYTHIA 8 ('POW-PYT', open circles) simulation, and various theoretical predictions with beyond-NLO precision (other points). Further details can be found in the caption of Fig. 105.
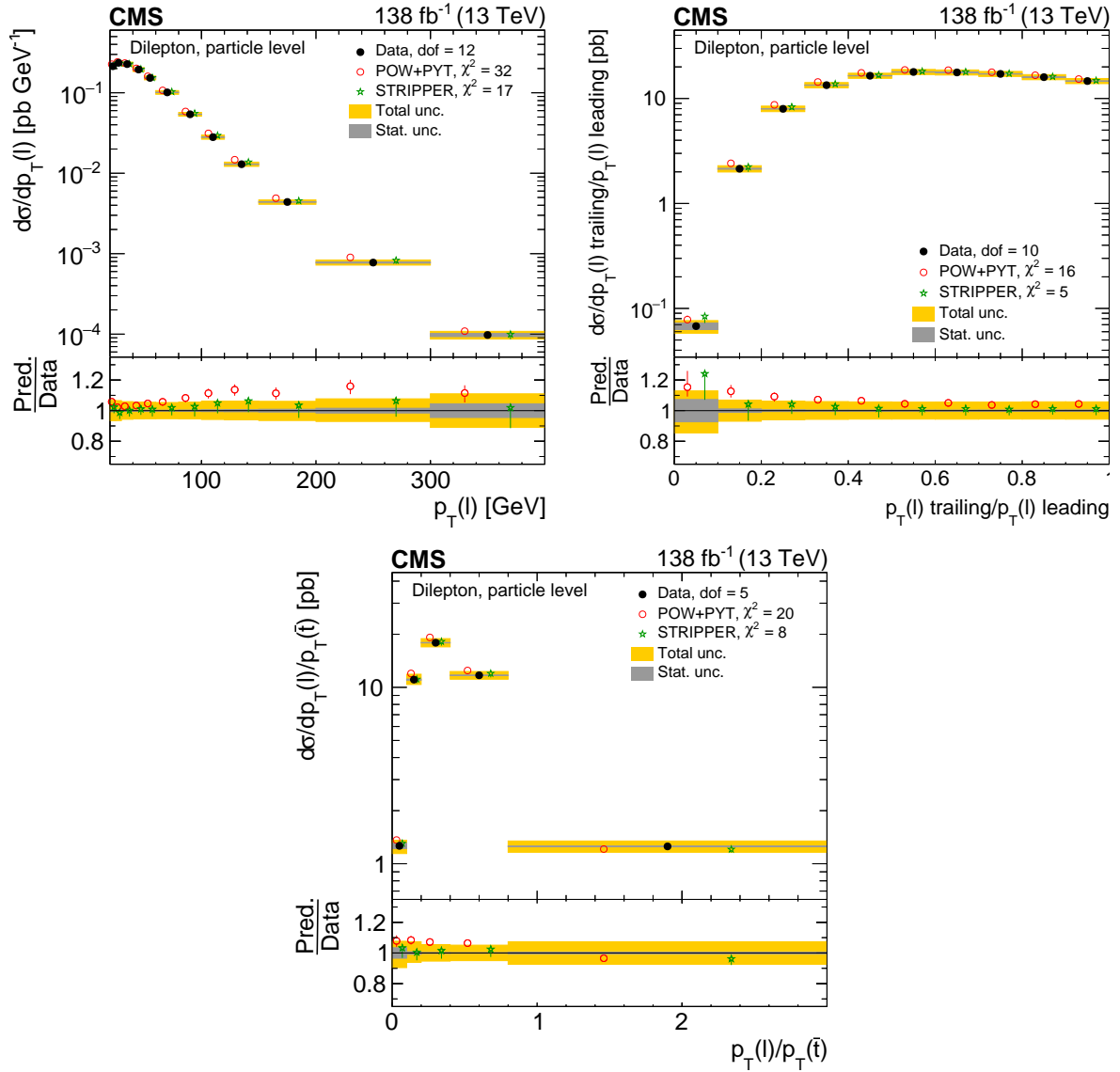
Figure 115: Absolute differential $t\bar{t}$ production cross sections as functions of p_T of the lepton (upper left), of the ratio of the trailing and leading lepton p_T (upper right), and of the ratio of lepton and top antiquark p_T (lower), measured at the particle level in a fiducial phase space. The data are shown as filled circles with grey and yellow bands indicating the statistical and total uncertainties (statistical and systematic uncertainties added in quadrature), respectively. For each distribution, the number of degrees of freedom (dof) is also provided. The cross sections are compared to predictions from the POWHEG+PYTHIA 8 ('POW-PYT', open circles) simulation and STRIPPER NNLO calculation (stars). The estimated uncertainties in the predictions are represented by vertical bars on the corresponding points. For each model, a value of χ^2 is reported that takes into account the measurement uncertainties. The lower panel in each plot shows the ratios of the predictions to the data.

Figure 116: Absolute differential t$\bar{\text{t}}$ production cross sections as functions of the p_T of the leading (upper left) and trailing (upper right) b jet, and $(p_\text{T}(\text{b}) + p_\text{T}(\bar{\text{b}}))/(p_\text{T}(\text{t}) + p_\text{T}(\bar{\text{t}}))$ (lower) d-NLO precision (other points). are shown for data (filled circles), POWHEG+PYTHIA 8 ('POW-PYT', open circles) simulation, and STRIPPER NNLO calculation (stars). Further details can be found in the caption of Fig. 115.
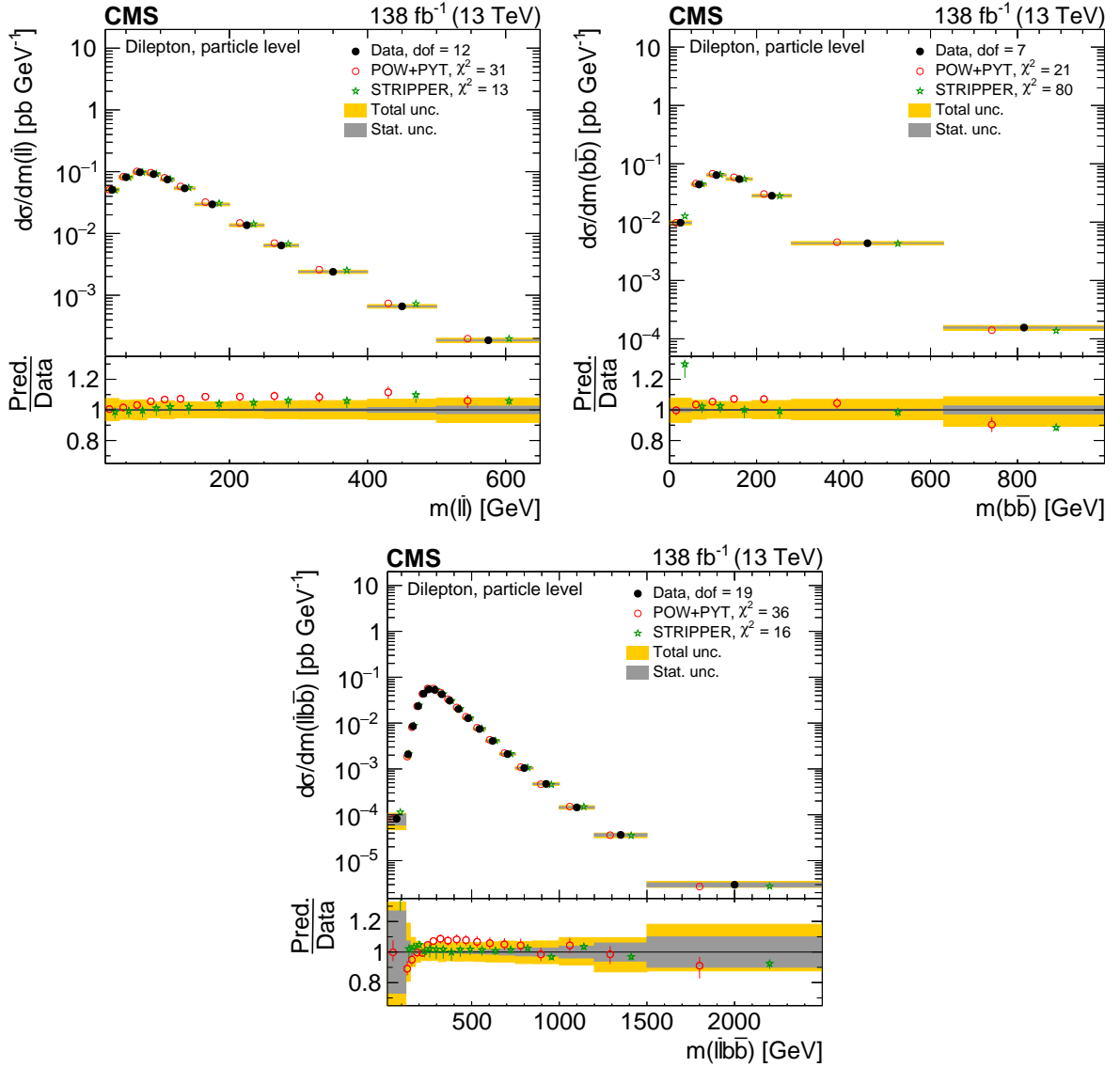
Figure 117: Absolute differential $t\bar{t}$ production cross sections as functions of $m(\ell\bar{\ell})$ (upper left), $m(b\bar{b})$ (upper right), and $m(\ell\bar{\ell}b\bar{b})$ (lower) are shown for data (filled circles), POWHEG+PYTHIA 8 ('POW-PYT', open circles) simulation, and STRIPPER NNLO calculation (stars). Further details can be found in the caption of Fig. 115.
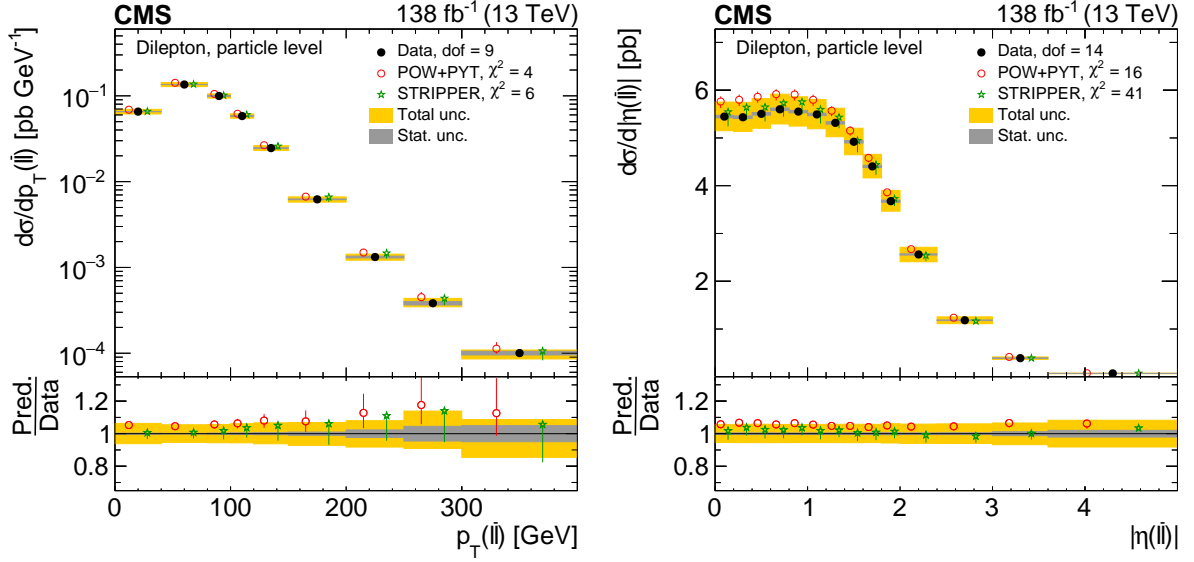
Figure 118: Absolute differential $t\bar{t}$ production cross sections as functions of $p_{\mathrm{T}}(\ell\bar{\ell})$ (left) and $|\eta(\ell\bar{\ell})|$ (right) are shown for data (filled circles), POWHEG+PYTHIA 8 ('POW-PYT', open circles) simulation, and STRIPPER NNLO calculation (stars). Further details can be found in the caption of Fig. 115.
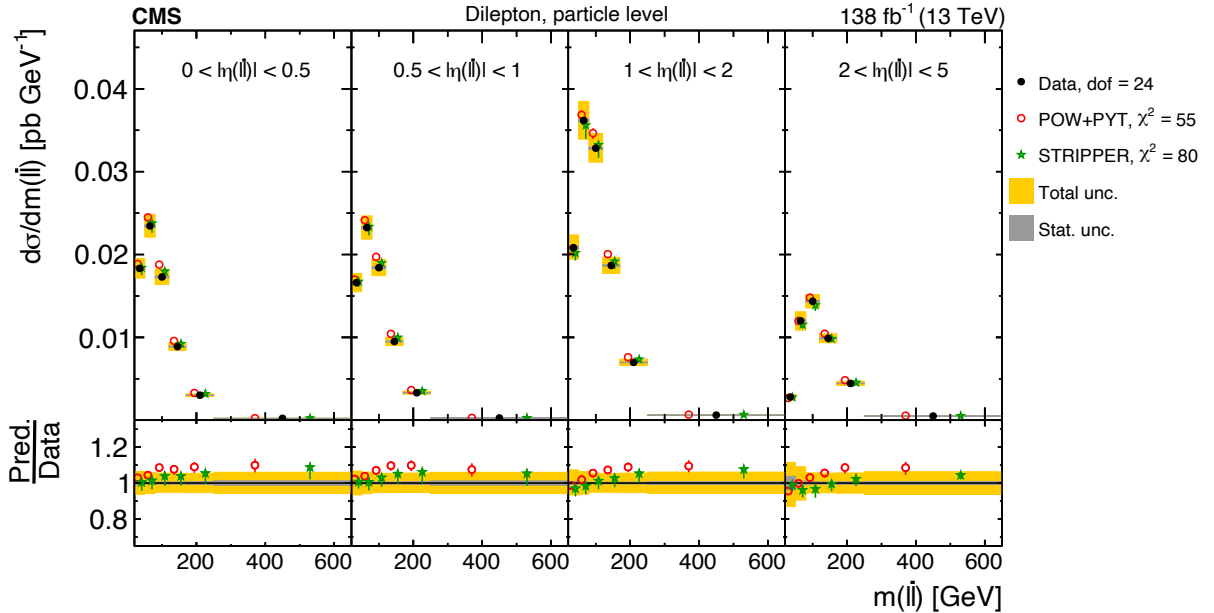
Figure 119: Absolute $[|\eta(\ell\bar{\ell})|, m(\ell\bar{\ell})]$ cross sections are shown for data (filled circles), POWHEG+PYTHIA 8 ('POW-PYT', open circles) simulation, and STRIPPER NNLO calculation (stars). Further details can be found in the caption of Fig. 115.
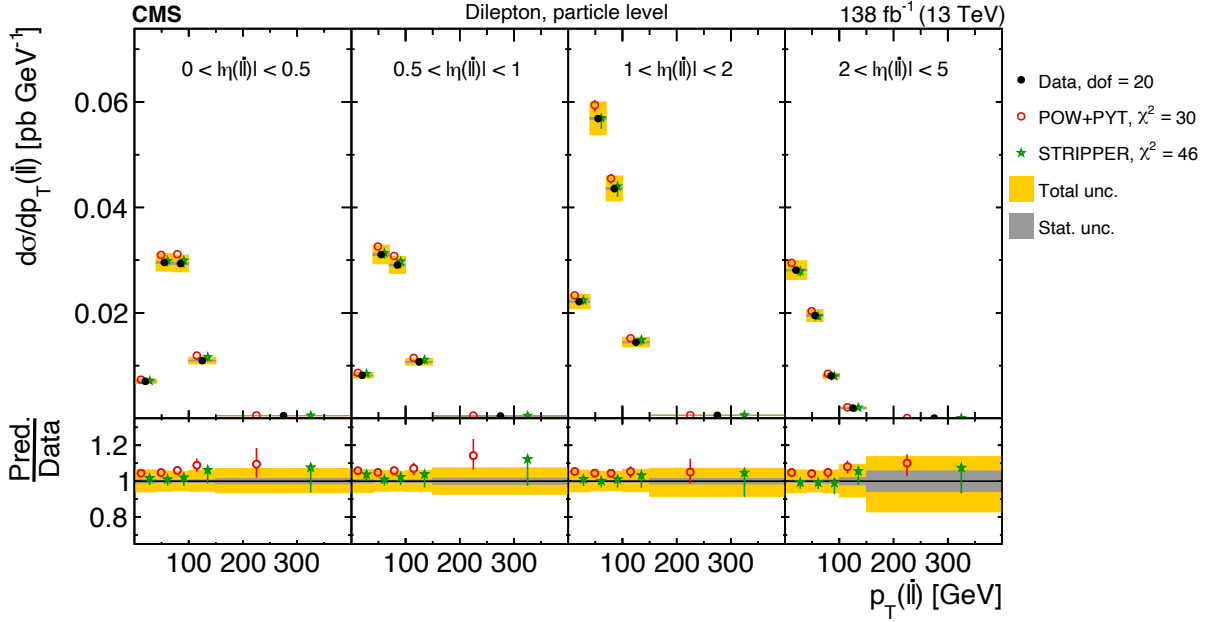
Figure 120: Absolute $[|\eta(\ell\bar\ell)|, p_T(\ell\bar\ell)]$ cross sections are shown for data (filled circles), POWHEG+PYTHIA 8 ('POW-PYT', open circles) simulation, and STRIPPER NNLO calculation (stars). Further details can be found in the caption of Fig. 115.
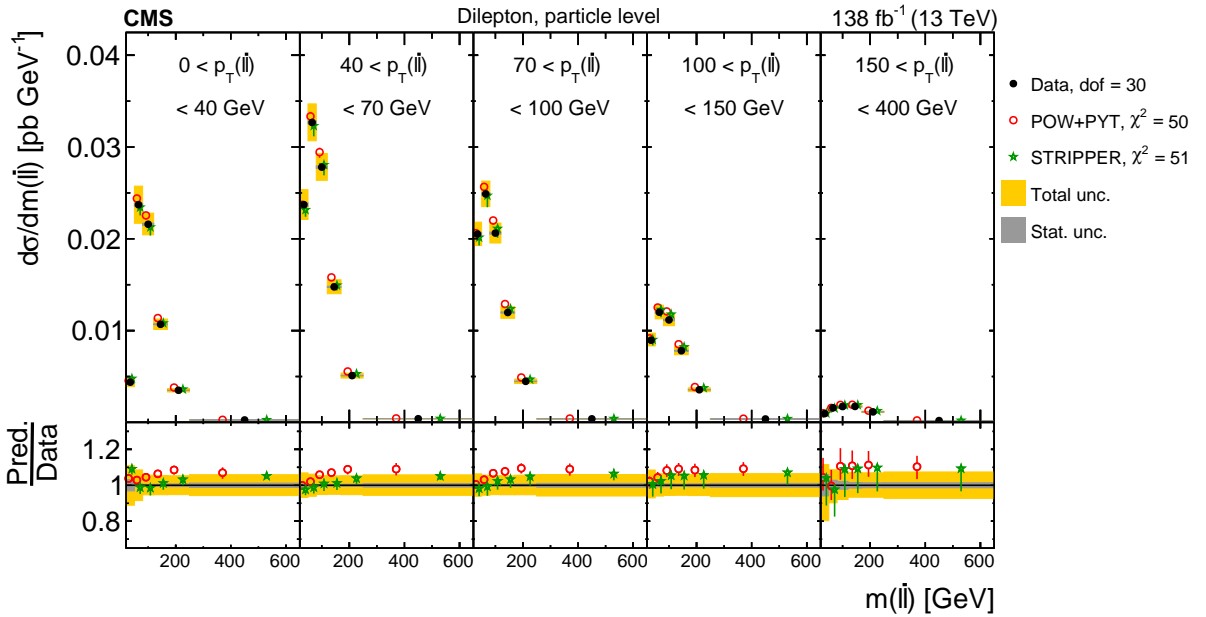
Figure 121: Absolute $[p_T(\ell\bar\ell), m(\ell\bar\ell)]$ cross sections are shown for data (filled circles), POWHEG+PYTHIA 8 ('POW-PYT', open circles) simulation, and STRIPPER NNLO calculation (stars). Further details can be found in the caption of Fig. 115.

Table 20: The χ^2 values and dof of the measured absolute single-differential cross sections for $t\bar{t}$ and top quark kinematic observables at the parton level are shown with respect to the POWHEG+PYTHIA8 ('POW-PYT') simulation and various theoretical predictions with beyond-NLO precision. The χ^2 values are calculated taking only measurement uncertainties into account and excluding theory uncertainties. For POW+PYT, the χ^2 values including theory uncertainties are indicated with the brackets (w. unc.).

Cross section variables	dof	POW+PYT (w. unc.)	χ^2 $a\mathrm{N^3LO}$	Matrix	Stripper	MiNNLOPS
$p_T(t)$	7	21 (13)	47	3	15	6
$p_T(\bar{t})$	7	19 (12)	—	5	10	7
$y(t)$	10	28 (24)	24	17	17	14
$y(\bar{t})$	10	33 (28)	—	15	26	22
$p_T(t\bar{t})$	7	24 (8)	—	7	10	51
$y(t\bar{t})$	12	13 (9)	—	7	10	9
$m(t\bar{t})$	7	6 (4)	—	6	5	2
$|\Delta\phi(t,\bar{t})|$	4	4 (2)	—	91	78	5
$|y(t)| - |y(\bar{t})|$	8	18 (10)	—	2	3	12
$p_T(t)/m(t\bar{t})$	5	39 (21)	—	4	5	9
$p_T(t\bar{t})/m(t\bar{t})$	9	20 (7)	—	253	235	18
$\log(\xi_1)$	9	16 (12)	—	—	15	12
$\log(\xi_2)$	9	14 (9)	—	—	13	7

Table 21: The χ^2 values and dof of the measured absolute single-differential cross sections for $t\bar{t}$ and top quark kinematic observables at the particle level are shown with respect to the POWHEG+PYTHIA 8 ('POW-PYT') simulation and the STRIPPER NNLO calculation. The χ^2 values are calculated taking only measurement uncertainties into account and excluding theory uncertainties. For POW+PYT, the χ^2 values including theory uncertainties are indicated with the brackets (w. unc.).

Cross section variables	dof	χ^2	
		POW+PYT (w. unc.)	STRIPPER
$p_T(t)$	7	22 (13)	3
$p_T(\bar{t})$	7	20 (12)	4
$y(t)$	10	24 (18)	11
$y(\bar{t})$	10	28 (23)	10
$p_T(t\bar{t})$	7	23 (8)	87
$y(t\bar{t})$	12	13 (8)	20
$m(t\bar{t})$	7	7 (4)	4
$\|\Delta\phi(t,\bar{t})\|$	4	4 (1)	1412
$\|y(t)\| - \|y(\bar{t})\|$	8	17 (11)	4
$p_T(t)/m(t\bar{t})$	5	33 (23)	9
$p_T(t\bar{t})/m(t\bar{t})$	9	21 (7)	285
$\log(\xi_1)$	9	16 (10)	10
$\log(\xi_2)$	9	12 (7)	10

Table 22: The χ^2 values and dof of the measured absolute multi-differential cross sections for $t\bar{t}$ and top quark kinematic observables at the parton level are shown with respect to the POWHEG+PYTHIA 8 ('POW-PYT') simulation and various theoretical predictions with beyond-NLO precision. The χ^2 values are calculated taking only measurement uncertainties into account and excluding theory uncertainties. For POW+PYT, the χ^2 values including theory uncertainties are indicated with the brackets (w. unc.).

Cross section variables	dof	χ^2				
		POW+PYT (w. unc.)	$a\mathrm{N^3LO}$	MATRIX	STRIPPER	MINNLOPS
$[\lvert y(t)\rvert, p_T(t)]$	16	48 (36)	35	24	25	21
$[m(t\bar{t}), p_T(t)]$	9	93 (36)	—	19	17	17
$[p_T(t), p_T(t\bar{t})]$	16	50 (25)	—	42	57	61
$[m(t\bar{t}), \lvert y(t\bar{t})\rvert]$	16	72 (46)	—	56	49	51
$[\lvert y(t\bar{t})\rvert, p_T(t\bar{t})]$	16	32 (17)	—	39	43	61
$[m(t\bar{t}), p_T(t\bar{t})]$	16	68 (47)	—	97	112	135
$[p_T(t\bar{t}), m(t\bar{t}), \lvert y(t\bar{t})\rvert]$	48	102 (71)	—	—	74	103
$[m(t\bar{t}), \lvert y(t)\rvert]$	16	67 (39)	—	36	31	49
$[m(t\bar{t}), \lvert \Delta\eta(t,\bar{t})\rvert]$	12	182 (34)	—	31	31	53
$[m(t\bar{t}), \lvert \Delta\phi(t,\bar{t})\rvert]$	12	82 (51)	—	—	42	89

Table 23: The χ^2 values and dof of the measured absolute multi-differential cross sections for $t\bar{t}$ and top quark kinematic observables at the particle level are shown with respect to the POWHEG+PYTHIA 8 ('POW-PYT') simulation and the STRIPPER NNLO calculation. The χ^2 values are calculated taking only measurement uncertainties into account and excluding theory uncertainties. For POW+PYT, the χ^2 values including theory uncertainties are indicated with the brackets (w. unc.).

Cross section variables	dof	χ^2	
		POW+PYT (w. unc.)	STRIPPER
$[|y(t)|, p_T(t)]$	16	44 (28)	17
$[m(t\bar{t}), p_T(t)]$	9	103 (37)	26
$[p_T(t), p_T(t\bar{t})]$	16	44 (21)	169
$[m(t\bar{t}), |y(t\bar{t})|]$	16	86 (41)	44
$[|y(t\bar{t})|, p_T(t\bar{t})]$	16	32 (19)	81
$[m(t\bar{t}), p_T(t\bar{t})]$	16	69 (37)	388
$[p_T(t\bar{t}), m(t\bar{t}), |y(t\bar{t})|]$	48	133 (69)	149
$[m(t\bar{t}), |y(t)|]$	16	64 (27)	21
$[m(t\bar{t}), |\Delta\eta(t,\bar{t})|]$	12	174 (32)	39
$[m(t\bar{t}), |\Delta\phi(t,\bar{t})|]$	12	80 (44)	426

Table 24: The χ^2 values and dof of the measured absolute single-differential cross sections for lepton and b-jet kinematic observables at the particle level are shown with respect to the POWHEG+PYTHIA 8 ('POW-PYT') simulation and the STRIPPER NNLO calculation. The χ^2 values are calculated taking only measurement uncertainties into account and excluding theory uncertainties. For POW+PYT, the χ^2 values including theory uncertainties are indicated with the brackets (w. unc.).

Cross section variables	dof	χ^2	
		POW+PYT (w. unc.)	STRIPPER
$p_T(\ell)$	12	32 (19)	17
$p_T(\ell)$ trailing/$p_T(\ell)$ leading	10	16 (11)	5
$p_T(\ell)/p_T(\bar{t})$	5	20 (17)	8
$p_T(b)$ leading	10	6 (5)	8
$p_T(b)$ trailing	7	7 (5)	4
$(p_T(b) + p_T(\bar{b}))/(p_T(t) + p_T(\bar{t}))$	4	24 (19)	9
$m(\ell\bar{\ell})$	12	31 (25)	13
$m(b\bar{b})$	7	21 (16)	80
$m(\ell\bar{\ell}b\bar{b})$	19	36 (19)	16
$p_T(\ell\bar{\ell})$	9	4 (3)	6
$|\eta(\ell\bar{\ell})|$	14	16 (10)	41
$[|\eta(\ell\bar{\ell})|, m(\ell\bar{\ell})]$	24	55 (29)	80
$[|\eta(\ell\bar{\ell})|, p_T(\ell\bar{\ell})]$	20	30 (15)	46
$[p_T(\ell\bar{\ell}), m(\ell\bar{\ell})]$	30	50 (39)	51

Table 25: The p-values are shown for the χ^2 tests of the measured normalized single-differential cross sections for $t\bar{t}$ and top quark kinematic observables at the parton level with respect to the predictions of various MC generators. The χ^2 values are calculated taking only measurement uncertainties into account and excluding theory uncertainties. For POW+PYT, the p-values of the χ^2 tests including theory uncertainties are indicated with the brackets (w. unc.).

Cross section	p-values of χ^2 (in %)		
variables	POW+PYT (w. unc.)	FxFx+PYT	POW+HER
$p_T(t)$	2 (10)	<1	51
$p_T(\bar{t})$	5 (16)	<1	41
$y(t)$	<1 (2)	<1	1
$y(\bar{t})$	<1 (<1)	<1	<1
$p_T(t\bar{t})$	<1 (32)	<1	<1
$y(t\bar{t})$	51 (74)	7	73
$m(t\bar{t})$	56 (77)	30	70
$|\Delta\phi(t,\bar{t})|$	82 (97)	15	7
$|y(t)| - |y(\bar{t})|$	3 (22)	<1	6
$p_T(t)/m(t\bar{t})$	<1 (<1)	<1	3
$p_T(t\bar{t})/m(t\bar{t})$	3 (62)	<1	<1
$\log(\xi_1)$	9 (26)	3	15
$\log(\xi_2)$	24 (54)	<1	51

C Tables with p-values of χ^2 tests

Tables 25–48 present the p-values of the performed χ^2 tests between the measured differential cross sections for $t\bar{t}$ production and various predictions. The corresponding χ^2 values and number of degrees of freedom can be found in the Tables 1–24.

Table 26: The *p*-values are shown for the χ^2 tests of the measured normalized single-differential cross sections for $t\bar{t}$ and top quark kinematic observables at the particle level with respect to the predictions of various MC generators. The χ^2 values are calculated taking only measurement uncertainties into account and excluding theory uncertainties. For POW+PYT, the *p*-values of the χ^2 tests including theory uncertainties are indicated with the brackets (w. unc.).

Cross section	*p*-values of χ^2 (in %)		
variables	POW+PYT (w. unc.)	FxFx+PYT	POW+HER
$p_T(t)$	<1 (7)	<1	47
$p_T(\bar{t})$	3 (15)	<1	59
$y(t)$	3 (7)	<1	2
$y(\bar{t})$	<1 (2)	<1	<1
$p_T(t\bar{t})$	<1 (33)	<1	<1
$y(t\bar{t})$	51 (81)	3	64
$m(t\bar{t})$	59 (81)	60	28
$\|\Delta\phi(t,\bar{t})\|$	82 (97)	36	10
$\|y(t)\| - \|y(\bar{t})\|$	4 (20)	4	1
$p_T(t)/m(t\bar{t})$	<1 (<1)	<1	2
$p_T(t\bar{t})/m(t\bar{t})$	2 (57)	<1	<1
$\log(\xi_1)$	8 (34)	3	2
$\log(\xi_2)$	32 (67)	3	29

Table 27: The p-values are shown for the χ^2 tests of the measured normalized multi-differential cross sections for $t\bar{t}$ and top quark kinematic observables at the parton level with respect to the predictions of various MC generators. The χ^2 values are calculated taking only measurement uncertainties into account and excluding theory uncertainties. For POW+PYT, the p-values of the χ^2 tests including theory uncertainties are indicated with the brackets (w. unc.).

Cross section	p-values of χ^2 (in %)		
variables	POW+PYT (w. unc.)	FxFx+PYT	POW+HER
$[|y(t)|,\ p_T(t)]$	<1 (<1)	<1	1
$[m(t\bar{t}),\ p_T(t)]$	<1 (<1)	<1	<1
$[p_T(t),\ p_T(t\bar{t})]$	<1 (14)	<1	<1
$[m(t\bar{t}),\ |y(t\bar{t})|]$	<1 (<1)	<1	<1
$[|y(t\bar{t})|,\ p_T(t\bar{t})]$	2 (44)	<1	<1
$[m(t\bar{t}),\ p_T(t\bar{t})]$	<1 (<1)	<1	<1
$[p_T(t\bar{t}),\ m(t\bar{t}),\ |y(t\bar{t})|]$	<1 (5)	<1	<1
$[m(t\bar{t}),\ |y(t)|]$	<1 (<1)	<1	<1
$[m(t\bar{t}),\ |\Delta\eta(t,\bar{t})|]$	<1 (<1)	<1	<1
$[m(t\bar{t}),\ |\Delta\phi(t,\bar{t})|]$	<1 (<1)	<1	<1

Table 28: The p-values are shown for the χ^2 tests of the measured normalized multi-differential cross sections for $t\bar{t}$ and top quark kinematic observables at the particle level with respect to the predictions of various MC generators. The χ^2 values are calculated taking only measurement uncertainties into account and excluding theory uncertainties. For POW+PYT, the p-values of the χ^2 tests including theory uncertainties are indicated with the brackets (w. unc.).

Cross section	p-values of χ^2 (in %)		
variables	POW+PYT (w. unc.)	FxFx+PYT	POW+HER
$[|y(t)|,\ p_T(t)]$	<1 (5)	<1	2
$[m(t\bar{t}),\ p_T(t)]$	<1 (<1)	<1	<1
$[p_T(t),\ p_T(t\bar{t})]$	<1 (21)	<1	<1
$[m(t\bar{t}),\ |y(t\bar{t})|]$	<1 (<1)	<1	<1
$[|y(t\bar{t})|,\ p_T(t\bar{t})]$	3 (28)	<1	<1
$[m(t\bar{t}),\ p_T(t\bar{t})]$	<1 (<1)	<1	<1
$[p_T(t\bar{t}),\ m(t\bar{t}),\ |y(t\bar{t})|]$	<1 (3)	<1	<1
$[m(t\bar{t}),\ |y(t)|]$	<1 (4)	<1	<1
$[m(t\bar{t}),\ |\Delta\eta(t,\bar{t})|]$	<1 (<1)	<1	<1
$[m(t\bar{t}),\ |\Delta\phi(t,\bar{t})|]$	<1 (<1)	<1	<1

Table 29: The p-values are shown for the χ^2 tests of the measured normalized single-differential cross sections for lepton and b-jet kinematic observables at the particle level with respect to the predictions of various MC generators. The χ^2 values are calculated taking only measurement uncertainties into account and excluding theory uncertainties. For POW+PYT, the p-values of the χ^2 tests including theory uncertainties are indicated with the brackets (w. unc.).

Cross section	p-values of χ^2 (in %)		
variables	POW+PYT (w. unc.)	FxFx+PYT	POW+HER
$p_T(\ell)$	<1 (8)	<1	9
$p_T(\ell)$ trailing/$p_T(\ell)$ leading	10 (30)	<1	66
$p_T(\ell)/p_T(\bar{t})$	4 (6)	<1	2
$p_T(b)$ leading	86 (92)	<1	55
$p_T(b)$ trailing	48 (70)	<1	35
$(p_T(b) + p_T(\bar{b}))/(p_T(t) + p_T(\bar{t}))$	<1 (<1)	<1	<1
$m(\ell\bar{\ell})$	2 (5)	<1	2
$m(b\bar{b})$	2 (7)	2	3
$m(\ell\bar{\ell}b\bar{b})$	2 (45)	6	6
$p_T(\ell\bar{\ell})$	86 (96)	9	31
$\|\eta(\ell\bar{\ell})\|$	40 (77)	7	58
$[\|\eta(\ell\bar{\ell})\|, m(\ell\bar{\ell})]$	<1 (23)	<1	4
$[\|\eta(\ell\bar{\ell})\|, p_T(\ell\bar{\ell})]$	10 (78)	<1	19
$[p_T(\ell\bar{\ell}), m(\ell\bar{\ell})]$	3 (15)	<1	<1

Table 30: The p-values are shown for the χ^2 tests of the measured normalized differential cross sections as a function of the additional-jet multiplicity in the events, at the parton level of the top quark and antiquark, with respect to the predictions of various MC generators. The χ^2 values are calculated taking only measurement uncertainties into account and excluding theory uncertainties. For POW+PYT, the p-values of the χ^2 tests including theory uncertainties are indicated with the brackets (w. unc.).

Cross section	p-values of χ^2 (in %)		
variables	POW+PYT (w. unc.)	FxFx+PYT	POW+HER
$N_{\text{jet}}(p_{\text{T}} > 40\,\text{GeV})$	34 (64)	<1	<1
$N_{\text{jet}}(p_{\text{T}} > 100\,\text{GeV})$	<1 (11)	<1	<1
$[N_{\text{jet}}, p_{\text{T}}(\text{t})]$	<1 (14)	<1	<1
$[N_{\text{jet}}, |y(\text{t})|]$	<1 (<1)	<1	<1
$[N_{\text{jet}}, p_{\text{T}}(\text{t}\bar{\text{t}})]$	<1 (<1)	<1	<1
$[N_{\text{jet}}, m(\text{t}\bar{\text{t}})]$	<1 (<1)	<1	<1
$[N_{\text{jet}}, |y(\text{t}\bar{\text{t}})|]$	46 (94)	<1	<1
$[N_{\text{jet}}, |\Delta\eta(\text{t},\bar{\text{t}})|]$	<1 (<1)	<1	<1
$[N_{\text{jet}}^{0,1+}, m(\text{t}\bar{\text{t}}), |y(\text{t}\bar{\text{t}})|]$	<1 (5)	<1	<1
$[N_{\text{jet}}^{0,1,2+}, m(\text{t}\bar{\text{t}}), |y(\text{t}\bar{\text{t}})|]$	<1 (1)	<1	<1
$[N_{\text{jet}}^{0,1,2,3+}, m(\text{t}\bar{\text{t}}), |y(\text{t}\bar{\text{t}})|]$	<1 (<1)	<1	<1

Table 31: The p-values are shown for the χ^2 tests of the measured normalized differential cross sections as a function of the additional-jet multiplicity in the events, at the particle level of the top quark and antiquark, with respect to the predictions of various MC generators. The χ^2 values are calculated taking only measurement uncertainties into account and excluding theory uncertainties. For POW+PYT, the p-values of the χ^2 tests including theory uncertainties are indicated with the brackets (w. unc.).

Cross section	p-values of χ^2 (in %)		
variables	POW+PYT (w. unc.)	FxFx+PYT	POW+HER
$N_{\mathrm{jet}}(p_{\mathrm{T}} > 40\,\mathrm{GeV})$	30 (63)	<1	12
$N_{\mathrm{jet}}(p_{\mathrm{T}} > 100\,\mathrm{GeV})$	<1 (8)	<1	19
$[N_{\mathrm{jet}}, p_{\mathrm{T}}(\mathrm{t})]$	<1 (12)	<1	<1
$[N_{\mathrm{jet}}, \lvert y(\mathrm{t})\rvert]$	<1 (1)	<1	<1
$[N_{\mathrm{jet}}, p_{\mathrm{T}}(\mathrm{t\bar{t}})]$	<1 (<1)	<1	<1
$[N_{\mathrm{jet}}, m(\mathrm{t\bar{t}})]$	<1 (<1)	<1	<1
$[N_{\mathrm{jet}}, \lvert y(\mathrm{t\bar{t}})\rvert]$	22 (94)	<1	65
$[N_{\mathrm{jet}}, \lvert \Delta\eta(\mathrm{t},\bar{\mathrm{t}})\rvert]$	<1 (<1)	<1	<1
$[N_{\mathrm{jet}}^{0,1+}, m(\mathrm{t\bar{t}}), \lvert y(\mathrm{t\bar{t}})\rvert]$	<1 (<1)	<1	<1
$[N_{\mathrm{jet}}^{0,1,2+}, m(\mathrm{t\bar{t}}), \lvert y(\mathrm{t\bar{t}})\rvert]$	<1 (<1)	<1	<1
$[N_{\mathrm{jet}}^{0,1,2,3+}, m(\mathrm{t\bar{t}}), \lvert y(\mathrm{t\bar{t}})\rvert]$	<1 (<1)	<1	<1

Table 32: The p-values are shown for the χ^2 tests of the measured normalized single-differential cross sections for t$\bar{\text{t}}$ and top quark kinematic observables at the parton level with respect to various fixed-order predictions. The χ^2 values are calculated taking only measurement uncertainties into account and excluding theory uncertainties. For POW+PYT, the p-values of the χ^2 tests including theory uncertainties are indicated with the brackets (w. unc.).

Cross section variables	p-values of χ^2 (in %)					
	POW+PYT (w. unc.)	aN^{3}LO	MATRIX	STRIPPER	MINNLOPS
$p_{\text{T}}(\text{t})$	2 (10)	<1	78	22	62
$p_{\text{T}}(\bar{\text{t}})$	5 (16)	—	69	14	49
$y(\text{t})$	<1 (2)	<1	6	6	8
$y(\bar{\text{t}})$	<1 (<1)	—	10	<1	<1
$p_{\text{T}}(\text{t}\bar{\text{t}})$	<1 (32)	—	33	15	<1
$y(\text{t}\bar{\text{t}})$	51 (74)	—	84	61	61
$m(\text{t}\bar{\text{t}})$	56 (77)	—	49	59	90
$|\Delta\phi(\text{t},\bar{\text{t}})|$	82 (97)	—	<1	<1	14
$|y(\text{t})| - |y(\bar{\text{t}})|$	3 (22)	—	94	86	10
$p_{\text{T}}(\text{t})/m(\text{t}\bar{\text{t}})$	<1 (<1)	—	58	41	28
$p_{\text{T}}(\text{t}\bar{\text{t}})/m(\text{t}\bar{\text{t}})$	3 (62)	—	<1	<1	1
$\log(\xi_1)$	9 (26)	—	—	6	16
$\log(\xi_2)$	24 (54)	—	—	17	52

Table 33: The *p*-values are shown for the χ^2 tests of the measured normalized single-differential cross sections for $t\bar{t}$ and top quark kinematic observables at the particle level with respect to the POWHEG+PYTHIA 8 ('POW-PYT') simulation and the STRIPPER NNLO calculation. The χ^2 values are calculated taking only measurement uncertainties into account and excluding theory uncertainties. For POW+PYT, the *p*-values of the χ^2 tests including theory uncertainties are indicated with the brackets (w. unc.).

Cross section	*p*-values of χ^2 (in %)	
variables	POW+PYT (w. unc.)	STRIPPER
$p_T(t)$	<1 (7)	83
$p_T(\bar{t})$	3 (15)	82
$y(t)$	3 (7)	29
$y(\bar{t})$	<1 (2)	37
$p_T(t\bar{t})$	<1 (33)	<1
$y(t\bar{t})$	51 (81)	6
$m(t\bar{t})$	59 (81)	73
$|\Delta\phi(t,\bar{t})|$	82 (97)	<1
$|y(t)| - |y(\bar{t})|$	4 (20)	81
$p_T(t)/m(t\bar{t})$	<1 (<1)	9
$p_T(t\bar{t})/m(t\bar{t})$	2 (57)	<1
$\log(\xi_1)$	8 (34)	28
$\log(\xi_2)$	32 (67)	33

Table 34: The p-values are shown for the χ^2 tests of the measured normalized multi-differential cross sections for $t\bar{t}$ and top quark kinematic observables at the parton level with respect to various fixed-order predictions. The χ^2 values are calculated taking only measurement uncertainties into account and excluding theory uncertainties. For POW+PYT, the p-values of the χ^2 tests including theory uncertainties are indicated with the brackets (w. unc.).

Cross section variables	p-values of χ^2 (in %)				
	POW+PYT (w. unc.)	aN^{3}LO	MATRIX	STRIPPER	MINNLOPS
$[|y(t)|, p_T(t)]$	<1 (<1)	<1	7	6	9
$[m(t\bar{t}), p_T(t)]$	<1 (<1)	—	7	4	6
$[p_T(t), p_T(t\bar{t})]$	<1 (14)	—	<1	<1	<1
$[m(t\bar{t}), |y(t\bar{t})|]$	<1 (<1)	—		<1	<1
$[|y(t\bar{t})|, p_T(t\bar{t})]$	2 (44)	—	<1	<1	<1
$[m(t\bar{t}), p_T(t\bar{t})]$	<1 (<1)	—	<1	<1	<1
$[p_T(t\bar{t}), m(t\bar{t}), |y(t\bar{t})|]$	<1 (5)	—	—	2	<1
$[m(t\bar{t}), |y(t)|]$	<1 (<1)	—	<1	1	
$[m(t\bar{t}), |\Delta\eta(t,\bar{t})|]$	<1 (<1)	—	<1	<1	<1
$[m(t\bar{t}), |\Delta\phi(t,\bar{t})|]$	<1 (<1)	—	—	<1	<1

Table 35: The p-values are shown for the χ^2 tests of the measured normalized multi-differential cross sections for $t\bar{t}$ and top quark kinematic observables at the particle level with respect to the POWHEG+PYTHIA 8 ('POW-PYT') simulation and the STRIPPER NNLO calculation. The χ^2 values are calculated taking only measurement uncertainties into account and excluding theory uncertainties. For POW+PYT, the p-values of the χ^2 tests including theory uncertainties are indicated with the brackets (w. unc.).

Cross section	p-values of χ^2 (in %)	
variables	POW+PYT (w. unc.)	STRIPPER
$[\lvert y(\mathrm{t})\rvert,\, p_\mathrm{T}(\mathrm{t})]$	<1 (5)	38
$[m(\mathrm{t\bar{t}}),\, p_\mathrm{T}(\mathrm{t})]$	<1 (<1)	2
$[p_\mathrm{T}(\mathrm{t}),\, p_\mathrm{T}(\mathrm{t\bar{t}})]$	<1 (21)	<1
$[m(\mathrm{t\bar{t}}),\, \lvert y(\mathrm{t\bar{t}})\rvert]$	<1 (<1)	<1
$[\lvert y(\mathrm{t\bar{t}})\rvert,\, p_\mathrm{T}(\mathrm{t\bar{t}})]$	3 (28)	<1
$[m(\mathrm{t\bar{t}}),\, p_\mathrm{T}(\mathrm{t\bar{t}})]$	<1 (<1)	<1
$[p_\mathrm{T}(\mathrm{t\bar{t}}),\, m(\mathrm{t\bar{t}}),\, \lvert y(\mathrm{t\bar{t}})\rvert]$	<1 (3)	<1
$[m(\mathrm{t\bar{t}}),\, \lvert y(\mathrm{t})\rvert]$	<1 (4)	18
$[m(\mathrm{t\bar{t}}),\, \lvert\Delta\eta(\mathrm{t},\bar{\mathrm{t}})\rvert]$	<1 (<1)	<1
$[m(\mathrm{t\bar{t}}),\, \lvert\Delta\phi(\mathrm{t},\bar{\mathrm{t}})\rvert]$	<1 (<1)	<1

Table 36: The p-values are shown for the χ^2 tests of the measured normalized single-differential cross sections for lepton and b-jet kinematic observables at the particle level with respect to the POWHEG+PYTHIA 8 ('POW-PYT') simulation and the STRIPPER NNLO calculation. The χ^2 values are calculated taking only measurement uncertainties into account and excluding theory uncertainties. For POW+PYT, the p-values of the χ^2 tests including theory uncertainties are indicated with the brackets (w. unc.).

Cross section	p-values of χ^2 (in %)	
variables	POW+PYT (w. unc.)	STRIPPER
$p_\mathrm{T}(\ell)$	<1 (8)	12
$p_\mathrm{T}(\ell)$ trailing$/p_\mathrm{T}(\ell)$ leading	10 (30)	81
$p_\mathrm{T}(\ell)/p_\mathrm{T}(\bar{\mathrm{t}})$	4 (6)	33
$p_\mathrm{T}(\mathrm{b})$ leading	86 (92)	64
$p_\mathrm{T}(\mathrm{b})$ trailing	48 (70)	81
$(p_\mathrm{T}(\mathrm{b}) + p_\mathrm{T}(\bar{\mathrm{b}}))/(p_\mathrm{T}(\mathrm{t}) + p_\mathrm{T}(\bar{\mathrm{t}}))$	<1 (<1)	4
$m(\ell\bar{\ell})$	2 (5)	32
$m(\mathrm{b}\bar{\mathrm{b}})$	2 (7)	<1
$m(\ell\bar{\ell}\mathrm{b}\bar{\mathrm{b}})$	2 (45)	68
$p_\mathrm{T}(\ell\bar{\ell})$	86 (96)	73
$|\eta(\ell\bar{\ell})|$	40 (77)	<1
$[|\eta(\ell\bar{\ell})|, m(\ell\bar{\ell})]$	<1 (23)	<1
$[|\eta(\ell\bar{\ell})|, p_\mathrm{T}(\ell\bar{\ell})]$	10 (78)	<1
$[p_\mathrm{T}(\ell\bar{\ell}), m(\ell\bar{\ell})]$	3 (15)	2

Table 37: The p-values are shown for the χ^2 tests of the measured absolute single-differential cross sections for $t\bar{t}$ and top quark kinematic observables at the parton level with respect to the predictions of various MC generators. The χ^2 values are calculated taking only measurement uncertainties into account and excluding theory uncertainties. For POW+PYT, the p-values of the χ^2 tests including theory uncertainties are indicated with the brackets (w. unc.).

| Cross section | p-values of χ^2 (in %) | | |
variables	POW+PYT (w. unc.)	FxFx+PYT	POW+HER
$p_{\mathrm{T}}(t)$	<1 (7)	<1	61
$p_{\mathrm{T}}(\bar{t})$	<1 (9)	<1	50
$y(t)$	<1 (<1)	<1	2
$y(\bar{t})$	<1 (<1)	<1	<1
$p_{\mathrm{T}}(t\bar{t})$	<1 (35)	<1	<1
$y(t\bar{t})$	38 (67)	9	78
$m(t\bar{t})$	55 (78)	28	76
$\|\Delta\phi(t,\bar{t})\|$	40 (81)	14	3
$\|y(t)\| - \|y(\bar{t})\|$	2 (23)	2	9
$p_{\mathrm{T}}(t)/m(t\bar{t})$	<1 (<1)	<1	3
$p_{\mathrm{T}}(t\bar{t})/m(t\bar{t})$	2 (66)	<1	<1
$\log(\xi_1)$	7 (23)	4	20
$\log(\xi_2)$	14 (47)	<1	60

Table 38: The *p*-values are shown for the χ^2 tests of the measured absolute single-differential cross sections for t$\bar{\text{t}}$ and top quark kinematic observables at the particle level with respect to the predictions of various MC generators. The χ^2 values are calculated taking only measurement uncertainties into account and excluding theory uncertainties. For POW+PYT, the *p*-values of the χ^2 tests including theory uncertainties are indicated with the brackets (w. unc.).

Cross section	*p*-values of χ^2 (in %)		
variables	POW+PYT (w. unc.)	FxFx+PYT	POW+HER
$p_T(t)$	<1 (7)	<1	46
$p_T(\bar{t})$	<1 (11)	<1	68
$y(t)$	<1 (5)	<1	4
$y(\bar{t})$	<1 (1)	<1	<1
$p_T(t\bar{t})$	<1 (37)	<1	<1
$y(t\bar{t})$	35 (78)	3	74
$m(t\bar{t})$	46 (80)	67	39
$|\Delta\phi(t,\bar{t})|$	40 (85)	43	13
$|y(t)| - |y(\bar{t})|$	3 (23)	5	2
$p_T(t)/m(t\bar{t})$	<1 (<1)	<1	1
$p_T(t\bar{t})/m(t\bar{t})$	1 (59)	<1	<1
$\log(\xi_1)$	7 (35)	4	3
$\log(\xi_2)$	22 (67)	3	36

Table 39: The p-values are shown for the χ^2 tests of the measured absolute multi-differential cross sections for $t\bar{t}$ and top quark kinematic observables at the parton level with respect to the predictions of various MC generators. The χ^2 values are calculated taking only measurement uncertainties into account and excluding theory uncertainties. For POW+PYT, the p-values of the χ^2 tests including theory uncertainties are indicated with the brackets (w. unc.).

Cross section	p-values of χ^2 (in %)		
variables	POW+PYT (w. unc.)	FxFx+PYT	POW+HER
$[\lvert y(t)\rvert,\, p_{\mathrm{T}}(t)]$	<1 (<1)	<1	2
$[m(t\bar{t}),\, p_{\mathrm{T}}(t)]$	<1 (<1)	<1	<1
$[p_{\mathrm{T}}(t),\, p_{\mathrm{T}}(t\bar{t})]$	<1 (6)	<1	<1
$[m(t\bar{t}),\, \lvert y(t\bar{t})\rvert]$	<1 (<1)	<1	<1
$[\lvert y(t\bar{t})\rvert,\, p_{\mathrm{T}}(t\bar{t})]$	<1 (37)	<1	<1
$[m(t\bar{t}),\, p_{\mathrm{T}}(t\bar{t})]$	<1 (<1)	<1	<1
$[p_{\mathrm{T}}(t\bar{t}),\, m(t\bar{t}),\, \lvert y(t\bar{t})\rvert]$	<1 (2)	<1	<1
$[m(t\bar{t}),\, \lvert y(t)\rvert]$	<1 (<1)	<1	<1
$[m(t\bar{t}),\, \lvert \Delta\eta(t,\bar{t})\rvert]$	<1 (<1)	<1	<1
$[m(t\bar{t}),\, \lvert \Delta\phi(t,\bar{t})\rvert]$	<1 (<1)	<1	<1

Table 40: The p-values are shown for the χ^2 tests of the measured absolute multi-differential cross sections for $t\bar{t}$ and top quark kinematic observables at the particle level with respect to the predictions of various MC generators. The χ^2 values are calculated taking only measurement uncertainties into account and excluding theory uncertainties. For POW+PYT, the p-values of the χ^2 tests including theory uncertainties are indicated with the brackets (w. unc.).

Cross section	p-values of χ^2 (in %)		
variables	POW+PYT (w. unc.)	FxFx+PYT	POW+HER
$[\lvert y(t)\rvert,\, p_{\mathrm{T}}(t)]$	<1 (3)	<1	4
$[m(t\bar{t}),\, p_{\mathrm{T}}(t)]$	<1 (<1)	<1	<1
$[p_{\mathrm{T}}(t),\, p_{\mathrm{T}}(t\bar{t})]$	<1 (17)	<1	<1
$[m(t\bar{t}),\, \lvert y(t\bar{t})\rvert]$	<1 (<1)	<1	<1
$[\lvert y(t\bar{t})\rvert,\, p_{\mathrm{T}}(t\bar{t})]$	1 (27)	<1	<1
$[m(t\bar{t}),\, p_{\mathrm{T}}(t\bar{t})]$	<1 (<1)	<1	<1
$[p_{\mathrm{T}}(t\bar{t}),\, m(t\bar{t}),\, \lvert y(t\bar{t})\rvert]$	<1 (3)	<1	<1
$[m(t\bar{t}),\, \lvert y(t)\rvert]$	<1 (5)	<1	<1
$[m(t\bar{t}),\, \lvert \Delta\eta(t,\bar{t})\rvert]$	<1 (<1)	<1	<1
$[m(t\bar{t}),\, \lvert \Delta\phi(t,\bar{t})\rvert]$	<1 (<1)	<1	<1

Table 41: The p-values are shown for the χ^2 tests of the measured absolute single-differential cross sections for lepton and b-jet kinematic observables at the particle level with respect to the predictions of various MC generators. The χ^2 values are calculated taking only measurement uncertainties into account and excluding theory uncertainties. For POW+PYT, the p-values of the χ^2 tests including theory uncertainties are indicated with the brackets (w. unc.).

Cross section	p-values of χ^2 (in %)		
variables	POW+PYT (w. unc.)	FxFx+PYT	POW+HER
$p_T(\ell)$	<1 (9)	<1	6
$p_T(\ell)$ trailing$/p_T(\ell)$ leading	9 (34)	<1	70
$p_T(\ell)/p_T(\bar{t})$	<1 (<1)	<1	2
$p_T(b)$ leading	85 (91)	<1	64
$p_T(b)$ trailing	46 (64)	<1	41
$(p_T(b) + p_T(\bar{b}))/(p_T(t) + p_T(\bar{t}))$	<1 (<1)	<1	<1
$m(\ell\bar{\ell})$	<1 (2)	<1	3
$m(b\bar{b})$	<1 (2)	2	4
$m(\ell\bar{\ell}b\bar{b})$	<1 (48)	6	10
$p_T(\ell\bar{\ell})$	88 (97)	6	34
$|\eta(\ell\bar{\ell})|$	32 (77)	7	63
$[|\eta(\ell\bar{\ell})|, m(\ell\bar{\ell})]$	<1 (22)	<1	7
$[|\eta(\ell\bar{\ell})|, p_T(\ell\bar{\ell})]$	7 (80)	<1	24
$[p_T(\ell\bar{\ell}), m(\ell\bar{\ell})]$	1 (12)	<1	<1

Table 42: The p-values are shown for the χ^2 tests of the measured absolute differential cross sections as a function of the additional-jet multiplicity in the events, at the parton level of the top quark and antiquark, with respect to the predictions of various MC generators. The χ^2 values are calculated taking only measurement uncertainties into account and excluding theory uncertainties. For POW+PYT, the p-values of the χ^2 tests including theory uncertainties are indicated with the brackets (w. unc.).

Cross section	p-values of χ^2 (in $)		
variables	POW+PYT (w. unc.)	FxFx+PYT	POW+HER
$N_{\mathrm{jet}}(p_{\mathrm{T}} > 40\,\mathrm{GeV})$	30 (56)	<1	<1
$N_{\mathrm{jet}}(p_{\mathrm{T}} > 100\,\mathrm{GeV})$	<1 (5)	<1	<1
$[N_{\mathrm{jet}},\ p_{\mathrm{T}}(\mathrm{t})]$	<1 (5)	<1	<1
$[N_{\mathrm{jet}},\ |y(\mathrm{t})|]$	<1 (<1)	<1	<1
$[N_{\mathrm{jet}},\ p_{\mathrm{T}}(\mathrm{t\bar{t}})]$	<1 (<1)	<1	<1
$[N_{\mathrm{jet}},\ m(\mathrm{t\bar{t}})]$	<1 (<1)	<1	<1
$[N_{\mathrm{jet}},\ |y(\mathrm{t\bar{t}})|]$	32 (87)	<1	<1
$[N_{\mathrm{jet}},\ |\Delta\eta(\mathrm{t},\bar{\mathrm{t}})|]$	<1 (<1)	<1	<1
$[N_{\mathrm{jet}}^{0,1+},\ m(\mathrm{t\bar{t}}),\ |y(\mathrm{t\bar{t}})|]$	<1 (3)	<1	<1
$[N_{\mathrm{jet}}^{0,1,2+},\ m(\mathrm{t\bar{t}}),\ |y(\mathrm{t\bar{t}})|]$	<1 (<1)	<1	<1
$[N_{\mathrm{jet}}^{0,1,2,3+},\ m(\mathrm{t\bar{t}}),\ |y(\mathrm{t\bar{t}})|]$	<1 (<1)	<1	<1

Table 43: The p-values are shown for the χ^2 tests of the measured absolute differential cross sections as a function of the additional-jet multiplicity in the events, at the particle level of the top quark and antiquark, with respect to the predictions of various MC generators. The χ^2 values are calculated taking only measurement uncertainties into account and excluding theory uncertainties. For POW+PYT, the p-values of the χ^2 tests including theory uncertainties are indicated with the brackets (w. unc.).

Cross section	p-values of χ^2 (in %)		
variables	POW+PYT (w. unc.)	FxFx+PYT	POW+HER
$N_{\text{jet}}(p_{\text{T}} > 40\,\text{GeV})$	29 (66)	<1	22
$N_{\text{jet}}(p_{\text{T}} > 100\,\text{GeV})$	<1 (5)	<1	25
$[N_{\text{jet}},\, p_{\text{T}}(\text{t})]$	<1 (9)	<1	<1
$[N_{\text{jet}},\, |y(\text{t})|]$	<1 (1)	<1	<1
$[N_{\text{jet}},\, p_{\text{T}}(\text{t}\bar{\text{t}})]$	<1 (<1)	<1	<1
$[N_{\text{jet}},\, m(\text{t}\bar{\text{t}})]$	<1 (<1)	<1	<1
$[N_{\text{jet}},\, |y(\text{t}\bar{\text{t}})|]$	13 (91)	<1	75
$[N_{\text{jet}},\, |\Delta\eta(\text{t},\bar{\text{t}})|]$	<1 (<1)	<1	<1
$[N_{\text{jet}}^{0,1+},\, m(\text{t}\bar{\text{t}}),\, |y(\text{t}\bar{\text{t}})|]$	<1 (<1)	<1	<1
$[N_{\text{jet}}^{0,1,2+},\, m(\text{t}\bar{\text{t}}),\, |y(\text{t}\bar{\text{t}})|]$	<1 (<1)	<1	<1
$[N_{\text{jet}}^{0,1,2,3+},\, m(\text{t}\bar{\text{t}}),\, |y(\text{t}\bar{\text{t}})|]$	<1 (<1)	<1	<1

Table 44: The p-values are shown for the χ^2 tests of the measured absolute single-differential cross sections for $t\bar{t}$ and top quark kinematic observables at the parton level with respect to various fixed-order predictions. The χ^2 values are calculated taking only measurement uncertainties into account and excluding theory uncertainties. For POW+PYT, the p-values of the χ^2 tests including theory uncertainties are indicated with the brackets (w. unc.).

Cross section variables	p-values of χ^2 (in %)				
	POW+PYT (w. unc.)	aN³LO	MATRIX	STRIPPER	MiNNLOPS
$p_T(t)$	<1 (7)	<1	84	4	55
$p_T(\bar{t})$	<1 (9)	—	71	17	47
$y(t)$	<1 (<1)	<1	8	7	17
$y(\bar{t})$	<1 (<1)	—	13	<1	2
$p_T(t\bar{t})$	<1 (35)	—	42	21	<1
$y(t\bar{t})$	38 (67)	—	86	65	72
$m(t\bar{t})$	55 (78)	—	51	61	94
$|\Delta\phi(t,\bar{t})|$	40 (81)	—	<1	<1	25
$|y(t)|-|y(\bar{t})|$	2 (23)	—	97	90	15
$p_T(t)/m(t\bar{t})$	<1 (<1)	—	60	38	9
$p_T(t\bar{t})/m(t\bar{t})$	2 (66)	—	<1	<1	3
$\log(\xi_1)$	7 (23)	—	—	8	23
$\log(\xi_2)$	14 (47)	—	—	18	66

Table 45: The p-values are shown for the χ^2 tests of the measured absolute single-differential cross sections for $t\bar{t}$ and top quark kinematic observables at the particle level with respect to the POWHEG+PYTHIA 8 ('POW-PYT') simulation and the STRIPPER NNLO calculation. The χ^2 values are calculated taking only measurement uncertainties into account and excluding theory uncertainties. For POW+PYT, the p-values of the χ^2 tests including theory uncertainties are indicated with the brackets (w. unc.).

Cross section	p-values of χ^2 (in %)	
variables	POW+PYT (w. unc.)	STRIPPER
$p_T(t)$	<1 (7)	88
$p_T(\bar{t})$	<1 (11)	82
$y(t)$	<1 (5)	33
$y(\bar{t})$	<1 (1)	43
$p_T(t\bar{t})$	<1 (37)	<1
$y(t\bar{t})$	35 (78)	6
$m(t\bar{t})$	46 (80)	80
$\lvert\Delta\phi(t,\bar{t})\rvert$	40 (85)	<1
$\lvert y(t)\rvert - \lvert y(\bar{t})\rvert$	3 (23)	87
$p_T(t)/m(t\bar{t})$	<1 (<1)	11
$p_T(t\bar{t})/m(t\bar{t})$	1 (59)	<1
$\log(\xi_1)$	7 (35)	34
$\log(\xi_2)$	22 (67)	37

Table 46: The p-values are shown for the χ^2 tests of the measured absolute multi-differential cross sections for $t\bar{t}$ and top quark kinematic observables at the parton level with respect to various fixed-order predictions. The χ^2 values are calculated taking only measurement uncertainties into account and excluding theory uncertainties. For POW+PYT, the p-values of the χ^2 tests including theory uncertainties are indicated with the brackets (w. unc.).

Cross section variables	POW+PYT (w. unc.)	aN³LO	MATRIX	STRIPPER	MINNLOPS
		p-values of χ^2 (in %)			
$[|y(t\bar{})|, p_{\mathrm{T}}(t)]$	<1 (<1)	<1	8	6	19
$[m(t\bar{t}), p_{\mathrm{T}}(t)]$	<1 (<1)	—	2	5	4
$[p_{\mathrm{T}}(t), p_{\mathrm{T}}(t\bar{t})]$	<1 (6)	—	<1	<1	<1
$[m(t\bar{t}), |y(t\bar{t})|]$	<1 (<1)	—	<1	<1	<1
$[|y(t\bar{t})|, p_{\mathrm{T}}(t\bar{t})]$	<1 (37)	—	<1	<1	<1
$[m(t\bar{t}), p_{\mathrm{T}}(t\bar{t})]$	<1 (<1)	—	<1	<1	<1
$[p_{\mathrm{T}}(t\bar{t}), m(t\bar{t}), |y(t\bar{t})|]$	<1 (2)	—	—	<1	<1
$[m(t\bar{t}), |y(t)|]$	<1 (<1)	—	<1	1	<1
$[m(t\bar{t}), |\Delta\eta(t,\bar{t})|]$	<1 (<1)	—	<1	<1	<1
$[m(t\bar{t}), |\Delta\phi(t,\bar{t})|]$	<1 (<1)	—	—	<1	<1

Table 47: The p-values are shown for the χ^2 tests of the measured absolute multi-differential cross sections for $t\bar{t}$ and top quark kinematic observables at the particle level with respect to the POWHEG+PYTHIA 8 ('POW-PYT') simulation and the STRIPPER NNLO calculation. The χ^2 values are calculated taking only measurement uncertainties into account and excluding theory uncertainties. For POW+PYT, the p-values of the χ^2 tests including theory uncertainties are indicated with the brackets (w. unc.).

Cross section	p-values of χ^2 (in %)	
variables	POW+PYT (w. unc.)	STRIPPER
$[\lvert y(t)\rvert,\ p_T(t)]$	<1 (3)	39
$[m(t\bar{t}),\ p_T(t)]$	<1 (<1)	<1
$[p_T(t),\ p_T(t\bar{t})]$	<1 (17)	<1
$[m(t\bar{t}),\ \lvert y(t\bar{t})\rvert]$	<1 (<1)	<1
$[\lvert y(t\bar{t})\rvert,\ p_T(t\bar{t})]$	1 (27)	<1
$[m(t\bar{t}),\ p_T(t\bar{t})]$	<1 (<1)	<1
$[p_T(t\bar{t}),\ m(t\bar{t}),\ \lvert y(t\bar{t})\rvert]$	<1 (3)	<1
$[m(t\bar{t}),\ \lvert y(t)\rvert]$	<1 (5)	20
$[m(t\bar{t}),\ \lvert \Delta\eta(t,\bar{t})\rvert]$	<1 (<1)	<1
$[m(t\bar{t}),\ \lvert \Delta\phi(t,\bar{t})\rvert]$	<1 (<1)	<1

Table 48: The p-values are shown for the χ^2 tests of the measured absolute single-differential cross sections for lepton and b-jet kinematic observables at the particle level with respect to the POWHEG+PYTHIA 8 ('POW-PYT') simulation and the STRIPPER NNLO calculation. The χ^2 values are calculated taking only measurement uncertainties into account and excluding theory uncertainties. For POW+PYT, the p-values of the χ^2 tests including theory uncertainties are indicated with the brackets (w. unc.).
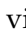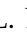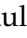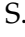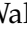
Cross section	p-values of χ^2 (in %)	
variables	POW+PYT (w. unc.)	STRIPPER
$p_{\mathrm{T}}(\ell)$	<1 (9)	14
$p_{\mathrm{T}}(\ell)$ trailing$/p_{\mathrm{T}}(\ell)$ leading	9 (34)	86
$p_{\mathrm{T}}(\ell)/p_{\mathrm{T}}(\bar{\mathrm{t}})$	<1 (<1)	14
$p_{\mathrm{T}}(\mathrm{b})$ leading	85 (91)	61
$p_{\mathrm{T}}(\mathrm{b})$ trailing	46 (64)	78
$(p_{\mathrm{T}}(\mathrm{b}) + p_{\mathrm{T}}(\bar{\mathrm{b}}))/(p_{\mathrm{T}}(\mathrm{t}) + p_{\mathrm{T}}(\bar{\mathrm{t}}))$	<1 (<1)	7
$m(\ell\bar{\ell})$	<1 (2)	36
$m(\mathrm{b}\bar{\mathrm{b}})$	<1 (2)	<1
$m(\ell\bar{\ell}\mathrm{b}\bar{\mathrm{b}})$	<1 (48)	66
$p_{\mathrm{T}}(\ell\bar{\ell})$	88 (97)	78
$|\eta(\ell\bar{\ell})|$	32 (77)	<1
$[|\eta(\ell\bar{\ell})|, m(\ell\bar{\ell})]$	<1 (22)	<1
$[|\eta(\ell\bar{\ell})|, p_{\mathrm{T}}(\ell\bar{\ell})]$	7 (80)	<1
$[p_{\mathrm{T}}(\ell\bar{\ell}), m(\ell\bar{\ell})]$	1 (12)	<1

D   The CMS Collaboration

Yerevan Physics Institute, Yerevan, Armenia
A. Tumasyan (iD)
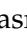
Institut für Hochenergiephysik, Vienna, Austria
W. Adam (iD), J.W. Andrejkovic, T. Bergauer (iD), S. Chatterjee (iD), K. Damanakis (iD), M. Dragicevic (iD), A. Escalante Del Valle (iD), P.S. Hussain (iD), M. Jeitler[1] (iD), N. Krammer (iD), L. Lechner (iD), D. Liko (iD), I. Mikulec (iD), P. Paulitsch, F.M. Pitters, J. Schieck[1] (iD), R. Schöfbeck (iD), D. Schwarz (iD), S. Templ (iD), W. Waltenberger (iD), C.-E. Wulz[1] (iD)
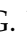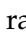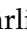
Universiteit Antwerpen, Antwerpen, Belgium
M.R. Darwish[2] (iD), T. Janssen (iD), T. Kello[3] (iD), H. Rejeb Sfar, P. Van Mechelen (iD)

Vrije Universiteit Brussel, Brussel, Belgium
E.S. Bols (iD), J. D'Hondt (iD), A. De Moor (iD), M. Delcourt (iD), H. El Faham (iD), S. Lowette (iD), S. Moortgat (iD), A. Morton (iD), D. Müller (iD), A.R. Sahasransu (iD), S. Tavernier (iD), W. Van Doninck, D. Vannerom (iD)
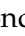
Université Libre de Bruxelles, Bruxelles, Belgium
B. Clerbaux (iD), G. De Lentdecker (iD), L. Favart (iD), J. Jaramillo (iD), K. Lee (iD), M. Mahdavikhorrami (iD), I. Makarenko (iD), A. Malara (iD), S. Paredes (iD), L. Pétré (iD), N. Postiau, E. Starling (iD), L. Thomas (iD), M. Vanden Bemden (iD), C. Vander Velde (iD), P. Vanlaer (iD)

Ghent University, Ghent, Belgium
D. Dobur (iD), J. Knolle (iD), L. Lambrecht (iD), G. Mestdach, M. Niedziela (iD), C. Rendón (iD), C. Roskas (iD), A. Samalan, K. Skovpen (iD), M. Tytgat (iD), N. Van Den Bossche (iD), B. Vermassen, L. Wezenbeek (iD)
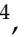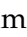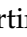
Université Catholique de Louvain, Louvain-la-Neuve, Belgium
A. Benecke (iD), G. Bruno (iD), F. Bury (iD), C. Caputo (iD), P. David (iD), C. Delaere (iD), I.S. Donertas (iD), A. Giammanco (iD), K. Jaffel (iD), Sa. Jain (iD), V. Lemaitre, K. Mondal (iD), J. Prisciandaro, A. Taliercio (iD), T.T. Tran (iD), P. Vischia (iD), S. Wertz (iD)

Centro Brasileiro de Pesquisas Fisicas, Rio de Janeiro, Brazil
G.A. Alves (iD), E. Coelho (iD), C. Hensel (iD), A. Moraes (iD), P. Rebello Teles (iD)

Universidade do Estado do Rio de Janeiro, Rio de Janeiro, Brazil
W.L. Aldá Júnior (iD), M. Alves Gallo Pereira (iD), M. Barroso Ferreira Filho (iD), H. Brandao Malbouisson (iD), W. Carvalho (iD), J. Chinellato[4], E.M. Da Costa (iD), G.G. Da Silveira[5] (iD), D. De Jesus Damiao (iD), V. Dos Santos Sousa (iD), S. Fonseca De Souza (iD), J. Martins[6] (iD), C. Mora Herrera (iD), K. Mota Amarilo (iD), L. Mundim (iD), H. Nogima (iD), A. Santoro (iD), S.M. Silva Do Amaral (iD), A. Sznajder (iD), M. Thiel (iD), F. Torres Da Silva De Araujo[7] (iD), A. Vilela Pereira (iD)

Universidade Estadual Paulista, Universidade Federal do ABC, São Paulo, Brazil
C.A. Bernardes[5] (iD), L. Calligaris (iD), T.R. Fernandez Perez Tomei (iD), E.M. Gregores (iD), P.G. Mercadante (iD), S.F. Novaes (iD), Sandra S. Padula (iD)

Institute for Nuclear Research and Nuclear Energy, Bulgarian Academy of Sciences, Sofia, Bulgaria
A. Aleksandrov (iD), G. Antchev (iD), R. Hadjiiska (iD), P. Iaydjiev (iD), M. Misheva (iD), M. Rodozov, M. Shopova (iD), G. Sultanov (iD)

University of Sofia, Sofia, Bulgaria

A. Dimitrov [iD], T. Ivanov [iD], L. Litov [iD], B. Pavlov [iD], P. Petkov [iD], A. Petrov [iD], E. Shumka [iD]

Beihang University, Beijing, China
T. Cheng [iD], T. Javaid[8] [iD], M. Mittal [iD], L. Yuan [iD]

Department of Physics, Tsinghua University, Beijing, China
M. Ahmad [iD], G. Bauer[9], Z. Hu [iD], S. Lezki [iD], K. Yi[9,10] [iD]

Institute of High Energy Physics, Beijing, China
G.M. Chen[8] [iD], H.S. Chen[8] [iD], M. Chen[8] [iD], F. Iemmi [iD], C.H. Jiang, A. Kapoor [iD], H. Liao [iD], Z.-A. Liu[11] [iD], V. Milosevic [iD], F. Monti [iD], R. Sharma [iD], J. Tao [iD], J. Thomas-Wilsker [iD], J. Wang [iD], H. Zhang [iD], J. Zhao [iD]

State Key Laboratory of Nuclear Physics and Technology, Peking University, Beijing, China
A. Agapitos [iD], Y. An [iD], Y. Ban [iD], C. Chen, A. Levin [iD], C. Li [iD], Q. Li [iD], X. Lyu, Y. Mao, S.J. Qian [iD], X. Sun [iD], D. Wang [iD], J. Xiao [iD], H. Yang

Sun Yat-Sen University, Guangzhou, China
J. Li, M. Lu [iD], Z. You [iD]

Institute of Modern Physics and Key Laboratory of Nuclear Physics and Ion-beam Application (MOE) - Fudan University, Shanghai, China
X. Gao[3] [iD], D. Leggat, H. Okawa [iD], Y. Zhang [iD]

Zhejiang University, Hangzhou, Zhejiang, China
Z. Lin [iD], C. Lu [iD], M. Xiao [iD]

Universidad de Los Andes, Bogota, Colombia
C. Avila [iD], D.A. Barbosa Trujillo, A. Cabrera [iD], C. Florez [iD], J. Fraga [iD]

Universidad de Antioquia, Medellin, Colombia
J. Mejia Guisao [iD], F. Ramirez [iD], M. Rodriguez [iD], J.D. Ruiz Alvarez [iD]

University of Split, Faculty of Electrical Engineering, Mechanical Engineering and Naval Architecture, Split, Croatia
D. Giljanovic [iD], N. Godinovic [iD], D. Lelas [iD], I. Puljak [iD]
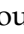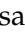
University of Split, Faculty of Science, Split, Croatia
Z. Antunovic, M. Kovac [iD], T. Sculac [iD]

Institute Rudjer Boskovic, Zagreb, Croatia
V. Brigljevic [iD], B.K. Chitroda [iD], D. Ferencek [iD], D. Majumder [iD], M. Roguljic [iD], A. Starodumov[12] [iD], T. Susa [iD]

University of Cyprus, Nicosia, Cyprus
A. Attikis [iD], K. Christoforou [iD], G. Kole [iD], M. Kolosova [iD], S. Konstantinou [iD], J. Mousa [iD], C. Nicolaou, F. Ptochos [iD], P.A. Razis [iD], H. Rykaczewski, H. Saka [iD]

Charles University, Prague, Czech Republic
M. Finger[12] [iD], M. Finger Jr.[12] [iD], A. Kveton [iD]
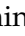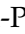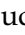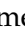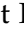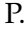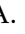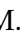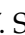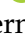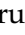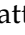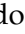
Escuela Politecnica Nacional, Quito, Ecuador
E. Ayala [iD]
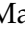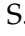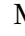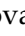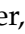
Universidad San Francisco de Quito, Quito, Ecuador
E. Carrera Jarrin [iD]
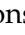
Academy of Scientific Research and Technology of the Arab Republic of Egypt, Egyptian

Network of High Energy Physics, Cairo, Egypt
S. Elgammal[13], A. Ellithi Kamel[14]

Center for High Energy Physics (CHEP-FU), Fayoum University, El-Fayoum, Egypt
A. Lotfy (iD), Y. Mohammed (iD)

National Institute of Chemical Physics and Biophysics, Tallinn, Estonia
S. Bhowmik (iD), R.K. Dewanjee (iD), K. Ehataht (iD), M. Kadastik, S. Nandan (iD), C. Nielsen (iD),
J. Pata (iD), M. Raidal (iD), L. Tani (iD), C. Veelken (iD)

Department of Physics, University of Helsinki, Helsinki, Finland
P. Eerola (iD), H. Kirschenmann (iD), K. Osterberg (iD), M. Voutilainen (iD)

Helsinki Institute of Physics, Helsinki, Finland
S. Bharthuar (iD), E. Brücken (iD), F. Garcia (iD), J. Havukainen (iD), M.S. Kim (iD), R. Kinnunen,
T. Lampén (iD), K. Lassila-Perini (iD), S. Lehti (iD), T. Lindén (iD), M. Lotti, L. Martikainen (iD),
M. Myllymäki (iD), J. Ott (iD), M.m. Rantanen (iD), H. Siikonen (iD), E. Tuominen (iD), J. Tuominiemi (iD)

Lappeenranta-Lahti University of Technology, Lappeenranta, Finland
P. Luukka (iD), H. Petrow (iD), T. Tuuva

IRFU, CEA, Université Paris-Saclay, Gif-sur-Yvette, France
C. Amendola (iD), M. Besancon (iD), F. Couderc (iD), M. Dejardin (iD), D. Denegri, J.L. Faure,
F. Ferri (iD), S. Ganjour (iD), P. Gras (iD), G. Hamel de Monchenault (iD), P. Jarry (iD), V. Lohezic (iD),
J. Malcles (iD), J. Rander, A. Rosowsky (iD), M.Ö. Sahin (iD), A. Savoy-Navarro[15] (iD), P. Simkina (iD),
M. Titov (iD)

**Laboratoire Leprince-Ringuet, CNRS/IN2P3, Ecole Polytechnique, Institut Polytechnique
de Paris, Palaiseau, France**
C. Baldenegro Barrera (iD), F. Beaudette (iD), A. Buchot Perraguin (iD), P. Busson (iD), A. Cappati (iD),
C. Charlot (iD), F. Damas (iD), O. Davignon (iD), B. Diab (iD), G. Falmagne (iD), B.A. Fontana Santos Alves (iD), S. Ghosh (iD), R. Granier de Cassagnac (iD), A. Hakimi (iD), B. Harikrishnan (iD),
J. Motta (iD), M. Nguyen (iD), C. Ochando (iD), L. Portales (iD), J. Rembser (iD), R. Salerno (iD),
U. Sarkar (iD), J.B. Sauvan (iD), Y. Sirois (iD), A. Tarabini (iD), E. Vernazza (iD), A. Zabi (iD), A. Zghiche (iD)

Université de Strasbourg, CNRS, IPHC UMR 7178, Strasbourg, France
J.-L. Agram[16] (iD), J. Andrea (iD), D. Apparu (iD), D. Bloch (iD), G. Bourgatte (iD), J.-M. Brom (iD),
E.C. Chabert (iD), C. Collard (iD), D. Darej, U. Goerlach (iD), C. Grimault, A.-C. Le Bihan (iD),
P. Van Hove (iD)

Institut de Physique des 2 Infinis de Lyon (IP2I), Villeurbanne, France
S. Beauceron (iD), C. Bernet (iD), G. Boudoul (iD), A. Carle, N. Chanon (iD), J. Choi (iD), D. Contardo (iD),
P. Depasse (iD), C. Dozen[17] (iD), H. El Mamouni, J. Fay (iD), S. Gascon (iD), M. Gouzevitch (iD),
G. Grenier (iD), B. Ille (iD), I.B. Laktineh, M. Lethuillier (iD), L. Mirabito, S. Perries, V. Sordini (iD),
L. Torterotot (iD), M. Vander Donckt (iD), P. Verdier (iD), S. Viret

Georgian Technical University, Tbilisi, Georgia
G. Adamov, I. Lomidze (iD), Z. Tsamalaidze[12] (iD)

RWTH Aachen University, I. Physikalisches Institut, Aachen, Germany
V. Botta (iD), L. Feld (iD), K. Klein (iD), M. Lipinski (iD), D. Meuser (iD), A. Pauls (iD), N. Röwert (iD),
M. Teroerde (iD)

RWTH Aachen University, III. Physikalisches Institut A, Aachen, Germany
S. Diekmann (iD), A. Dodonova (iD), N. Eich (iD), D. Eliseev (iD), M. Erdmann (iD), P. Fackeldey (iD),

B. Fischer [iD], T. Hebbeker [iD], K. Hoepfner [iD], F. Ivone [iD], M.y. Lee [iD], L. Mastrolorenzo, M. Merschmeyer [iD], A. Meyer [iD], S. Mondal [iD], S. Mukherjee [iD], D. Noll [iD], A. Novak [iD], F. Nowotny, A. Pozdnyakov [iD], Y. Rath, W. Redjeb [iD], H. Reithler [iD], A. Schmidt [iD], S.C. Schuler, A. Sharma [iD], L. Vigilante, S. Wiedenbeck [iD], S. Zaleski

RWTH Aachen University, III. Physikalisches Institut B, Aachen, Germany
C. Dziwok [iD], G. Flügge [iD], W. Haj Ahmad[18], O. Hlushchenko, T. Kress [iD], A. Nowack [iD], O. Pooth [iD], A. Stahl[19] [iD], T. Ziemons [iD], A. Zotz [iD]
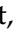
Deutsches Elektronen-Synchrotron, Hamburg, Germany
H. Aarup Petersen [iD], M. Aldaya Martin [iD], S. Amoroso, I. Andreev [iD], P. Asmuss, S. Baxter [iD], M. Bayatmakou [iD], O. Behnke [iD], A. Bermúdez Martínez [iD], S. Bhattacharya [iD], A.A. Bin Anuar [iD], F. Blekman[20] [iD], K. Borras[21] [iD], D. Brunner [iD], A. Campbell [iD], A. Cardini [iD], C. Cheng [iD], F. Colombina [iD], S. Consuegra Rodríguez [iD], G. Correia Silva [iD], M. De Silva [iD], L. Didukh [iD], G. Eckerlin, D. Eckstein [iD], L.I. Estevez Banos [iD], O. Filatov [iD], E. Gallo[20] [iD], A. Geiser [iD], A. Giraldi [iD], G. Greau, A. Grohsjean [iD], V. Guglielmi [iD], M. Guthoff [iD], A. Jafari[22] [iD], N.Z. Jomhari [iD], B. Kaech [iD], A. Kasem[21] [iD], M. Kasemann [iD], H. Kaveh [iD], C. Kleinwort [iD], R. Kogler [iD], M. Komm [iD], D. Krücker [iD], W. Lange, D. Leyva Pernia [iD], K. Lipka [iD], W. Lohmann[23] [iD], R. Mankel [iD], I.-A. Melzer-Pellmann [iD], M. Mendizabal Morentin [iD], J. Metwally, A.B. Meyer [iD], G. Milella [iD], M. Mormile [iD], A. Mussgiller [iD], A. Nürnberg [iD], Y. Otarid, D. Pérez Adán [iD], A. Raspereza [iD], B. Ribeiro Lopes [iD], J. Rübenach, A. Saggio [iD], A. Saibel [iD], M. Savitskyi [iD], M. Scham[24,21] [iD], V. Scheurer, S. Schnake[21] [iD], P. Schütze [iD], C. Schwanenberger[20] [iD], M. Shchedrolosiev [iD], R.E. Sosa Ricardo [iD], D. Stafford [iD], N. Tonon[+] [iD], M. Van De Klundert [iD], F. Vazzoler [iD], A. Velyka, A. Ventura Barroso [iD], R. Walsh [iD], D. Walter [iD], Q. Wang [iD], Y. Wen [iD], K. Wichmann, L. Wiens[21] [iD], C. Wissing [iD], S. Wuchterl [iD], Y. Yang [iD], A. Zimermmane Castro Santos [iD]

University of Hamburg, Hamburg, Germany
R. Aggleton, A. Albrecht [iD], S. Albrecht [iD], M. Antonello [iD], S. Bein [iD], L. Benato [iD], M. Bonanomi [iD], P. Connor [iD], K. De Leo [iD], M. Eich, K. El Morabit [iD], F. Feindt, A. Fröhlich, C. Garbers [iD], E. Garutti [iD], M. Hajheidari, J. Haller [iD], A. Hinzmann [iD], H.R. Jabusch [iD], G. Kasieczka [iD], R. Klanner [iD], W. Korcari [iD], T. Kramer [iD], V. Kutzner [iD], J. Lange [iD], T. Lange [iD], A. Lobanov [iD], C. Matthies [iD], A. Mehta [iD], L. Moureaux [iD], M. Mrowietz, A. Nigamova [iD], Y. Nissan, A. Paasch [iD], K.J. Pena Rodriguez [iD], M. Rieger [iD], O. Rieger, P. Schleper [iD], M. Schröder [iD], J. Schwandt [iD], H. Stadie [iD], G. Steinbrück [iD], A. Tews, M. Wolf [iD]
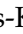
Karlsruher Institut fuer Technologie, Karlsruhe, Germany
J. Bechtel [iD], S. Brommer [iD], M. Burkart, E. Butz [iD], R. Caspart [iD], T. Chwalek [iD], A. Dierlamm [iD], A. Droll, N. Faltermann [iD], M. Giffels [iD], J.O. Gosewisch, A. Gottmann [iD], F. Hartmann[19] [iD], M. Horzela [iD], U. Husemann [iD], P. Keicher [iD], M. Klute [iD], R. Koppenhöfer [iD], S. Maier [iD], S. Mitra [iD], Th. Müller [iD], M. Neukum, G. Quast [iD], K. Rabbertz [iD], J. Rauser, D. Savoiu [iD], M. Schnepf, D. Seith, I. Shvetsov [iD], H.J. Simonis [iD], N. Trevisani [iD], R. Ulrich [iD], J. van der Linden [iD], R.F. Von Cube [iD], M. Wassmer [iD], M. Weber [iD], S. Wieland [iD], R. Wolf [iD], S. Wozniewski [iD], S. Wunsch

Institute of Nuclear and Particle Physics (INPP), NCSR Demokritos, Aghia Paraskevi, Greece
G. Anagnostou, P. Assiouras [iD], G. Daskalakis [iD], A. Kyriakis [iD], A. Stakia [iD]

National and Kapodistrian University of Athens, Athens, Greece
M. Diamantopoulou, D. Karasavvas, P. Kontaxakis [iD], A. Manousakis-Katsikakis [iD], A. Panagiotou, I. Papavergou [iD], N. Saoulidou [iD], K. Theofilatos [iD], E. Tziaferi [iD], K. Vellidis [iD],

E. Vourliotis [iD], I. Zisopoulos [iD]

National Technical University of Athens, Athens, Greece

G. Bakas [iD], T. Chatzistavrou, K. Kousouris [iD], I. Papakrivopoulos [iD], G. Tsipolitis [iD], A. Zacharopoulou

University of Ioánnina, Ioánnina, Greece

K. Adamidis, I. Bestintzanos, I. Evangelou [iD], C. Foudas, P. Gianneios [iD], C. Kamtsikis, P. Katsoulis, P. Kokkas [iD], P.G. Kosmoglou Kioseoglou [iD], N. Manthos [iD], I. Papadopoulos [iD], J. Strologas [iD]

HUN-REN Wigner Research Centre for Physics, Budapest, Hungary

M. Bartók[25] [iD], G. Bencze, C. Hajdu [iD], D. Horvath[26,27] [iD], F. Sikler [iD], V. Veszpremi [iD]

MTA-ELTE Lendület CMS Particle and Nuclear Physics Group, Eötvös Loránd University, Budapest, Hungary

M. Csanád [iD], K. Farkas [iD], M.M.A. Gadallah[28] [iD], S. Lökös[29] [iD], P. Major [iD], K. Mandal [iD], G. Pásztor [iD], A.J. Rádl[30] [iD], O. Surányi [iD], G.I. Veres [iD]

HUN-REN ATOMKI - Institute of Nuclear Research, Debrecen, Hungary

N. Beni [iD], S. Czellar, D. Fasanella [iD], J. Karancsi[25] [iD], J. Molnar, Z. Szillasi, D. Teyssier [iD]
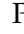
Institute of Physics, University of Debrecen, Debrecen, Hungary

P. Raics, B. Ujvari[31] [iD]

Karoly Robert Campus, MATE Institute of Technology, Gyongyos, Hungary

T. Csorgo[30] [iD], F. Nemes[30] [iD], T. Novak [iD]

Panjab University, Chandigarh, India

J. Babbar [iD], S. Bansal [iD], S.B. Beri, V. Bhatnagar [iD], G. Chaudhary [iD], S. Chauhan [iD], N. Dhingra[32] [iD], R. Gupta, A. Kaur [iD], A. Kaur [iD], H. Kaur [iD], M. Kaur [iD], S. Kumar [iD], P. Kumari [iD], M. Meena [iD], K. Sandeep [iD], T. Sheokand, J.B. Singh[33] [iD], A. Singla [iD], A. K. Virdi [iD]
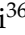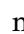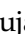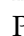
University of Delhi, Delhi, India

A. Ahmed [iD], A. Bhardwaj [iD], B.C. Choudhary [iD], M. Gola, S. Keshri [iD], A. Kumar [iD], M. Naimuddin [iD], P. Priyanka [iD], K. Ranjan [iD], S. Saumya [iD], A. Shah [iD]

Saha Institute of Nuclear Physics, HBNI, Kolkata, India

S. Baradia [iD], S. Barman[34] [iD], S. Bhattacharya [iD], D. Bhowmik, S. Dutta [iD], S. Dutta, B. Gomber[35] [iD], M. Maity[34], P. Palit [iD], P.K. Rout [iD], G. Saha [iD], B. Sahu [iD], S. Sarkar

Indian Institute of Technology Madras, Madras, India

P.K. Behera [iD], S.C. Behera [iD], P. Kalbhor [iD], J.R. Komaragiri[36] [iD], D. Kumar[36] [iD], A. Muhammad [iD], L. Panwar[36] [iD], R. Pradhan [iD], P.R. Pujahari [iD], A. Sharma [iD], A.K. Sikdar [iD], P.C. Tiwari[36] [iD], S. Verma [iD]
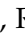
Bhabha Atomic Research Centre, Mumbai, India

K. Naskar[37] [iD]

Tata Institute of Fundamental Research-A, Mumbai, India

T. Aziz, I. Das [iD], S. Dugad, M. Kumar [iD], G.B. Mohanty [iD], P. Suryadevara

Tata Institute of Fundamental Research-B, Mumbai, India

S. Banerjee [iD], R. Chudasama [iD], M. Guchait [iD], S. Karmakar [iD], S. Kumar [iD], G. Majumder [iD], K. Mazumdar [iD], S. Mukherjee [iD], A. Thachayath [iD]
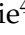
National Institute of Science Education and Research, An OCC of Homi Bhabha National Institute, Bhubaneswar, Odisha, India

S. Bahinipati[38] (iD), A.K. Das, C. Kar (iD), P. Mal (iD), T. Mishra (iD), V.K. Muraleedharan Nair Bindhu[39] (iD), A. Nayak[39] (iD), P. Saha (iD), N. Sur (iD), S.K. Swain (iD), D. Vats[39] (iD)

Indian Institute of Science Education and Research (IISER), Pune, India

A. Alpana (iD), S. Dube (iD), B. Kansal (iD), A. Laha (iD), S. Pandey (iD), A. Rastogi (iD), S. Sharma (iD)

Isfahan University of Technology, Isfahan, Iran

H. Bakhshiansohi[40,41] (iD), E. Khazaie[41] (iD), M. Zeinali[42]
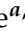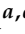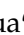
Institute for Research in Fundamental Sciences (IPM), Tehran, Iran

S. Chenarani[43] (iD), S.M. Etesami (iD), M. Khakzad (iD), M. Mohammadi Najafabadi (iD)
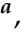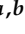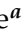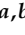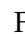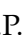
University College Dublin, Dublin, Ireland

M. Grunewald (iD)

INFN Sezione di Bari^a, Università di Bari^b, Politecnico di Bari^c, Bari, Italy

M. Abbrescia^{a,b} (iD), R. Aly^{a,b,44} (iD), C. Aruta^{a,b} (iD), A. Colaleo^a (iD), D. Creanza^{a,c} (iD), N. De Filippis^{a,c} (iD), M. De Palma^{a,b} (iD), A. Di Florio^{a,b} (iD), W. Elmetenawee^{a,b} (iD), F. Errico^{a,b} (iD), L. Fiore^a (iD), G. Iaselli^{a,c} (iD), M. Ince^{a,b} (iD), G. Maggi^{a,c} (iD), M. Maggi^a (iD), I. Margjeka^{a,b} (iD), V. Mastrapasqua^{a,b} (iD), S. My^{a,b} (iD), S. Nuzzo^{a,b} (iD), A. Pellecchia^{a,b} (iD), A. Pompili^{a,b} (iD), G. Pugliese^{a,c} (iD), R. Radogna^a (iD), D. Ramos^a (iD), A. Ranieri^a (iD), G. Selvaggi^{a,b} (iD), L. Silvestris^a (iD), F.M. Simone^{a,b} (iD), Ü. Sözbilir^a (iD), A. Stamerra^a (iD), R. Venditti^a (iD), P. Verwilligen^a (iD), A. Zaza^{a,b} (iD)
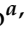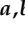
INFN Sezione di Bologna^a, Università di Bologna^b, Bologna, Italy

G. Abbiendi^a (iD), C. Battilana^{a,b} (iD), D. Bonacorsi^{a,b} (iD), L. Borgonovi^a (iD), L. Brigliadori^a, R. Campanini^{a,b} (iD), P. Capiluppi^{a,b} (iD), A. Castro^{a,b} (iD), F.R. Cavallo^a (iD), M. Cuffiani^{a,b} (iD), G.M. Dallavalle^a (iD), T. Diotalevi^{a,b} (iD), F. Fabbri^a (iD), A. Fanfani^{a,b} (iD), P. Giacomelli^a (iD), L. Giommi^{a,b} (iD), C. Grandi^a (iD), L. Guiducci^{a,b} (iD), S. Lo Meo^{a,45} (iD), L. Lunerti^{a,b} (iD), S. Marcellini^a (iD), G. Masetti^a (iD), F.L. Navarria^{a,b} (iD), A. Perrotta^a (iD), F. Primavera^{a,b} (iD), A.M. Rossi^{a,b} (iD), T. Rovelli^{a,b} (iD), G.P. Siroli^{a,b} (iD)

INFN Sezione di Catania^a, Università di Catania^b, Catania, Italy

S. Costa^{a,b,46} (iD), A. Di Mattia^a (iD), R. Potenza^{a,b}, A. Tricomi^{a,b,46} (iD), C. Tuve^{a,b} (iD)
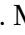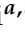
INFN Sezione di Firenze^a, Università di Firenze^b, Firenze, Italy

G. Barbagli^a (iD), B. Camaiani^{a,b} (iD), A. Cassese^a (iD), R. Ceccarelli^{a,b} (iD), V. Ciulli^{a,b} (iD), C. Civinini^a (iD), R. D'Alessandro^{a,b} (iD), E. Focardi^{a,b} (iD), G. Latino^{a,b} (iD), P. Lenzi^{a,b} (iD), M. Lizzo^{a,b} (iD), M. Meschini^a (iD), S. Paoletti^a (iD), R. Seidita^{a,b} (iD), G. Sguazzoni^a (iD), L. Viliani^a (iD)
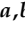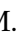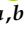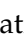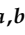
INFN Laboratori Nazionali di Frascati, Frascati, Italy

L. Benussi (iD), S. Bianco (iD), S. Meola[19] (iD), D. Piccolo (iD)
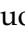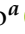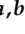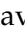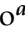
INFN Sezione di Genova^a, Università di Genova^b, Genova, Italy

M. Bozzo^{a,b} (iD), F. Ferro^a (iD), R. Mulargia^a (iD), E. Robutti^a (iD), S. Tosi^{a,b} (iD)
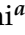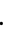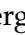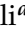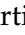
INFN Sezione di Milano-Bicocca^a, Università di Milano-Bicocca^b, Milano, Italy

A. Benaglia^a (iD), G. Boldrini^a (iD), F. Brivio^{a,b} (iD), F. Cetorelli^{a,b} (iD), F. De Guio^{a,b} (iD), M.E. Dinardo^{a,b} (iD), P. Dini^a (iD), S. Gennai^a (iD), A. Ghezzi^{a,b} (iD), P. Govoni^{a,b} (iD), L. Guzzi^{a,b} (iD), M.T. Lucchini^{a,b} (iD), M. Malberti^a (iD), S. Malvezzi^a (iD), A. Massironi^a (iD), D. Menasce^a (iD), L. Moroni^a (iD), M. Paganoni^{a,b} (iD), D. Pedrini^a (iD), B.S. Pinolini^a, S. Ragazzi^{a,b} (iD), N. Redaelli^a (iD), T. Tabarelli de Fatis^{a,b} (iD), D. Zuolo^{a,b} (iD)
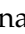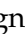
INFN Sezione di Napoli[a], Università di Napoli 'Federico II'[b], Napoli, Italy; Università della Basilicata[c], Potenza, Italy; Scuola Superiore Meridionale (SSM)[d], Napoli, Italy

S. Buontempo[a] (iD), F. Carnevali[a,b], N. Cavallo[a,c] (iD), A. De Iorio[a,b] (iD), F. Fabozzi[a,c] (iD), A.O.M. Iorio[a,b] (iD), L. Lista[a,b,47] (iD), P. Paolucci[a,19] (iD), B. Rossi[a] (iD), C. Sciacca[a,b] (iD)
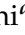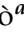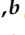
INFN Sezione di Padova[a], Università di Padova[b], Padova, Italy; Università di Trento[c], Trento, Italy

P. Azzi[a] (iD), M. Bellato[a] (iD), M. Benettoni[a] (iD), A. Bergnoli[a] (iD), P. Bortignon[a] (iD), A. Bragagnolo[a,b] (iD), P. Checchia[a] (iD), T. Dorigo[a] (iD), F. Gasparini[a,b] (iD), U. Gasparini[a,b] (iD), G. Grosso[a], L. Layer[a,48], E. Lusiani[a] (iD), M. Margoni[a,b] (iD), A.T. Meneguzzo[a,b] (iD), J. Pazzini[a,b] (iD), P. Ronchese[a,b] (iD), R. Rossin[a,b] (iD), F. Simonetto[a,b] (iD), G. Strong[a] (iD), M. Tosi[a,b] (iD), H. Yarar[a,b], M. Zanetti[a,b] (iD), P. Zotto[a,b] (iD), A. Zucchetta[a,b] (iD), G. Zumerle[a,b] (iD)
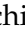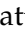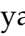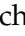
INFN Sezione di Pavia[a], Università di Pavia[b], Pavia, Italy

C. Aimè[a,b] (iD), A. Braghieri[a] (iD), S. Calzaferri[a,b] (iD), D. Fiorina[a,b] (iD), P. Montagna[a,b] (iD), V. Re[a] (iD), C. Riccardi[a,b] (iD), P. Salvini[a] (iD), I. Vai[a] (iD), P. Vitulo[a,b] (iD)

INFN Sezione di Perugia[a], Università di Perugia[b], Perugia, Italy

P. Asenov[a,49] (iD), G.M. Bilei[a] (iD), D. Ciangottini[a,b] (iD), L. Fanò[a,b] (iD), M. Magherini[a,b] (iD), G. Mantovani[a,b], V. Mariani[a,b] (iD), M. Menichelli[a] (iD), F. Moscatelli[a,49] (iD), A. Piccinelli[a,b] (iD), M. Presilla[a,b] (iD), A. Rossi[a,b] (iD), A. Santocchia[a,b] (iD), D. Spiga[a] (iD), T. Tedeschi[a,b] (iD)

INFN Sezione di Pisa[a], Università di Pisa[b], Scuola Normale Superiore di Pisa[c], Pisa, Italy; Università di Siena[d], Siena, Italy

P. Azzurri[a] (iD), G. Bagliesi[a] (iD), V. Bertacchi[a,c] (iD), R. Bhattacharya[a] (iD), L. Bianchini[a,b] (iD), T. Boccali[a] (iD), E. Bossini[a,b] (iD), D. Bruschini[a,c] (iD), R. Castaldi[a] (iD), M.A. Ciocci[a,b] (iD), V. D'Amante[a,d] (iD), R. Dell'Orso[a] (iD), M.R. Di Domenico[a,d] (iD), S. Donato[a] (iD), A. Giassi[a] (iD), F. Ligabue[a,c] (iD), E. Manca[a,c] (iD), G. Mandorli[a,c] (iD), D. Matos Figueiredo[a] (iD), A. Messineo[a,b] (iD), M. Musich[a,b] (iD), F. Palla[a] (iD), S. Parolia[a,b] (iD), G. Ramirez-Sanchez[a,c] (iD), A. Rizzi[a,b] (iD), G. Rolandi[a,c] (iD), S. Roy Chowdhury[a,c] (iD), T. Sarkar[a,34] (iD), A. Scribano[a] (iD), N. Shafiei[a,b] (iD), P. Spagnolo[a] (iD), R. Tenchini[a] (iD), G. Tonelli[a,b] (iD), N. Turini[a,d] (iD), A. Venturi[a] (iD), P.G. Verdini[a] (iD)

INFN Sezione di Roma[a], Sapienza Università di Roma[b], Roma, Italy

P. Barria[a] (iD), M. Campana[a,b] (iD), F. Cavallari[a] (iD), D. Del Re[a,b] (iD), E. Di Marco[a] (iD), M. Diemoz[a] (iD), E. Longo[a,b] (iD), P. Meridiani[a] (iD), G. Organtini[a,b] (iD), F. Pandolfi[a] (iD), R. Paramatti[a,b] (iD), C. Quaranta[a,b] (iD), S. Rahatlou[a,b] (iD), C. Rovelli[a] (iD), F. Santanastasio[a,b] (iD), L. Soffi[a] (iD), R. Tramontano[a,b] (iD)

INFN Sezione di Torino[a], Università di Torino[b], Torino, Italy; Università del Piemonte Orientale[c], Novara, Italy

N. Amapane[a,b] (iD), R. Arcidiacono[a,c] (iD), S. Argiro[a,b] (iD), M. Arneodo[a,c] (iD), N. Bartosik[a] (iD), R. Bellan[a,b] (iD), A. Bellora[a,b] (iD), J. Berenguer Antequera[a,b] (iD), C. Biino[a] (iD), N. Cartiglia[a] (iD), M. Costa[a,b] (iD), R. Covarelli[a,b] (iD), N. Demaria[a] (iD), M. Grippo[a,b] (iD), B. Kiani[a,b] (iD), F. Legger[a] (iD), C. Mariotti[a] (iD), S. Maselli[a] (iD), A. Mecca[a,b] (iD), E. Migliore[a,b] (iD), E. Monteil[a,b] (iD), M. Monteno[a] (iD), M.M. Obertino[a,b] (iD), G. Ortona[a] (iD), L. Pacher[a,b] (iD), N. Pastrone[a] (iD), M. Pelliccioni[a] (iD), M. Ruspa[a,c] (iD), K. Shchelina[a] (iD), F. Siviero[a,b] (iD), V. Sola[a] (iD), A. Solano[a,b] (iD), D. Soldi[a,b] (iD), A. Staiano[a] (iD), M. Tornago[a,b] (iD), D. Trocino[a] (iD), G. Umoret[a,b] (iD), A. Vagnerini[a,b] (iD)

INFN Sezione di Trieste[a], Università di Trieste[b], Trieste, Italy

S. Belforte[a] (iD), V. Candelise[a,b] (iD), M. Casarsa[a] (iD), F. Cossutti[a] (iD), A. Da Rold[a,b] (iD), G. Della Ricca[a,b] (iD), G. Sorrentino[a,b] (iD)

Kyungpook National University, Daegu, Korea

S. Dogra ⓘ, C. Huh ⓘ, B. Kim ⓘ, D.H. Kim ⓘ, G.N. Kim ⓘ, J. Kim, J. Lee ⓘ, S.W. Lee ⓘ, C.S. Moon ⓘ, Y.D. Oh ⓘ, S.I. Pak ⓘ, S. Sekmen ⓘ, Y.C. Yang ⓘ

Chonnam National University, Institute for Universe and Elementary Particles, Kwangju, Korea

H. Kim ⓘ, D.H. Moon ⓘ

Hanyang University, Seoul, Korea

E. Asilar ⓘ, T.J. Kim ⓘ, J. Park ⓘ

Korea University, Seoul, Korea

S. Cho, S. Choi ⓘ, S. Han, B. Hong ⓘ, K. Lee, K.S. Lee ⓘ, J. Lim, J. Park, S.K. Park, J. Yoo ⓘ

Kyung Hee University, Department of Physics, Seoul, Korea

J. Goh ⓘ

Sejong University, Seoul, Korea

H. S. Kim ⓘ, Y. Kim, S. Lee

Seoul National University, Seoul, Korea

J. Almond, J.H. Bhyun, J. Choi ⓘ, S. Jeon ⓘ, W. Jun ⓘ, J. Kim ⓘ, J. Kim ⓘ, J.S. Kim, S. Ko ⓘ, H. Kwon ⓘ, H. Lee ⓘ, J. Lee ⓘ, S. Lee, B.H. Oh ⓘ, M. Oh ⓘ, S.B. Oh ⓘ, H. Seo ⓘ, U.K. Yang, I. Yoon ⓘ

University of Seoul, Seoul, Korea

W. Jang ⓘ, D.Y. Kang, Y. Kang ⓘ, D. Kim ⓘ, S. Kim ⓘ, B. Ko, J.S.H. Lee ⓘ, Y. Lee ⓘ, J.A. Merlin, I.C. Park ⓘ, Y. Roh, M.S. Ryu ⓘ, D. Song, I.J. Watson ⓘ, S. Yang ⓘ

Yonsei University, Department of Physics, Seoul, Korea

S. Ha ⓘ, H.D. Yoo ⓘ

Sungkyunkwan University, Suwon, Korea

M. Choi ⓘ, H. Lee, Y. Lee ⓘ, Y. Lee ⓘ, I. Yu ⓘ

College of Engineering and Technology, American University of the Middle East (AUM), Dasman, Kuwait

T. Beyrouthy ⓘ, Y. Maghrbi ⓘ

Riga Technical University, Riga, Latvia

K. Dreimanis ⓘ, A. Gaile ⓘ, A. Potrebko ⓘ, T. Torims ⓘ, V. Veckalns[50] ⓘ

Vilnius University, Vilnius, Lithuania

M. Ambrozas ⓘ, A. Carvalho Antunes De Oliveira ⓘ, A. Juodagalvis ⓘ, A. Rinkevicius ⓘ, G. Tamulaitis ⓘ

National Centre for Particle Physics, Universiti Malaya, Kuala Lumpur, Malaysia
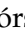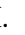
N. Bin Norjoharuddeen ⓘ, S.Y. Hoh[51] ⓘ, I. Yusuff[51] ⓘ, Z. Zolkapli

Universidad de Sonora (UNISON), Hermosillo, Mexico
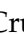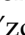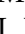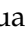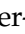
J.F. Benitez ⓘ, A. Castaneda Hernandez ⓘ, H.A. Encinas Acosta, L.G. Gallegos Maríñez, M. León Coello ⓘ, J.A. Murillo Quijada ⓘ, A. Sehrawat ⓘ, L. Valencia Palomo ⓘ

Centro de Investigacion y de Estudios Avanzados del IPN, Mexico City, Mexico

G. Ayala ⓘ, H. Castilla-Valdez ⓘ, I. Heredia-De La Cruz[52] ⓘ, R. Lopez-Fernandez ⓘ, C.A. Mondragon Herrera, D.A. Perez Navarro ⓘ, A. Sánchez Hernández ⓘ

Universidad Iberoamericana, Mexico City, Mexico
C. Oropeza Barrera (iD), F. Vazquez Valencia (iD)

Benemerita Universidad Autonoma de Puebla, Puebla, Mexico
I. Pedraza (iD), H.A. Salazar Ibarguen (iD), C. Uribe Estrada (iD)

University of Montenegro, Podgorica, Montenegro
I. Bubanja (iD), J. Mijuskovic[53] (iD), N. Raicevic (iD)

National Centre for Physics, Quaid-I-Azam University, Islamabad, Pakistan
A. Ahmad (iD), M.I. Asghar, A. Awais (iD), M.I.M. Awan, M. Gul (iD), H.R. Hoorani (iD), W.A. Khan (iD), M. Shoaib (iD), M. Waqas (iD)

AGH University of Krakow, Faculty of Computer Science, Electronics and Telecommunications, Krakow, Poland
V. Avati, L. Grzanka (iD), M. Malawski (iD)

National Centre for Nuclear Research, Swierk, Poland
H. Bialkowska (iD), M. Bluj (iD), B. Boimska (iD), M. Górski (iD), M. Kazana (iD), M. Szleper (iD), P. Zalewski (iD)

Institute of Experimental Physics, Faculty of Physics, University of Warsaw, Warsaw, Poland
K. Bunkowski (iD), K. Doroba (iD), A. Kalinowski (iD), M. Konecki (iD), J. Krolikowski (iD)

Laboratório de Instrumentação e Física Experimental de Partículas, Lisboa, Portugal
M. Araujo (iD), P. Bargassa (iD), D. Bastos (iD), A. Boletti (iD), P. Faccioli (iD), M. Gallinaro (iD), J. Hollar (iD), N. Leonardo (iD), T. Niknejad (iD), M. Pisano (iD), J. Seixas (iD), O. Toldaiev (iD), J. Varela (iD)

VINCA Institute of Nuclear Sciences, University of Belgrade, Belgrade, Serbia
P. Adzic[54] (iD), M. Dordevic (iD), P. Milenovic (iD), J. Milosevic (iD)

VINCA Institute of Nuclear Sciences, University of Belgrade, Belgrade, Serbia
V. Rekovic

Centro de Investigaciones Energéticas Medioambientales y Tecnológicas (CIEMAT), Madrid, Spain
M. Aguilar-Benitez, J. Alcaraz Maestre (iD), A. Álvarez Fernández (iD), M. Barrio Luna, Cristina F. Bedoya (iD), C.A. Carrillo Montoya (iD), M. Cepeda (iD), M. Cerrada (iD), N. Colino (iD), B. De La Cruz (iD), A. Delgado Peris (iD), D. Fernández Del Val (iD), J.P. Fernández Ramos (iD), J. Flix (iD), M.C. Fouz (iD), O. Gonzalez Lopez (iD), S. Goy Lopez (iD), J.M. Hernandez (iD), M.I. Josa (iD), J. León Holgado (iD), D. Moran (iD), C. Perez Dengra (iD), A. Pérez-Calero Yzquierdo (iD), J. Puerta Pelayo (iD), I. Redondo (iD), D.D. Redondo Ferrero, L. Romero, S. Sánchez Navas (iD), J. Sastre (iD), L. Urda Gómez (iD), J. Vazquez Escobar (iD), C. Willmott

Universidad Autónoma de Madrid, Madrid, Spain
J.F. de Trocóniz (iD)

Universidad de Oviedo, Instituto Universitario de Ciencias y Tecnologías Espaciales de Asturias (ICTEA), Oviedo, Spain
B. Alvarez Gonzalez (iD), J. Cuevas (iD), J. Fernandez Menendez (iD), S. Folgueras (iD), I. Gonzalez Caballero (iD), J.R. González Fernández (iD), E. Palencia Cortezon (iD), C. Ramón Álvarez (iD), V. Rodríguez Bouza (iD), A. Soto Rodríguez (iD), A. Trapote (iD), C. Vico Villalba (iD)

Instituto de Física de Cantabria (IFCA), CSIC-Universidad de Cantabria, Santander, Spain
J.A. Brochero Cifuentes (iD), I.J. Cabrillo (iD), A. Calderon (iD), J. Duarte Campderros (iD), M. Fernandez (iD), C. Fernandez Madrazo (iD), A. García Alonso, G. Gomez (iD), C. Lasaosa García (iD),

C. Martinez Rivero, P. Martinez Ruiz del Arbol, F. Matorras, P. Matorras Cuevas, J. Piedra Gomez, C. Prieels, A. Ruiz-Jimeno, L. Scodellaro, I. Vila, J.M. Vizan Garcia

University of Colombo, Colombo, Sri Lanka
M.K. Jayananda, B. Kailasapathy[55], D.U.J. Sonnadara, D.D.C. Wickramarathna
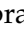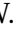
University of Ruhuna, Department of Physics, Matara, Sri Lanka
W.G.D. Dharmaratna[56], K. Liyanage, N. Perera, N. Wickramage
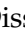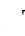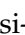
CERN, European Organization for Nuclear Research, Geneva, Switzerland
D. Abbaneo, J. Alimena, E. Auffray, G. Auzinger, J. Baechler, P. Baillon[†], D. Barney, J. Bendavid, M. Bianco, B. Bilin, A. Bocci, E. Brondolin, C. Caillol, T. Camporesi, G. Cerminara, N. Chernyavskaya, S.S. Chhibra, S. Choudhury, M. Cipriani, L. Cristella, D. d'Enterria, A. Dabrowski, A. David, A. De Roeck, M.M. Defranchis, M. Deile, M. Dobson, M. Dünser, N. Dupont, A. Elliott-Peisert, F. Fallavollita[57], A. Florent, L. Forthomme, G. Franzoni, W. Funk, S. Ghosh, S. Giani, D. Gigi, K. Gill, F. Glege, L. Gouskos, E. Govorkova, M. Haranko, J. Hegeman, V. Innocente, T. James, P. Janot, J. Kaspar, J. Kieseler, N. Kratochwil, S. Laurila, P. Lecoq, E. Leutgeb, A. Lintuluoto, C. Lourenço, B. Maier, L. Malgeri, M. Mannelli, A.C. Marini, F. Meijers, S. Mersi, E. Meschi, F. Moortgat, M. Mulders, S. Orfanelli, L. Orsini, F. Pantaleo, E. Perez, M. Peruzzi, A. Petrilli, G. Petrucciani, A. Pfeiffer, M. Pierini, D. Piparo, M. Pitt, H. Qu, T. Quast, D. Rabady, A. Racz, G. Reales Gutiérrez, M. Rovere, H. Sakulin, J. Salfeld-Nebgen, S. Scarfi, M. Selvaggi, A. Sharma, P. Silva, P. Sphicas[58], A.G. Stahl Leiton, S. Summers, K. Tatar, V.R. Tavolaro, D. Treille, P. Tropea, A. Tsirou, J. Wanczyk[59], K.A. Wozniak, W.D. Zeuner
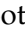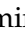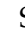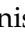
PSI Center for Neutron and Muon Sciences, Villigen, Switzerland
L. Caminada[60], A. Ebrahimi, W. Erdmann, R. Horisberger, Q. Ingram, H.C. Kaestli, D. Kotlinski, C. Lange, M. Missiroli[60], L. Noehte[60], T. Rohe

ETH Zurich - Institute for Particle Physics and Astrophysics (IPA), Zurich, Switzerland
T.K. Aarrestad, K. Androsov[59], M. Backhaus, P. Berger, A. Calandri, K. Datta, A. De Cosa, G. Dissertori, M. Dittmar, M. Donegà, F. Eble, M. Galli, K. Gedia, F. Glessgen, T.A. Gómez Espinosa, C. Grab, D. Hits, W. Lustermann, A.-M. Lyon, R.A. Manzoni, L. Marchese, C. Martin Perez, A. Mascellani[59], M.T. Meinhard, F. Nessi-Tedaldi, J. Niedziela, F. Pauss, V. Perovic, S. Pigazzini, M.G. Ratti, M. Reichmann, C. Reissel, T. Reitenspiess, B. Ristic, F. Riti, D. Ruini, D.A. Sanz Becerra, J. Steggemann[59], D. Valsecchi[19], R. Wallny
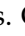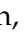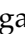
Universität Zürich, Zurich, Switzerland
C. Amsler[61], P. Bärtschi, C. Botta, D. Brzhechko, M.F. Canelli, K. Cormier, A. De Wit, R. Del Burgo, J.K. Heikkilä, M. Huwiler, W. Jin, A. Jofrehei, B. Kilminster, S. Leontsinis, S.P. Liechti, A. Macchiolo, P. Meiring, V.M. Mikuni, U. Molinatti, I. Neutelings, A. Reimers, P. Robmann, S. Sanchez Cruz, K. Schweiger, M. Senger, Y. Takahashi

National Central University, Chung-Li, Taiwan
C. Adloff[62], C.M. Kuo, W. Lin, S.S. Yu

National Taiwan University (NTU), Taipei, Taiwan
L. Ceard, Y. Chao, K.F. Chen, P.s. Chen, H. Cheng, W.-S. Hou, Y.y. Li, R.-S. Lu, E. Paganis, A. Psallidas, A. Steen, H.y. Wu, E. Yazgan, P.r. Yu

High Energy Physics Research Unit, Department of Physics, Faculty of Science, Chulalongkorn University, Bangkok, Thailand
C. Asawatangtrakuldee ⓘ, N. Srimanobhas ⓘ

Çukurova University, Physics Department, Science and Art Faculty, Adana, Turkey
D. Agyel ⓘ, F. Boran ⓘ, Z.S. Demiroglu ⓘ, F. Dolek ⓘ, I. Dumanoglu[63] ⓘ, E. Eskut ⓘ, Y. Guler[64] ⓘ, E. Gurpinar Guler[64] ⓘ, C. Isik ⓘ, O. Kara, A. Kayis Topaksu ⓘ, U. Kiminsu ⓘ, G. Onengut ⓘ, K. Ozdemir[65] ⓘ, A. Polatoz ⓘ, A.E. Simsek ⓘ, B. Tali[66] ⓘ, U.G. Tok ⓘ, S. Turkcapar ⓘ, E. Uslan ⓘ, I.S. Zorbakir ⓘ

Middle East Technical University, Physics Department, Ankara, Turkey
G. Karapinar, K. Ocalan[67] ⓘ, M. Yalvac[68] ⓘ

Bogazici University, Istanbul, Turkey
B. Akgun ⓘ, I.O. Atakisi ⓘ, E. Gülmez ⓘ, M. Kaya[69] ⓘ, O. Kaya[70] ⓘ, Ö. Özçelik ⓘ, S. Tekten[71] ⓘ

Istanbul Technical University, Istanbul, Turkey
A. Cakir ⓘ, K. Cankocak[63] ⓘ, Y. Komurcu ⓘ, S. Sen[72] ⓘ

Istanbul University, Istanbul, Turkey
O. Aydilek ⓘ, S. Cerci[66] ⓘ, B. Hacisahinoglu ⓘ, I. Hos[73] ⓘ, B. Isildak[74] ⓘ, B. Kaynak ⓘ, S. Ozkorucuklu ⓘ, C. Simsek ⓘ, D. Sunar Cerci[66] ⓘ
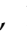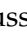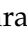
Institute for Scintillation Materials of National Academy of Science of Ukraine, Kharkiv, Ukraine
B. Grynyov ⓘ
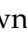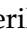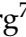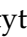
National Science Centre, Kharkiv Institute of Physics and Technology, Kharkiv, Ukraine
L. Levchuk ⓘ
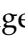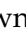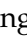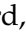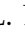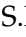
University of Bristol, Bristol, United Kingdom
D. Anthony ⓘ, E. Bhal ⓘ, J.J. Brooke ⓘ, A. Bundock ⓘ, E. Clement ⓘ, D. Cussans ⓘ, H. Flacher ⓘ, M. Glowacki, J. Goldstein ⓘ, G.P. Heath, H.F. Heath ⓘ, L. Kreczko ⓘ, B. Krikler ⓘ, S. Paramesvaran ⓘ, S. Seif El Nasr-Storey, V.J. Smith ⓘ, N. Stylianou[75] ⓘ, K. Walkingshaw Pass, R. White ⓘ

Rutherford Appleton Laboratory, Didcot, United Kingdom
A.H. Ball, K.W. Bell ⓘ, A. Belyaev[76] ⓘ, C. Brew ⓘ, R.M. Brown ⓘ, D.J.A. Cockerill ⓘ, C. Cooke ⓘ, K.V. Ellis, K. Harder ⓘ, S. Harper ⓘ, M.-L. Holmberg[77] ⓘ, J. Linacre ⓘ, K. Manolopoulos, D.M. Newbold ⓘ, E. Olaiya, D. Petyt ⓘ, T. Reis ⓘ, G. Salvi ⓘ, T. Schuh, C.H. Shepherd-Themistocleous ⓘ, I.R. Tomalin ⓘ, T. Williams ⓘ

Imperial College, London, United Kingdom
R. Bainbridge ⓘ, P. Bloch ⓘ, S. Bonomally, J. Borg ⓘ, S. Breeze, C.E. Brown ⓘ, O. Buchmuller, V. Cacchio, V. Cepaitis ⓘ, G.S. Chahal[78] ⓘ, D. Colling ⓘ, J.S. Dancu, P. Dauncey ⓘ, G. Davies ⓘ, J. Davies, M. Della Negra ⓘ, S. Fayer, G. Fedi ⓘ, G. Hall ⓘ, M.H. Hassanshahi ⓘ, A. Howard, G. Iles ⓘ, J. Langford ⓘ, L. Lyons ⓘ, A.-M. Magnan ⓘ, S. Malik, A. Martelli ⓘ, M. Mieskolainen ⓘ, D.G. Monk ⓘ, J. Nash[79] ⓘ, M. Pesaresi ⓘ, B.C. Radburn-Smith ⓘ, D.M. Raymond, A. Richards, A. Rose ⓘ, E. Scott ⓘ, C. Seez ⓘ, A. Shtipliyski, R. Shukla ⓘ, A. Tapper ⓘ, K. Uchida ⓘ, G.P. Uttley ⓘ, L.H. Vage, T. Virdee[19] ⓘ, M. Vojinovic ⓘ, N. Wardle ⓘ, S.N. Webb ⓘ, D. Winterbottom ⓘ

Brunel University, Uxbridge, United Kingdom
K. Coldham, J.E. Cole ⓘ, A. Khan, P. Kyberd ⓘ, I.D. Reid ⓘ

Baylor University, Waco, Texas, USA

S. Abdullin, A. Brinkerhoff, B. Caraway, J. Dittmann, K. Hatakeyama, A.R. Kanuganti, B. McMaster, M. Saunders, S. Sawant, C. Sutantawibul, J. Wilson

Catholic University of America, Washington, DC, USA

R. Bartek, A. Dominguez, R. Uniyal, A.M. Vargas Hernandez
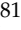
The University of Alabama, Tuscaloosa, Alabama, USA

A. Buccilli, S.I. Cooper, D. Di Croce, S.V. Gleyzer, C. Henderson, C.U. Perez, P. Rumerio[80], C. West
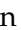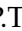
Boston University, Boston, Massachusetts, USA

A. Akpinar, A. Albert, D. Arcaro, C. Cosby, Z. Demiragli, C. Erice, E. Fontanesi, D. Gastler, S. May, J. Rohlf, K. Salyer, D. Sperka, D. Spitzbart, I. Suarez, A. Tsatsos, S. Yuan
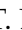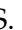
Brown University, Providence, Rhode Island, USA

G. Benelli, B. Burkle, X. Coubez[21], D. Cutts, M. Hadley, U. Heintz, J.M. Hogan[81], T. Kwon, G. Landsberg, K.T. Lau, D. Li, J. Luo, M. Narain, N. Pervan, S. Sagir[82], F. Simpson, E. Usai, W.Y. Wong, X. Yan, D. Yu, W. Zhang

University of California, Davis, Davis, California, USA

J. Bonilla, C. Brainerd, R. Breedon, M. Calderon De La Barca Sanchez, M. Chertok, J. Conway, P.T. Cox, R. Erbacher, G. Haza, F. Jensen, O. Kukral, G. Mocellin, M. Mulhearn, D. Pellett, B. Regnery, D. Taylor, Y. Yao, F. Zhang
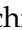
University of California, Los Angeles, California, USA

M. Bachtis, R. Cousins, A. Datta, D. Hamilton, J. Hauser, M. Ignatenko, M.A. Iqbal, T. Lam, W.A. Nash, S. Regnard, D. Saltzberg, B. Stone, V. Valuev
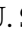
University of California, Riverside, Riverside, California, USA

Y. Chen, R. Clare, J.W. Gary, M. Gordon, G. Hanson, G. Karapostoli, O.R. Long, N. Manganelli, W. Si, S. Wimpenny
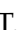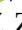
University of California, San Diego, La Jolla, California, USA

J.G. Branson, P. Chang, S. Cittolin, S. Cooperstein, D. Diaz, J. Duarte, R. Gerosa, L. Giannini, J. Guiang, R. Kansal, V. Krutelyov, R. Lee, J. Letts, M. Masciovecchio, F. Mokhtar, M. Pieri, B.V. Sathia Narayanan, V. Sharma, M. Tadel, F. Würthwein, Y. Xiang, A. Yagil
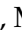
University of California, Santa Barbara - Department of Physics, Santa Barbara, California, USA

N. Amin, C. Campagnari, M. Citron, G. Collura, A. Dorsett, V. Dutta, J. Incandela, M. Kilpatrick, J. Kim, A.J. Li, B. Marsh, P. Masterson, H. Mei, M. Oshiro, M. Quinnan, J. Richman, U. Sarica, R. Schmitz, F. Setti, J. Sheplock, P. Siddireddy, D. Stuart, S. Wang

California Institute of Technology, Pasadena, California, USA

A. Bornheim, O. Cerri, I. Dutta, J.M. Lawhorn, N. Lu, J. Mao, H.B. Newman, T. Q. Nguyen, M. Spiropulu, J.R. Vlimant, C. Wang, S. Xie, R.Y. Zhu
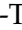
Carnegie Mellon University, Pittsburgh, Pennsylvania, USA

J. Alison, S. An, M.B. Andrews, P. Bryant, T. Ferguson, A. Harilal, C. Liu, T. Mudholkar, S. Murthy, M. Paulini, A. Roberts, A. Sanchez, W. Terrill
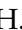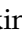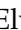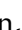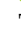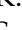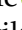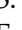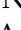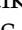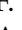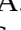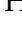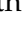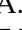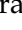
University of Colorado Boulder, Boulder, Colorado, USA
J.P. Cumalat, W.T. Ford, A. Hassani, G. Karathanasis, E. MacDonald, F. Marini, R. Patel, A. Perloff, C. Savard, N. Schonbeck, K. Stenson, K.A. Ulmer, S.R. Wagner, N. Zipper
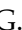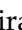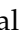
Cornell University, Ithaca, New York, USA
J. Alexander, S. Bright-Thonney, X. Chen, D.J. Cranshaw, J. Fan, X. Fan, D. Gadkari, S. Hogan, J. Monroy, J.R. Patterson, D. Quach, J. Reichert, M. Reid, A. Ryd, J. Thom, P. Wittich, R. Zou
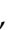
Fermi National Accelerator Laboratory, Batavia, Illinois, USA
M. Albrow, M. Alyari, G. Apollinari, A. Apresyan, L.A.T. Bauerdick, D. Berry, J. Berryhill, P.C. Bhat, K. Burkett, J.N. Butler, A. Canepa, G.B. Cerati, H.W.K. Cheung, F. Chlebana, K.F. Di Petrillo, J. Dickinson, V.D. Elvira, Y. Feng, J. Freeman, A. Gandrakota, Z. Gecse, L. Gray, D. Green, S. Grünendahl, O. Gutsche, R.M. Harris, R. Heller, T.C. Herwig, J. Hirschauer, L. Horyn, B. Jayatilaka, S. Jindariani, M. Johnson, U. Joshi, T. Klijnsma, B. Klima, K.H.M. Kwok, S. Lammel, D. Lincoln, R. Lipton, T. Liu, C. Madrid, K. Maeshima, C. Mantilla, D. Mason, P. McBride, P. Merkel, S. Mrenna, S. Nahn, J. Ngadiuba, V. Papadimitriou, N. Pastika, K. Pedro, C. Pena[83], F. Ravera, A. Reinsvold Hall[84], L. Ristori, E. Sexton-Kennedy, N. Smith, A. Soha, L. Spiegel, J. Strait, L. Taylor, S. Tkaczyk, N.V. Tran, L. Uplegger, E.W. Vaandering, H.A. Weber, I. Zoi

University of Florida, Gainesville, Florida, USA
P. Avery, D. Bourilkov, L. Cadamuro, V. Cherepanov, R.D. Field, D. Guerrero, M. Kim, E. Koenig, J. Konigsberg, A. Korytov, K.H. Lo, K. Matchev, N. Menendez, G. Mitselmakher, A. Muthirakalayil Madhu, N. Rawal, D. Rosenzweig, S. Rosenzweig, K. Shi, J. Wang, Z. Wu
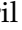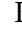
Florida State University, Tallahassee, Florida, USA
T. Adams, A. Askew, R. Habibullah, V. Hagopian, R. Khurana, T. Kolberg, G. Martinez, H. Prosper, C. Schiber, O. Viazlo, R. Yohay, J. Zhang
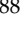
Florida Institute of Technology, Melbourne, Florida, USA
M.M. Baarmand, S. Butalla, T. Elkafrawy[85], M. Hohlmann, R. Kumar Verma, D. Noonan, M. Rahmani, F. Yumiceva

University of Illinois Chicago, Chicago, Illinois, USA
M.R. Adams, H. Becerril Gonzalez, R. Cavanaugh, S. Dittmer, O. Evdokimov, C.E. Gerber, D.J. Hofman, D. S. Lemos, A.H. Merrit, C. Mills, G. Oh, T. Roy, S. Rudrabhatla, M.B. Tonjes, N. Varelas, X. Wang, Z. Ye, J. Yoo
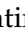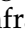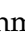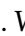
The University of Iowa, Iowa City, Iowa, USA
M. Alhusseini, K. Dilsiz[86], L. Emediato, R.P. Gandrajula, G. Karaman, O.K. Köseyan, J.-P. Merlo, A. Mestvirishvili[87], J. Nachtman, O. Neogi, H. Ogul[88], Y. Onel, A. Penzo, C. Snyder, E. Tiras[89]

Johns Hopkins University, Baltimore, Maryland, USA
O. Amram, B. Blumenfeld, L. Corcodilos, J. Davis, A.V. Gritsan, L. Kang, S. Kyriacou, P. Maksimovic, J. Roskes, S. Sekhar, M. Swartz, T.Á. Vámi
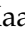
The University of Kansas, Lawrence, Kansas, USA
A. Abreu, L.F. Alcerro Alcerro, J. Anguiano, P. Baringer, A. Bean, Z. Flowers,

T. Isidori, S. Khalil, J. King, G. Krintiras, M. Lazarovits, C. Le Mahieu, C. Lindsey, J. Marquez, N. Minafra, M. Murray, M. Nickel, C. Rogan, C. Royon, R. Salvatico, S. Sanders, E. Schmitz, C. Smith, Q. Wang, J. Williams, G. Wilson
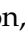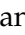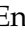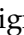
Kansas State University, Manhattan, Kansas, USA
B. Allmond, S. Duric, R. Gujju Gurunadha, A. Ivanov, K. Kaadze, D. Kim, Y. Maravin, T. Mitchell, A. Modak, K. Nam, J. Natoli, D. Roy
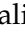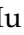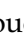
Lawrence Livermore National Laboratory, Livermore, California, USA
F. Rebassoo, D. Wright
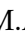
University of Maryland, College Park, Maryland, USA
E. Adams, A. Baden, O. Baron, A. Belloni, A. Bethani, S.C. Eno, N.J. Hadley, S. Jabeen, R.G. Kellogg, T. Koeth, Y. Lai, S. Lascio, A.C. Mignerey, S. Nabili, C. Palmer, C. Papageorgakis, M. Seidel, L. Wang, K. Wong

Massachusetts Institute of Technology, Cambridge, Massachusetts, USA
D. Abercrombie, R. Bi, W. Busza, I.A. Cali, Y. Chen, M. D'Alfonso, J. Eysermans, C. Freer, G. Gomez-Ceballos, M. Goncharov, P. Harris, M. Hu, D. Kovalskyi, J. Krupa, Y.-J. Lee, K. Long, C. Mironov, C. Paus, D. Rankin, C. Roland, G. Roland, Z. Shi, G.S.F. Stephans, J. Wang, Z. Wang, B. Wyslouch
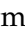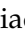
University of Minnesota, Minneapolis, Minnesota, USA
R.M. Chatterjee, B. Crossman, A. Evans, J. Hiltbrand, Sh. Jain, B.M. Joshi, C. Kapsiak, M. Krohn, Y. Kubota, D. Mahon, J. Mans, M. Revering, R. Rusack, R. Saradhy, N. Schroeder, N. Strobbe, M.A. Wadud

University of Mississippi, Oxford, Mississippi, USA
L.M. Cremaldi
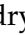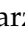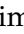
University of Nebraska-Lincoln, Lincoln, Nebraska, USA
K. Bloom, M. Bryson, D.R. Claes, C. Fangmeier, L. Finco, F. Golf, C. Joo, I. Kravchenko, I. Reed, J.E. Siado, G.R. Snow[+], W. Tabb, A. Wightman, F. Yan, A.G. Zecchinelli
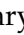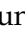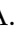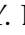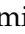
State University of New York at Buffalo, Buffalo, New York, USA
G. Agarwal, H. Bandyopadhyay, L. Hay, I. Iashvili, A. Kharchilava, C. McLean, M. Morris, D. Nguyen, J. Pekkanen, S. Rappoccio, A. Williams
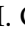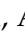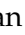
Northeastern University, Boston, Massachusetts, USA
G. Alverson, E. Barberis, Y. Haddad, Y. Han, A. Krishna, J. Li, J. Lidrych, G. Madigan, B. Marzocchi, D.M. Morse, V. Nguyen, T. Orimoto, A. Parker, L. Skinnari, A. Tishelman-Charny, T. Wamorkar, B. Wang, A. Wisecarver, D. Wood

Northwestern University, Evanston, Illinois, USA
S. Bhattacharya, J. Bueghly, Z. Chen, A. Gilbert, T. Gunter, K.A. Hahn, Y. Liu, N. Odell, M.H. Schmitt, M. Velasco
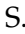
University of Notre Dame, Notre Dame, Indiana, USA
R. Band, R. Bucci, S. Castells, M. Cremonesi, A. Das, R. Goldouzian, M. Hildreth, K. Hurtado Anampa, C. Jessop, K. Lannon, J. Lawrence, N. Loukas, L. Lutton, J. Mariano, N. Marinelli, I. Mcalister, T. McCauley, C. Mcgrady, K. Mohrman, C. Moore, Y. Musienko[12], H. Nelson, R. Ruchti, A. Townsend, M. Wayne, H. Yockey, M. Zarucki, L. Zygala

The Ohio State University, Columbus, Ohio, USA
B. Bylsma, M. Carrigan, L.S. Durkin, B. Francis, C. Hill, A. Lesauvage, M. Nunez Ornelas, K. Wei, B.L. Winer, B. R. Yates

Princeton University, Princeton, New Jersey, USA
F.M. Addesa, B. Bonham, P. Das, G. Dezoort, P. Elmer, A. Frankenthal, B. Greenberg, N. Haubrich, S. Higginbotham, A. Kalogeropoulos, G. Kopp, S. Kwan, D. Lange, D. Marlow, K. Mei, I. Ojalvo, J. Olsen, D. Stickland, C. Tully

University of Puerto Rico, Mayaguez, Puerto Rico, USA
S. Malik, S. Norberg
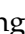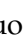
Purdue University, West Lafayette, Indiana, USA
A.S. Bakshi, V.E. Barnes, R. Chawla, S. Das, L. Gutay, M. Jones, A.W. Jung, D. Kondratyev, A.M. Koshy, M. Liu, G. Negro, N. Neumeister, G. Paspalaki, S. Piperov, A. Purohit, J.F. Schulte, M. Stojanovic[15], J. Thieman, F. Wang, R. Xiao, W. Xie

Purdue University Northwest, Hammond, Indiana, USA
J. Dolen, N. Parashar

Rice University, Houston, Texas, USA
D. Acosta, A. Baty, T. Carnahan, M. Decaro, S. Dildick, K.M. Ecklund, P.J. Fernández Manteca, S. Freed, P. Gardner, F.J.M. Geurts, A. Kumar, W. Li, B.P. Padley, R. Redjimi, J. Rotter, W. Shi, S. Yang, E. Yigitbasi, L. Zhang[90], Y. Zhang, X. Zuo
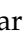
University of Rochester, Rochester, New York, USA
A. Bodek, P. de Barbaro, R. Demina, J.L. Dulemba, C. Fallon, T. Ferbel, M. Galanti, A. Garcia-Bellido, O. Hindrichs, A. Khukhunaishvili, E. Ranken, R. Taus, G.P. Van Onsem

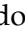**The Rockefeller University, New York, New York, USA**
K. Goulianos

Rutgers, The State University of New Jersey, Piscataway, New Jersey, USA
B. Chiarito, J.P. Chou, Y. Gershtein, E. Halkiadakis, A. Hart, M. Heindl, O. Karacheban[23], I. Laflotte, A. Lath, R. Montalvo, K. Nash, M. Osherson, S. Salur, S. Schnetzer, S. Somalwar, R. Stone, S.A. Thayil, S. Thomas, H. Wang

University of Tennessee, Knoxville, Tennessee, USA
H. Acharya, A.G. Delannoy, S. Fiorendi, T. Holmes, E. Nibigira, S. Spanier

Texas A&M University, College Station, Texas, USA
O. Bouhali[91], M. Dalchenko, A. Delgado, R. Eusebi, J. Gilmore, T. Huang, T. Kamon[92], H. Kim, S. Luo, S. Malhotra, R. Mueller, D. Overton, D. Rathjens, A. Safonov

Texas Tech University, Lubbock, Texas, USA
N. Akchurin, J. Damgov, V. Hegde, K. Lamichhane, S.W. Lee, T. Mengke, S. Muthumuni, T. Peltola, I. Volobouev, Z. Wang, A. Whitbeck

Vanderbilt University, Nashville, Tennessee, USA
E. Appelt, S. Greene, A. Gurrola, W. Johns, A. Melo, F. Romeo, P. Sheldon,

S. Tuo (iD), J. Velkovska (iD), J. Viinikainen (iD)

University of Virginia, Charlottesville, Virginia, USA
B. Cardwell (iD), B. Cox (iD), G. Cummings (iD), J. Hakala (iD), R. Hirosky (iD), M. Joyce (iD), A. Ledovskoy (iD), A. Li (iD), C. Neu (iD), C.E. Perez Lara (iD), B. Tannenwald (iD)

Wayne State University, Detroit, Michigan, USA
P.E. Karchin (iD), N. Poudyal (iD)

University of Wisconsin - Madison, Madison, Wisconsin, USA
S. Banerjee (iD), K. Black (iD), T. Bose (iD), S. Dasu (iD), I. De Bruyn (iD), P. Everaerts (iD), C. Galloni, H. He (iD), M. Herndon (iD), A. Herve (iD), C.K. Koraka (iD), A. Lanaro, A. Loeliger (iD), R. Loveless (iD), J. Madhusudanan Sreekala (iD), A. Mallampalli (iD), A. Mohammadi (iD), S. Mondal, G. Parida (iD), D. Pinna, A. Savin, V. Shang (iD), V. Sharma (iD), W.H. Smith (iD), D. Teague, H.F. Tsoi (iD), W. Vetens (iD)

Authors affiliated with an international laboratory covered by a cooperation agreement with CERN
V. Blinov[93], T. Dimova[93] (iD), L. Kardapoltsev[93] (iD), A. Kozyrev[93] (iD), I. Ovtin[93] (iD), O. Radchenko[93] (iD), Y. Skovpen[93] (iD), A. Babaev (iD), V. Okhotnikov (iD)

Authors affiliated with an institute formerly covered by a cooperation agreement with CERN
S. Afanasiev (iD), D. Budkouski (iD), I. Golutvin (iD), I. Gorbunov (iD), V. Karjavine (iD), V. Korenkov (iD), A. Lanev (iD), A. Malakhov (iD), V. Matveev[93] (iD), V. Palichik (iD), V. Perelygin (iD), M. Savina (iD), V. Shalaev (iD), S. Shmatov (iD), S. Shulha (iD), V. Smirnov (iD), O. Teryaev (iD), N. Voytishin (iD), B.S. Yuldashev[94], A. Zarubin (iD), I. Zhizhin (iD), G. Gavrilov (iD), V. Golovtcov (iD), Y. Ivanov (iD), V. Kim[93] (iD), E. Kuznetsova[95] (iD), P. Levchenko (iD), V. Murzin (iD), D. Sosnov (iD), V. Sulimov (iD), L. Uvarov (iD), A. Vorobyev, Yu. Andreev (iD), A. Dermenev (iD), S. Gninenko (iD), N. Golubev (iD), A. Karneyeu (iD), D. Kirpichnikov (iD), M. Kirsanov (iD), N. Krasnikov (iD), G. Pivovarov (iD), I. Tlisova (iD), A. Toropin (iD), T. Aushev (iD), V. Epshteyn (iD), V. Gavrilov (iD), N. Lychkovskaya (iD), A. Nikitenko[96] (iD), V. Popov (iD), A. Stepennov (iD), M. Toms (iD), E. Vlasov (iD), A. Zhokin (iD), R. Chistov[93] (iD), M. Danilov[93] (iD), A. Oskin, P. Parygin (iD), S. Polikarpov[93] (iD), D. Selivanova (iD), V. Andreev (iD), M. Azarkin (iD), I. Dremin (iD), M. Kirakosyan, A. Terkulov (iD), A. Belyaev (iD), E. Boos (iD), V. Bunichev (iD), M. Dubinin[83] (iD), L. Dudko (iD), A. Ershov (iD), V. Klyukhin (iD), S. Obraztsov (iD), M. Perfilov (iD), S. Petrushanko (iD), V. Savrin (iD), P. Volkov (iD), V. Kachanov (iD), D. Konstantinov (iD), S. Slabospitskii (iD), A. Uzunian (iD), V. Borshch (iD), V. Ivanchenko (iD), E. Tcherniaev (iD), V. Chekhovsky, A. Litomin, V. Makarenko (iD)

†: Deceased
[1]Also at TU Wien, Vienna, Austria
[2]Also at Institute of Basic and Applied Sciences, Faculty of Engineering, Arab Academy for Science, Technology and Maritime Transport, Alexandria, Egypt
[3]Also at Université Libre de Bruxelles, Bruxelles, Belgium
[4]Also at Universidade Estadual de Campinas, Campinas, Brazil
[5]Also at Federal University of Rio Grande do Sul, Porto Alegre, Brazil
[6]Also at UFMS, Nova Andradina, Brazil
[7]Also at The University of the State of Amazonas, Manaus, Brazil
[8]Also at University of Chinese Academy of Sciences, Beijing, China
[9]Also at Nanjing Normal University, Nanjing, China
[10]Now at The University of Iowa, Iowa City, Iowa, USA
[11]Also at University of Chinese Academy of Sciences, Beijing, China
[12]Also at an institute formerly covered by a cooperation agreement with CERN

[13]Now at British University in Egypt, Cairo, Egypt

[14]Now at Cairo University, Cairo, Egypt

[15]Also at Purdue University, West Lafayette, Indiana, USA

[16]Also at Université de Haute Alsace, Mulhouse, France

[17]Also at Department of Physics, Tsinghua University, Beijing, China

[18]Also at Erzincan Binali Yildirim University, Erzincan, Turkey

[19]Also at CERN, European Organization for Nuclear Research, Geneva, Switzerland

[20]Also at University of Hamburg, Hamburg, Germany

[21]Also at RWTH Aachen University, III. Physikalisches Institut A, Aachen, Germany

[22]Also at Isfahan University of Technology, Isfahan, Iran

[23]Also at Brandenburg University of Technology, Cottbus, Germany

[24]Also at Forschungszentrum Jülich, Juelich, Germany

[25]Also at Institute of Physics, University of Debrecen, Debrecen, Hungary

[26]Also at HUN-REN ATOMKI - Institute of Nuclear Research, Debrecen, Hungary

[27]Now at Universitatea Babes-Bolyai - Facultatea de Fizica, Cluj-Napoca, Romania

[28]Also at Physics Department, Faculty of Science, Assiut University, Assiut, Egypt

[29]Also at Karoly Robert Campus, MATE Institute of Technology, Gyongyos, Hungary

[30]Also at HUN-REN Wigner Research Centre for Physics, Budapest, Hungary

[31]Also at Faculty of Informatics, University of Debrecen, Debrecen, Hungary

[32]Also at Punjab Agricultural University, Ludhiana, India

[33]Also at UPES - University of Petroleum and Energy Studies, Dehradun, India

[34]Also at University of Visva-Bharati, Santiniketan, India

[35]Also at University of Hyderabad, Hyderabad, India

[36]Also at Indian Institute of Science (IISc), Bangalore, India

[37]Also at Indian Institute of Technology (IIT), Mumbai, India

[38]Also at IIT Bhubaneswar, Bhubaneswar, India

[39]Also at Institute of Physics, Bhubaneswar, India

[40]Also at Deutsches Elektronen-Synchrotron, Hamburg, Germany

[41]Now at Department of Physics, Isfahan University of Technology, Isfahan, Iran

[42]Also at Sharif University of Technology, Tehran, Iran

[43]Also at Department of Physics, University of Science and Technology of Mazandaran, Behshahr, Iran

[44]Now at INFN Sezione di Bari, Università di Bari, Politecnico di Bari, Bari, Italy

[45]Also at Italian National Agency for New Technologies, Energy and Sustainable Economic Development, Bologna, Italy

[46]Also at Centro Siciliano di Fisica Nucleare e di Struttura Della Materia, Catania, Italy

[47]Also at Scuola Superiore Meridionale, Università di Napoli 'Federico II', Napoli, Italy

[48]Also at Università di Napoli 'Federico II', Napoli, Italy

[49]Also at Consiglio Nazionale delle Ricerche - Istituto Officina dei Materiali, Perugia, Italy

[50]Also at Riga Technical University, Riga, Latvia

[51]Also at Department of Applied Physics, Faculty of Science and Technology, Universiti Kebangsaan Malaysia, Bangi, Malaysia

[52]Also at Consejo Nacional de Ciencia y Tecnología, Mexico City, Mexico

[53]Also at IRFU, CEA, Université Paris-Saclay, Gif-sur-Yvette, France

[54]Also at Faculty of Physics, University of Belgrade, Belgrade, Serbia

[55]Also at Trincomalee Campus, Eastern University, Sri Lanka, Nilaveli, Sri Lanka

[56]Also at Saegis Campus, Nugegoda, Sri Lanka

[57]Also at INFN Sezione di Pavia, Università di Pavia, Pavia, Italy

[58]Also at National and Kapodistrian University of Athens, Athens, Greece

[59]Also at Ecole Polytechnique Fédérale Lausanne, Lausanne, Switzerland

[60]Also at Universität Zürich, Zurich, Switzerland

[61]Also at Stefan Meyer Institute for Subatomic Physics, Vienna, Austria

[62]Also at Laboratoire d'Annecy-le-Vieux de Physique des Particules, IN2P3-CNRS, Annecy-le-Vieux, France

[63]Also at Near East University, Research Center of Experimental Health Science, Mersin, Turkey

[64]Also at Konya Technical University, Konya, Turkey

[65]Also at Izmir Bakircay University, Izmir, Turkey

[66]Also at Adiyaman University, Adiyaman, Turkey

[67]Also at Necmettin Erbakan University, Konya, Turkey

[68]Also at Bozok Universitetesi Rektörlügü, Yozgat, Turkey

[69]Also at Marmara University, Istanbul, Turkey

[70]Also at Milli Savunma University, Istanbul, Turkey

[71]Also at Kafkas University, Kars, Turkey

[72]Also at Hacettepe University, Ankara, Turkey

[73]Also at Istanbul University - Cerrahpasa, Faculty of Engineering, Istanbul, Turkey

[74]Also at Ozyegin University, Istanbul, Turkey

[75]Also at Vrije Universiteit Brussel, Brussel, Belgium

[76]Also at School of Physics and Astronomy, University of Southampton, Southampton, United Kingdom

[77]Also at University of Bristol, Bristol, United Kingdom

[78]Also at IPPP Durham University, Durham, United Kingdom

[79]Also at Monash University, Faculty of Science, Clayton, Australia

[80]Also at Università di Torino, Torino, Italy

[81]Also at Bethel University, St. Paul, Minnesota, USA

[82]Also at Karamanoğlu Mehmetbey University, Karaman, Turkey

[83]Also at California Institute of Technology, Pasadena, California, USA

[84]Also at United States Naval Academy, Annapolis, Maryland, USA

[85]Also at Ain Shams University, Cairo, Egypt

[86]Also at Bingol University, Bingol, Turkey

[87]Also at Georgian Technical University, Tbilisi, Georgia

[88]Also at Sinop University, Sinop, Turkey

[89]Also at Erciyes University, Kayseri, Turkey

[90]Also at Institute of Modern Physics and Key Laboratory of Nuclear Physics and Ion-beam Application (MOE) - Fudan University, Shanghai, China

[91]Also at Texas A&M University at Qatar, Doha, Qatar

[92]Also at Kyungpook National University, Daegu, Korea

[93]Also at another institute formerly covered by a cooperation agreement with CERN

[94]Also at Institute of Nuclear Physics of the Uzbekistan Academy of Sciences, Tashkent, Uzbekistan

[95]Also at University of Florida, Gainesville, Florida, USA

[96]Also at Imperial College, London, United Kingdom